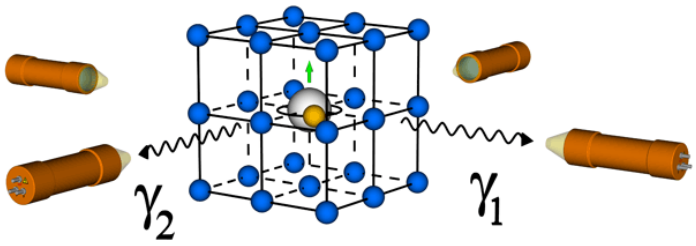

Local probing spinel and perovskite complex magnetic systems

Gonçalo Oliveira
MAP-FIS doctoral Program in Physics
Department of Physics and Astronomy
Faculty of Sciences
University of Porto
2017

Supervisor
Prof. João Pedro Esteves de Araújo, FCUP

Co-Supervisor
Dr. Armandina Maria Lima Lopes, FCUP

Gonçalo Nuno de Pinho Oliveira

Local Probing spinel and perovskite complex magnetic systems

Supervisor: *Prof. João Pedro Esteves de Araújo*
Co-Supervisor: *Dr. Armandina Maria Lima Lopes*

Thesis submitted to the Faculty of Sciences of the University of Porto in partial fulfilment of the requirements for the degree of Doctor in Physics

Department of Physics and Astronomy
Faculty of Sciences of the University of Porto
2017

Institutions involved in this thesis:

Funding:

“The Wheel of Time turns, and Ages come and pass, leaving memories that become legend. Legend fades to myth, and even myth is long forgotten when the Age that gave it birth comes again. In one Age, called the Modern Age by some, an Age yet to come, an Age long past, a wind rose in the Mountains of Mist. The wind was not the beginning. There are neither beginnings nor endings to the turning of the Wheel of Time. But it was a beginning.”

***Robert Jordan**,*
“The Wheel of Time Series”

Acknowledgements

Over the last years, I had the privilege of working with different people, in different places and in different conditions. In all those situations I have been surrounded by professionals who helped me one way or another in the progress of my work and to whom I will always save a space in my heart. Unfortunately, here, I can only name some, so A big ”THANK YOU” to all those who know who they are.

First, I would like to thank the organizations involved in my work because without them, among other things I would not have a space to work: the Institute of Nanoscience and Nanotechnology (IFIMUP-IN) of the University of Porto, the Center of Nuclear Physics of Lisbon university (CFNUL), the Nuclear and Technological Institute (now Center of Sciences and Nuclear Technologies C2TN), the Physics and Astronomy department of the Faculty of Sciences of University of Porto (FCUP), Fundação para a Ciência e a Tecnologia (FCT) and the European Organization for Nuclear Research (CERN). Also, FCT for my PhD scholarship with reference SFRH/BD/80112/2011.

Secondly, I am truly grateful to a large number of people which have assisted me during the last years that I would like to leave a personal word of acknowledgement:

I am sincerely grateful to my supervisor, Professor Doctor João Pedro Araújo, from IFIMUP-IN, who has welcome me in his group, giving me the opportunity to work with him and his co-workers. For everything he did for me.

To my co-supervisor Doctor Armandina Maria Lima Lopes for the opportunity to work in such wonderful environment during this period; for the opportunity to work with a very exotic technique. Without her constant dedication and motivation this work could never have even been started. For her encouragement and guidance during my pos-graduate studies.

I have to express my gratitude to all members of IFIMUP-IN, for all their dedication, support and friendship. They showed to be good coworkers but above all showed to be very good friends. Their help and support were crucial to overcome the many difficulties and those moments when everything seemed to go wrong.

They are (in alphabetic order): Ana Pires, André Pereira, Aurélio, Arlete Apolinário, Catarina Dias, Célia Sousa, Daniel silva, Francisco Carpinteiro, Inês Figueiredo, João Amaral, João Horta, João Ventura, Joel Puga, José Miguel Teixeira, Luís Guerra, Maria Paz, Mariana Proença, Marcelo Barbosa, Paula Quitério, Sara Pinto, Rita Ribeiro and Tânia Mendonça.

A very special thanks to André Pereira is needed, for always being there helping me and for believing in my work. For his timeless patience helping me with fullprof, Origin, Carine, ... and tutoring me how to operate many of the experiments I had to work with.

I will not forget his help and the many conversations we shared since the time we were shift partners at the ISOLDE-CERN experiment runs. For all the scientific talks and insights but mostly for his friendship and encouraging words in the ”low” states that sometimes I found myself in. For all the places he showed me and for the conferences which we attended together that with his presence were more interesting. If everything else fail we will always have Grenoble and Dresden :).

To João Ventura for the ”nagging” all the time but most importantly for the right words in crucial times.

To João Horta as a friend and as collaborator. For all those breaks and coffees...they where in dire need.

To Arlete Apolinário for the cheering and personality. Always with a positive personality to cheer me and all those around her.

To Ana Pires for the friendship and the great moments during lunch ”I say things without thinking them first”. To Inês Figueiredo for the friendship and amazing personality. You have been two rays of sunshine in a cloudy day.

To Joel Puga for his friendship and for the group ”RunForrestRun”.

To Francisco Carpinteiro for the crucial help in maintaining the experiments and fabricating many of the set-ups I had to work with.

To Ricardo Teixeira my ”PAC partner” and friend.

To the other members of IFIMUP-IN, the professionalism and constant dedication of Isabel Alves for helping in many bureaucratic aspects of a researcher life.

To all members of the ISOLDE Collaboration at cern, specially Doctor João Guilherme Correia, who kept an eye on the progress of my work. Whom I thank for providing the Perturbed Angular Correlation (PAC) spectrometers helping in the experiments and to all those who helped at some point in the PAC experiments. To Karl Johnston for the support and professionalism during the beam times.

To Doctor Pedro Tavares that was always available when I needed his advice and for allowing the use of the x-ray diffractometer from the Electronic Microscopy Unit in the University of Trás- os-Montes e Alto-Douro (UTAD).

I would also like to acknowledge Doctor Lurdes Gano and the Center of Nuclear Physics of the University of Lisbon for the support they gave me, especially in the PAC diffusion experiments.

Finally, I thank my family, especially my parents, for their unwavering support throughout my educational career.

My deepest gratitude goes to my girlfriend Inês, whose support and encouragement during graduate school made it all worthwhile. Through all the ups and downs her patience, love, and kindness has filled my life with balance and happiness. We have shared many wonderful experiences together and I look forward where the future will take us.

I deeply apologize if I forgot anyone.

Resumo

Materiais multifuncionais que integram duas ou mais propriedades físicas são cruciais para uma sociedade moderna, especialmente aqueles que exibem um forte acoplamento entre os graus de liberdade da estrutura, do spin e da carga. Esta capacidade, ainda muito inexplorada, promete trazer uma mudança no paradigma no que respeita ao desenvolvimento de novas tecnologias nas áreas da refrigeração, armazenamento magnético de dados, dispositivos magnéticos de alta frequência, spintronica, e sistemas micro-eletromecânicos.

Além da compreensão das propriedades destes materiais, nos dias de hoje, temos também como objetivo paralelo melhorar-los, tornar-los mais pequenos e mais eficientes. A miniaturização de dispositivos, aumentando a capacidade de armazenamento de dados é também considerada uma tendência do ponto vista da ciência e tecnologia moderna. Nesta área, a integração de várias funções num sistema material tornou-se altamente desejável.

A investigação nesta área já salientou materiais magnéticos complexos com potencial para aplicações multifuncionais baseados em estruturas do tipo espinela tal como $CdMn_2O_4$, multifferroico $CdCr_2S_4$ ou ainda em estruturas ortorrômbicas distorcidas da familia das perovskites $RCrO_3$.

Entretanto, a alta sensibilidade dos óxidos complexos para distorções da rede cristalina oferece muitos outros caminhos para fabricação e desenvolvimento de novos materiais funcionais.

Tendo em mente estas ideias, esta tese amplia o conhecimento sobre as propriedades macroscópicas de materiais que exibem potencial para se tornarem materiais multifuncionais, almejando melhorar as propriedades multiferróicas dos mesmos e contribuir para uma melhor compreensão do acoplamento magneto-elétrico a nível fundamental (a sua origem e formas de os melhorar), abrindo deste modo um caminho para a redução de escala destes materiais e assim ganhar a possibilidade de os incorporar em nano-estruturas. Estas propriedades são analisadas junto às transições de fase, induzidas através de diferentes estímulos externos, tal como temperatura, pressão, campo elétrico ou magnético. De modo a atingirem-se estes objetivos foi seguida uma estratégia complementada em três frentes: O uso adequado de ferramentas de síntese para a produção dos materiais com as composições desejadas; Estudo do efeito magneto-elétrico e das ordens ferroicas nos compostos sintetizados usando estudos tradicionais de caracterização magnética, elétrica e de polarização. Combinação da informação obtida à escala local (análise do campo magnético hiperfino, do gradiente de campo elétrico e de informações da estrutura local) com os dados macroscópicos e

deste modo obter assinaturas locais do efeito magneto-elétrico, permitindo uma melhor compreensão, do ponto de vista fundamental, da origem das propriedades exibidas por estes sistemas macroscopicamente.

Em particular, esta tese centra-se no desenvolvimento da síntese de materiais, na caracterização geral, em estudos físicos alargados e em estudos à escala local. As propriedades da espinela calcogenoide de enxofre $CdCr_2S_4$ foram investigadas com detalhe e revelaram um deslocamento do ião magnético Cr da sua posição central de equilíbrio, originando desta forma uma correlação peculiar entre os graus de liberdade elétrico e magnéticos, que se estabilizam na fase paramagnética, na forma de aglomerados onde a interação magnética é de curto alcance. O efeito da pressão hidrostática nos resultados de magnetização e difração de raios-x mostram que existe uma competição entre as interações de troca direta (ferromagnética) e de super-troca (antiferromagnética) neste material. Os aglomerados com interação magnética de curto alcance originados pelas distorções locais do Cr são fortemente influenciados pelo aumento da pressão, influenciando assim as propriedades magnéticas macroscópicas do composto $CdCr_2S_4$.

Foram também estudadas neste trabalho as manganites ($CdMn_2O_4$) e as suas tão características distorções Jahn-Teller. Paralelamente com a interessante aplicabilidade, estes materiais proporcionam um campo de trabalho fértil para a física fundamental, onde a (potencial) frustração, as distorções locais, as interações de curto alcance, e os mecanismos dinâmicos ainda não são completamente compreendidos. As distorções tetragonais da manganite com estrutura de espinela $CdMn_2O_4$ foram estudadas à escala atómica através da evolução do gradiente de campo elétrico com a temperatura. Observou-se uma distorção dinâmica da estrutura, evidenciada por flutuações dependentes do tempo do gradiente de campo elétrico, o que sugere a presença de uma instabilidade estrutural neste material. Embora nenhuma transição de fase macroscópica (tetragonal para cúbica) tenha sido observada a alta temperatura, a nível local os octaedros de MnO_6 surgem com distorções Jahn-Teller relaxadas numa matriz não distorcida e o seu numero cresce com o aumento da temperatura.

Ortocromites com terras raras na sua composição com a fórmula $RCrO_3$ (R=Yb, Er, Y ou Sm), têm mostrado um grande potencial para serem utilizadas como materiais multifuncionais em diversas aplicações. Nesta tese, apresentamos os resultados de medidas de magnetização, estrutura e de propriedades magnetocalóricas num magnete duro, $YCrO_3$. A refrigeração magnética baseada no efeito magnetocalórico tem dado passos de gigante nos últimos anos e, hoje em dia, promete tornar-se uma ferramenta de refrigeração para aplicações à temperatura ambiente e bem como temperaturas criogénicas. Assim, de modo a maximizar as propriedades magnetocalóricas destes materiais, estudou-se o efeito da pressão química nestas estruturas ortorrômbicas da família das perovskites (mudando R=Yb, Er, Y, Sm) sobre esta propriedade e na capacidade de refrigeração. Discute-se também a influência da utilização de um átomo magnético R (R=Yb, Er, Sm) nessas estruturas e o seu efeito nas referidas

propriedades.

Por fim, apresentamos um estudo à escala atómica do gradiente de campo elétrico e do campo magnético hiperfino nestas estruturas encontrando-se uma correlação entre os nossos resultados com o proposto aparecimento de ferroeletricidade nestes materiais.

Abstract

Materials with multifunctional physical properties are crucial for the modern society, especially those which display a strong coupling between magnetic, lattice and polar degrees of freedom. This by far unexploited capability promises new paradigm-shift technologies for cooling technologies, magnetic data storage, high-frequency magnetic devices, spintronics, and micro-electromechanical systems.

Alongside with the understanding of the properties of these materials, the need to improve them and to make them smaller and more efficient is a current goal. Device miniaturization towards very high-density data storage stands also as a trend in modern science and technology. Here, the integration of several functions into one material system has become highly desirable.

Research in this area has already highlighted complex magnetic materials with potential for multifunctional applications based on spinel type structures like $CdMn_2O_4$ or multiferroic $CdCr_2S_4$ or even $RCrO_3$ with orthorhombically distorted perovskite structure.

Nevertheless, the high sensitivity of complex oxides to crystal chemistry and lattice distortions offers many paths to tailor and engineer new functional materials.

Following these ideas, this thesis extends the knowledge about the bulk properties of some potential multifunctional materials, aiming to enhance multiferroic properties and to contribute to the fundamental understanding of magnetoelectric coupling (its origin and how to enhance it). In this way, it opens a pathway for the down scaling of these materials namely for the incorporation into nanostructures. The material's properties are analyzed across phase transitions induced by different external stimuli such as temperature, pressure, magnetic or electric field. To achieve these goals a three way complementary strategic research was followed: Use of adequate experimental synthesis tools for the production of materials of desired compositions; Study the magnetoelectric effect and ferroic orders in synthesized compounds using traditional magnetic/dielectric and polarization studies; Combining local scale information (analysis of the magnetic hyperfine field, electric field gradient and local structural information) with macroscopic data to obtain local signatures of the magnetoelectric effect and to better understand, from a fundamental point of view, the origin of the macroscopic properties they exhibit.

In particular, this thesis focuses on the development of materials synthesis, general characterization, extended physical studies combined local scale ones. We investigated in detail the properties of chalcogenide sulphur spinel $CdCr_2S_4$ and unveiled the off-centering of the magnetic $Cr-$ion which gives rise to a peculiar entanglement between the polar and magnetic degrees of freedom, stabilizing, in the paramagnetic phase,

short range magnetic clusters. Our DC magnetization results and x-ray diffraction measurements under hydrostatic pressure show that a competition between direct antiferromagnetic and superexchange ferromagnetic interactions exists in this compound. The short-range magnetic clusters promoted by the Cr local distortions are strongly influenced by pressure increase, thus influencing the $CdCr_2S_4$ magnetic properties.

Manganites and their characteristic Jahn-Teller distortion were also studied in this thesis. Alongside with their interesting applicability, these materials provide a fertile playground for fundamental physics, where (the potential) frustration, local distortions, local range order, and dynamic mechanisms are yet to be fully understood. Here, the tetragonally distorted $CdMn_2O_4$ spinel manganite was studied trough atomic scale probing of the electric field gradient. We observed a dynamic lattice distortion, evidenced by time dependent EFG fluctuations, suggesting a structural instability in this material. Although no macroscopic tetragonal to cubic phase transition was observed at high temperature, local MnO_6 octahedra with relaxed Jahn-Teller distortions emerged in non-distorted matrix and their number grew with raising temperature.

Finally, we studied rare earth orthochromites with the formula $RCrO_3$ (R = Yb, Er, Y or Sm) which show great potential application as multifunctional materials. We present the results of structural, DC magnetization measurements and magnetocaloric properties for $YCrO_3$ hard magnet. Magnetic refrigeration based on the magnetocaloric effect has given giant steps in recent years and promises, nowadays, to become a cooling tool for both cryogenic and room temperature applications. Thus, in order maximize such magnetocaloric properties in these materials, we studied the effect of chemical pressure (by changing R = Yb, Er, Y, Sm) on the magnetocaloric effect and refrigerant capacity properties of these orthorhombic perovskite-like structures. The influence of using R-magnetic atoms (R = Yb, Er, Sm) in these properties is also analyzed. Finally, we present an atomic scale study of the electric field gradient and magnetic hyperfine field in these structures and correlate our findings with the appearance of ferroelectricity.

Contents

List of Figures

List of Tables

List of Abreviations

- **AFM**, Antiferromagnetic
- **BSE**, Backscattered Electrons
- **C2TN**, Centro de Ciências e Tecnologias Nucleares
- **CEMUP**, Centro de Materiais da Universidade do Porto
- **CERN**, European Organization for Nuclear Research
- **CMCE**, Colossal Magnetocaloric Effect
- **CMR**, Colossal Magnetoresistence
- **DFT**, Density Functional Theory
- **DM**, Dzyaloshinskii-Moriya
- **EDS**, Energy Dispersive X-ray Spectroscopy
- **EDX**, Energy Dispersive X-ray Spectroscopy
- **EFG**, Electric Field Gradient
- **E**, Electric Field
- **ESCA**, Electron Spectroscopy for Chemical Analysis
- **FC**, Field-Cooling
- **FCC**, Field-Cool Cooling
- **FCH**, Field-Cool Heating
- **FCUP**, Faculdade Ciências da Universidade do Porto
- **FE**, Ferroelectric
- ***F***, Free Energy
- **FEP**, Ferroelectric Polarization
- **FeRAMs**, Ferroelectric Random-Access Memories
- **FLAPW**, Full-Potential Linearized-Augmented Plane-Wave
- **FM**, Ferromagnetic
- **FOPT**, First Order Phase Transition
- **FWHM**, Full Width at Half Maximum
- **GGA**, Generalized Gradient Approximation
- **GKA**, Goodenough-Kanamori-Anderson
- **GMCE**, Giant Magnetocaloric Effect
- **GMR**, Giant Magnetoresitance
- ***H***, Magnetic Field
- **HI**, Hyperfine Interactions
- **IFIMUP-IN**, Instituto de Física dos Materiais da Universidade do Porto
- **ISOLDE**, On-line Isotope Mass Separator
- **JT**, Jahn-Teller
- **LE**, Local Environment
- **LRMI**, Long Range Magnetic Interactions
- **LSDA**, Local-Density Approximation
- ***M***, Magnetization
- **MCE**, Magnetocaloric Effect
- **ME**, Magnetoelectric
- **MES**, Mössbauer Effect Spectroscopy
- **MHF**, Magnetic Hyperfine Field
- **MRAMs**, Magnetic random-access memories
- **MR**, Magnetic Refrigeration
- **MMMN**, Multifunctional Magnetic Materials and Nanostructures
- **NMR**, Nuclear Magnetic Resonance
- **NO**, Nuclear Orientation
- **PAC**, Perturbed Angular Correlations
- **PAD**, Perturbed Angular Distribution
- **PCM**, Point Charge Model
- **PDF**, Pair Distribution Function
- **P**, Polarization

- **PSB**, Proton-Synchrotron Booster
- **PXRD**, Powder X-ray Diffraction
- **RKKY**, Rudermann-Kittel-Kasuya-Yosida
- **RT**, Room Temperature
- **SSR**, Solid State Reaction
- **SE**, Secondary Electrons
- **SGM**, Sol-Gel Method
- **SOPT**, Second Order Phase Transition
- **SQUID**, Superconducting Quantum Interference Device
- **SRMC**, Short Range Magnetic Correlations
- **SRMI**, Short Range Magnetic Interactions
- **SRMO**, Short Range Magnetic Ordering
- **TGA**, Thermogravimetric Analysis
- **TIM**, Insulator-Metal Transition
- **TSL**, Triangular Spin Lattice
- ***V***, Volume
- **XAS**, X-ray Absorption Spectroscopy
- **XPS**, X-ray Photoelectron Spectroscopy
- **XRD**, X-ray Diffraction
- **ZFC**, Zero Field Cooling
- N_A, Avogadro's number
- ΔT_{ad}, Adiabatic Temperature change
- k_B, Boltzman constant
- μ_B, Bohr magneton
- θ_P, Curie-weiss Temperature
- $\Delta\chi$, Variation of Magnetic Susceptibility
- μ_{eff}, Effective paramagnetic moment
- J_{AFM}, Antiferromagnetic interaction
- J_{FM}, Ferromagnetic interaction
- ΔS_M, Magnetic Entropy change
- B_{hf}, Magnetic Hyperfine Field
- χ, Magnetic susceptibility
- $M(H)$, M vs H
- $M(T)$, M vs T
- $P(E)$, P vs E
- χ^{-1}, Reciprocal susceptibility
- σ, Stress
- ϵ, Strain
- T_C, Curie Temperature
- T_N, Néel Temperature
- T, Temperature
- T_{PM}, Temperature Polar-Magnetic interaction
- T_{SR}, Spin Reorientation Temperature

Thesis outline

The coupling between magnetic, strain and dielectric degrees of freedom recently revived the interest on multiferroics oxides. Profiting from such an exquisite coupling multiferroic oxides promise to be key materials to future multifunctional devices. The present thesis addresses the production of materials with magnetic/electric enhanced properties and aims to contribute to a better comprehension of the magnetoelectric coupling in multiferroic oxides, following three complementary strategic research vectors: The production of these materials and the use of advanced experimental techniques to physically study the materials aiming, in the future, to tune competing interactions and down-scaling, having always in mind the search for novel phenomena. To achieve multi-scale insight, to unveil the underlying physics grounding the ferroic orders and their coupling, local scale studies were performed and combined with macroscopic ones.

Accordingly, the major aim of this thesis was to produce solid state samples and study the mechanisms responsible for them having multiferroic properties (at macro and nanoscale) with the possibility to be used in multifunctional devices. This thesis reports the work developed on the synthesis and characterization of those materials. All samples were produced by solid state reaction from respective oxide precursors. Structural, magnetic and electric characterization were performed at the macroscopic scale. Additionally, local scale studies were performed to unveil the origin of many properties of these materials by means of Perturbed Angular Correlation and Pair Distribution Function.

This PhD work has been performed under the collaboration between the research group of Multifunctional Magnetic Materials and Nanostructures (MMMN) from Instituto de Física dos Materiais da Universidade do Porto (IFIMUP-IN Institute of Nanoscience and Nanotechnology) at the Faculty of Sciences of the Porto University (FCUP) led by Prof. João Pedro Araújo, the research Laboratory from Centro de Física Nuclear da Universidade de Lisboa, at the interdisciplinary Complex of the Universidade de Lisboa led by Dra. Armandina Lopes and the research facility ISOLDE at the research center CERN in Switzerland led by Dr. João Guilherme Correia.

This thesis is structured in 6 chapters, comprising an Introduction, the Experimental techniques, 3 chapters on the main Results and Discussion and a chapter with Conclusions and Future Perspectives. A brief summary is given:

Chapter 1 introduces the field of multiferroic and magnetoelectric materials. We present the basic principles of these materials giving an historical background; Also we aim to give a perspective about the importance of these materials and about the physics underlying their properties.

In Chapter 2 we present a summary of the used experimental techniques. This comprises the synthesis method (solid state reaction), followed by a detailed description of the characterization techniques (such as Electron Microscopy, X-Ray diffraction, Superconducting Quantum Interference Device magnetometer, Perturbed Angular Correlation and Pair Distribution Function techniques).

Chapter 3 presents a study on the properties of cadmium chalcogenide sulphur spinel $CdCr_2S_4$. The chapter is composed by two major sections. Section 3.1 reports on the off-centering of the magnetic $Cr-$ion that gives a peculiar entanglement between the polar and magnetic degrees of freedom, stabilizing, in the paramagnetic phase, short range magnetic clusters. Section 3.2 follows the work of the previous section, where we further pursuit the nature of these short range magnetic clusters. Our results of dc magnetization and x-ray diffraction measurements under hydrostatic pressure show that the $CdCr_2S_4$ magnetic properties are strongly sensitive to pressure variations and the Cr local distortions promote a competition between direct exchange antiferromagnetic and superexchange ferromagnetic interactions within the short-range magnetic clusters.

Chapter 4 deals with the Jahn-Teller distortion characteristic of manganites. The tetragonally distorted $CdMn_2O_4$ spinel manganite is local-probed by studying the electric field gradient. We observed a dynamic lattice distortion, evidenced by time dependent EFG fluctuations, suggesting a structural instability in this material. Although no macroscopic tetragonal to cubic phase transition was observed at high temperature, a local MnO_6 octahedra with relaxed Jahn-Teller distortions emerged and growed in number within the low temperature matrix.

In chapter 5 we present a study of rare earth orthochromites with the formula $RCrO_3$ (R = Yb, Er, Y or Sm) which show great potential applications as multifunctional materials. Within the chapter three sections are presented. In the first section, section 5.1, we present the results of structural, dc magnetization measurements and magnetocaloric properties for $YCrO_3$ hard magnet. Section 5.2 shows the effect of chemical pressure (by changing R = Yb, Er, Y or Sm) on the magnetocaloric effect and refrigerant capacity properties of these orthorhombic perovskite-like structures. It is also discussed the influence of using R-magnetic atoms in these properties. In section 5.3 we present an atomic scale study of the electric field gradient and magnetic hyperfine field in these structures and correlate our findings with the appearance of ferroelectricity.

Finally, the main conclusions and perspectives are summarized in Chapter 6.

CHAPTER 1

Introduction

In the beginning of mankind technology was used as a tool for making survival an easier endeavor. The development, synthesis and use of new materials with desired properties has changed considerably the quality of life and nowadays it has been elevated to such level that it has a major impact on modern society. The use of these materials in a vast field of applications has marked entire civilizations and sometimes even categorizes periods in the human history.

Our society has witnessed (or, should we say, has demanded) a shift in the role of technology. The influence that it has over us is at a level that one could dare to say that we cannot live without it. Nevertheless, it will continue to play its role for generations to come. In the modern-day world, it is no longer a tool for survival but a tool for communication, entertainment, life support among others. We can even dare to say that technology governs our day to day life (see Fig. 1.1).

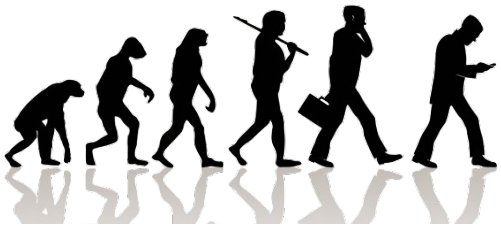

Figure 1.1 – Illustration of technology evolution.

Technology, whereas in the form of applications or devices, has a close relation with the development and understanding of materials. Thus, we can say that inorganic ceramic materials are a big factor to take into consideration in the development of new technological items. Among the diversity of materials available around us, there are those that exhibit certain properties which make them more appealing. The magnetic, piezoelectric, pyroelectric and ferroelectric materials, just to name some, have a vast influence in most aspects of modern science and technology[1,2].

The twenty-first century saw the rise of the number of materials where the exquisite coupling between lattice, spin, orbit and charge degrees of freedom still challenges our understanding and offers the prospect for new applications and devices. Applications and devices, that in part due to miniaturization, require more and more the use of mate-

rials presenting not only one interesting property but the more the merrier. This leads, thus, to the development and study of multifunctional materials.

1.1 Multifunctional materials

Multifunctional materials are those designed and fabricated to meet specific needs and applications through the tailoring of their properties. Sometimes also designated by smart materials because they have the ability to react upon an external stimulus and in this way, give a desired response. Furthermore, many of these materials are designed to mimic nature, but with improved performances and durability. In this way, materials science is now capable of producing materials built from molecules to complete structures presenting specific desirable electronic, magnetic, optical, thermal, or other properties to satisfy previously unattainable performance metrics. Here, the different properties exhibited by them are combined with each other, or with specific mechanical properties including stiffness, ductility, and strength. With these ideas in background, production of materials has become so challenging that nowadays, *e.g.* Physics, Chemistry, Biology work side by side in their pursuit[3].

In one hand, composite materials can be considered multifunctional, because by a proper selection of different materials assembling them together, with the right combination, one achieves a new material with multifunctionality. On the other hand, almost all biological material systems which typically are granted with a superior set of properties are composites that can perform astonishing well a variety of functions (*e.g.*, the bones are natural organic/inorganic composites that have various important functions such as supporting the body, moving the muscles, and producing blood). Furthermore, nature itself present us, already with a great number of multifunctional materials, that have, among other, functions as sensing, actuating and healing[4,5]. In this way, an increasing number of materials with multifunctionalities is achieved by mimicking the structural formations created by nature from nano to micro and to macroscales (bottom-up design approach).

In a broad spectrum analysis, multifunctional materials can be divided into three groups: structural composite materials, smart or intelligent materials or nanostructured materials.

Structural composite materials are composed of individual phases, a matrix phase that surrounds that of the reinforcement giving the structure support and the reinforcement ones, with special properties that enhances those of the matrix[4]. The combination of materials in this way, provide a unique final character to the product.

Examples of reinforcing of materials can be found throughout history (ancient Greeks used to cement iron rods into marbles so as to increase the span in marble building constructions) but major advances are usually connected to periods of great instability in history, namely wars. It has been during First and Second World Wars that this tech-

nology blossomed, *e.g.* glass fiber was developed as a substitute for asbestos[6] and applications in tooling, as filament winding and sandwich structures or fire resistance composites[7].

The evolution of composite materials has reached a state of development that now it's providing engineering applications with special material combinations that can address strict requirements and withstand very demanding environments. At the present state, composites such as glass and carbon fiber reinforced plastics, can be easily tailored (as far as strength and stiffness are considered) to suit the requirements of their end applications, however only a single combination of properties can be meet. New emerging challenging applications and mixtures are in the background of developing multifunctional composite structures, like multifunctional wearable devices for diagnosis and therapy of movement disorders, as shown in Fig. 1.2.

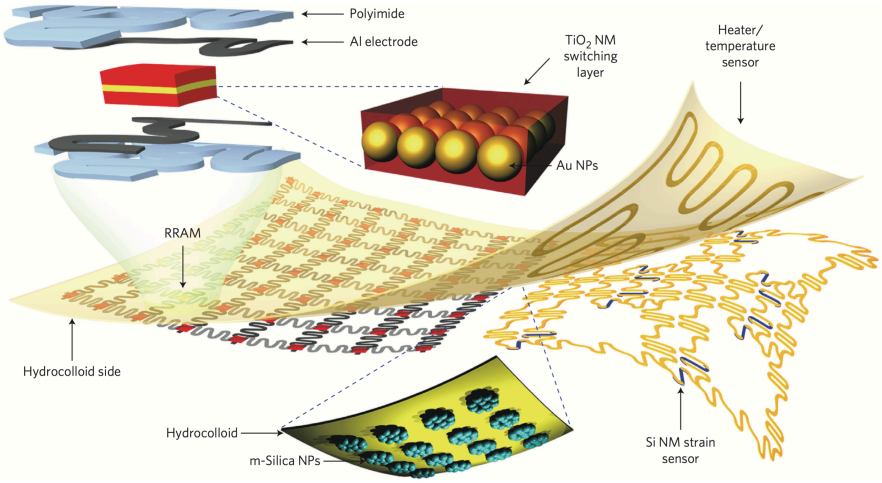

Figure 1.2 – Wearable electronic patch composed of data storage modules, diagnostic tools and therapeutic actuating elements. Wearable memory array consisting of a TiO_2 nanomembrane–Au nanoparticles–TiO_2 nanomembrane switching layer and Al electrodes. The memory array on the bottom side of an elastomeric hydrocolloid skin patch, the electroresistive heater/temperature sensor on the top-side of the patch, with the Si strain sensor on the opposite side. The mesoporous silica nanoparticles array on the hydrocolloid side of the patch. (From ref. 8)

Smart or intelligent materials can respond to external stimuli with particular changes in some of their variables. Contrarily to composite materials which are designed and processed to offer only a limited set of responses to external stimuli and are characterized by their inability to adapt to the environmental changes in real time, smart materials can act simultaneously as actuators and sensors[4].

The state-of-the-art smart materials mimic natural materials and are able to change their properties (mechanical, electrical, and appearance), their structure or composition, or their functions depending on the stimuli received. Nature is full of examples of materials that respond to external stimuli and adapt their shape in real time, *e.g.* the surface of a leaf that follows the direction of sunlight[9]. They possess the capability to sense their environment, process these data and respond accordingly. Mankind is currently embedding smart materials in systems (*e.g.* buildings, airplanes, and in the automotive

industry) in order to provide them with advanced functionalities like providing full reports on performance history, location of defects, in addition to the ability to counteract unwanted or potentially dangerous conditions, namely the excessive vibration. They can also attempt self-repair.

Among the many smart materials and devices some examples are: piezoelectric materials, shape memory alloys, pH-sensitive polymers, polychromic, chromogenic, halochromic materials and many magnetoelectric materials (transformers and gyrators, microwave devices, resonators, filters)[10–13].

Nanostructured materials are part of the major outcomes of nanotechnology research undertaken during the last decade, where materials and devices can be controlled on a molecular and atomic scale.

The development of these materials leads to a basic knowledge necessity concerning aspects such as how materials are formed and what are their characteristics and properties in atomic and molecular scale. They are fabricated using two different approaches namely: top-down (transformative approach where nanostructures are progressively miniaturized from larger scale structures) and the bottom-up (synthetic, where structures are built from their atomic or molecular components mimicking living organisms)[4].

Top-down processes include lithography (electron beam, ion beam, scanning probe, and optical near field), thin film deposition, laser beam processing, mechanical (machining, grinding, lapping, polishing), and electrochemical material removal processes (electroforming and hot embossing lithography)[14,15].

Bottom-up processes include contact printing, imprinting, spinodal wetting/dewetting, laser trapping/tweezer, assembly and joining (self- and directed-assembly), template growth, electrostatic (coatings, fibers), colloidal aggregation, and 2-photon confocal processing[14,15].

Among the different types of multifunctional devices, here we will focus the attention into those where the properties in question are those related to lattice, spin and charge. To be more precise, we are interested in the study of materials that present several ferroic orders (multiferroic) and in which the possibility to manipulate, couple and tune them exists. Therefore, making them very appealing materials. In fact, the industry of sensors and actuators depends heavily on ferroelectric (FE) materials where upon an external electric field (E) it is possible to reverse the spontaneous polarization (P). This happens because most ferroelectric materials, *e.g.* perovskite oxides, are high-performance ferroelastics or piezoelectrics with spontaneous strain (ϵ). In this way, the coexistence of polarization and strain makes them prime subjects to be used in many applications based in the conversion of elastic energy to electric energy or vice-versa[16]. Also widely used are the magnetic counterpart of these type of sensors. As an example we have stress sensors, where it is measured the variation of the material's magnetic susceptibility ($\Delta\chi$) when a mechanical stress (σ) is applied[17].

Another important example of these type of required properties can be found in solid

materials where a crossing effect between magnetism and electricity is present, and thus originating a magnetoelectric effects, such as magnetic (electric) induction of polarization (magnetization)[18]. These materials have already gained their place under the spotlight of industries working with data storage. In fact, magnetic memory technology has given giant steps since the discovery of the giant magnetoresistance (GMR) effect which since then has lead us to an era of magnetoelectronics or spintronics[19].

In these fields, the flow of electric charges was exploited in microprocessors, transistors and a vast set of other domestic appliances. However, with the objective to improve the existing materials and to go forward in the multi-functionality of devices (for example, carrying out data processing and storage on the same device), researchers have been exploring another intrinsic property of electrons - the spin. It was discovered that spin could carry information among devices, similar to what is accomplished by the charge flow. In fact, spin shows some advantages, because it can be manipulated by external magnetic field and possess a long relaxation time that enable processing of information. These characteristics put forward the possibility to develop new and more efficient devices than those using the charge paradigm. Since then the goal in this area has been well defined, namely to achieve high-density integration and overcome the large handicap of the relatively high writing energy. This, leads to a relentless pursuit of the fundamental and application issues connected with magnetic random-access memories (MRAMs) and related devices[20]. Parallel to the development of MRAMs a large effort has also been devoted to the ferroelectric random-access memories (FeRAMs) and in their promotion as superior novel non-volatile and high-speed memory media in comparison to semiconductor flash memories[21].

Alongside with the understanding of the properties of these materials, we find also the need to improve them and to make them smaller and more efficient. Device miniaturization conserving high-density data storage stands also as a trend in modern science and technology. Also here, the integration of several functionalities into one material system is highly desirable. Rising from the vast area of applications of magnetic and ferroelectric materials, it appears natural to pursuit a line of new memories and sensing/actuating devices based on materials which combine, in an effective and intrinsic manner, magnetism and ferroelectricity[22–25] (as schematically shown in Fig. 1.3).

1.2 Multiferroicity and Magnetoelectric effect

Multifunctional materials with at least two ferroic orders, *i.e.* multiferroics, have an important place under the spotlight of condensed matter physics and materials science. According to *Eerenstein et al*[26] multiferroic materials are those exhibiting two or even three ferroic properties, namely ferroelectricity, ferromagnetism and ferroelasticity, in the same phase (see Fig. 1.3 (a)). On the other hand, magnetoelectric materials belong to the group of compounds that are electrically and magnetically polarizable and in

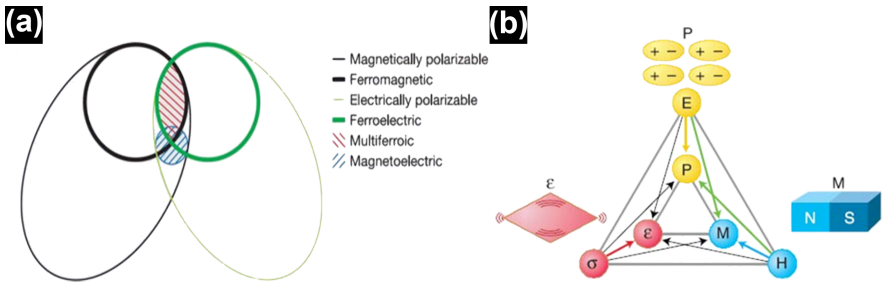

Figure 1.3 – **(a)** The relationship between multiferroic and magnetoelectric materials. **(b)** The electric field E, magnetic field H, and stress σ control the electric polarization P , magnetization M , and strain ε, respectively. In a ferroic material, P , M , or ε are spontaneously formed to produce ferromagnetism, ferroelectricity, or ferroelasticity, respectively. In a multiferroic material, the coexistence of at least two ferroic ordering forms leads to additional interactions. (From refs. 26 and 27)

addition develop polarization when under a magnetic field and magnetization in the presence of an electric field[26,28]. However, in current literature, the definition of multiferroic materials is extended to include non-primary order parameters, like antiferromagnetism and ferrimagnetism. This extension conjugated with the search for multiferroic materials and magnetic coupling effects from the known magnetic and electrical materials (see Fig. 1.3 (a))[26] opened considerably the group of materials to be studied.

The study of multiferroicity and multiferroic materials offers an opportunity to embark in the exploration of some important issues which have rarely been reachable (from the point of view of fundamental physics or even in applications)[1]. This does not mean that properties like ferroelectricity and magnetism have been left forgotten, quite the contrary, they have been the focus of condensed matter physics and materials science since their discovery. However, dealing with multiferroicity within the framework of fundamental physics and technological applications gave birth to a number of challenges. The fact that are so many magnetic ferroelectric materials, when theory predicts so few, makes the investigation of coexistence and coupling effect between the magnetic and ferroelectric orders in multiferroic materials an interesting and important physical issue[29–32].

In a general way we can divide theses challenges in two fundamental issues to be addressed. The first one arise from the difficulty in proving the coexistence of magnetism (spin order) and of ferroelectricity (electric dipole order) in a single material. The second one, is related to the efficient coupling between the two orders in a multiferroic system (*i.e.* magnetoelectric coupling). The coupling from an application point of view, can be considered more important than their coexistence. This coupling represents the basic principle for cross-control, *i.e.* control of the two orders by either an electric field or magnetic field. The studies devoted to this second point have shown that it is more challenging the realization of a such strong coupling than coexistence of the two orders, and is, thus, the cornerstone of the many recent studies in multiferroic materials (see Fig. 1.4).

The physics of multiferroic systems can be extremely complicated when considering

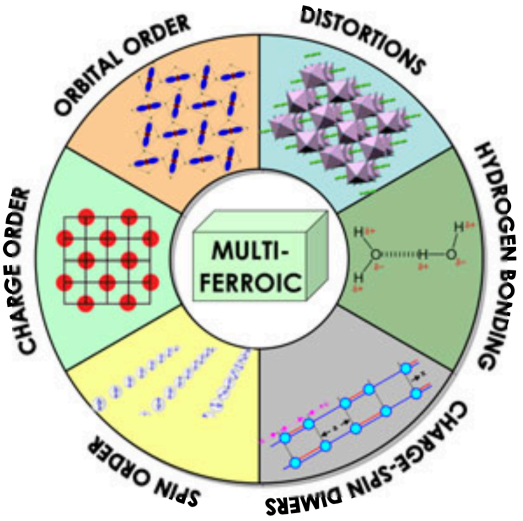

Figure 1.4 – Schematic representation of the different microscopic mechanisms that can lead to multiferroicity. (Adapted from ref. 31)

that a strong coupling between ferroelectricity and magnetism arising from intrinsic properties is fundamental to a multi-functionality of these materials. Furthermore, it comes also clearer that multiferroicity and the cross coupling of its orders provides a more extensive base to pursuit the physics of strongly correlated electronic systems, in addition to other materials like high T_C superconductor and colossal magnetoresistance (CMR) materials.

The cross coupling of different ferroic order opens the possibility to a new and diversified field of applications and devices. However, before entering into the world of ferroic or coupled ferroic orders one should first define the concept of ”ferroic”. The origin of the ferroic concept is related to a behavior due to the interaction between the adjacent atoms or ions, where, in a spontaneous way, below a critical temperature, an order of a certain parameter emerges forming a regular structure with the physical parameter aligned in the same direction in some micro regions (cooperative phenomena). In these materials an applied external driving field will change the parameter exhibiting hysterysis loop behavior due to the existence of the referred ferroic order. Examples of that are the cases of $M(H)$ and $P(E)$ loops in the ferromagnetic and ferroelectric materials [33], as shown in Fig. 1.5.

Among the different types of ferroic orders in materials the four basic primary ferroic order include ferroelectric, ferromagnetic, ferrotoroidic, and ferroelastic order. Thus, if a material exhibits two or more ferroic orders, *e.g.* such as ferroelectric and ferromagnetic order, it is called multiferroic material[i]. Ferromagnetic materials possess spontaneous

[i]Originally proposed by *H. Schmid* [33], multiferroics have been defined as materials presenting more than one primary ferroic order parameter simultaneously within a single phase [34]. Yet, there were those who considered materials to be multiferroics only if they exhibited coupled primary order parameters. Nowadays, the definition of multiferroics expanded to include non-primary order parameters, such as antiferromagnetism or ferrimagnetism.

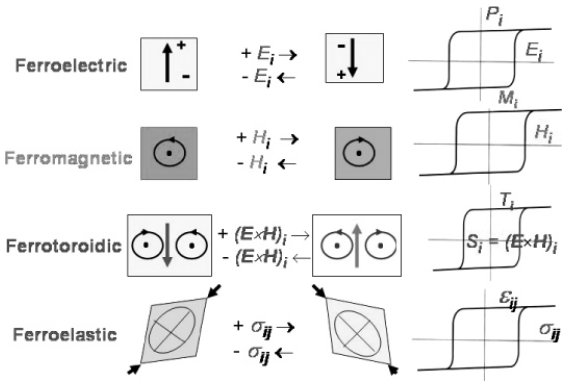

Figure 1.5 – Differents kind of ‘‘Ferroic’’ order in materials. (From ref. 33)

magnetization which can be switched hysteretically by the influence of a magnetic field. In the same way, ferroelectric materials present spontaneous electric polarization which can be switched by an electric field. Ferroelectricity and ferromagnetism are on the top of the list of properties researched in solid state materials. In the scopus of this thesis, in addition to the coexistence of different ferroic orders (specially ferroelectric and ferromagnetic), it is pursued a direct or an indirect coupling between the ferroic orders in multiferroic materials (magnetoelectric materials).

The existence of coupling between two or more ferroic orders, opens new pathways into the development of new applications, where some interesting and useful physical phenomena are present. Phenomena that governs their properties and can be transferred to other materials in their tailoring or tuning. For example, the coupling between orders can have useful effects: coupling between ferroelectric and ferroelastic orders can produce piezoelectric (used in electromechanical conversion); coupling between the ferromagnetic and ferroelastic order can produce magnetostriction (applied in magnetic sensors); coupling between the ferromagnetic order and ferroelectric order can produce new magnetoelectric devices and applications (new generation of energy-efficient memories)[1,30]. We can then, push their versatility where the ability to efficiently control magnetization or/and polarization by an electric field or/and magnetic field is desirable. Prototype devices with high performance for spintronics, for example, reading the spin states, and writing the polarization states to reverse the spin states (by an electric field) and thus overcome the high writing energy in MRAMs (see Fig 1.6). Figure 1.6 shows some examples of magnetic and spintronic properties that can be controlled by an electric field and thus demonstrating the possibilities applications of a material with magnetoelectric coupling[35].

The magnetoelectric effect, in a general sense, describes the coupling between electric and magnetic fields in matter (*i.e.* induction of magnetization (*M*) by an electric field (*E*) or polarization (*P*) generated by a magnetic field (*H*))[1,36]. From the point of view of thermodynamics, and considering Landau theory framework, the systematic progression of contributions to the magnetoelectric effect can be approached by the expansion

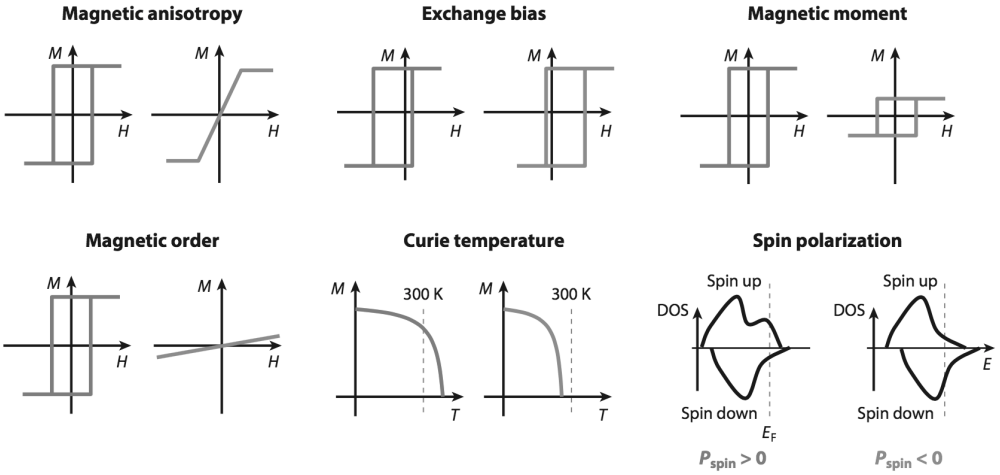

Figure 1.6 – Magnetic and spintronic properties that can be controlled by an electric field. DOS denotes density of states. (From ref. 35)

of ground state free energy (F) for a magnetoelectric system:

$$-F(E,H) = \overbrace{\tfrac{1}{2}\epsilon_0\epsilon_{ij}E_iE_j}^{P(E)} + \overbrace{\tfrac{1}{2}\mu_0\mu ijH_iH_j}^{M(H)} + \overbrace{\alpha_{ij}E_iH_j}^{\text{linear ME}} + \overbrace{\tfrac{1}{2}\beta_{ijk}E_iH_jH_k + \tfrac{1}{2}\gamma_{ijk}H_iE_jE_k + \ldots}^{\text{higher-order coupling terms}}, \qquad (1.1)$$

where E denotes the electric field, H the magnetic field (subscripts $[i,j,k]$ refer to the three components of a variable in spatial coordinates), ϵ_0 and μ_0 are the dielectric and magnetic susceptibilities of vacuum and ϵ_{ij} and μ_{ij} are the second-order tensors of dielectric and magnetic susceptibilities

The first term describes the contribution resulting from the electrical response to an electric field. The second term describes the magnetic equivalent of the first term, where μ is magnetic relative permeability. The third term describes the linear magnetoelectric coupling via α (the most important parameter, at least from the point of view of coupled orders). Designated as the linear magnetoelectric effect, it relates to the induction of polarization by a magnetic field or a magnetization by an electric field. Differentiating $F(E,H)$ the magnetoelectric effect can be defined in the form of $P_i(H_j)$ or $M_i(E_j)$ as follow:

$$P_i(H_j) = \alpha_{ij}H_j + \tfrac{1}{2}\beta_{ijk}H_jH_k + \ldots, \qquad (1.2)$$

$$M_i(E_j) = \alpha_{ij}E_i + \tfrac{1}{2}\gamma_{ijk}E_jE_k + \ldots. \qquad (1.3)$$

Higher-order ME effects parameters can supplement our interpretation of cross coupling effect, like β and γ. However, for most studies the linear ME effect is enough and thus when referring to the ME effect in fact they are just referring to the linear effect[31,37].

The range of applicability of the magnetoelectric effect in single phase compounds is still narrow because this effect is most of the times very small. However in cases like multilayered structures where piezoelectric and ferromagnetic layers are put together, this effect can be extremely enhanced and a giant magnetoelectric effect is accom-

plished (*e.g.* $La_{0.67}Sr_{0.33}MnO_3/BaTiO_3$ heterostructure)[1,36,38,39].

After the prediction of a magnetoelectric effect in Cr_2O_3 by Dzyaloshinskii[40] and its measurement[41], many new multiferroic and/or magnetoelectric materials were reported during the 1960s and 1970s. In fact, the first discovered magnetoelectric material, Cr_2O_3, is not a multiferroic. Recently, special attention was given to materials where a strong coupling between the magnetic and dielectric degrees of freedom is present.

J. F. Scott at the turn of the 21st century published an article entitled ”Ferroelectric Memories”[21], reviewing the use of ferroelectrics as non-volatile memories, making a strong argument in their use. However it is only in 2003 that the research in multiferroics geared up after the discovery of large polarization in a $BiFeO_3$ thin film[42]. Along with $BiFeO_3$, other perovskites such as $TbMnO_3$ were reported to have a strong magnetoelectric (ME) coupling[43,44]. In the quest for practical ME materials many families of multiferroics have been explored, re-discovered, and newly developed, realizing a variety of ME controls[45–50]. In fact, in this recent history of multiferroic materials and magnetoelectric physics, the number of review articles available show that researchers are keeping a close eye in this area and of the importance of the theme.

Just two years later, in 2005 we can track two important articles: one by *Fiebig* (“Revival of the magnetoelectric effect”)[36] about the history and situation point of magnetoelectric materials. In fact, the work was more devoted to the phenomenological theory of magnetoelectric composites in part due to the scarce understanding of many materials like $BiFeO_3$ and $TbMnO_3$; And another co-authored with *N. A. Spaldin* (”The renaissance of magnetoelectric multiferroics”) with a short explanation about magnetoelectric and multiferroic materials[27].

Since then a greater interest about this topic was observed and is in fact still growing. Later that year (in 2005), *Prellier et al* (“The single-phase multiferroic oxides: from bulk to thin film”)[51] published a detailed collection of the available experimental results on $BiMnO_3$, $BiFeO_3$, $RMnO_3$, and RMn_2O_5 (R=Y, Ho, Er, Tm, Yb, Lu).

In 2006, *Eerenstein et al* (“Multiferroic and magnetoelectric materials”)[26], published a short review article where great attention was given to single phase multiferroics, but not neglecting the composite materials, focusing on the symmetry issue of multiferroic order parameters. Multiferroics as quantum electromagnets were also brought forward by *Tokura*[52] in that year.

The next year, it was the time for multiferroic thin films to be the subject of review by *Ramesh et al* “Multiferroics: progress and prospects in thin films”)[53], where the various aspects of multiferroic thin films where discussed, with particular attention to $BiFeO_3$ thin films alongside with the magnetoelectric coupling based novel device physics and relevant issues. *Kimura* also published about magnetoelectrics multiferroics where the ferroelectric order develops upon a magnetic phase transition into a spiral magnetic ordered phase (*e.g.* $TbMnO_3$ and $Ni_3V_2O_8$)[54]. This topic was further pursued by *Tokura* in 2009[18] and again in 2014[55].

It took another year for a classification about the origin of ferroelectricity to be pre-

sented. In the work of *Cheong et al* ("Multiferroics: a magnetic twist for ferroelectricity")[56] ferroelectric materials were divided into two families: proper and improper ferroelectrics[56,57]. In the case of proper ferroelectric the polarization would arise from two mechanisms: a coordinated bonding from the $3d^0$ metal ion and the anion or from a $6s^2$ lone pair of electrons. In the first case, the d^0 property orbitals usually do not allow for a magnetic order to appear (that requires unpaired electrons) and therefore not showing multiferroicity. In the later case, which is characteristic of ABO_3 perovskites like $BiFeO_3$, $PbTiO_3$, and $Pb(Fe_{0.5}Nb_{0.5})O_3$, ferroelectricity originates from the A cation while magnetism arises from the transition metal in the B site (magnetism and ferroelectricity come from two different atomic sub-lattices and have a chemically different origin). In this way allowing the coexistence of multiple ferroic orders in a single material but resulting in different ordering temperatures and most of the times in a small magnetoelectric (ME) coupling.

In the case of improper ferroelectricity we have to deviate from traditional mechanism and consider new ones: structural transition driven (the so-called geometric ferroelectricity), charge-ordering driven (the so-called electronic ferroelectricity), or magnetic ordering driven (the so-called magnetic ferroelectricity). A schematic representation of these driving mechanisms is shown in Fig. 1.7.

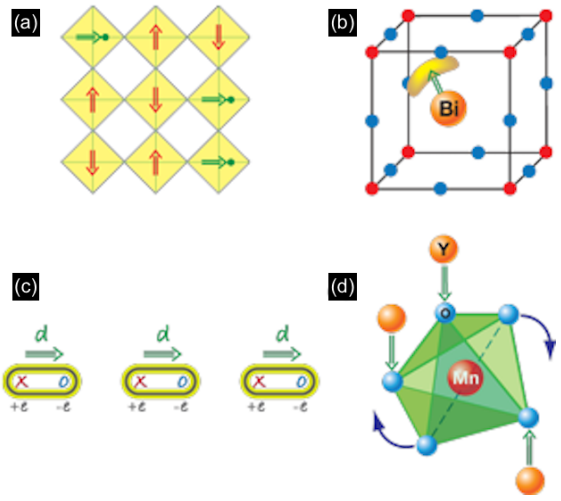

Figure 1.7 – Different microscopic mechanisms found in type-I multiferroics. **(a)** Magnetically driven. In "mixed" perovskites with ferroelectrically active d^0 ions (green circles) and magnetic d^n ions (red), shifts of d^0 ions from the centers of O_6 octahedra (yellow plaquettes) leads to polarization (green arrows), coexisting with magnetic order (red arrows). **(b)** Lone pair electrons. In materials like $BiFeO_3$ and PbVO3, the ordering of lone pairs (yellow "lobe") of Bi^{3+} and Pb^{2+} ions (orange), contributes to the polarization (green arrow). **(c)** Charge ordered. In charge ordered systems, the coexistence of inequivalent sites with different charges, and inequivalent (long and short) bonds, leads to ferroelectricity. **(d)** Geometric configuration. The"geometric" mechanism of generation of polarization in $YMnO_3$ describes the tilting of a rigid MnO_5 block with a magnetic Mn remaining at the center. Because of the tilting, the Y – O bonds form dipoles (green arrows), and there appears two "down" dipoles per one"up" dipole so that the system becomes ferroelectric (and multiferroic when Mn spins order at lower temperatures). (From ref. 58)

The multiferroic mechanisms, and effects were revisited two years later by *Khomskii* ("Classifying multiferroics: Mechanisms and effects")[58]. At that time it was purposed

the division of multiferroics in two major types although they can by further sub-divided. Type-I multiferroics gathering the majority of multiferroics are those where ferroelectricity does not have magnetic origin (*e.g.* $BiFeO_3$ although it has a magnetic ion). Here the spontaneous polarization (T_C ferroelectric) appears above the magnetic ordering temperature (T_C or T_N ferro-(antiferro)magnetic). Type-II or "improper" ferroelectrics those where ferroelectricity arises due to a magnetic order (*e.g.* $TbMnO_3$) and the polarization starts to develop below or at the magnetic ordering temperature. Although Type-II multiferroics exhibit smaller polarization values than Type-I ferroelectrics, the magnetoelectric coupling between the magnetization (M) and polarization (P) is much higher. The last were considered a step trough in the multiferroic community due to their physical importance[59].

Also in that year, and taking into consideration the origin of ferroelectric polarization, the electronic magnetic ferroelectrics were further divided into spin-ordering driven and charge-ordering driven, by *Picozzi et al* ("First principles studies of multiferroic materials")[37].

Another work still in the year 2009, published by *Wang et al* ("Multiferroicity: the coupling between magnetic and polarization orders")[1] presented a comprehensive survey on all aspects of multiferroic researches, focused in the challenges to integrate the magnetism and ferroelectricity into a single-phase system and summarized various strategies used to combine the two types of order. *Spaldin et al* publish a shorter article about "Multiferroics: Past, present, and future"[60]. *Martin et al* covered the advances in the growth and characterization of magnetic, ferroelectric, and multiferroic oxide thin films[61].

Multiferroic and magnetoelectric bulk and heterostructures were also covered in an article by *Velev et al* ("Multi-ferroic and magnetoelectric materials and interfaces")[62] in 2011. In recent years the topic of multiferroic and magnetoelectric materials has been extend to different materials like hexaferrites[63], perovskite manganites[64], heterostructures and their interfaces[65–68], into theoretical calculations[31] and synthesis techniques and routes to new single-phase multiferroics[69] or even to diffraction studies in multiferroics[70].

In 2015 and 2016 researchers are still reviewing the topic of controlling magnetism by electric fields[71] and the related aspects with multiferroic materials and magnetoelectric physics[30]. *Ortega et al* published an interesting review on multifunctional magnetoelectric materials for device applications[72].

Despite the fact that materials can exhibit the presence of ferroelectricity and (anti)ferromagnetism, the relation between the two orders is not a sufficient condition for a strong magneto-electric coupling, allowing to achieve a good mutual control among them. Luckily, recent works in this area managed to create and find more materials exhibiting such properties, especially in frustrated magnets, where a strong and intrinsic magnetoelectric coupling is present[23,26,27,73,74] (*e.g.* $TbMnO_3$, $TbMn_2O_5$, $Ni_3V_2O_8$, hexaferrites (*e.g.* $Ba_{0.5}Sr_{1.5}Zn_2Fe_{12}O_{22}$), $Pb(Fe_{0.5}Nb_{0.5})O_3 - Co_{0.65}Zn_{0.35}Fe_2O_4$[75] or

$SrCuTe_2O_6$)[76]. From the many multiferroic systems synthesized so far we can find the transition metal oxides with perovskite and spinel structures on top of the list. Typically they are strongly correlated electronic systems where the correlations among spin, charge and orbital and lattice play a fundamental role.

1.3 Magnetocaloric Effect and Materials

Nowadays, one observes a growing interest in using the magnetocaloric effect (MCE) as the cornerstone physical property behind an alternative technology for refrigeration both at room and at cryogenic temperatures. This is in part due to it's environmentally friendly technology since it eliminates ozone depleting gases, reducing the need for global warming greenhouse effect gases, and other hazardous gaseous refrigerants. Curiously, the appearance of hydrofluorocarbons (HFC), as a suitable replacement for ozone depleting substances, was regarded as the long awaited solution. However, an unintended negative side effect of their use, is that they are contributing to an unwanted climate change all around the world. Thus, revealing that in fact they are not the perfect solution[77]. Furthermore, magnetic refrigeration (MR) offers up to 60% of Carnot efficiency, much larger than in conventional refrigeration technologies. Health and medicine (hyperthermia) is another field in witch MCE is being investigated.

The MCE was first observed in 1881, when *Warburg* first discovered a thermal effect on metal iron when applying it a varying magnetic field[78]. However it was only later that its origin, cooling via adiabatic demagnetization, was independently explained by *Debye* in 1926[79] and *Giauque* in 1927[80]. Half a decade later, *Giauque* and *MacDougall* achieved the lowest temperature up to that time, 250 mK, using paramagnetic salts[81].

The entropy thermal dependence of a magnetic system as a function of the applied field can be illustrated by a schematic diagram of Temperature-Entropy (see Fig. 1.8 (a)).

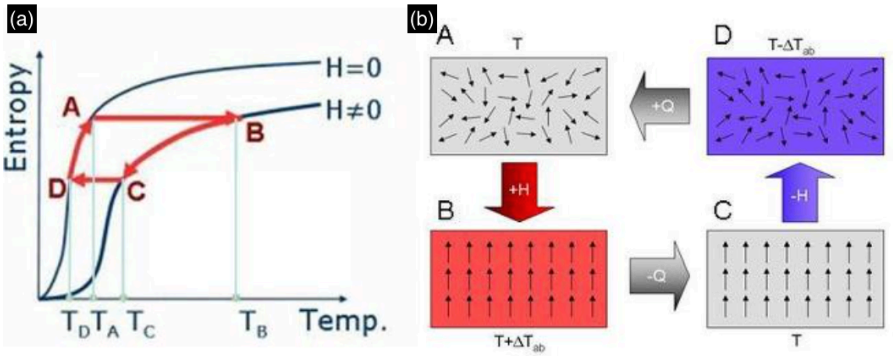

Figure 1.8 – **(a)** Thermal dependence of the entropy of a magnetic system depending on the applied field. **(b)** Magnetic cooling cycle. Schematic picture that shows the basic processes of the magnetocaloric effect when a magnetic field is applied or removed in a magnetic system: the isothermal process, which leads to an entropy change, and the adiabatic process, which yields a variation in temperature. (From ref. 82)

In a simple way the MCE can be described as an intrinsic property of all magnetic materials and can be quantified in two ways: the material's reversible change in temperature when a magnetic field change takes place in an adiabatic process ($A \rightarrow B$ [$\uparrow H$] and $C \rightarrow D$ [$\downarrow H$]). Here, the total entropy remains constant but the magnetic entropy is decreased/increased, and thus lattice and electronic entropy has to increase/decrease to compensate it. This causes a temperature increase/decrease (ΔT_{ad}) which depends on the applied magnetic field strength. Or as the reversible change of magnetic entropy (ΔS_m) if the field change is brought about in an isothermal process. Here, the ordered magnetic spin system returns to its original alignment by exchanging energy with the lattice, which decreases the lattice entropy, returning the sample to its original temperature. The first occurs when the entropy is kept constant, while the second when the temperature is kept constant. This effect is also currently called adiabatic demagnetization[83]. Both properties are characteristic of the magnetocaloric effect and depend on the initial temperature and magnitude of the magnetic field change. An increase on the order of the magnetic spins and a corresponding decrease of the magnetic entropy are observed with an increasing value of the external magnetic field change.

A magnetic refrigeration system/cycle relies on a mechanical part (a magnetic working material, a magnetizing/demagnetizing system, hot and cold heat exchangers and a heat transfer system) and in an operation principle which is illustrated in Fig. 1.8 (b). Let us consider a system in its normal state A. When a magnetic field is applied in an adiabatic way, the once randomly oriented spins will align and a temperature increase is verified ($A \rightarrow B$). Placing a heat sink near the material will allow the material to reject the former increase of temperature to its surroundings ($B \rightarrow C$). Upon removal of the magnetic field, the magnetic spins return to their randomized state at the cost of thermal energy ($C \rightarrow D$). At this point the material exchanges heat from the space to be cooled or heat source ($D \rightarrow A$) returning to its original state and the cycle is repeated.

The MCE can also be described as a variation of the entropy in the system, leading to a temperature variation which can be worked out from the free energy F, itself a function of temperature (T), volume (V) and magnetization (M). The free energy $F(T, M)$ at constant V, is defined as:

$$F(T, M) = U - TS \qquad \text{where} \quad S = S_{el} + S_{lat} + S_M \; . \tag{1.4}$$

The total value of the entropy (S) depends on H and T, and results from the contributions of the lattice (S_{lat}), electronic (S_{el}) and magnetic (S_M) entropies.

Considering a constant temperature value and considering that S_{lat} and S_{el} are field-independent, the MCE can be expressed as the isothermal magnetic entropy change, $\Delta S_M(T)_{T,\Delta H}$, given by:

$$\Delta S_M(T) = S_M(T, H_f) - S_M(T, H_i) \; , \tag{1.5}$$

where H_i and H_f are the initial and the final magnetic fields, respectively.

When the magnetic field is applied adiabatically, the total entropy should be pre-

served and the lattice and electronic entropies should change to $-\Delta S_M$, resulting in the adiabatic temperature change, ΔT_{ad}:

$$\Delta T_{ad}(T) = T(S, H_f) - T(S, H_i) \,, \tag{1.6}$$

The MCE can be evaluated directly by measuring the temperature variation of the sample, or indirectly by measuring the magnetization and/or the heat capacity with the use of thermodynamics[83]. The ΔS_M associated with a variation of the magnetic field can be obtained from:

$$\Delta S_M = \int_{H_{min}}^{H_{max}} \left(\frac{\partial S}{\partial H}\right)_T dH = \int_{H_{min}}^{H_{max}} \left(\frac{\partial M}{\partial T}\right)_H dH \,, \tag{1.7}$$

resulting from the Maxwell thermodynamic relation:

$$\left(\frac{\partial S_M}{\partial H}\right)_T = \left(\frac{\partial M}{\partial T}\right)_H \,. \tag{1.8}$$

When this relation is considered, the ΔS_M is estimated by using magnetization data and a numerical approximation of the integral:

$$\Delta S_M \simeq \sum \frac{(M_n - M_{n+1})_H}{T_{n+1} - T_n} \Delta H_n \,, \tag{1.9}$$

where n represents the sequence of experimental points.

The estimation of MCE using magnetization data is nowadays one of the most discussed topics on the MR community[84–87]. In fact, some considerations need to be addressed to estimate the MCE as *Amaral et al.* suggests for first order phase transitions[84]. To have a reasonable estimation without using a very complex data treatment, the same authors suggest to measure $M(H)$ upon increase and decrease of H and estimate both ΔS curves using the Maxwell relation. The ΔS_M obtained under H increase will be an overestimated value, whereas for H decrease it will be an underestimated value, thus allowing to infer about the magnitude of ΔS_M[84,88].

In the recent history of the MCE (last twenty years) we can point two major developments that have boosted exponentially its interest: the creation of a proof-of-concept magnetic refrigerator demonstrating that magnetic refrigeration is a viable and competitive cooling technology in the near room temperature region[89] with potential energy savings of up to 30% and the discovery of the giant MCE (GMCE) in $Gd_5(Si_2Ge_2)$[90].

Since then many materials have been studied in the attempt to increase the magnetic entropy variation and to switch it towards room temperature. In fact, to a greater or lesser extent all magnetic materials show a MCE. However, MR technology requires the search for suitable materials and only those presenting a higher MCE become potential candidates for it. Ideally, these materials should present a series of characteristics in order to be used as cooling material[91–93]: low Debye temperature values; Curie tem-

perature near working temperature; large temperature difference (ΔT_{ad}) in the vicinity of phase transition; no thermal or magnetic hysteresis to enable high operating frequency and, consequently, large cooling power; low specific heat and high thermal conductivity, thereby allowing large changes in temperature and facilitating the processes of heat transfer and increasing efficiency; high electrical resistance in order to avoid Foucault currents in the processes of rapid change in magnetic field; non-toxic; resistant to corrosion; good mechanical properties; low manufacturing costs necessary for commercial viability; and low environmental impact.

Among the substantial research on magnetocaloric materials, the majority are concentrated on the search for materials for room temperature operation, studying their properties and feasibility of being produced economically. Still, every now and then, MCE studies on different/new materials appear in literature. At the moment there is a wide range of materials that present a noteworthy MCE for a wide spectrum of temperatures. Most of those materials are rare-earth based ones, either pure or combined in alloys, in particular the notable example of gadolinium and some of its alloys (*e.g.* $Gd_5Si_2Ge_2$)[94]. Another prominent example is praseodymium alloyed with nickel ($PrNi_5$), that due to his strong MCE, has allowed to approach temperatures near the absolute zero (to within one milliKelvin)[95]. Additionally, we can find RCo_2-based systems (R=Er, Ho, Dy)[96], $Gd_5Si_2Ge_2$ and $Gd_5(Si_{1-x}Ge_x)_4$ and related 5 : 4 materials[90], Mn-based compounds and $MnAs_{1-x}Sb_x$ series[97] (associated with first order phase transitions and therefore with the inherent practical obstacles because of the nature of this transition), $La(Fe_{13-x}M_x)$-based compounds like $La(Fe_{1-x}Co_x)_{11.9}Si_{1.1}$ series (second order phase transition material that can be obtained through powder metallurgical processes allowing its production on an industrial scale and Curie temperature tunable through the adjustment of Co content[98], $Fe_{49}Rh_{51}$ [99] (known to have the highest MCE value near room temperature. However, the high cost of Rh means that it can only be considered for very specific applications) and also in many manganites ($(La_{1-x}M_x)MnO_3$ where M = Ca and Sr) just to name some[92]. Fig. 1.9 summarizes the variation of the magnetic entropy of some important magnetocaloric materials versus their Curie temperature.

Looking into the Fig. 1.9 there are two aspects that are easily noted: the first one is related with the decrease of $-\Delta S_m$ when going from low temperature to room temperature[100] and the second one is related with a largest values presented by first order magnetic transition (FOMT) materials compared to those of materials presenting a second order magnetic transition (SOMT). From the large number of magnetic materials those more promising to be applied in MR are those presenting a first order transition magnetic transition because they can reach higher values of ΔS_m and ΔT_{ad}, thud presenting a Giant MCE[90]. However, the thermal and magnetic hysteresis, slow kinetic and MCE in a narrow temperature range in these materials can alter the refrigerators performance. About ten years ago theoretical studies brought forward a promising alternative, *i.e.* use of ferrofluids (colloidal suspension of ferromagnetic particles)[101,102].

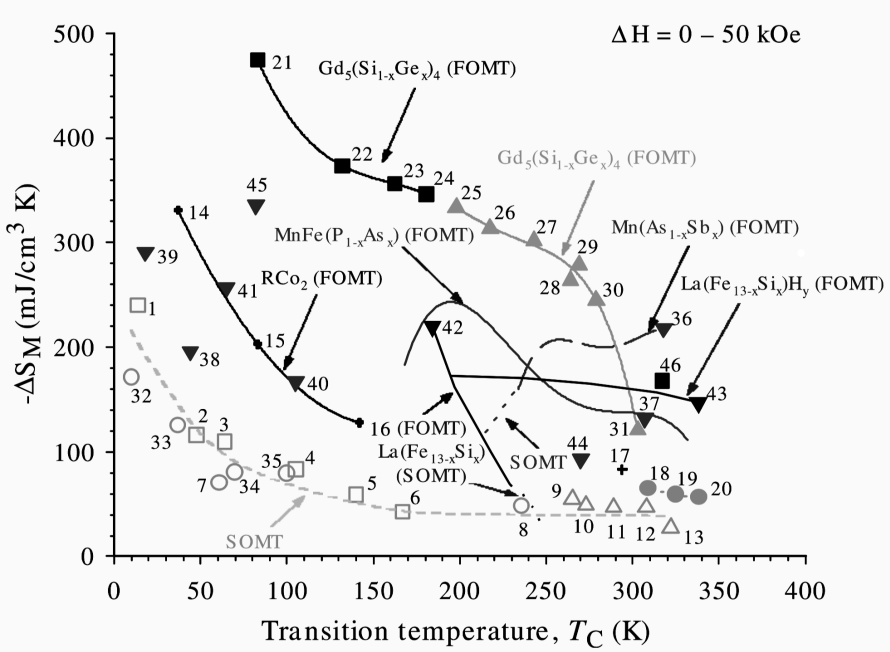

Figure 1.9 – The magnetic entropy change for H = 50 kOe for the RCo_2, RAl_2, $Gd_5(Si_{1-x}Ge_x)_4$, $Mn(As_{1-x}Sb_x)$, $MnFe(P_{1-x}As_x)$ and $La(Fe_{13-x}Si_x)$ families plus a number of individual compounds versus the Curie temperature. (From ref. 92)

Still, further research in these materials has to be performed in order to overcome some technical problems like suspensions with high concentrations of magnetic particles as well as solving heat transfer problems associated with the processes.

The great ecological advantage of using magnetic refrigeration has boosted the research in this field in the last years. The magnetic refrigeration process may be compared with the conventional vapor compression technology, especially for the processes of magnetization-demagnetization (compression and expansion, respectively. See Fig. 1.10 (a))[89,92,95,103,104].

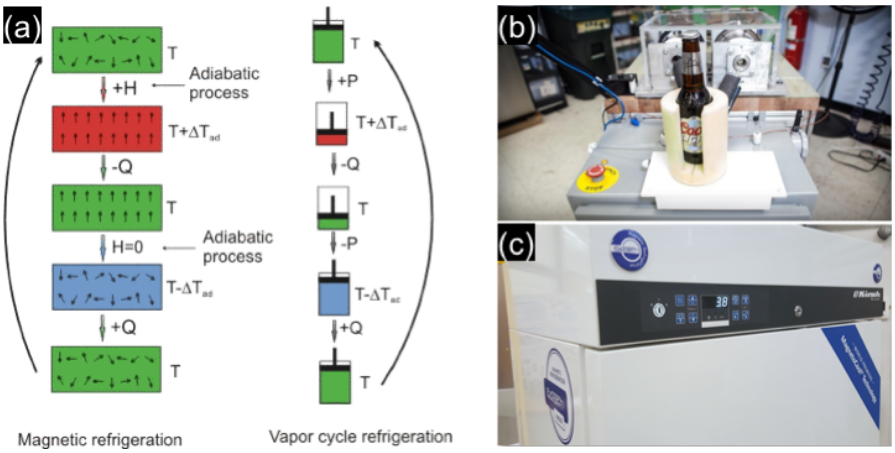

Figure 1.10 – **(a)** Analogy between magnetic refrigeration and vapor cycle one (conventional refrigeration). H = externally applied magnetic field; Q = heat quantity; P = pressure; ΔT_{Ad} = adiabatic temperature variation. **(b)** General Electrics ”beer cooler”. **(c)** Cooltech Medical Refrigerator. (Adapted from refs. 33,105–107)

Magnetic refrigerators are constituted by a solid refrigerant and common heat transfer fluids (*e.g.* water, water-alcohol solution, air or helium gas). These devices are more efficient than the commercial refrigeration units operating well below the maximum theoretical efficiency (Carnot cycle). The cooling efficiency of magnetic refrigerators working with Gd has been shown to reach 60% of the Carnot limit, compared to only about 40% of the best gas-compression refrigerators[108].

In the middle of the 70's, Brown presented the first room temperature refrigerator applying adiabatic magnetization and demagnetization[104]. After the discovery of the GMCE in $Gd_5Si_2Ge_2$[90], many scientists and industrial representatives of the refrigeration community realized that this new technology (applying permanent magnets and the GMCE) had potential for a remarkable entrance into the refrigeration market. Since then, magnetic refrigeration development has come a long way and many solutions have been presented to the public, *e.g.* General Electrics with "beer cooling fridges" (see Fig. 1.10 (b))[106] or just last year Cooltech Applications with a medical refrigerator (see Fig. 1.10 (c))[107]. The first room temperature magnetic refrigerator containing permanent magnets was designed and built in 2001 by Astronautics Corporation, USA[104]. Up to the present, more than thirty prototypes have been produced and distributed around the globe, but with special incidence in Asia, since the used magnetic materials are based on the rare-earth elements extracted in this region[108]. A few years ago main refrigeration industries such as Toshiba Corp. and BASF started to sponsor these prototypes which also lead to the creation of several spin-offs such as Camfridge, Magnetic Development, Inc., Magcool, Advanced Magnetic Technologies Consulting Ltd. and Cooltech Applications.

1.4 Spinels compounds: ABX_4

The concept of spinels was used in the 16^{th} century to denote different red gems, which derived from the Latin "spina" (thorn), probably as a result of their sharp octahedral shape. Two centuries later, the spinel crystallographic structure was observed for the first time in a crystal of magnetite ($FeFe_2O_4$) and in the mineral $MgAl_2O_4$, which is considered the parent compound of spinels[109–111].

The binary spinel compounds are represented by the general formula AB_2X_4, where X represents an anion (–2 valence state) and A and B are cations (+2 and +3 valence states, respectively). The crystal structure is characterized by a face-centered cubic (fcc) arrangement with a large unit cell, containing eight formula units (8 A-cations, 16 B-cations and 32 X-anions)[112], in a close-packed arrangement of the anions, with the cations located in the interstitial positions. In the spinel crystal two different interstitial positions are present, one called the A-site position where the anions (X^{2-}) are at the vertices of a tetrahedron and divalent cation (*e.g.* Cd^{2+}) at its center and a B-site with divalent anions in the vertices of an octahedron and the trivalent cation (*e.g.* Cr^{3+}) at

the center. The cations occupy one-eight of the interstices formed by the tetrahedra and one-half of those formed by the octahedrals. As a consequence, the spinel structure presents large lattice parameters (for instance in natural $MgAl_2O_4$, a = 8.0898(9) Å).

For many purposes, as in the study of electric quadrupole interactions, the atomic point symmetry is crucial. In this way the A-site can be described as a cubic environment, and thus it possess four threefold axes resulting in a null electric field gradient. On the other hand the atoms at B and X sites have a axial symmetric field gradients due to an unique threefold axis. Furthermore, from the point of view of each three-fold axis in the structure, a stacking of different layers is present where only cations in octahedral coordination exist alternate with those where the tetrahedral and octahedral sites are filled in the ratio two to one[109,110]. A schematic model of the structure can be visualized in Fig. 1.11.

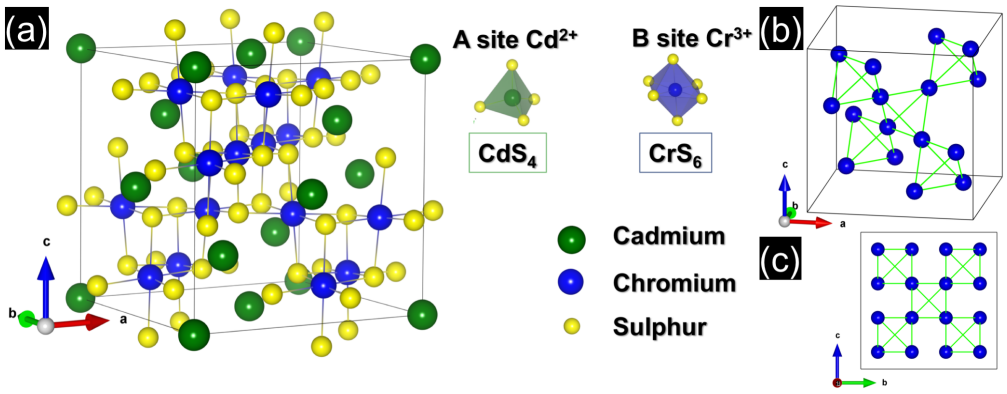

Figure 1.11 – Schematic representation of the $CdCr_2S_4$ spinel crystallographic structure. **(a)** Ball and stick model of the $CdCr_2S_4$ structure. **(b)** and **(c)** Pyrochlore lattice arrangement of the Cr^{3+} magnetic ions.

There are two types of spinels depending of the distribution of the cations among the available sites: the normal ones $A[B_2]X_4$, and the inverse ones $(B[AB]X_4)$. Here, the square parenthesis indicate the ions in the octahedral sites. A random distribution of the divalent and trivalent cations, is also possible to be formed in the inverse structure (see Fig. 1.12).

The common formula of these distributions can be written as $(A^t_{1-x}B^t_x)[A^o_xB^o_{2-x}]O_4$, where *o* and *t* refer to the octahedral and tetrahedral sites of the spinel structure and x is the so-called degree of inversion, equal to zero and unity for the normal and inverse arrangements, respectively[114,115]. Usually the distribution of cations among the A and B sites can be deduced from their ionic radius (see structural sorting map for AB_2X_4 on Fig. 1.12). Additionally, different type of spinels can also appear because they are very sensitive to the stoichiometry of the reactant elements in their synthesis and to heating and cooling rates[115]. In this thesis only the normal spinel structure will be considered.

The normal spinel structure crystallizes in the cubic $Fd\bar{3}m$ space group[112,116] although the symmetry can be lowered by Jahn-Teller and other effects[117–119] and in some cases leading to the formation of complex superstructures[115,120].

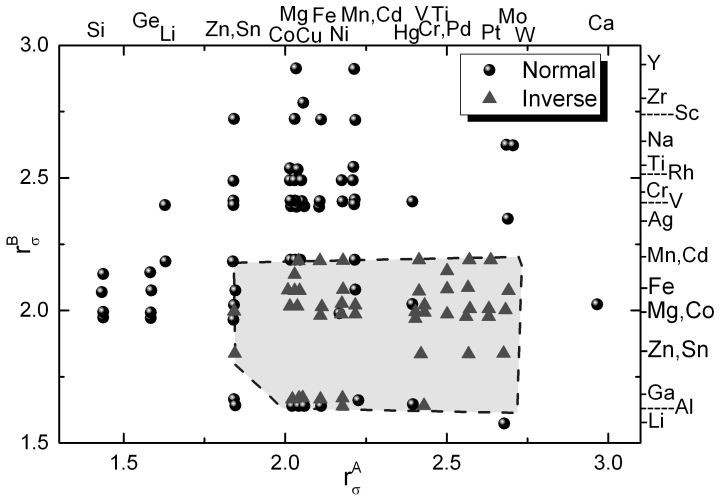

Figure 1.12 – Structural sorting map for AB_2X_4 spinels with normal and inverse structure (where X is O, S, Se, Te), using r_σ^A and r_σ^B as indices. Because of the proximity of r_σ for some elements (*e.g.* Cr, Pd and Mn, Cd) several points represent more than one data point. Also the nature of X is not distinguished in this plot. (Adapted from ref. 113)

Among the vast number of ternary spinel-type compounds, those with Cr as transition metal (magnetic ion), with the general formula ACr_2X_4 (A = Zn, Cd, or Hg and X = O, S or Se, chalcogens), form a special group of magnetic semiconductors and have been the focus of an intensive study due to their exotic physical properties (electrical, magnetic, and others)[121,122]. The compounds where X = O are called oxyspinels and the compounds with X=S thiospinels.

Chromium spinels have been studied for more than half a century because they present an enormous range of magnetic exchange strengths and different magnetic ground states[121,123,124]. This is mostly due to the different elements (in the A and X sites) that can integrate these structures (and their different sizes), leading to different lattice constants and thus different Cr – Cr distances. Thus, making it possible for these compounds to exhibit Curie-Weiss (CW) temperatures (θ_{CW}) ranging from – 400 to 200 K, and to order at low temperature either in an antiferro or ferromagnetic way[121,123]. In fact, the CW temperatures (extrapolated from the linear inverse susceptibility paramagnetic phase) for chromium oxide spinels predict an antiferromagnetic ordering at temperatures one order of magnitude larger than those actually observed (of the order of 10 K). This arises from the fact that the Cr spins in oxide spinels form a pyrochlore lattice where a strong geometrical frustration exists. On the other side of the chromium based spinels, we find sulphur and selenide spinels which order ferromagnetically at temperatures in the order of 100 K[125,126]. Here we find also examples of frustration (spin and orbital) like in the cases of $MnSc_2S_4$ and $FeSc_2S_4$ spinels[127,128].

In a general way, the dominating exchange interactions in these systems are governed by the interatomic distances. For small Cr – Cr distances a strong direct AFM exchange dominates while increasing the distance, the 90° FM Cr – X – Cr superexchange becomes important. *Rudolf et al* suggested that in all of these spinels and for all the

different interatomic spacings, a complex Cr – X – A – X – Cr antiferromagnetic super exchange (SE) is active, being although very weak[124].

As described earlier, in a normal chromium based spinel structure configuration, the Cr ions ($3d^3$) occupy the B-sites (octahedral environment). However, a splitting of the *d* level into a lower t_{2g} triplet (single occupation in each orbital) and an excited empty e_g doublet is observed due to the influence of the octahedral crystal field. This results in an almost spherical charge distribution and minimal spin-orbit coupling. In fact, we can expected that these materials show no role or a minimal one due to charge effects because of orbital effects are or completely or partial quenched. In the cases where A = Cd or Hg, the A^{2+} have filled d^{10} orbitals and therefore do not contribute to the magnetic or orbital degrees of freedom. However, because of the relatively large size of the A-ions, these systems show a tendency to ionic off-center distortions[129,130].

In some of these systems, the competing magnetic exchange interactions and geometric frustration of the magnetic pyrochlore lattice[131] gave origin to interesting phenomena like complex magnetic ground states[132], strong metamagnetism[125,133], and even multiferroic behavior[128,134].

Spin-phonon coupling in systems with strong electronic correlations has also been under the attention of researchers. Here structural distortions and their role in AFM ordering of geometrically frustrated oxides have shown the important role they play in the way that these systems lift frustration, where in simple terms, the lattice distorts to gain exchange energy[135,136].

Two interesting examples of complex magnetic mechanism presented by chromium spinels can be observed in $ZnCr_2S_4$ and $ZnCr_2Se_4$. In the former one, almost equivalent (in strength) exchange interactions (FM and AFM) are present and the magnetic order results from a strong bond-frustration. In the later, on the other way, despite being dominated by FM exchange interactions it orders antiferromagnetically at T_N = 21 K[124,131]. Also, in $ZnCr_2O_4$[137] and $CdFe_2O_4$[138], transition metal spinel compounds, geometric frustration is an important factor in defining the magnetic properties of the system[139]. In these spinels, the octahedral cation lattice own a similarity to the lanthanide cation lattice in pyrochlore. However, in the case of transition metal spinel compounds, the strong coupling between spin and lattice degrees of freedom results in a structural transition coupled to the magnetic ordering[140].

Geometric frustration is also claimed to be responsible for the relaxor properties in the $CdCr_2S_4$ spinel, an important example for this thesis[128] (see section 3.2). The critical role of frustration in the magnetic and electric properties in other transition metal sulfide spinels can be found in several works in the recent literature[127,135,136,141–143].

Some characteristic parameters of chromium spinel compounds (oxides, sulfites and selenites) are summarized in table 1.1: lattice constant, paramagnetic effective moment, Curie-Weiss temperature, magnetic ordering temperatures, magnetic frustration parameter $f = |\theta_{CW}|/T_M$ and type of magnetic ordering.

In a first look into the table, it comes into attention that an increase of the lattice

Table 1.1 – Summary of parameters of some chromium spinels. Lattice constants a_0(Å), effective PM moment μ_{eff} (μ_B), CW temperature θ_{CW} (K), magnetic ordering temperature T_M (K), magnetic frustration parameter $f = |\theta_{CW}|/T_M$ and magnetic order (MO). Data taken from refs. 125,126,131,134, 144–146.

Compound		a_0	μ_{eff}	θ_{CW}	T_M	f	MO
$ZnCr_2O_4$	ZCO	8.328(2)	3.85	-398	~ 15	32	AFM
$MgCr_2O_4$	MCO	8.319(3)	3.71	-346	12.7	27	AFM
$CdCr_2O_4$	CCO	8.596(2)	4.03	-71	8.2	8.7	AFM
$HgCr_2O_4$	HCO	8.658(1)	3.72	-32	5.8	5.5	AFM
$ZnCr_2S_4$	ZCS	9.983(2)	3.86	7.9	~ 12	0.5	AFM
$MgCr_2S_4$	MCS	10.108(2)	1.27	-12	80	0.1	FM
$CdCr_2S_4$	CCS	10.239(2)	3.88	155	84.5	1.8	FM
$HgCr_2S_4$	HCS	10.244(1)	3.90	140	22	6.4	AFM
$ZnCr_2Se_4$	ZCSe	10.498(1)	4.04	90	21	4.3	AFM
$HgCr_2Se_4$	HCSe	10.743(9)	3.89	200	106	1.9	FM
$CdCr_2Se_4$	CCSe	10.745(3)	3.82	184	130	1.4	FM

constant leads to an increase of the CW temperatures, going from strongly negative AFM exchange in the oxides to moderately FM exchange in the selenides. As referred before, in the oxides, due to the small Cr – Cr distances a strong direct AFM exchange dominates. Increasing the Cr – Cr distance, they become weaker and compete with the 90° FM Cr – X – Cr exchange that becomes dominating in the selenides. In fact, the Hg and Cd selenides show high FM ordering temperatures compared to the small ordering temperatures of the AFM oxides (bottom and top of the table, respectively). The later exhibit also strong geometrical frustration. In chromium spinel, where chromium is the only magnetic ion, the lack of spin-orbit coupling is verified by the almost spin-only values (S = 3/2, yielding 3.87 μ_B for the PM moment) of the Cr moments.

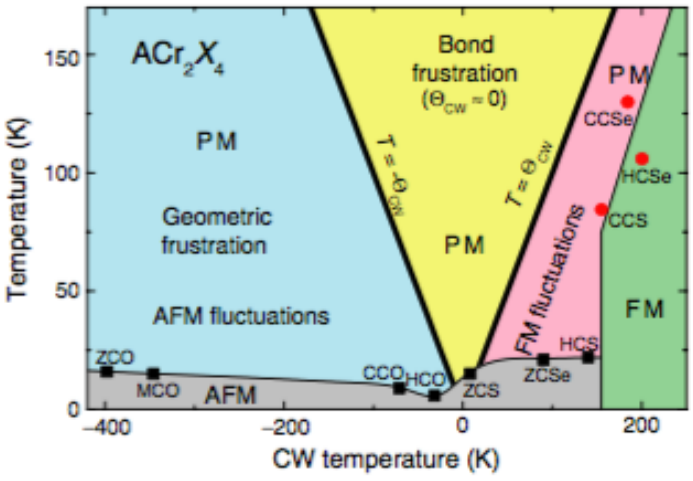

Figure 1.13 – Schematic magnetic phase diagram of ACr_2X_4 compounds, where characteristic temperatures are plotted versus the CW temperature: FM (red circles) and AFM (black squares) ordering temperatures. Hypothetical magnetic ordering temperatures ($T = \pm\theta_{CW}$) are indicated by thick solid lines. Thin solid lines separate magnetically ordered from PM phases and are drawn to guide the eye. (From ref. 126)

Recently, several authors reported on the abundance and complexity of the physics characteristic of these systems, demonstrated by the observation of geometric[139] and orbital frustration[127,139] or even the observation of an orbital-glass state[128,131]. A schematic representation where some of these characteristics (*e.g.* type of frustration

and magnetic order) for chromium based spinels is shown in Figure 1.13 (characteristic ordering versus θ_{CW} temperatures).

In the complete range of these chromium based spinels, spanning from strongly frustrated oxides to the ferromagnetic sulphides and selenides we observe a change of almost 600 K (−400 K to 200 K) in the θ_{CW} temperatures. Furthermore, different spin arrangements can be observed: $ZnCr_2O_4$ shows an incommensurate spiral phase order (long spiral with the spins aligned in the *ac*-plane)[147,148], $ZnCr_2S_4$, as stated, shows almost equivalent AFM and FM exchange interactions and present a mixed spiral and a collinear structures[131,149], $ZnCr_2Se_4$ and $HgCr_2S_4$ show strong FM spin fluctuations but order antiferromagnetically with FM planes[150–152] or chromium spinels ordering ferromagnetically at higher temperatures as $CdCr_2Se_4$, $HgCr_2Se_4$ and $CdCr_2S_4$[121].

1.4.1 Chromium chalcogenide thiospinel $CdCr_2S_4$

Chromium chalcogenide thiospinel, $CdCr_2S_4$, crystallizes in the cubic space group $Fd\bar{3}m$ with the following lattice parameters a = 10.244 Å and is characterized as being a ferromagnetic material with a Curie temperature of T_C = 84.5 K[112,116]. The saturation moment is about 5.96 μ_B per unit formula, in agreement with ferromagnetically ordered Cr^{3+} spins due to the superexchange interaction between Cr−S−Cr atoms. The distance between neighboring Cr ions is too large for a direct exchange and instead a 90° superexchange via the S ions occurs. Moreover, it has a paramagnetic Curie-Weiss temperature of θ_{CW} = 152 K[112].

Since its discovery in the 1960s, $CdCr_2S_4$ has been the focus of many studies from fundamental properties to applications, *e.g.* already in 1965 its magnetic properties were investigated by *Baltzer et al*[121], who found a ferromagnetic insulator state below 97 K.

Since then, many other studies have been performed searching for an explanation for the unusual nature of some experimental results, like an abnormal negative thermal expansion at low temperatures[153,154] simultaneously with an unexpected broadening of the diffraction lines[154], which was found to correspond to a mode softening in the spinel structure. Furthermore, a strong blue shift of the absorption edge[155], accompanied by an abnormally large phonon shift and damping effects were observed near the magnetic transition temperature T_C[156].

However it was only in 1997 that the interest in chromium based thiospinels was triggered by the rediscovery of the colossal magnetoresistance (CMR) in $FeCr_2S_4$ and $CuCr_2S_4$[157,158]. CMR was later also observed in $CdCr_2S_4$ spinel by *Sun et al*[159] (see Fig. 1.14). Moreover, $CdCr_2S_4$ is among the relaxor-like systems and is one of the rare compounds that exhibits four colossal effects (the magnetocapacitive, electrocapacitive, electroresistive, and magnetoresistive effects)[159]. Since then $CdCr_2S_4$ spinel has been exhaustively studied due to the mutual coupling between magnetic and electric properties and for being potential candidate for semiconductor spintronic devices.

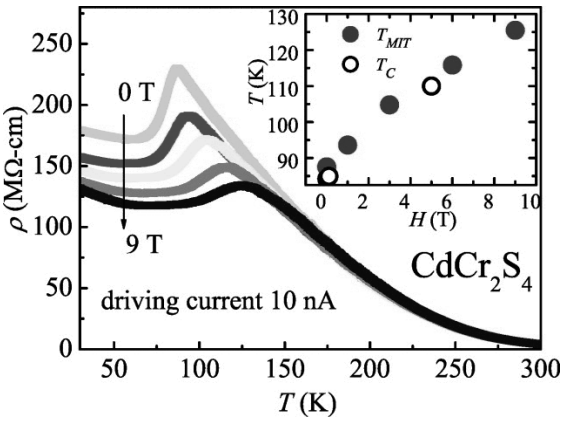

Figure 1.14 – Magnetoresistance versus temperature for $CdCr_2S_4$. In the inset, T_{MIT} (metal-insulator transition) and T_C were plotted to compare two characteristic temperatures from the transport and magnetic measurements, respectively. (Adapted from ref. 159)

The coexistence of ferromagnetism and relaxor-like ferroelectricity (0.5 μCcm^{-2}) together with colossal magnetocapacitance claimed in a seminal paper by *J. Hemberger* and coauthors[128] has revived the attention on $CdCr_2S_4$.

Later, the discovery of dielectric relaxational dynamics above the Curie temperature (T_C), responsible for the strongly increased dielectric permittivity of $CdCr_2S_4$ [26,129], has driven an intense debate in the research community[128,160] (see Fig. 1.15).

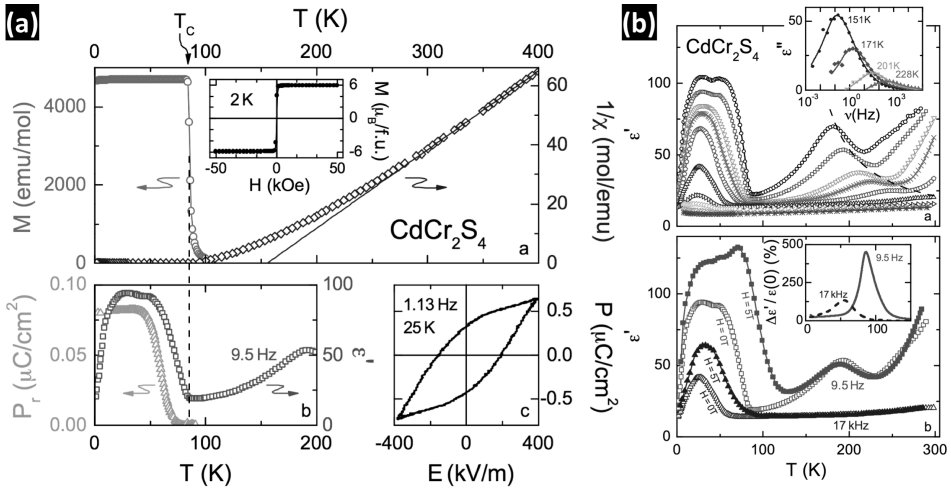

Figure 1.15 – Magnetic and dielectric characterization of $CdCr_2S_4$. **(a)** $M(T)$ (left scale top), $1/\chi(T)$ (right scale top) at 100 Oe and ferromagnetic hysteresis at 2 K (inset top) in $CdCr_2S_4$. $\epsilon'(T)$ (right scale bottom) and $P(T)$ (left scale bottom). $P(E)$, showing a ferroelectric hysteresis. **(b)** Magnetocapacitive behavior of $CdCr_2S_4$. (top) $\epsilon'(T)$ at different frequencies. (top inset) $\epsilon'(\nu)$ for various temperatures above 150 K (lines are to guide the eye). (bottom) Dielectric permittivity versus temperature, measured at zero field and in an external magnetic field of 5 T, directed perpendicular to the electric field. (bottom inset) Magnetocapacitive effect in $CdCr_2S_4$. (Adapted from ref. 128)

The debate started with *Hemberger et al*[128] description of $CdCr_2S_4$ as a multiferroic relaxor, due to the observed relaxor-like dielectric properties and colossal magnetocapacitance (surpassing 500%). However, *Catalan et al*[160] argued that these results could originate from a conductive artifact. They went further, arguing that the polariza-

tion hysteresis loops published by *Hemberger et al*[128] had an uncharacteristic ferroelectric shape and that in fact it resembled more those of a lossy dielectric, like in the case of some semiconducting thiospinels. Furthermore, they pointed out that just the fact that the larger "remanent" polarization in comparison to the pyroelectric one, should suffice to question the validity of the results, because the switchable polarization must always be smaller than the pyroelectric polarization. Here, the observed pyroelectric polarizations were relatively small for any proper ferroelectric (0.05–0.07 μC cm^{-2}), and were in accordance with thermally stimulated discharge of space-charge injected during poling. Albeit *Hemberger et al* were able to counter point each of these arguments, the doubt about the ferroelectric character of $CdCr_2S_4$ would linger among the scientific community and the origin for an intrinsic multiferroic behavior would remain undisclosed.

First-principles calculations excluded softening of the polar modes as a possible origin of the anomalous dielectric behavior[119]. *Sun et al* observation of a glassy dipolar state near T_C and a ferroelectric ordering near $T_P \sim 56$ K contributed to the ongoing discussion[161]. *Ramirez et al*[162] had already suggested that geometric frustration within a room temperature highly symmetric cubic lattice could drive the relaxor-like freezing observed at low temperatures[162]. Other models proposed that the spin-driven polar moments could have their origin from an off-centering of the Cr^{3+} ions[128]. As a matter of fact, the $Fd\bar{3}m$ space group of the overall crystal structure forbids the existence of ferroelectric order but *Gnezdilov et al.* recently suggested that a symmetry reduction below T_C from the $Fd\bar{3}m$ to the $F\bar{4}3m$ non-centrosymmetric space group would permit the existence of electric dipoles[163].

In detail, *Gnezdilov et al*[163] observed pronounced phonon anomalies indicating a possible symmetry reduction and Cr off-centering in the cubic unit cell of $CdCr_2S_4$. The microscopic origin of the spin driven polar moments was suggested to be associated to ferroelectric distortions that could be the result of this off-centering position of the Cr^{3+} ions. The off-centering of Cr^{3+} ions being at the origin of a local polar character that results in a macroscopic isotropic ferroelectric cluster state[130,163] (see Fig. 1.16). Interestingly, the discovery of phonon anomalies at $T_F < 130$ K by means of Raman light scattering suggests that the electronic polarizability was enhanced by the $Cr-S$ distance and respective bond hybridization[163].

Still undisclosed is the origin of the strong coupling of magnetization and dielectric permittivity in this compound. As pointed out, the relaxation dynamics of the polar moments is accelerated below T_C[129], but it remains to be clarified what is the microscopic origin of the detected relaxation dynamics and why the dynamics couples so strongly to the magnetic order parameter. A coupling via exchange-striction, *i.e.*, volume changes arising from the magnetic exchange energy was suggested[129]. As proposed, the onset of spin order leads to a softening of the lattice thereby reducing the energy barriers against dipolar reorientation and thus enhancing the mean relaxation rate[129,164]. An alternative explanation proposed was to consider a magnetic-field-induced variation of charge-carrier mobility or density[129,164].

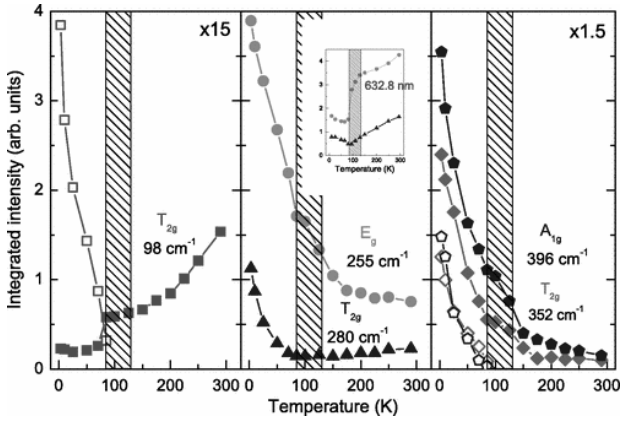

Figure 1.16 – Integrated Raman light scattering intensity of $CdCr_2S_4$ as a function of temperature. The open symbols in the left and right panels correspond to the low-temperature modes at 106, 352, and 390 cm^{-1}, respectively. The inset in the middle panel shows the results of the Raman light scattering intensity experiment with λ = 632.8 nm. (Adapted from ref. 163)

Though much scientific effort has been dedicated to unveil the nature of such effects (*e.g.* origin of the peculiar dynamic dielectric regime above T_C) and to settle multiferroism in this system, the understanding of these phenomena requires an adequate description of the structural, magnetic and charge degrees of freedom. In this way, our interest on $CdCr_2S_4$ stems essentially from the fact that detailed local structural characterization and local probe techniques presents a good opportunity to shed some light into this material and that on the future our findings can be conveyed onto other ferromagnetic semiconductor materials.

1.4.2 Cadmium manganese oxyspinel $CdMn_2O_4$

The understanding of the physical properties of the 3*d* transition-metal oxides, in particular those of the spinel type (*e.g.* spinel oxides AB_2O_4)[165], has made them an interesting subject of study. Up to now, the interest which has been devoted to them has given fruits in many important applications, *e.g.* electronics, optics, magnetic, catalysis, energy storage and conversion[166]. Parallel to an interest in their applicability, these materials provide a fertile playground for fundamental physics where (the potential) frustration (*e.g.* $f_{CdMn_2O_4}$ = 6.7), local distortions, local range order and dynamic mechanisms are yet to be fully understood (*e.g.* in $CdCr_2O_4$, $CdCr_2S_4$, Sr_2RuO_4)[132,167–170].

In particular, manganese based spinels AMn_2O_4 are multifunctional materials in which the tuning of the quantity and the chemical identity of A^{2+} permits to reach a wide range of properties[171]. These spinels belong to a family of compounds which are isomorphous with the mineral hausmannite (Mn_3O_4), characterized by a full replacement of the Mn^{2+} ions on the tetrahedral sites by Zn^{2+}, Mg^{2+} or Cd^{2+} ions accompanied by large tetragonal distortions[172].

In the majority of the cases, the structural distortion can be controlled in some extent by suitable parameters, *e.g.*, the substitution of A or B site cations[173], and it is known

that the Jahn-Teller (JT) effect increases with increasing size of the A – site cation[165].

More particular yet, $CdMn_2O_4$ spinel was found to be an excellent candidate for being used as an active component in highly sensitive mixed potential electrochemical sensors of oxide gases such as NO_x[174–178]. *Miura et al* performed a study to develop new type NOx sensors, using stabilized zirconia and an oxide sensing electrode. Among the various oxides examined for the sensing electrode, $CdMn_2O_4$ was found to be the most excellent material. Here, using a sputtered $CdMn_2O_4$ layer attached to planar or tubular devices, a good response to NO_2 as well as NO in air at higher temperature (such as 500 °C) was obtained.

The $CdMn_2O_4$ crystal structure (space group $I4_1/amd$ with a, b = 5.81, c = 9.87, and c/a = 1.699) can be described as a tetragonal spinel with only diamagnetic cations (Cd^{2+}) on tetrahedral A – sites and magnetic Mn^{3+} cations on the octahedral voids B-sites (normal spinel), has a close-packed O layers in c stacking, and edge-linked MnO_6 octahedra share vertices to form a 3D-framework with units of four octahedra sharing faces with an empty central tetrahedron.

The tetragonal distortions are caused by the JT instability of the Mn^{3+} (d^4) ions[165]. While the divalent A – site cation has a fully filled shell and, thus, it is JT inactive, the trivalent B – site (Mn^{3+} cation), is not.

In the last decade many studies have been dedicated to deepen the understanding of the JT effect and its role in the distortion effect in spinel manganites. These studies included the measurement of the JT splitting by x-ray absorption spectroscopy (XAS)[165] in AMn_2O_4 (A =Zn, Mg, and Cd) as well as the suppression of Jahn-Teller distortion in the case of the $LiMn_2O_4$ particles[179]. In addition, high pressures have been used to study the parallelism between lowering the temperature and increasing the pressure and their effect in inducing a transition to another tetragonal phase, as a consequence of the increase of the Mn occupation at tetragonal sites[180]. The importance of these phenomena is highlighted in recent literature[181,182].

The works of *S. K. Dey et al*[183,184] opened already a pathway in comprehending the physical properties observed in $Cd_xMn_{3-x}O_4$, where we find those of particular interest for this work when x = 1 ($CdMn_2O_4$). Two important aspects found between 600 – 700 K were evidenced in that work: a broad discontinuous peak on differential thermal analysis curves and a deviation from linearity of the magnetic susceptibility. These reported anomalies are, in a final way, ascribed to a crystallographic phase change (structural transition from cubic to tetragonal at T_S = 600 K)[165,172,183,185] (see Fig. 1.17).

Furthermore, $CdMn_2O_4$ spinel manganite shows an antiferromagnetic behavior (T_N = 70 K) with the magnetic susceptibility exhibiting a temperature-independent behavior over a small range of temperatures and with Curie-Weiss temperature of θ_{CW} = −470 K.

The literature shows several spinel families where it is possible to observe a high temperature phase transition, which is usually connected to the sample's oxygen stoichiometry change[186–192]. In $MgMn_2O_4$ and $ZnMn_2O_4$ systems[193,194] a JT- distortion

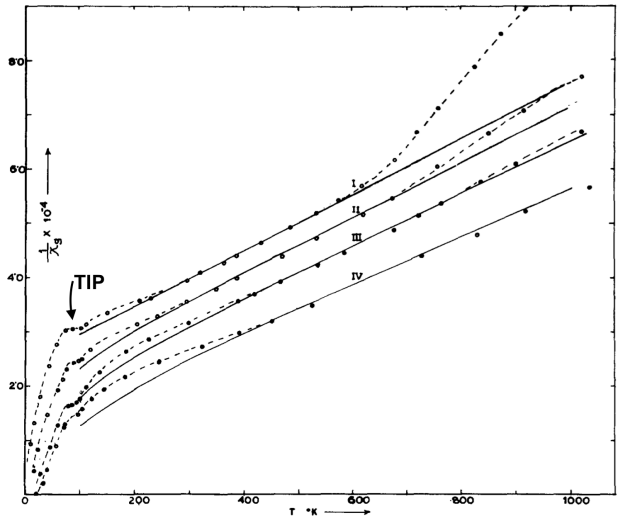

Figure 1.17 – The inverse mass susceptibility as a function of temperature $\frac{1}{\chi_g}(T)$ for $Cd_xMn_{3-x}O_4$ with x=1.0, 0.8, 0.6 and 0.4 corresponding to I, II.III and IV respectively. The solid lines are drawn from $\chi = \frac{C}{T+\theta} + \frac{C'}{T}$ while the circles represent the experimental values. (Adapted from ref. 184)

and a cubic to tetragonal transition was reported at high temperatures (> 1000 K). However, this has not been observed in $CdMn_2O_4$. Also, in some spinels it was observed a local symmetry lowering at high temperatures. Here the point symmetry of some sites is subjected to modifications and these local structural instabilities can be observed in the form of anomalies in macroscopic properties[169,170,195].

Thus we set ourselves with the task to pursue the origin of these observed anomalies and relate them with the magnetization behavior, Jahn-Teller distortion, and the possible structural phase transformation observed in the $CdMn_2O_4$ by performing local probe studies. Studying the electric field gradient tensor obtained from the nuclear quadrupole hyperfine interaction, will allows us to reconstruct the atomic and electronic environment of the atomic probe in the material and provide new data, which can assist in clarifying the nature of the previously reported anomalies in macroscopic properties.

1.5 Perovskite compounds: RBO_3

The perovskite name arises from the parent mineral $CaTiO_3$. Discovered by Gustav Rose, who name it after the Russian mineralogist L.A. Perovski[196], was then adopted to materials with similar structure. Having the chemical composition RBX_3, where R and B are metallic cations (R being the biggest) and X an anion usually from the family of halogens (*e.g.* Fluor, Bromine) or more commonly Oxygen. Among the most studied perovskites we find the perovskite oxides $BaTiO_3$ and $LaMnO_3$.

Oxygen based perovskites, RBO_3 have been known and synthesized since the early 1950s[197,198]. Since then, they have been under the spotlight in the physics research area due to the exhibited different physical properties and have been employed in many applications[199,200]. Usually, a certain crystallographic structure is associated with a

certain magnetic or electric behavior. Up to now, literature refers that small local distortions and/or inhomogeneities in the composition of the oxides are responsible for the diversity of properties manifested. However, still lacking is a good understanding of the mechanisms behind those properties that would allow the prediction of new structures with desired properties.

Originally described with a cubic configuration, different structures can be obtained by varying of the trivalent ionic radius of R and B. Elements like Li, K, Cs, Ca, Ba, Sr, Pb or rare-earths are some of the over twenty elements that typically can be in the R-site, while in the B-site transition metals like Cr, Mn, Fe, Co, Ni, Ti, Zr, Ta, Nb can be found.

A simple but effective way of describing the normal perovskites (cubic) structure is to consider the R cation in a cube centre, surrounded by 8 corner linked BO_6 octahedra, with a B cation in their center. R cations have a XII fold coordination with oxygen (the oxygen atoms occupy 12 positions in the middle of each side of the cube).

All sites are occupied and the strong ionic bonds do not permit much freedom to atoms and electrons to deviate from their lattice sites. As a consequence, electron mobility through the crystal is commonly very small. Besides, the ionic bonds are isotropic which makes properties like compressibility and electric conductivity to be also isotropic. These ideal cubic perovskites are in fact electric insulators. However, many perovskites have their structure slightly distorted, mainly because the R-site cation is much smaller than the one in the cube vertices (B-site), and so the oxygen atoms and sometimes the atoms in the B-sites are dislocated from their positions. In this way, changing the physical properties of the perovskites.

In a general way, it is possible to describe three main types of structural distortions occurring in perovskites. One arising from the displacement of cations from their central positions but conserving their local coordination environment, the other arising from the distortion of the octahedra themselves (because of the active Jahn-Teller central atom) and finally the one that has the larger effect on structural symmetry and unit cell, the tilting or buckling of BO_6 octahedra. A combination of the displacement of cations and octahedra tilting is the more commonly, but some materials like $BiMnO_3$ can exhibit all three types of distortions[201] (see Fig. 1.18).

The different structural distortions present in these compounds can have different magnitudes and thus change the structure from cubic to orthorhombic or rhombohedric symmetries[203–206]. This can be achieved by external parameters like temperature, pressure or chemical composition. It is in these structures that the real interest lies upon and where interesting physical phenomena (*e.g.* like magnetic and electric orders) confers them great scientific and technological interest[207,208]: metal-insulator transition[209], high T_C superconductivity[210], magnetocaloric properties[211,212], colossal magnetoresistance[213,214] or ferroelectricity[10]. The last appears in distorted perovskites, because the R cations are slightly deviated in relation to the cube centre. Here, the octahedra, who's axes are aligned to the edge of the cube in an ideal perovskite, will tilt and rotate, making the R site cubical spacial symmetry to change to tetragonal,

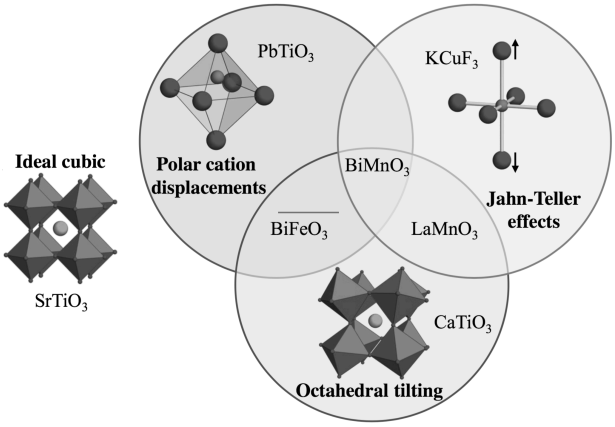

Figure 1.18 – The three main distortions of the perovskite structure: cation displacements, octahedral tilts, and first-order Jahn-Teller effects. Materials in the overlapping regions adopt multiple distortions. (From ref. 202)

rhombohedral or orthorhombic.

In this case a charge shift can originate the appearance of electric polarization[ii] and the material will become ferroelectric. As described before, ferroelectric materials are very interesting for their possible use in electronic devices. This is the case of $BaTiO_3$, which is probable the most known commercial perovskite.

Some examples of rhombohedral, orthorhombic, hexagonal and cubic symmetry that can take place in RBO_3 perovskite oxides (where B is a transition metal) are illustrated in Fig. 1.19, as a function of the R and B ionic radius.

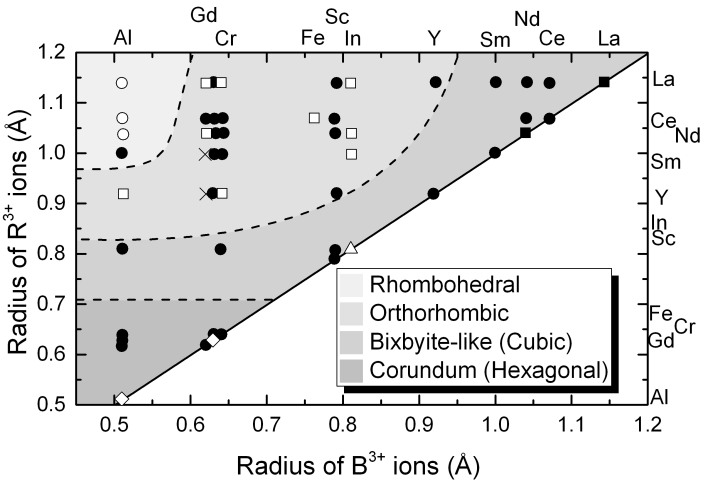

Figure 1.19 – Classification of the $R^{3+}B^{3+}O_3$ type compounds according to the constituent ionic radii. ○ - Rhombohedral perovskite, $\alpha > 90°$; □, orthorhombic perovskite $CaTiO_3$ type; △, Tl_2O_3 structure type; ◊, corundum structure type; ■, La_2O_3 structure type; ●, compounds assumed to have the structure by the areas bounded by dashes. (Adapted from ref. 198)

In 1926 *Goldschmidt* proposed a way to determine the resulting perovskite structure based on the average ionic radius of its composing elements[216]. Nowadays, the same

[ii] Sometimes, with an external applied electric field the same effect can occur[215].

indicator is also used to predict the stability and distortion of other crystal structures[217]. The Goldschmidt tolerance factor, t, is determined by:

$$t = \frac{r_R + r_O}{\sqrt{2}\,(r_B + r_O)}\,, \tag{1.10}$$

where, r_R, r_B, and r_O are the average ionic radius of the R, B, and O ions, respectively.

An ideal perovskite cubic structure has $t = 1$, where B–O–B form a 180° angle, however deviations from this values can arise due to the different ionic radius sizes in the 1:1:3 stoichiometry. Hexagonal or tetragonal structures exist for $t > 1$. Rhombohedral or orthorhombic symmetry appear when $t < 1$ and in these cases its observed a decrease in the B–O–B angle. When $t < 1$, there is a compression of the B–O bonds, which in turn induces a tension on R–O bonds. A cooperative rotation of the BO_6 octahedra and a distortion of the cubic structure counteract these stresses. In fact, the larger number of perovskites studied fall in the range $0.71 \leq t \leq 1.00$. Furthermore, between $0.75 < t < 0.90$, an increased orthorhombic (*Pbnm*) structure is obtained, like in the case of $GdFeO_3$, by the cooperatively tilt of BO_6 octahedra. While for $0.90 < t < 1.0$, no cooperative tilt of the octahedra is found and the small distortions lead to lower symmetry structures.

RBO_3 compounds, in particular $RCrO_3$ compounds have a crystallographic orthorhombic perovskite type structure (space group *Pbnm*)[iii] similar to that of $GdFeO_3$ [218,219]. A schematic polyhedron model of the structure can be visualized in Fig. 1.20.

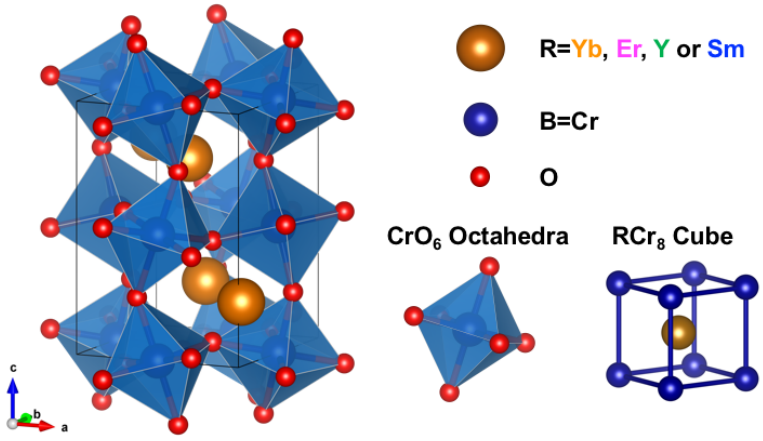

Figure 1.20 – Schematic representation of the $RCrO_3$ perovskite structure.

The orthorhombic structure has four formula units per unit cell ($Z = 4$), the rhombohedral has $Z = 2$, and hexagonal has $Z = 6$ as compared to $Z = 1$ in the case of ideal cubic perovskite. As we can see in Fig. 1.20, the BO_6 distorted octahedra are rotated about the z−axis and tilted about [110]-axis, *i.e.*, looking into any two connected octahedra, if the B atoms are in the same (different) layer, the rotations are in the opposite (same)

[iii] In some publications,a *Pnma* or a pseudo-cubic lattice are introduced for $RCrO_3$ perovskites. There is a 45°rotation between the *Pbnm* and the pseudo-cubic indexing. Axes are switched between the *Pbnm* and *Pnma* indexing.

direction. Furthermore, all nearest neighbor octahedra are tilted in opposite directions.

The *Pbnm* crystal structure of these perovskite permits the existence of a spin canting perpendicular to the spin easy axis following any of the four main magnetic orders (A, C, F and G-type) and thus gripping the attention of researchers in terms of non-collinear magnetism studies.

Interestingly, from these main magnetic collinear orders (A, C, F, G; see description below and Fig. 1.21), three of them are compatible with a ferromagnetic component via spin canting of the AFM order (perpendicular to this axis accompanying any of the four main magnetic orders) and thus obtain a net magnetization [220].

Furthermore, a relationship between the amplitude of the canting, the amplitude of the oxygen rotations and the ratio between the Dzyaloshinskii-Moriya (DM) vector and the superexchange interaction (J) was proposed [74]. Accordingly, systems exhibiting low T_N's are characterized by having large octahedral rotations and not too large J (*e.g.* $NaFeF_3$), while in ferrites the simultaneous large octahedral rotations and the very strong J leads to higher T_N's (with small cantings).

The magnetic ions in a compound often form a simple cubic sub-lattice, where the B-sites in perovskite RBO_3 are an example. In Fig. 1.21 we show a schematic depiction of the *A*, *C*, *G* and *E* type antiferromagnetic structures that are possible in cubic perovskites RBO_3 [220].

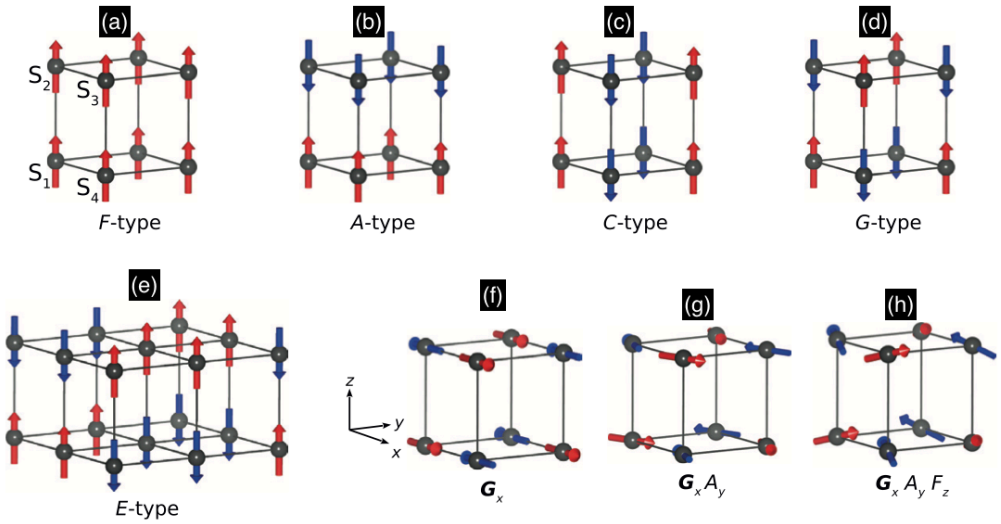

Figure 1.21 – Schematic representation of **(a)** F-type, **(b)**, A-type, **(c)** C-type, **(d)** G-type and **(e)** E-type collinear magnetic orders that are possible in cubic perovskites RBO_3 (for simplicity, spins are directed along the *z* axis). **(f)**, **(g)** and **(h)** represent the G_x, G_xA_y and $G_xA_yF_z$ non-collinear orders. (Adapted from ref. 220)

A-type: The intra-plane coupling is ferromagnetic while inter-plane coupling is antiferromagnetic.

C-type: The intra-plane coupling is antiferromagnetic while inter-plane coupling is ferromagnetic (a.k.a "checkerboard").

G-type: Both intra-plane and inter-plane coupling are antiferromagnetic (the sys-

tems is antiferromagnetic in all directions).

E-type: Following a cube edge, two spins point in one direction and the next two in the other (a.k.a. “zigzag chains”).

F-type: Both intra-plane and inter-plane coupling are ferromagnetic (the systems is ferromagnetic in all directions).

The properties of perovskites have been studied for long, however its only in 1986 with the discovery of the first high-T_C superconductor and with with the rediscovery of colossal magnetoresistance in the beginning of the 90’s decade (like in the case of spinels and other compounds) that a revival of the research on them was lift up. Among the many perovskites studied since then, one of the most interesting ones are the transition metal oxides based perovskites.

Transition metal oxides based perovskites possess a wide range of electronic and magnetic properties[74,220]. They can exhibit different metal-oxygen bonds and thus present insulator (*e.g.* $BaTiO_3$), ionic or metallic behavior (*e.g.* $LaNiO_3$)[221]. Curiously, they can change between these regimes with composition, pressure or temperature (*e.g.* V_2O_3 or $La_{1-x}Sr_xVO_3$) or exhibit different electronic/magnetic properties[74]. Thus, perovskite systems present rich phase diagrams where we can find different magnetic behaviors and phenomena like spin glass, charge ordering (CO), orbital ordering and electronic phase separation[222–226]. In the form of single crystals, polycrystalline samples or thin films these materials present commonly a complex combination of spin, lattice, charge, and orbital degrees of freedom providing researchers with a rich set of materials where the properties can be tuned in order to achieve desired physical phenomena. In fact, as described before, multifunctional materials like multiferroics and magnetoelectric ones, have found in these class of materials many interesting examples with possible applications as well as from the fundamental physics point of view[29,39,160,227].

Among the large number of perovskites studied in recent years, $BiFeO_3$[227] and $BiMnO_3$[45,228] are among the most important examples. However, other compositions have been reported as to exhibit a simultaneous electrical and magnetic ordering, like in some $LnMnO_3$ (Ln=rare-earth), $LnMn_2O_5$, $La_2Mn(Co/Ni)O_6$, $LuFe_2O_4$[229], Ln_2BaNiO_5, $(LnGa)FeO_3$, or even $YCrO_3$[230], Bi_2MnNiO_6, perovskite-like $YBaCuFeO_5$[231] among numerous others[51,232–235].

1.5.1 Orthorhombic rare-earth chromites $RCrO_3$

The understanding of functional RBO_3 perovskite oxides is a very active research area with relevance to both fundamental and application related issues. Their ability to accommodate a series of different structural distortions, due to the capacity to incorporate almost every element of the periodic table, makes them exhibit a rich magnetic phase diagram and even in some cases a ferroelectric order. In fact, perovskites $RCrO_3$ are the ones selected for this thesis, because like in the larger family, here, the orthorhombic distortion, octahedral tilt angle, can be continuously tuned by the ionic size of the

R^{3+} ion and thus allowing us to tune their properties[92,236].

Actually, over the last few decades, the production and characterization of orthochromites has been the object of study in many works[208,237–244]. Their interest on these orthochromites falls largely on the different ferroic orders that these perovskites may exhibit, such as ferromagnetism, ferroelectricity, and/or ferroelasticity[26,91,212].

Some members of the $RCrO_3$ family (R=Ce, Gd, Tm and Yb) show magnetization reversal (or negative magnetization) phenomena, with compensation temperatures of 133 K, 130 K, 25 K and 18 K respectively[245–248], which would be useful for applications like non-volatile memories[249,250] and spin resolving devices for charged particles[251]. On orthochromites similarly to orthoferrites, a gradual magnetization of the R spins above their sub-lattice ordering temperature is observed. This occurs in an opposite direction to the Cr weak FM component[220] as illustrated schematically on Fig. 1.22.

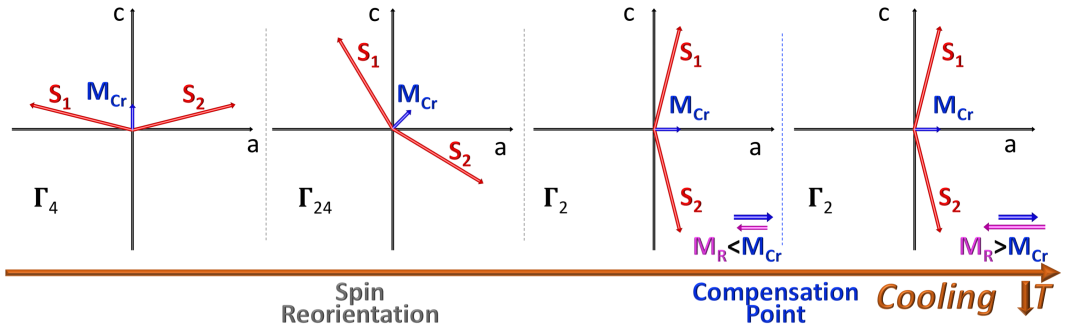

Figure 1.22 – Schematic view of the continuous spin reorientation observed in some $RCrO_3$. The orange arrow at the bottom indicates the decreasing temperature; S_1 and S_2 are the two pairs of spins for Cr^{3+}; M_{Cr} is the net FM moment of Cr^{3+} and M_R is the moment of R^{3+}. (Adapted from refs. 252 and 220)

Recently, alongside with the observation of complex magnetic properties in some of the rare earth orthochromites, also interesting dielectric and ferroelectric properties have been described. There has been a few reports on rare-earth orthochromites suggesting them as potential magnetoelectric multiferroic materials[206,208,218,230,253,254]. Still under debate are the ferroelectric transition temperatures and their origin[255–257].

Suspicions of ferroelectricity in rare earth orthochromites RBO_3 R=Dy, Ho, Yb, Lu, Pr and Y (but not La) started back in 1968 with the work of *Rao et al*[253]. The authors findings, anomalies in the electrical conductivities curves, narrowing of the dielectric hysteresis loops and maxima in pyroelectric currents, were suggested to be associated to a para-ferroelectric transition observed at $T \gg T_N$ (750-900 K). Later on, in the work of *Niitaka et al* on $BiCrO_3$ a structural phase transition from orthorhombic *Pnma* with centrosymmetry to monoclinic C_2 without centrosymmetry at 440 K was suggested[206]. This phase transition was accompanied by an anomaly of the dielectric permittivity, implying also a ferroelectric transition. A parasitic ferromagnetic ordering occurring at 114 K was also reported.

Actually, $YCrO_3$ was also proposed by *Serrao et al* to exhibit a ferroelectric phase[230].

The authors observed a dielectric anomaly at 473 K, higher than the magnetic ordering temperature of $YCrO_3$ (T_N = 140 K), accompanied by a leaky hysteresis loop at 300 K. Moreover, the same authors suggested that non-centrosymmetry in $YCrO_3$, required for a polar order to appear, has a local nature. Based on their results in $YCrO_3$, ferroelectric order is suggested to also be possible in other chromites of heavier rare earths with R = Er, Ho, Yb or Lu. The authors preliminary measurements point to $LuCrO_3$ to be ferromagnetic at T_N=115 K and ferroelectric at T_{FE} =488 K.

A large increase in the dielectric permittivity with an important frequency dispersion, when R = Ho, Er, Yb and Lu, was reported by *Sahu et al*[218] further sustaining this claim (see Fig. 1.23 for the cases of $ErCrO_3$ and $YCrO_3$).

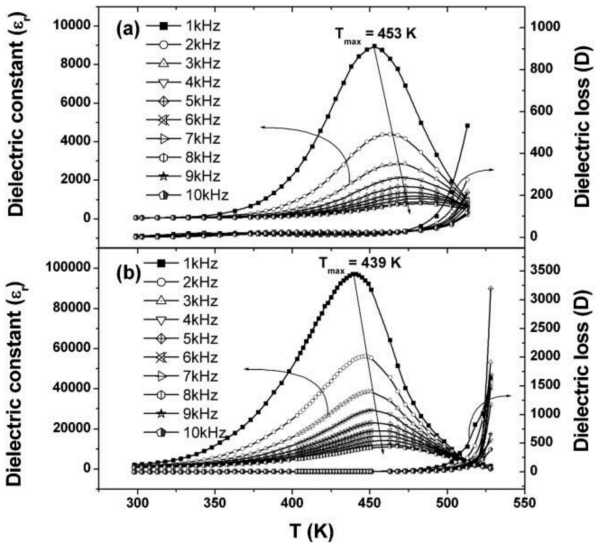

Figure 1.23 – Temperature dependence of the dielectric permittivity of **(a)** ErCrO3 and **(b)** YbCrO3 at different frequencies. (From ref. 218)

This behavior was labeled as a relaxor-like and initially attributed to a weak ferroelectric-like response mirroring that of $YCrO_3$[230]. Thus, these materials were proposed to be multiferroic, exhibiting canted antiferromagnetism at low temperatures (T_N = 113-140 K) and a ferroelectric transition in the 472–516 K range. In fact, a theoretical prediction of a possible magnetoelectric coupling between the rare earth and Cr^{3+} ions in these materials was brought forward[218,230,258]. For the case of $LuCrO_3$, without a magnetic R ion, the effect was only predicted by first-principle calculations and suggested by *Serrao et al*[230]. In the cases of $LaCrO_3$ or $NdCrO_3$ no anomalies were found and thus not included as possible multiferroic materials.

The magnetic and electric properties of rare-earth orthochromites (R = Sm, Gd, Tb, Er, Tm, Lu, and Y) were revisited in the work of *Rajeswaran et al*[208]. The authors report field-induced switchable polarization in these compounds ($P \sim 0.2$–$0.8\ \mu Ccm^{-2}$) , but only when the rare-earth ion is magnetic and occurring below the Néel temperature of chromium (T_N^{Cr} = 120–300 K) and further support multiferroicity in these systems. In fact, no intrinsic electric polarization was observed in the case of $LuCrO_3$ or $YCrO_3$, *i.e.*

compounds with nonmagnetic R ions. It is suggested by the authors that in addition to the magnetic R ion, the weak ferromagnetism of the Cr sub-lattice is also vital for inducing polarization in these orthochromites. Multiferroic behavior of these systems is caused by the combined effect of the poling field that breaks the R ion symmetry and its exchange field on the Cr sub-lattice that stabilizes the polar state[208,254]. Here, small displacements of the R atoms can occur created by the poling procedure used for measuring polarization, promoting metastable states that are still visible after the poling process. Furthermore, the authors argue that the observed ferroelectric polarization and its dependence on the magnetic field can be explained if exchange striction mechanism or magnetoelastic effect are present in these systems (magnetically induced ferroelectrics [$T_N^{Cr} = T_{FE}$]), in which the magnetic order determine the electric polarization.

Some light on this debate appeared in 2014 when *Gosh et al*[259] reported a local non-centrosymmetric *Pna*2$_1$ space-group for $SmCrO_3$, observed using x-ray synchrotron pair distribution function results, somewhat above the appearance of spontaneous ferroelectric polarization (see Fig. 1.24).

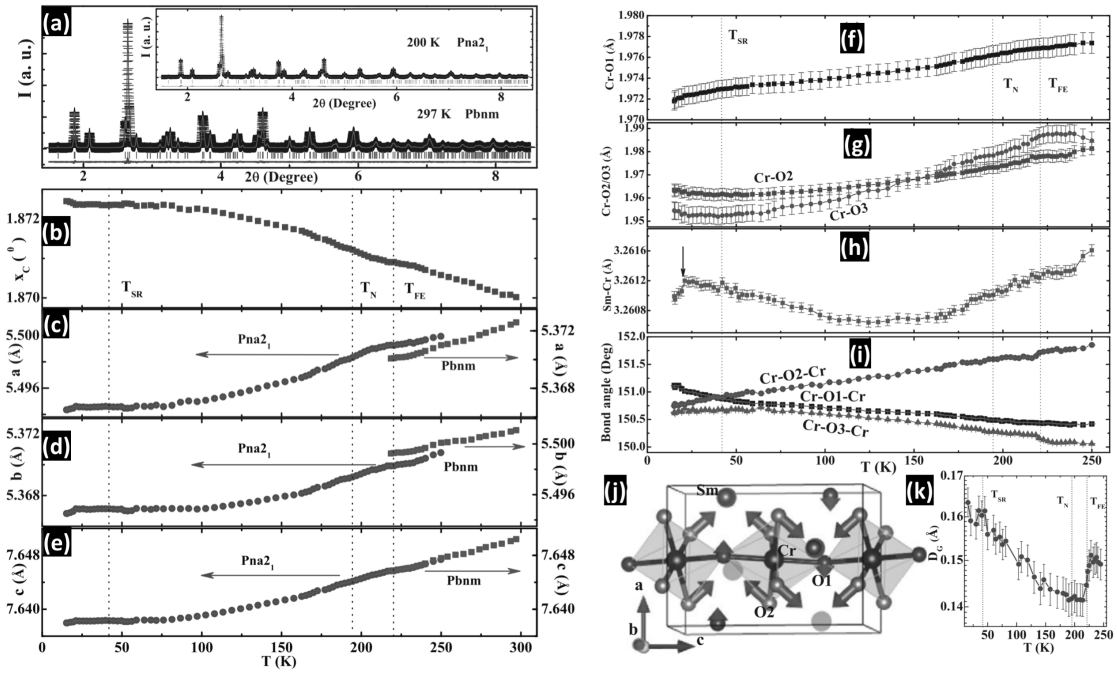

Figure 1.24 – $SmCrO_3$ pair distribution function (PDF) results. **(a)** Rietveld refinement of $SmCrO_3$ x-ray powder diffraction pattern at 297 K using *Pbnm* space group and the inset shows the same at 200 K *Pna*2$_1$ space group. **(b)** Thermal variation of the shift of the peak position (X_c) of the (400) plane, **(c)** lattice constants *a*), **(d)** *b*, **(e)** *c*. Temperature variations of **(f)** Cr-O1, **(g)** Cr-O2/O3, **(h)** Sm-Cr bond lengths, and **(i)** Cr-O1/O2/O3-Cr bond angles for $SmCrO_3$. **(j)** Displacements of Sm, O1 and O2 for the transformation from *Pbnm* to *Pna*2$_1$. **(k)** Global distortion parameter (D_G) with *T*. (From ref. 259)

The appearance of a local non-centrosymmetric space group is proposed to be related to rotations of polar CrO_6 octahedra and Sm displacement that in turn promotes the emergence of polar order at a significantly higher temperature than T_N. The appearance of a polar order was found to be extended over a large temperature range in-

creasing gradually with decreasing temperature. Furthermore, the authors suggest that the relaxor behavior observed in $SmCrO_3$ occurs due to freezing of polar order. These results bring an important contribution to the origin of spontaneous electric polarization in orthochromites suggesting that they are not improper ferroelectric materials[259].

Moreover, these findings made us question wether the appearance of a noncentrosymmetric structure close to the onset of polar order could *per se* be enough to induce a spontaneous electric polarization without the requirements proposed by *Rajeswaran et al*[208]. In this way, allowing for electric polarization to be possible in orthochromites without a magnetic R ion, like in the case of $YCrO_3$ where in fact local noncentrosymmetry has been observed[219].

In Fig. 1.25 are plotted the magnetic ordering temperature of the Cr (T_N^{Cr}) and R (T_N^R) sub-lattices of some orthochromites along with the ferroelectric temperatures (T_{FE}) proposed by *Sahu et al*[218] and *Serrao et al*[230] and respective polarization values. Initial reports suggest T_{FE} at very high temperatures, however recent ones place the ferroelectric transition concomitantly with the magnetic transition. The elements for which that has been reported are identified by downward arrows (R = Sm, Gd, Tb, Er, Tm, Lu, and Y)[208,218,220,256].

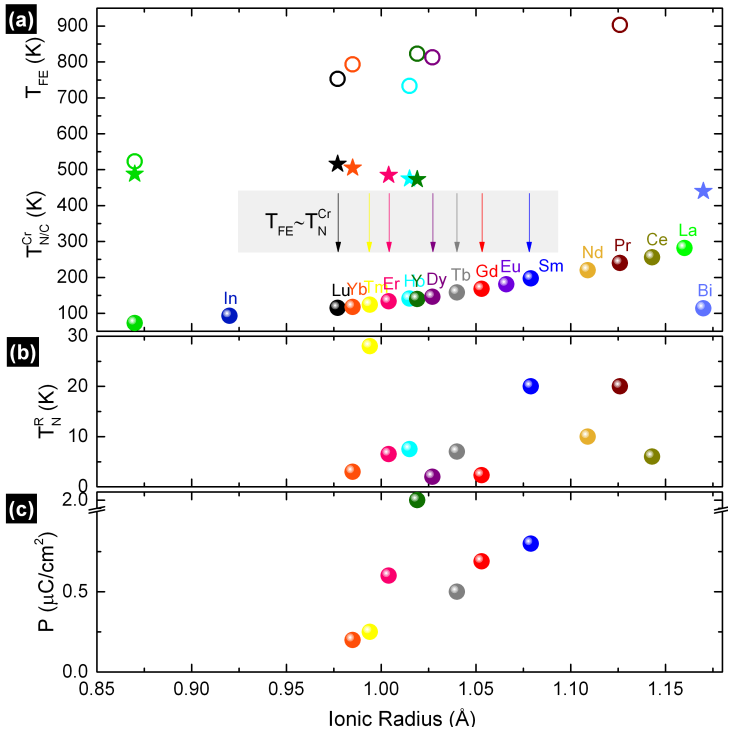

Figure 1.25 – **(a)** Magnetic ordering of Cr sub-lattice and ferroelectric transition temperatures reported in literature for some $RCrO_3$. **(b)** Magnetic ordering of R sub-lattice. Polarization values of some $RCrO_3$ taken from refs. 208,218,220,253,256. Systems identified with an arrow were recently reported to present $T_{FE} \sim T_N^{Cr}$[208].

Looking into Fig. 1.25 it is easily understood that the increase of R ionic radius is accompanied by an increase in the ferromagnetic ordering temperature of the Cr sub-lattice and a decrease of the proposed ferroelectric ordering temperature, at least

considering the cases where ferroelectric order is proposed to appear well above T_N^{Cr}. A clear exception to this trend is the case of $BiCrO_3$, which has a structural transition (*Pbnm* $\rightarrow$ *C*2/*c*) and different physical properties when compared to other orthochromites with only one magnetic ion (because of the lone electron pair of Bi^{3+} and the covalency of the $Bi^{3+}-O$ bonds)[260]. Studying the evolution of the proposed polarization values, one finds also an almost linear increase with the rare earth ionic radius increase. Curiously, it is in the case of $YCrO_3$ that a deviation of this trend is observed, yet it is where the largest polarization value is observed.

The magnetic properties of orthorhombic rare-earth chromites $RCrO_3$ are usually described using as a starting point the properties of orthoferrites like $BiFeO_3$. So, one can say that orthorhombic rare-earth chromites have similar magnetic orders to those of orthoferrites, however due to the lower moment of the Cr ions compared to that of Fe, they exhibit lower T_N's. Described as canted anfiterromagnets (CAFM) they order antiferromagnetically but due to the spin canting between them a weak ferromagnetic component is also observed[230]. An antiferromagnetic alignment of the spins is observed between the Cr ions and in some cases between the weak ferromagnetic component of the Cr ions and those of the R ions. The R^{3+} sub-lattice undergoes an antiferromagnetic ordering at very low temperatures. The Néel magnetic transition temperature of Cr sub-lattice (T_N^{Cr}) on these materials decreases with decreasing radius of the R^{3+} ions (*e.g.*, T_N = 282 K in $LaCrO_3$ and T_N = 73 K in $ScCrO_3$, see Fig. 1.25) and table 1.2. Concomitantly is observed a decrease in the octahedral tilting angle deviating from the 180°, and a consistent decrease of the $Cr^{3+}-Cr^{3+}$ bond.

Contrarily to other magnetic systems, where the magnetization direction is switched by a change in the direction of the applied magnetic field. Some $RCrO_3$ compounds (R=Nd, Sm, Gd, Er) however do not require a change of the direction of the external magnetic field and rely on a Cr^{3+} spin-reorientation transitions at lower temperatures (T_{SR})[245,261] from Γ_4 to Γ_2 or Γ_1.

In the orthochromites with *Pbnm* structure, the following three types of G-type antiferromagnetic configurations are observed: Γ_1(*Ax*, *Gy*, *Cz*), Γ_2(*Fx*, *Cy*, *Gz*), Γ_4(*Gx*, *Ay*, *Fz*) following the Bertaut notation[262] (see Fig. 1.26).

One should note that from the three configurations Γ_1 is the only one that does not have a spin canting and thus not exhibiting a weak ferromagnetic component. However, Γ_2 and Γ_4 exhibit one along the *x* and *z* directions, respectively[208]. Γ_4 is observed below T_N^{Cr} when R=Sc, In, Y, Tb, Eu or La, while for the cases where R=Lu, Yb, Tm, Ho, Dy, Gd,Sm or Ce, Γ_2 is observed. These configurations are observed in all temperature range with the exception of R=Gd, Sm and Ce, where a spin reorientation at low temperatures gives rise to Γ_2 and in the cases of R=Er or Nd, to Γ_1. The spin reorientation is continuous in the former cases (see Fig. 1.22), and discontinuous in the latter ones. In fact a spin reorientation may also occur in $YCrO_3$ but not like the former cases where is caused by the interaction of the R and Cr moments but by applying a magnetic field along the *a* direction[263].

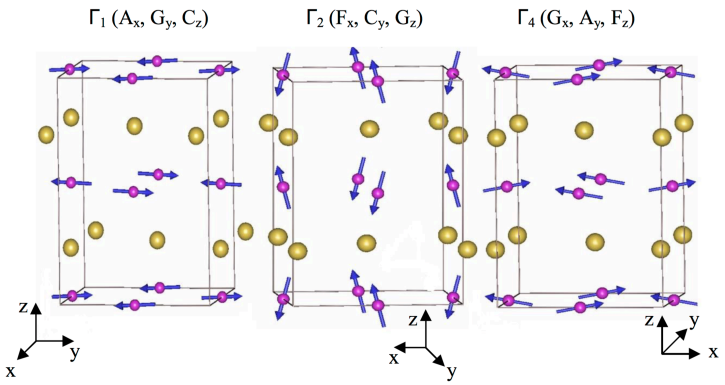

Figure 1.26 – Spin structures in Γ_1, Γ_2, and Γ_4 with *Pbnm* space group symmetry showing absence of spin canting in Γ_1. The location of the R ion is marked by spheres without spin. (From ref. 208)

Table 1.2 summarizes several magnetic parameters of orthochromites, where IOR is the ionic radius of the R ion considering a XII coordination. T_N^{Cr} and T_N^{R} are the ordering temperatures of the Cr and R sub-lattices, respectively. Cr-order denotes the magnetic arrangement of spins of the Cr ions in the lattice according to the Bertaut notation[262]. T_{comp} is the compensation temperature between the Cr and R sub-lattices. C is the Curie constant, θ_{CW} is the Curie Weiss temperature and μ_{eff} is the total paramagnetic moment of the system. The values present in the table were collected from refs. 74, 202,203,206,218,220,240,264,265 and references therein.

Table 1.2 – Summary of magnetic properties of some orthochromites.

Compound	IOR (Å)	T_{FE} (K)	T_N^{Cr} (K)	Cr-order	T_N^{R} (K)	T_{comp} (K)	C (emu/mol·K)	θ_{CW} (K)	μ_{eff} (μ_B)
$ScCrO_3$	0.870	523 [218];488 [230]	73	Γ_4				-150	3.96
$InCrO_3$	0.920		93	Γ_4				-141	3.95
$LuCrO_3$	0.977	753 [253];516 [218]	112	Γ_2			2.4	-174	3.87
$YbCrO_3$	0.985	793 [253];505 [218]	118	Γ_2	10	18	4.4	-49	5.97
$TmCrO_3$	0.994	127 [208]	127	Γ_2	6	25	8.6	-32	8.49
$ErCrO_3$	1.004	485 [218];133 [208]	133	$\Gamma_4 \xrightarrow{22K} \Gamma_1$	6-13		12.8	-24	10.33
$HoCrO_3$	1.015	733 [253];475 [218]	140	Γ_2	7-12		15.7	-21	11.28
$YCrO_3$	1.019	823 [253];473 [218,230]	140	Γ_4			2.51	-408	3.87
$DyCrO_3$	1.027	813 [253];144 [266]	146	Γ_2	2-4		15.7	-24	11.33
$TbCrO_3$	1.040	157 [208]	157	Γ_4	3		12.9	-26	10.46
$GdCrO_3$	1.053	167 [208]	167	$\Gamma_4 \xrightarrow{7K} \Gamma_2$	2.3	130	7.3	-29	8.83
$EuCrO_3$	1.066		181	Γ_4			3.4	-198	5.15
$SmCrO_3$	1.079	197 [208]	197	$\Gamma_4 \xrightarrow{40K} \Gamma_2$	5		3.5	-724	5.30
$NdCrO_3$	1.109		291	$\Gamma_4 \xrightarrow{34K} \Gamma_1$	10		3.8	-189	5.29
$PrCrO_3$	1.126	903 [253]	237	Γ_2	3	6	3.3	-160	5.21
$CeCrO_3$	1.143		260	$\Gamma_4 \xrightarrow{16K} \Gamma_2$		133		-292	4.52
$LaCrO_3$	1.160		282	Γ_4			3.3	-800	3.87
$BiCrO_3$	1.170	440 [206,230]	114				1.94	-359	1.88

The exhibited properties (*e.g.* magnetic and ferroelectric order and local properties) alongside with the debated appearance of ferroelectricity and their evolution with temperature, R ionic radius, crystallographic structure as well as T_N still need clarification thus calling for further studies.

One should call to the attention that in the present thesis our interest falls upon perovskite oxides where B = Cr and R = Y, Sm, Er, Yb). They were chosen due to their interesting physical properties (see sections 5.1, 5.2 and 5.3). Clearly there is a need of

further investigations to fully understand the multiferroic and magnetoelectric properties of many chromites. In particular, the origin (or even existence) of the ferroelectric order in these perovskite oxides continues to be shrouded with debate. Thus, in this thesis we hope to give valuable information to this problematic by pursuing one of the proposed mechanism for the appearance of ferroelectricity, namely, by trying to answer to the question wether local symmetry changes are at the origin of ferroelectricity? In addition we explore their possible use in magneto refrigeration technology.

CHAPTER 2

Experimental Techniques and Materials

In this chapter, we will present a brief description of the synthesis methods used to produce the studied materials, followed by an overview of the experimental techniques used to characterize them in this thesis. Firstly, the traditional solid state synthesis process, used to produce polycrystalline samples. In a second part, several macroscopic and microscopic methods are shortly reviewed, namely techniques for their structural and morphological, magnetic and electric characterization. Finally technical information on the Local Probe technique is provided. For completeness we will give reference to previous works where the techniques are described in more detail, when in-depth knowledge is required.

2.1 Sample Preparation

Nowadays solid-state chemistry continues to have major role in an enormous set of disciplines. Given that the discovery of new physical phenomena greatly depends on the development of new materials, the synthesis of novel stable solid-state materials having the desired properties is of great importance. The synthesis processes utilized to prepare inorganic materials are different from those used by organic chemists. The former has to work with complete lattices, either building or modifying them which is necessarily a complex task[267]. In fact the preparation of solids with the desired structure, composition and properties is still a challenge to chemists, material scientists and engineers.

Historically, the preparation of solid-state materials has been accomplished with the use of high temperature solid-state diffusion reactions, generally yielding the most thermodynamically stable phases. A variety of techniques have been developed to overcome the limitations inherent to this traditional approach. As an example of other methods now available, the ACr_2O_4[268] or $BaMP_2O_7$ (M=Mn, Cu)[269] systems have been already prepared by, *e.g.* hydrothermal synthesis. Also, sol-gel technique (urea sol-gel process[270], glycine nitrate process, ethylene glycol process[271], sol-gel microwave combustion or solution combustion synthesis) have been employed in the fabrication of many other materials.

2.1.1 Solid-State Reaction Synthesis

In a solid state reaction the reactants chemically react or diffuse without the use of a solvent. It can be also called a dry media reaction. A standard chemical reaction is typically accomplished by placing the reacting agents in a solvent before the reaction take place. These reactants react to form a new substance. After the reaction is completed, it's possible to remove the new product from the solvent.

Solid state reactions happen through solid state diffusion, *i.e.*, the movement and transport of atoms without leaving the solid phase. The diffusion process takes place preferentially trough lattice defects, vacancies and interstitial ions. It can also occur along grain boundaries, dislocations, inner and outer surfaces, etc. Notice that diffusion along linear, planar and surface defects is most of the times faster than in the 3D lattice. This is the reason why they are also termed high diffusivity or easy diffusion paths.

In oxides and other inorganic compounds, temperature, partial pressures/activities of the constituents, the microstructure, grain size and porosity are some of the factors that will affect the relative contribution of the different types of diffusion. The method used to prepare the solid precursors and the pretreatment they receive prior to reaction, will influence profoundly their reactivity. The sizes and shapes of the constituent particles of a precursor powder exert an obvious control over the reaction rates. Furthermore, the degree of available surfaces will affect the crystal nucleation and thus the geometry of interface development.

Normally, these reactions happen in a sequence of steps, where the reactant of each later stage is the product of the preceding reaction and has probably undergone lattice reorganization, with changes in the size, shapes and degree of perfection of the component crystallites. These changes are of particular significance when dehydration (or loss of other ligand) precedes the reaction of interest. In many cases, product crystallinity is seriously dependent on the prevailing availability of water vapor during the dehydration process. Grinding and other forms of mechanical pre-treatment, exposure to diverse forms of radiation and aging of the reactant during storage may also have a fundamental role in the course of subsequent decomposition. Impurities present in the reactants can also play a positive role in the reaction process when doping is desired [272].

Although there are many benefits to developing solid state reactions, there are also many drawbacks. The ideal procedure should result in a homogeneous, or uniform substance, and some solid state reactions do not yield this result. Furthermore, solid state reactions reactions need to be performed in different atmospheres like: Air, O_2 rich atmosphere, inert atmosphere (Ar, N_2) or vacuum (*e.g.* evacuated ampoule) in order to have stoichiometric samples or avoid them.

In summary, formation of solids by solid state reaction method is controlled by the diffusion of atoms and ionic species through reactants and products and thus requires repeated grinding, pelletizing and calcination of reactants (oxides, carbonates and nitrates) for longer durations (than soft chemical routes) at high-temperatures [273,274].

2.2 Structural and Morphological Characterization

2.2.1 X-Ray Diffraction

2.2.1.1 General aspects

The most common tool for phase identification of polycrystalline solids is powder x-ray diffraction ("PXRD or XRD")[i].

Each crystalline solid produces a characteristic "fingerprint" diffraction pattern which can be used for phase identification or, if sufficiently high-quality data is collected, for structural refinement. The theory of diffraction is well established and the experimental setup of a modern laboratory diffractometer is described at length in many textbooks and it can be reviewed, *e.g.* in the references 276–279. Here this subject will be covered only briefly.

To generate x-rays, electrons are accelerated by an electric field and directed against a metal target (*e.g.* copper metal (Cu) being the most common choice). Here, the incoming electron has to have enough energy to create a hole in the inner *K*-shell (1*s*) of the copper atoms (this energy corresponds to the Cu absorption edge). This hole can be filled by an electron from the *L*-shell (K_α radiation) or the *M*-shell (K_β radiation). Specifically, the electrons that fall back into the *K*-shel from the *L*-shell can be distinguished by their origin $2p_{3/2}$ and $2p_{1/2}$, $K_{\alpha 1}$ and $K_{\alpha 2}$ respectively. The beam is made K_α monochromatic ($\lambda_{K\alpha}^{Cu}$ = 1.5418 Å) by using a Ni filter that selectively removes the K_β, with a relatively much smaller loss of K_α.

In a powder sample, the various lattice planes are found in every possible orientation. Thus, a convergent x-ray beam focused on a polycrystalline sample is diffracted in cones of radiation, whose pattern is determined by the internal architecture of the sample, see Fig. 2.1.

The powder diffractometer has a detector, which scans a range of 2θ values (*e.g.*, $10 < 2\theta < 90$) at a constant angular velocity. A collection can take from minutes to hours depending on the desired quality of the data and on the specific instrument properties. There are multiple parameters that can be adjusted to tailor analysis when using an x-ray diffractometer. The most common of these are: scan range, scan speed or time per step, step width, source power and slit width.

After a pattern is collected, it can be quickly compared to known powder diffraction patterns of that sample or to other patterns of compounds containing some or all the

[i] "x-ray was the name given by W. C. Roentgen to the highly penetrating rays, which emanated when high energy electrons struck a metal target. On 8 November 1895, he noted for the first time this phenomenon and on 28 December 1895, he astonished the scientific world with his preliminary report *Über Eine Neue Art von Strahlen* (along with experimental radiographs and by the x-ray image of his wife's hand) given to the president of the Wurzburg Physical- Medical Society. A few weeks later, C.H.F. Muller was able to construct on his Hamburg factory the first commercial x-ray tube for one of the local hospitals. This was a milestone of what was to become a major technical industry. X-ray technology is one of the most important inventions of the nineteenth century. It plays a major role in our daily life. X-ray is nowadays one of the most powerful tools to investigate hard and soft matter, hence the necessity to develop new sources to achieve more high-intensity beams" [275].

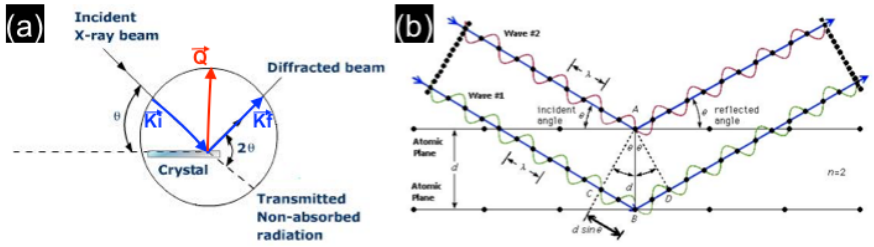

Figure 2.1 – Scheme of x-ray diffraction. **(a)** A simple representation of x-ray diffraction. principle.**(b)** Bragg's radiation reflection.

elements of the sample under examination. X-ray diffraction patterns are most often used for qualitative phase identification, however, if the sample is unknown, the data can also be used to determine the structure.

Structural characterization of the samples studied in this thesis were performed mainly by means of x-ray diffraction technique. The diffraction of short wavelength particles such as x-ray photons, electrons and thermal neutrons is the most accurate tool in order to determine crystallographic structures and lattice parameters. The wavelength of the above mentioned radiation has values of the order of 1 Å, which is the typical value of the lattice parameters in crystalline solids. Therefore, the coherent interference of the scattered radiation in these solids will form a diffraction pattern.

Taking into account only elastic scattering, the maximum intensity will appear for scattering directions that results from the addition of the moment of the incident particle and any vector belonging to the reciprocal lattice of the solid. These directions are called Bragg positions or Bragg peaks, and a set of Miller indexes can be assigned to them. The diffraction experiments provide a picture of the reciprocal lattice, and therefore the lattice in the real space can be obtained as the Fourier transform of the reciprocal space. Every Bragg peak position satisfies the Bragg's law:

$$\lambda = 2d_{hkl}sin(\theta)\ , \tag{2.1}$$

where λ is the wavelength of the incident wave, d_{hkl}[ii] is the distance between planes with Miller indexes (hkl), and $\phi_{hkl} = 2\theta$ is the angle formed by the propagation vectors of the incident and scattered waves. It can be shown that θ is the angle formed by the crystallographic plane and the momentum of the incident wave.

Diffraction patterns are usually represented as the number of diffracted particles counts versus 2θ or d_{hkl}. The Bragg's law (see Eq. 2.1) can be used to associate interplane distances to each Bragg peak.

In non-textured polycrystalline solids, the grains have their crystallographic axes randomly oriented. The diffraction theory sets that the Bragg peaks are then substituted for maximal intensity at the Scherrer cones, which have axial symmetry around the incident momentum direction. The diffraction profiles in this work will always result as the inter-

[ii] $d_{hkl} = \frac{d}{n}$, where d is the distance between atomic planes and n is the diffraction order.)

section of the plane of the detectors with the Scherrer cones, giving rise to the powder diffraction profiles.

2.2.1.2 Data collection

The x-ray diffraction measurements were performed at the x-ray spectroscopy service at the Institute of Nanoscience and Nanotechnology (IFIMUP-IN) and at the Electronic Microscopy Unit in the University of Trás-os-Montes e Alto-Douro (UTAD). The diffractometer Siemens Bruker AXS D5000 $\theta - 2\theta$ goniometer with a copper ($K\alpha_{1;2}$ radiation λ = 1.540598 and 1.544418 Å) anode x-ray tube operated at 40 kV and 30 mA and pan'alytical, X'Pert Pro x-ray diffraction with detector X'Celerator and secondary monochromator operated at 50 kV and 40 mA, respectively. Temperature dependence x-ray measurements were collected at Centro de Física da Universidade do Minho using a Bruker D8 Discover diffractometer ($\lambda^{Cu}_{K\alpha}$ = 1.5406 Å).

2.2.1.3 Sample preparation methods

The analysis of an x-ray spectrum relies on the fact that the sample contains crystals of all possible orientations. Here, the information obtained is an average of all the planes that are examined by the x-rays. If only some orientations are examined, *i.e.* only some planes are perpendicular to the diffraction vector[iii], then the analysis is invalid for that particular sample. A good way to test this is by rotating the sample on the sample stage. In a well prepared sample there will be no change in the output data. Thus, the x-ray diffraction pattern can be collected in two different ways, using sample pellets fixed to the sample holder with the help of a small piece of plasticine or using sample powders where a liquid with some viscosity was used to fix the powder into the sample holder. Liquids like ethanol or isopropanol, were used in the set of XRD patterns presented in this work. When powder patterns are presented, a background contribution is, most of the times visible. Nevertheless such background intensity is not so important when compared with the attenuation created by the much higher relative intensities of some peaks if a preferential growth of the polycrystalline samples occur. Thus, whenever it was possible XRD patterns were collected in grinded samples to have a better understanding of the crystallographic phases present.

2.2.1.4 Data analysis

There are several refinement analysis methods and tools available for studying XRD patterns. *Rodriguez-Carvajal et al.* developed a library of programs that apply the Le Bail and Rietveld method to any X-ray or neutron diffraction pattern[279–281]. These

[iii] The diffraction vector $\vec{Q} = \vec{k_f} - \vec{k_i}$ where $\vec{k_i}$ is the incident beam vector and $\vec{k_f}$ is the diffracted beam vector as presented in Fig. 2.1 (a).

libraries are known by the name of Fullprof. The Fullprof software has been used to analyze diffraction profiles presented in this work.

The Rietveld method was designed to analyze powder diffraction profiles and extract accurate quantitative information. Its role is twofold: first, according to the diffraction laws, the Bragg positions must be indexed within an hypothetical crystallographic space group. This analysis provides the lattice parameters and the actual atomic positions (Le Bail method). Once the space group is determined, the shape of the peaks and the relative intensities must be fitted, which requires the assumption of a precise shape for the peak. This analysis provides the atomic occupancy as well as microstructural information such as internal strain and the shape of the grains. Making use of all the input information, the Rietveld method aims to minimize the difference between the calculated intensity and the observed one by means of the least squares criteria[282,283].

It must be noted that only when a thorough analysis of the sample was desired (usually at the end of a complete annealing set), data with considerable statistics was collected in order to perform a Rietveld refinement. Otherwise, standard data was collected and a Le Bail pattern matching was performed to determine the phases present and their corresponding lattice parameters. The Le Bail analysis provides all the information necessary to characterize the crystallographic phases present in a sample. When a deeper analysis is desired extra information (as indicated before) can be obtained from the Rietveld refinement.

2.2.2 Scanning Electron Microscopy

The scanning electron microscopy (SEM) allows the observation and characterization on nanometer (nm) to micrometer (μm) length scale of heterogeneous organic and inorganic materials. The popularity of the SEM arises from its capability of obtaining three-dimensional-like images of the surfaces of a very wide range of materials. SEM images are used to characterize a wide range of samples, from pellets to insects. Its popularity is patent in the use of SEM images among scientific journals, popular magazines and, more recently, in the movies. Although the major use of SEM is to obtain topographic images in the magnification range 10 – 10000×, the SEM is much more versatile.

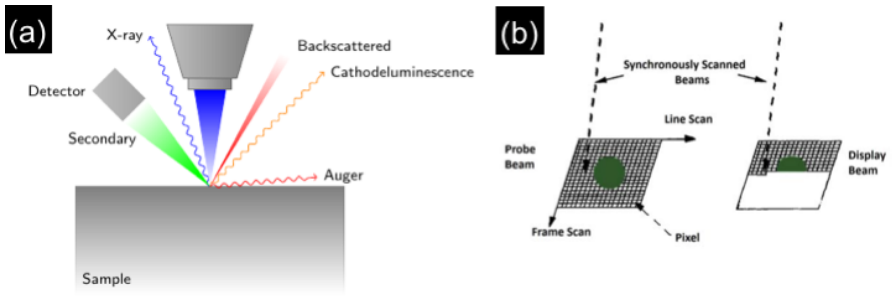

Figure 2.2 – Schematic illustration of: **(a)** the incident electron beam and type os signals produced. **(b)** the basic mapping principle of the scanning electron microscopy. (Adapted from ref. 284)

In the SEM analysis, the area to be examined or the microvolume to be analyzed is irradiated with a finely focused electron beam, see Fig. 2.2, which may be swept across the surface of the specimen to form images or may be static to obtain an analysis at given position. The type of signals produced from the interaction of the electron beam with the sample include secondary electrons[iv], backscattered electrons[v], characteristic x-rays, and other photons of various energies (see Fig. 2.2 (a)). These signals are obtained from specific emission volumes within the sample and can be used to examine many characteristics of the sample (surface topography, morphology, composition. etc.).

The imaging signals of greatest interest are the secondary and backscattered electrons because these vary primarily as a result of differences in surface topography (see Fig. 2.2 (b)). The secondary electron emission, confined to a very small volume near the beam impact area for certain choices of the beam energy, permits images to be obtained at a resolution of the same order of magnitude of the size of the focused electron beam. The three-dimensional (3D) appearance of images has its origin due to the large depth of the field as well as to the shadow relief effect of the secondary and backscattered electron contrast.

In the SEM, as a result of electron bombardment, characteristic x-rays are also emitted. The analysis of the characteristic x-ray radiation emitted from samples can supply both quantitative elemental information and qualitative identification from regions of a specimen nominally 1 μm in diameter and 1 μm in depth under normal operating conditions, see section 2.2.3.

The SEM measurements presented in this work were performed at the “Centro de Materiais da Universidade do Porto (CEMUP)” with a FEI Quanta 400FEG SEM. Before the measurements the samples pellet surface was gently polished and was mounted into the SEM sample holder with carbon tape.

For a detailed description of the experimental apparatus, technical specifications and measurement principles see ref. 285.

2.2.3 Energy Dispersive X-ray Spectroscopy

Energy Dispersive X-ray Spectroscopy (EDS or EDX) is a microanalysis technique used together with scanning electron microscopy (SEM) for the chemical elemental analysis, chemical characterization of a sample, etc.[vi].

[iv] Secondary electrons (SE) are those electrons emitted by the specimen, under irradiation by the beam, which have energies between 0 and 50 eV. Because of their low energy the SE only travel relatively short distances in the specimen (3 – 10 nm) and thus they emerge from a shallow “escape” region beneath the surface.

[v] Backscattered electrons (BSE) are those electrons emitted from the specimen which have energies between 50 eV and the incident beam energy E_0. Unlike the secondary electrons which are produced as the result of the incident electron irradiation, backscattered electrons are incident electrons which have been scattered through angles approaching 180° within the sample and consequently leave the sample again.

[vi] Foreign material analysis, corrosion evaluation, coating composition analysis, rapid material alloy identification, small component material analysis, phase identification and distribution.

EDS is a spectroscopic technique that gathers information about a sample through interaction between electromagnetic radiation and matter, mainly by analyzing x-rays emitted as a response of an initial beam charged particles[vii] that hits the sample. Its characterization capabilities[viii] are due in large part to the fundamental principle that each chemical element has a unique electronic structure thus producing x-rays that are characteristic of the element in question allowing its identification.

At rest, an atom within the sample contains ground state (or unexcited) electrons in discrete energy levels or electron shells bound to the nucleus. The incident beam may excite an electron in an inner shell, ejecting it from the shell and this way creating an electron hole. Because a hole in a lower level of the electron shell doesn't correspond to a stable configuration, an electron from an outer shell will then fill this hole. The difference in energy between the higher energy shell and the lower energy shell may be released in the form of x-ray radiation, see Fig. 2.3 (a). The number and energy of the x-rays emitted from a sample can be measured by an energy dispersive spectrometer. Because the energy of the x-rays are characteristic of the difference in energy between the two shells, and of the electronic structure of the element from which they were emitted, it is possible to determine the elemental composition of the sample to be measured.

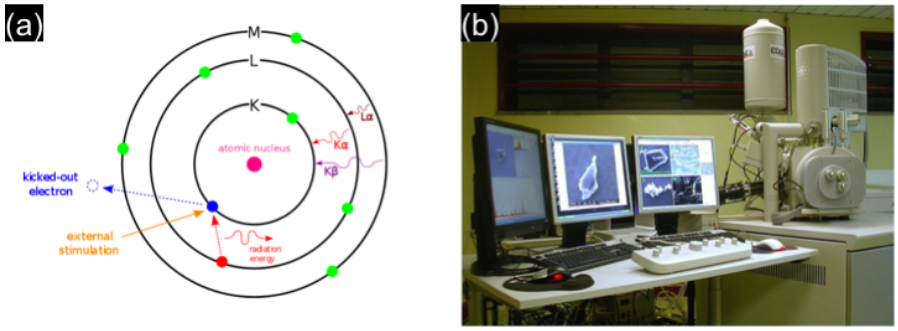

Figure 2.3 – **(a)** Electron shell model with different types of radiation emitted when an electron from the inner shell is removed. (Adapted from ref. 286) **(b)** FEI Quanta 400FEG ESEM/EDAX Genesis X4M

The EDS x-ray detector measures the relative abundance of emitted x-rays versus their energy. The detector is typically a lithium-drifted silicon, solid-state device. When an incident x-ray hits the detector, a charge pulse proportional to the energy of the x-ray is created. The charge pulse is converted to a voltage pulse (which remains proportional to the x-ray energy) by a charge-sensitive preamplifier. The signal is then transmitted to a multichannel analyzer where the pulses are sorted by voltage. The energy, as determined from the voltage measurement, for each incident x-ray is sent to a computer for display and further data evaluation. The spectrum of x-ray energy versus counts is evaluated to determine the elemental composition of the sampled volume. The obtained

[vii] To stimulate the emission of characteristic x-rays from a specimen, a high energy beam of charged particles such as electrons or protons, or a beam of x-rays, is focused into the sample in study.
[viii] Features or phases as small as 1 μm or less can be analyzed.

EDS spectrum is compared with spectra of individual elements allowing to quantify the relative amount of an element in the sample.

The minimum detection limits of the EDS vary from approximately 0.1 to a few atomic percent, depending on the element and the sample matrix. Elements with atomic numbers above that of beryllium and up to uranium can be detected.

Samples up to 200 mm in diameter can be readily analyzed with EDS. Larger samples, up to approximately 300 mm in diameter, can be loaded with limited stage movement. A maximum sample height of approximately 50 mm can be accommodated. Samples must also be compatible with a moderate vacuum atmosphere (pressures of 2 Torr or less).

When performing a microanalysis by EDS several considerations have to taken into account. Changing the over-voltage of the EDS will result in different peak sizes - Raising over-voltage on the EDS will shift the spectrum to the larger energies making higher-energy peaks larger while making lower energy peaks smaller and also overlapping peaks can appear for some elements. x-ray escaping the specimen, and thus being available to detect and measure, depend on the energy of the x-ray and the amount and density of material it has to pass through. This can result in reduced accuracy in inhomogeneous or rough samples.

To evaluate at the micrometer scale the chemical homogeneity of the sample (SEM-EDS) measurements were performed. The measurements presented in this work were performed at the ”Centro de Materiais da Universidade do Porto (CEMUP)” with a FEI Quanta 400FEG ESEM/EDAX Genesis X4M (see Fig. 2.3 (b)).

For a detailed description of the experimental apparatus, technical specifications and measurement principles see ref. 284.

2.3 Magnetic Characterization - SQUID Magnetometry

2.3.1 Superconducting Quantum Interference Device

Superconducting Quantum Interference Device (SQUID), see Fig. 2.4 (a), are very sensitive magnetometers used to measure extremely small magnetic fields. It is a flux-voltage converter. It turns a small, hardly detectable, flux variation into a measurable voltage variation. The output voltage is a periodic function of the applied flux, with period ϕ_0 (the magnetic flux quantum) one can detect an output signal which corresponds to a flux much smaller than ϕ_0. SQUIDs can thus measure any physical quantity which can be transformed into a flux, such as a magnetic field or its gradient, a current, a voltage, a displacement or a magnetic susceptibility. SQUIDs combine two physical phenomena, flux quantization in a superconducting ring, and the Josephson effect[ix].

[ix] A Josephson junction is made up of two superconductors, separated by an insulating layer so thin that electrons can pass through.

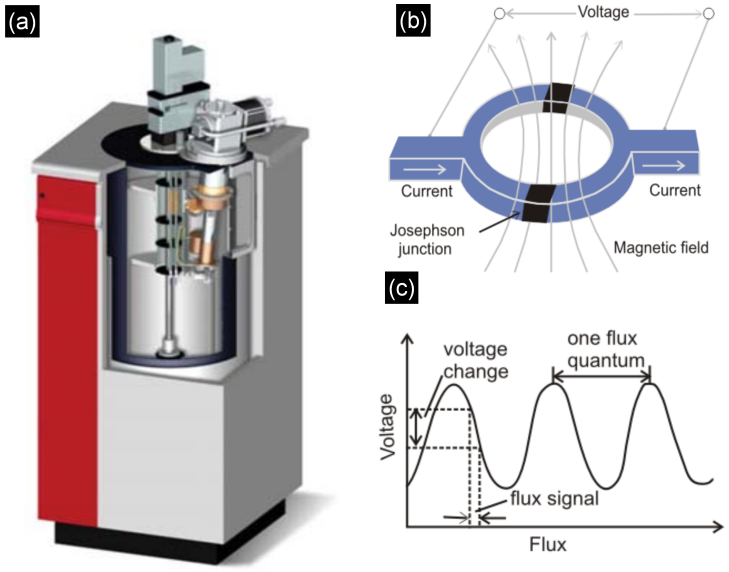

Figure 2.4 – **(a)** Figure of MPMS squid apparatus system, with dewar and Evercool system. **(b)** The two Josephson junctions forming a superconducting ring, which forms the DC SQUID. **(c)** Output voltage as a function of applied flux. A tiny flux signal produces a corresponding voltage swing across the SQUID, which conventional electronics can measure. (Adapted from Refs. 287 and 288)

SQUIDs are usually made of either a lead alloy (with 10% gold or indium) and/or niobium, often consisting of the tunnel barrier sandwiched between a base electrode of niobium and the top electrode of lead alloy.

There exist two types of SQUIDs: A radio frequency (RF) squid that is made up of one Josephson junction, which is mounted on a superconducting ring. An oscillating current is applied to an external circuit, whose voltage changes as an effect of the interaction between it and the ring. The magnetic flux is then measured; A direct current (DC) SQUID, which is much more sensitive, consists of two Josephson junctions employed in parallel so that electrons tunneling through the junctions demonstrate quantum interference, dependent upon the strength of the magnetic field within a loop (see Fig. 2.4 (b)). DC SQUIDs demonstrate resistance in response to even tiny variations in a magnetic field, which is the capacity that enables detection of such minute changes (see Fig. 2.4 (c)).

Although RF SQUIDs are more common on the market, DC SQUIDs are more sensitive. They are sensitive enough to measure fields as low as 5 aT (5×10^{-18} T) within a few days of averaged measurements. Their noise levels are as low as 3 fTHz$^{-1/2}$. For comparison, a typical refrigerator magnet produces 0.01 Tesla (10^{-2} T), and some processes in animals produce very small magnetic fields between 1 fT and 1 μT.

2.3.2 Magnetic measurements

The magnetic measurements with a SQUID (superconducting quantum interference device), should be performed with a magnetically virgin superconducting coil, in order to

avoid remanent fields and field inhomogeneities. When that is not possible and a remanent field is present, the sample magnetization in the paramagnetic phase can be used to determine this remanent field, and perform a correction to the applied field. In magnetic measurements one defines the magnetic susceptibility as:

$$\chi = \frac{M}{H} , \tag{2.2}$$

where M is the sample magnetization and H the magnetic applied field. This expression is valid only in the paramagnetic phase, although sometimes we also use it in the magnetic ordered phase when using low field and where a linear regime is observed.The way atomic magnetic moments order in a material can be inferred by the behavior of the magnetic susceptibility of the sample.

As a matter of fact, in the paramagnetic phase the temperature dependence of the susceptibility is given by the well-known Curie-Weiss law:

$$\chi = \frac{C}{T - \theta_{CW}} , \tag{2.3}$$

where θ_{CW} is the Curie-Weiss temperature[x] and is related with the exchange interaction between atomic magnetic moments, T is absolute temperature measured in kelvins and C is a material-specific Curie constant.

Notice that Curie's law is only valid at the low field regime and does not apply in the high-field regime where saturation of magnetization occurs and the magnetic moments are aligned with the external applied field. When the spins are aligned, increasing the external field will not increase the total magnetization.

In a general way, the curie constant is given by:

$$C = \chi T = \frac{N_A \mu_{\text{eff}}^2}{3k_B} \quad \text{where} \quad \mu_{\text{eff}} = g_J \mu_B \sqrt{J(J+1)} , \tag{2.4}$$

where k_B is Boltzmann"s constant, where N_A the Avogadro's number, μ_B the Bohr magneton, μ_{eff} effective paramagnetic moment and J the angular momentum quantum number ($J = L + S$). The constant g_J is known as the Landé g-factor and can be written by:

$$g_J = \frac{3}{2} + \frac{S(S+1) - L(L+1)}{2J(J+1)} , \tag{2.5}$$

For a paramagnetic ion with spin quantum number S and quenched angular momentum, $\langle L \rangle = 0$ so that $J = S$ and $g_J = 2$, the effective paramagnetic moment is then given by $2\mu_B\sqrt{S(S+1)}$.

All of the magnetization measurements necessary to this thesis were performed at IFIMUP-IN in a squid magnetometer (MPMS Quantum design, see Fig. 2.4). This mag-

[x] sometimes referred as Curie-Weiss constant or just Weiss constant. The Θ or θ_P or θ_{CW} are used indiscriminately.

netometer has a 10^{-7} emu (10^{-10} Am^2) resolution and is equipped with 5.5 Tesla superconducting coil. This system allows accurate magnetization measurements in low applied Fields in a 4 to 380 K temperature range. To perform the necessary measurements samples with needle shape were used[xi]. These samples were mounted in plastic straws either glued with a special low temperature tape (Kapton tape) or inside a gelatin capsule secured with cotton strings at the top and bottom. In all magnetic measurement the secure accommodation of the sample in the straw was always checked. There are several reasons for this precaution. Among those we can name one that we consider essential: one of the requirements for a good measurement is the uniformity and centering of the sample between the superconducting coils. Because the straw contracts and expands with the variation of the temperature (also the vibrating movement of the support) the sample could dislocate and a loss of signal could give to erroneous interpretation of the results.

To obtain the sample magnetic parameters such as Curie (T_C), Néel (T_N) temperature, low field magnetization measurements can be performed. For this purpose the thermal dependence of magnetization (in low fields) is acquired after the sample has been cooled without applied magnetic field (ZFC procedure) and/or field cooled (FC procedure), such that:

Zero field cooling - ZFC , the sample is cooled with $H = 0$ to the lowest temperature then, the magnetic field is applied and the subsequent magnetization measurements are performed while sweeping the temperature in a variable range of temperatures (that can go from 4 K up to 380 K).

Field cooling - FC , the sample is cooled down to the desired temperature under an applied field. The measurement is then performed, with constant applied field, while heating the sample in the same range of temperatures. In some situations it is interesting to perform the measurements while cooling. Thus, this type of measurements are designated as FCC or FCH depending wether the measurement is performed while cooling or while heating, respectively. In the lack of further information one should consider the measurement performed while heating.

In the following chapters, to compare the magnetization curves at different fields, one approximates the susceptibility in the ordered phase as defined in Eq. 2.2 (low coercive fields and remanence).

Isothermal curves (M vs. H curves or $M(H)$) were also obtained in order evaluate the saturation magnetization. In these cases measurements were performed while decreasing the applied magnetic field from 5 to 0 Tesla.

$M(H)$ curves can also be useful for the calculation of the magnetic entropy variation of a magnetic material. As described in sec. 1.3 the MCE of a magnetic material can be evaluated directly by measuring its temperature variation, or indirectly by measuring the

[xi] Needle-like samples were used in order to reduce demagnetization effects.

magnetization and/or the heat capacity. Here, it is possible to calculate the magnetic entropy variation associated with a variation of the magnetic field in a material. A mathematical approximation defined in Eq. 1.9, derived from the use of thermodynamics and corresponding Maxwell relations relies on $M(H)$ curves as a data source for that end. Therefore, in our experiments, the $M(H)$ curves used for the calculation of the MCE were measured as follows: First, the sample was cooled-down to the lowest temperature to be measured. After stabilizing the temperature, the measurement was performed varying the field from 0 up to 50 kOe (in 40 steps). At each step the magnetization was measured at a fixed temperature and field. After the maximum field was reached the measurement was performed decreasing the field. Once back at initial field (0 kOe) the sample was heated up all the way into the paramagnetic region. Only then the sample is cooled to a new measurement temperature above the previous one. This methodology was introduced by *Caron et al* and is referred as the loop process[289]. This was repeated over the temperature range of interest (usually 0.7 $T_N < T_N < 1.3\ T_N$).

For a detailed description of the experimental apparatus, technical specifications and measurement principles, see Refs. 290 and 291 or the individual sections, where detailed information about the proceedings are given.

2.4 Dielectric properties characterization

For understanding the dynamics of dielectric systems, measurements of the complex dielectric permittivity as a function of temperature play an important role. This can be obtained by making a parallel face capacitor, in which the sample in study is the dielectric, see Fig. 2.5 (a) (In vacuum) and 2.5 (b) (with dielectric).

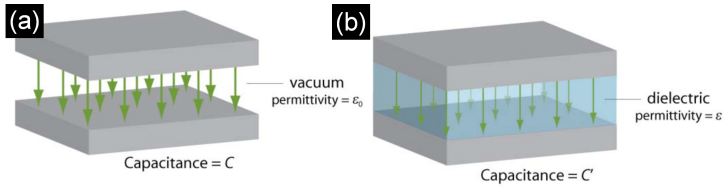

(a) In Vacuum (b) With dielectric

Figure 2.5 – Scheme of a capacitor.

The experimental method used consists in the analysis of the impedance of the system in study. Once the samples are not perfect insulators, the dielectric permittivity (ϵ) is a complex quantity having in this way a relationship between the electric current and the alternate electric voltage in the following way:

$$I = i\omega\epsilon^*(\omega)C_0V = \omega\epsilon''(\omega)C_0V + i\omega\epsilon'(\omega)C_0V \tag{2.6}$$

where C_0 is the capacitor capacity. The initial part of the Eq. 2.6 represents the resistive

part of the circuit, with a equivalent resistance

$$R_P = \frac{1}{\omega \epsilon''(\omega) C_0} , \tag{2.7}$$

connected in parallel with an ideal capacitor, of reactance

$$\frac{1}{\omega \epsilon'(\omega) C_0} . \tag{2.8}$$

The current intensity that passes thought the circuit in the assembly can be defined as:

$$I = \left(\frac{1}{R_P} + i\omega C \right) V . \tag{2.9}$$

Comparing with the equations described above, is possible to write:

$$\epsilon' = \frac{C}{C_0} \tag{2.10}$$

and

$$\epsilon'' = \frac{1}{\omega R_P C_0} . \tag{2.11}$$

The tangent of the angle that measures the phase difference between the current and the potential is given by:

$$\tan \delta = \frac{\epsilon''(\omega)}{\epsilon'(\omega)} . \tag{2.12}$$

The experimental technique is based on the measurement of the capacity and the dielectric losses (*e.g.* conduction, relaxation phenomena, molecular resonances) as a function of temperature. The measurements presented in this work were performed at the Polarizable materials and functional nanostructures, group leaded by Prof. Abílio Almeida at IFIMUP-IN, in Faculty of Sciences of Porto University.

The complex dielectric permittivity was measured with an impedance analyzer (for the frequency of 1 MHz), that is connected to a cryogenic refrigerator ($\approx$ 10 K to 300 K) equipped with a temperature controller and meter, that has the ability to change the rate of the heating/cooling process. The experimental data were collected with a software that allows a direct acquisition of the capacity and dielectric losses.

2.5 Local Probe Techniques

Interactions between the nuclear moments (electric and magnetic) and extranuclear electromagnetic fields are defined as nuclear hyperfine interactions. These interactions, electromagnetic fields interacting with the nuclear moments lead to a rearrangement in the nuclear level structure. Therefore, measurement of these interactions offer an precise method to investigate condensed matter phenomena yielding direct information

of the local charge distribution and magnetic hyperfine fields. The systems studied in this work, present very distinct macroscopic properties which in most cases have an origin in subtle differences in microscopic phenomena. Thus, it becomes clear the great importance of the use of nuclear hyperfine methods for the studying these solid state systems.

Among the numerous experimental techniques that rely on hyperfine interactions and therefore probe a material at a nuclear level, some do not require the use of radioactive probes like nuclear magnetic resonance (NMR) and nuclear quadrupole resonance spectroscopies (NQR) while others are based on their use like Mössbauer effect (ME), β – NMR or perturbed angular correlations (PAC).

As mentioned above, these experimental methods collect information through the electric and magnetic hyperfine interaction, *i.e.* the interaction between the nuclear moments of a specific probe nuclei and the magnetic and/or electric fields induced by the surroundings (valence electrons, conduction electrons, neighbor atoms, neighboring defects or distortions). These techniques working at the atomic scale, have many advantages for studying structural, electronic and dynamical properties of the host atoms, single impurities, and impurity-defect complexes because they probe only a small sample volume and they have a high sensitivity.

Moreover, the information obtained by these techniques is of particular interest in highly correlated materials, where intrinsic disorder requires real lattice atomic scale studies.

In this section the most relevant aspects of the Perturbed Angular Correlations (PAC) technique will be presented. The mathematical formalism of PAC is complex and can be found in detail in several textbooks, PhD thesis and review articles[169,292–294]. Therefore, only a brief description of the theoretical and experimental aspects of the PAC technique will be presented.

2.5.1 Perturbed Angular Correlation - PAC

Perturbed angular correlation technique has a special place when compared with the other hyperfine techniques. This is due to the fact that: the amount of the material under study can be very small (normally small quantities as 1 – 100 mg can be used), it's sensitivity is temperature independent (contrary to what happens in MES and in NMR), can be measured with no external magnetic field and no high-frequency equipment is required (in opposition to NMR), normally can resolve weaker nuclear quadrupole interaction (than MES) and uses small quantities of radioactive nuclei probes (around 10^{10} – 10^{13}, that are orders of magnitude lower than for MES and NMR)[292,293,295].

Perturbed angular correlation is based on the emission of two consecutive γ rays (or electrons like in the case of $e-\gamma$) from internal decay of a probe nucleus (see Fig. 2.6 (a)). A correlation between the emission direction of the first gamma, γ_1, and the second one, γ_2, exists ($\vec{k}_1$ and $\vec{K}_2$ respectively), because conservation of the angular momen-

tum, $\vec{I}$, occurs (see Fig. 2.6 (b)). In fact, in a normal scenario the nucleus spins are randomly oriented in space and thus the radiation is emitted isotropically. Therefore, in order for an anisotropic γ angular distribution to exist, the population on the nucleus degenerate sub-levels have to be different, *i.e.*, the state from which the radiation is emitted has to be polarized or aligned. In the case of angular correlations the oriented set of nuclei is obtained by choosing only those nuclei whose spins happen to lie in a preferred direction.

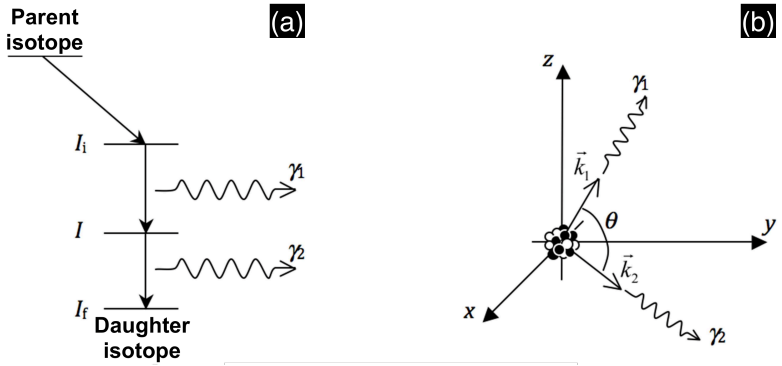

Figure 2.6 – Two gamma nuclear cascade. (From ref. 296)

Let us consider the emission of two successive γ-rays from a nuclei, where the initial nuclear state is randomly oriented *i.e.*, equal occupation of the different states. The observation of γ_1 in a fixed direction $\vec{k}_1$ (that we can define as the z axis) will determine a group of nuclei in the intermediate state whose magnetic sub-levels are no longer equally populated. This is a consequence of the angular momentum conservation and the angular distribution of the electromagnetic radiation with respect to its angular momentum, $\vec{L}$. An anisotropic emission pattern of γ_2 will be observed being angular correlated with respect to the observation direction of γ_1 due to the alignment of the intermediate state.

In this way, it is possible to define the probability, $W(\theta)$, of finding γ_2 in a certain direction, $\vec{k}_2$, at an angle θ with respect to $\vec{k}_1$ and in coincidence with γ_1 as[297]:

$$W\left(\vec{k}_1, \vec{k}_2\right) = W(\theta) = \sum_{k=0}^{k=k_{max}} A_k(\gamma_1)\, A_k(\gamma_2)\, P_k(\cos(\theta)) \ . \tag{2.13}$$

The sum runs over for even values of k as a result of parity conservation of the electromagnetic radiation. The cascade anisotropy terms, $A_k(\gamma_1)$ and $A_k(\gamma_2)$, describe the deviation of the coincidence probability from the isotropic case where $W(\theta) = 1$. Here, coefficient $A_k(\gamma_1)$ depends only on the first transition and $A_k(\gamma_2)$ only on the second, more specifically they depend on the correspondent angular momentum of the involved levels and on the type and multipolarity of emitted radiation. Finally, the Legendre polynomials P_k reflect the spatial angular distributions of the emitted particles.

Experimentally, by placing two detectors in a plane, one of them being fixed and the

other movable, the emission pattern described previously can be obtained (see Fig. 2.7)

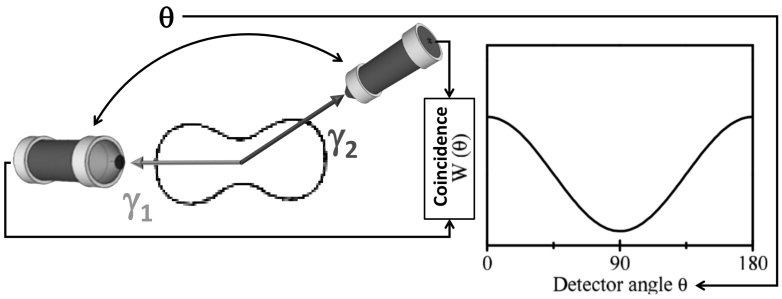

Figure 2.7 – Schematic representation of $W(\theta)$ anisotropy. The γ_2 intensity angular dependence profile with respect to the emission direction of γ_1, $W(\theta)$, in an experimental $\gamma - \gamma$ angular correlation setup. Adapted from ref. 293

When the nucleus is surrounded by other atoms interactions will occur. These interactions can be due to fields created by the atomic vicinity. In the presence of external fields an interaction with the nucleus magnetic or/and quadrupole moments appears and Eq. 2.13 is no longer valid. When that is the case, a time dependent perturbation in the angular correlation function of the emitted gammas has to be considered.

The nuclear magnetic sub-levels can be split when the nuclear quadrupole moment couples with an Electric Field Gradient (EFG) and/or the nuclear magnetic moment couples with a Magnetic Hyperfine Field (MHF) occurs (see Fig. 2.8). If that is the case, during the time τ that the probe remains at the intermediate state, the nucleus is under the effect of a hyperfine interaction that promotes different occupations of the magnetic sub-levels. Thus, the emission probability of γ_2, in a certain direction, becomes time dependent.

Figure 2.8 shows the electric quadrupole splitting of nucleus angular momentum (I = 5/2) by an axially symmetric EFG and evolution of the splitting as the EFG looses the axial symmetry. The energy splitting between the sub-levels is given by a frequency triplet ω_1, ω_2 and ω_3. In this particular case for an axially symmetric EFG we have $\omega_2 \sim 2\omega_1$ and $\omega_3 \sim 3\omega_1$.

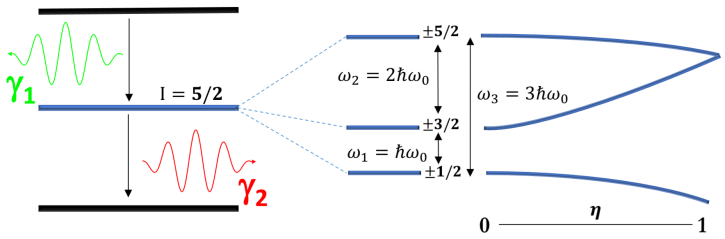

Figure 2.8 – Electric quadrupole splitting of nucleus angular momentum (I = 5/2) by an axially symmetric EFG (η = 0). Evolution of the splitting as a function of the asymmetry parameter.

The perturbed time differential angular correlation depends on the crystalline structure of the material where the radioactive source is placed. However, in polycrystalline materials is greatly simplified. In this case the function is obtained by averaging the

angular correlation over all possible orientations of the EFG/MHF fields and only the relative angle between the two emission directions becomes relevant. Moreover, if the interaction hamiltonian is static and diagonal (as in the case of axially symmetric quadrupole interactions) it can be expressed by:

$$W(\theta, t) = \sum_{k=0}^{k=k_{max}} A_k(\gamma_1) A_k(\gamma_2) G_{kk}(t) P_k(cos(\theta)) \,, \tag{2.14}$$

where $G_{kk}(t)$ the perturbation factor, contains all the information on the hyperfine interaction. In fact, this term gives the information about the energy splitting of the sub-levels of the intermediate state, and thus the hyperfine fields can be measured through a PAC experiment.

The perturbation function $G_{kk}(t)$ for a static axial symmetric electric quadrupole interaction in a polycrystalline sample is then is defined as:

$$G_{kk}(t) = \sum_{n=0}^{n_{max}} S_{kn} cos(n\omega_0 t) \,, \tag{2.15}$$

where S_{kn} are the frequency amplitudes, $n = |m^2 - m'^2|/2$ for I half integer and $n = |m^2 - m'^2|$ for I integer[xii].

In order to determine the perturbation factor $G_{kk}(t)$, where all information about the hyperfine fields is contained, the coincidence count rates, N, as a function of time between the emission of the two gamma-rays, γ_1 and γ_2, at a fixed detector angle, $N(\theta, t)$ should be measured. A PAC experimental apparatus consisting of a group of detectors geometrically arranged in such way that the angles between pairs of detectors is 90°or 180°is used. Usually, more than two detectors are used, allowing for data acquisition to be statistically accumulated (normally a set-up of four or six detectors is used). In this way, if a *gamma* with a correct energy is detected in a detector (γ_1), a clock is started. After a certain time a second gamma will be detected in one of the other detectors. The clock will then stop, if this second γ has the expected energy. This event will be stored in the coincidence counter with angular (pair of detector) and time information.

The twelve (thirty) time spectra obtained for all possible combinations of the four (six) detectors are used, after background subtraction and appropriate average[xiii] of all coincidence rate ($N(\theta, t)$), to calculate the experimental perturbation function $R(t)$ given by:

$$R(t) = 2\frac{N(180^\circ, t) - N(90^\circ, t))}{N(180^\circ, t) + 2N(90^\circ, t)} \,. \tag{2.16}$$

Examples of the $R(t)$ function and correspondent Fourier transforms are given on Fig. 2.9 for different asymmetry parameters.

[xii] m and m' are the projected spin angular momentum quantum numbers of the initial and final state of the probe.

[xiii] Geometric average of all spectra taken at the same detectors angle aims to correct for detector efficiency differences [298].

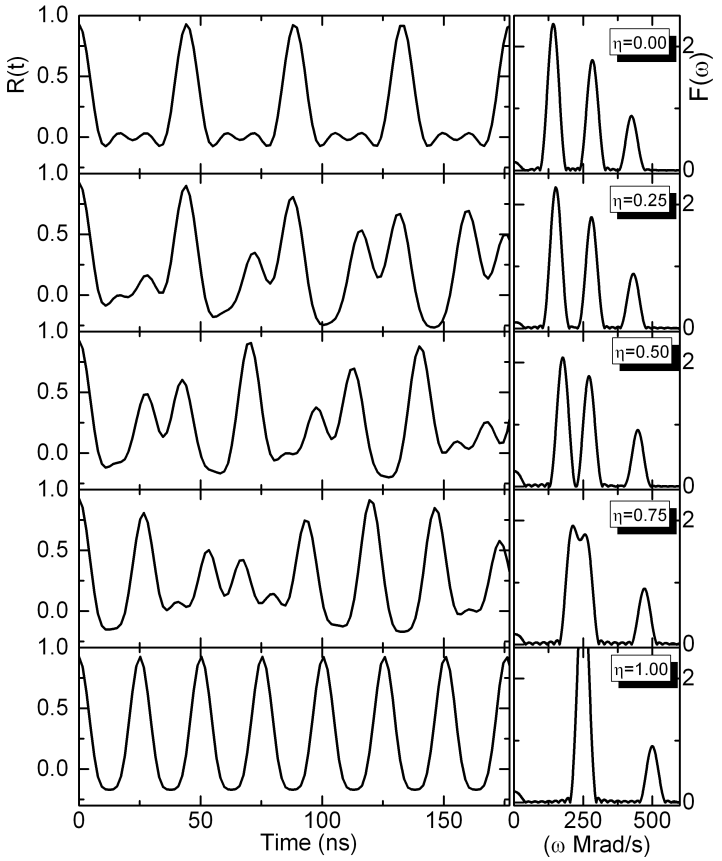

Figure 2.9 – Example of a experimental R(t) function for different η values. On the right hand side, the corresponding Fourier transform is presented. The three frequencies (ω_1, ω_2, ω_3) in the Fourier transform are characteristic from a spin 5/2 and fully characterize the EFG parameters, V_{ZZ} and η.

In addition, the experimental perturbation function, $R(t)$, can be related with $G_{kk}(t)$ that contains the information about the hyperfine fields. In the case of a static axial symmetric electric quadrupole interaction in polycrystalline samples the perturbation function is given by:

$$R(t) = A_{kk} \sum_{n=1}^{n_{max}} f_n G'_{kk}(t) \ , \tag{2.17}$$

where f are the relative fractions for different EFG's contributing to the PAC spectrum and $G'_{kk}(t)$ the corresponding perturbation factors after taking into account the finite time resolution of the PAC setup. Therefore, the $G_{kk}(t)$ (defined in Eq.2.15) is modified multiplying each term in the sum by $P(F^*_{whm}, \omega_n)$. A second term, $D(F_{whm}, t)$, is also multiplied to account for possible EFG distributions (these terms will be defined below in section 2.5.1.1 by Eq. 2.24 and Eq. 2.25). The perturbation factor is then written as:

$$G'_{kk} = \sum_n S_{kn} cos(\omega_n t)\, D\,(F_{whm}, t)\ P\left(F^*_{whm}, \omega_n\right) \ . \tag{2.18}$$

Using PAC technique the electric field gradient around the nuclear probe on a lattice site can be asserted. The EFG tensor V_{ij} is composed by three diagonal components

V_{xx}, V_{yy} and V_{zz} that are by definition sorted in descending order of magnitude *i.e.*:

$$|V_{zz}| \geq |V_{yy}| \geq |V_{xx}| \ . \tag{2.19}$$

The EFG tensor is traceless ($V_{xx} + V_{yy} + V_{zz} = 0$) and fully described by the largest of the three components V_{zz} and the asymmetry parameter η,

$$\eta = \frac{V_{xx} - V_{yy}}{V_{zz}} \qquad \text{with } 0 \leq \eta \leq 1 \ , \tag{2.20}$$

representing the deviation of the EFG tensor from axial symmetry ($\eta = 0$). The electric field gradient strength is represented by the quadrupole frequency constant ν_Q, defined by

$$\nu_Q = \frac{eQV_{zz}}{h} = \omega_0 \frac{4I\,(2I-1)}{2\pi k} \ , \tag{2.21}$$

where $k = 3$ (for I integer) or $k = 6$ (I half-Integer)

On the other hand, the magnetic dipolar energy E_m can be introduced from a classical description and the following expression be obtained:

$$E_m = -\vec{\mu}\vec{B} \ , \tag{2.22}$$

where μ and B are the nuclear magnetic moment and B the magnetic hyperfine field, respectively.

The splitting between two adjacent sub-levels is

$$\Delta E_m = \hbar\omega_L \ , \tag{2.23}$$

where $\omega_L = \gamma B$ is the Larmor frequency.

When both magnetic and electric interactions are present the hamiltonian for such combined static interactions, in the proper reference frame of the EFG tensor, cannot be diagonalized analytically and its eigenvalues and eigenvectors must be calculated numerically.

2.5.1.1 R(t) Attenuation

In PAC experimental results, an attenuation of the time spectrum is frequently present. This attenuation can arise from static and/or dynamic mechanisms.

Static Interactions - The damping of the static perturbation function stems from two sources. The first one is due to the finite time resolution of the apparatus ($\tau_{\text{set-up}}$), which reduces the amplitude of the cosines by a factor related to the time resolution defined by the full width at half maximum (F^*_{whm}) of the energy gated prompt peak.

The time resolution (prompt) function of the spectrometer (that is a function of the

observed frequencies) is assumed to be gaussian-like and has the form:

$$P\left(F^*_{whm}, \omega_n\right) = e^{-\frac{F^{*2}_{whm}}{16\ln 2}\omega_n^2} = e^{-\frac{1}{2}\tau^2_{\text{set-up}}\omega_n^2} \,. \tag{2.24}$$

The second source of damping is due to a static distribution of the electric-field gradient components arising from random inhomogeneities in the local environment of the probe nucleus. Conventionally, is assumed to be either Lorentzian or Gaussian in shape. In most cases it is considered the case of a Lorentzian fields distribution, and thus the attenuation function, in time space, can be written as:

$$D_{\text{Lorentz}}\left(F_{whm}, t\right) = e^{-\frac{F_{whm}}{2}t} \,. \tag{2.25}$$

Here in a Lorentzian distribution the EFG distribution full width at half maximum is used (F_{whm}) and is often given as a fraction (δ) of the fundamental frequency written as $\delta = \sigma/\omega_0$ and defined as $\sigma = F_{whm}/2$, where σ, is the standard deviation when a Gaussian distribution is considered,

Dynamic Interactions - A third reason for damping of the R(t) function is time dependent changes (fluctuations) of the magnitude and/or orientation of the EFG tensor within a time-scale comparable to the PAC probe state lifetime. Dynamic effects always present in matter, *e.g.* diffusion of impurities or defects in the crystal or slow lattice dynamics might be observed in the perturbation function to a more or less extent. As a consequence, when such dynamic process has a characteristic time-scale of the order of the probe state lifetime, a correction to the perturbed time differential angular correlation function is needed. Because these dynamic interactions can have different time-scales, three possible cases can be defined. They can be grouped considering the mean fluctuation time of the given dynamic effect, τ_c, and its relation to the life time of the probe in the intermediate state, τ.

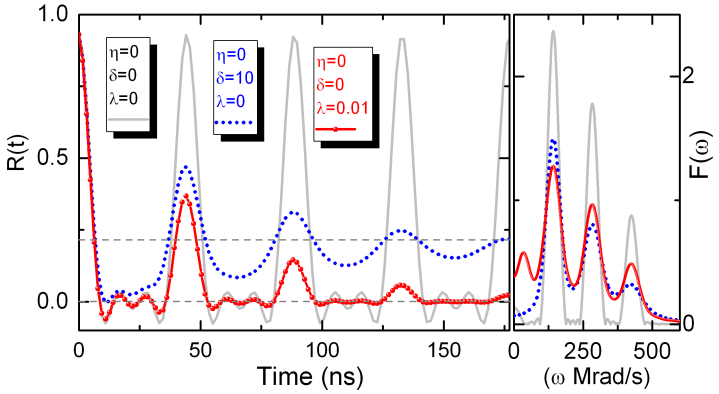

Figure 2.10 – Schematic representation of a $R(t)$ function for a EFG with $\eta = 0$ with no attenuation (continuous line), with a static attenuation (dashed line) and with dynamic attenuation (line plus symbol). The correspondent Fourier transforms are shown in the right hand side. In the frequency space the attenuation to ω_1, ω_2, ω_3 amplitudes diminish by the same factor in the case of damping due to dynamic interactions while for a static damping the attenuation is proportional to the frequency itself.

$\tau_c \gg \tau$ - When τ_c is much greater than the perturbation measuring time, there is a great probability of no fluctuations be observed during the measurement time. In this case only a static attenuation is considered.

$\tau_c \ll \tau$ - When the fluctuation characteristic time is much smaller than the PAC measuring scale, the anisotropy present in the creation of the intermediate state tends to zero, because the random transition between the substates tend to equal the respective populations. In this case, the perturbation of the angular correlation can be described simply by an exponential attenuation:

$$G_{kk} = e^{-\lambda_k t} , \tag{2.26}$$

in which $\lambda_k \propto \tau_c \overline{\omega_0^2}$, with $\overline{\omega_0^2}$ being the mean quadratic frequency of the interactions in the case of static interactions.

$\tau_c \approx \tau$ - When the time of the fluctuation is of the same order of magnitude of the time of the measurement, the model of random phase approximation is adopted, which is valid for many cases where we have a variation of the EFG's, including the lattice vibration effects and the diffusion of defects. In a first approach we can consider that the perturbed angular correlation oscillations amplitude due to these interactions is attenuated by a time decreasing exponential factor:

$$G_{22} = e^{-\lambda t} \sum_{n=0} s_{2n} cos(n\omega_0 t) , \tag{2.27}$$

for $k = 2$ and for a single EFG of $\eta = 0$.

For a more in-depth knowledge many sources are available, from previous works to dedicated books about the the hyperfine techniques[292,293,295].

2.5.1.2 Lattice Electric Field Gradient

The information obtained from the analysis of PAC data allows the determination of the electric field gradient parameters: the principal component of the EFG tensor, V_{zz}, and the asymmetry parameter, η, which are defined in equations 2.21 and 2.20. The EFG is non-zero if the charges surrounding the nucleus do not possess cubic symmetry (electrons and ion cores). Therefore, the deviation of charge distribution from cubic symmetry is characterized by measuring the EFG, which is highly sensitive to the electronic density in the immediate vicinity of a nucleus.

For a long time, the use of phenomenological models was the only approach to estimate EFGs in solids. These models assumed the EFG as sum of two contributions: one from the neighboring ion cores (ionic lattice contribution, V_{zz}^{latt}), and one from the electrons, probe core electrons, V_{zz}^{core}, and conduction electrons, V_{zz}^{el}, (electronic contribution). Summing up these contributions, the EFG is given by[292,299,300]:

$$V_{zz} = V_{zz}^{latt} + V_{zz}^{core} + V_{zz}^{el} \qquad \text{where} \qquad V_{zz}^{core} = -\gamma_\infty V_{zz}^{latt} \,. \tag{2.28}$$

The contribution of the probe core-electrons results from a polarization effect leading to an amplification of the lattice EFG, being γ_∞ the Sternheimer antishielding coefficient. This coefficient ranges from -100 to -10 depending on the element and ion charge state and can be found tabulated in literature[299–306].

For the case of ionic insulators, with non overlapping ion cores, the EFG can be approximated as[292]:

$$V_{zz} = (1 - \gamma_\infty)\, V_{zz}^{latt} \,. \tag{2.29}$$

In metals the computation of V_{zz}^{el} is particularly difficult, due to the fact that the electrons in a metal cannot be treated as uniformly distributed, requiring accurate band-structure calculations. Nevertheless, a relation between the electronic and lattice contributions to the EFG has been suggested by *Raghavan et al*[307]. This expression, known as ”universal EFG systematics”, states that the measured V_{ZZ} is also proportional to the lattice EFG, in the absence of point defects:

$$V_{zz}^{el} = -K V_{zz}^{latt} (1 - \gamma_\infty) \qquad (\text{with } K = 3) \,. \tag{2.30}$$

The former relation is the result of a systematic comparison of measured V_{zz} and EFG lattice contribution (calculated by point charge model).

From Eq. 2.28 and Eq. 2.30 one can write that the measured V_{zz} is also proportional to the lattice EFG:

$$V_{zz} = V_{zz}^{latt} (1 - \gamma_\infty) (1 - K) \,. \tag{2.31}$$

This phenomenological model allows an estimation of the lattice EFG independently of the probing atom. By using phenomenological models, the theoretical estimation of the EFG was limited to point charge models using Sternheimer antishielding factors. The point charge models (PCM) can provide fair estimations in the case of ionic solids although in covalent solids large deviations are observed. Still, in the absence of more sophisticated techniques, this method has been used extensively *e.g.* to estimate EFGs at the A site in perovskite oxides[308–314].

In the next sub-sections, both point charge model (PCM) and first principle calculations will be presented, including details needed for the calculations performed in ABX_2 and $RCrO_3$ studied systems.

2.5.1.3 Electric Field gradient point charge model calculations

Point charge model (PCM) calculations are extremely useful in order to obtain an estimative on the value of the EFG around a determined nucleus probe. For this calculations the ions cores are treated as point charges, $Z_i e$, that are located at the ions lattice sites, giving in this way an approximation to the real lattice contribution to the EFG, V_{ij}^{latt}. In

order to calculate the EFG, the second partial derivates of potential, at the probe site due to the influence of external charges z_i that are at a position r_i in relation to the origin, must be calculated. The contributions of all lattice atoms, normally within the distance of a few tens of angstroms and with the exception of the probe itself, have to be added, resulting in:

$$V_{ij}^{PCM} = \sum_i \frac{z_i e}{4\pi\epsilon_0 r_i^5} \begin{pmatrix} 3x_i^2 - r_i^2 & 3x_i y_i & 3x_i z_i \\ 3y_i x_i & 3y_i^2 - r_i^2 & 3y_i z_i \\ 3z_i x_i & 3z_i y_i & 3z_i^2 - r_i^2 \end{pmatrix} \tag{2.32}$$

After a diagonalization of the matrix the eigenvalues are obtained, corresponding to the EFG tensor and are chosen considering that $|V_{zz}| \geq |V_{yy}| \geq |V_{xx}|$ from which η the asymmetry parameter can be obtained.

In the case of ionic solids this model gives a fair approximation to the observable EFG. However for covalent solids only poor agreement is obtained. In this work the PCM was used to obtain information about expected EFG for the ^{111}In probes in the A and B site in the $CdMn_2O_4$ [183,194] and $CdCr_2S_4$ structures [122].

2.5.1.4 Electric Field gradient first principle calculations

The development of new materials and their understanding, relies nowadays in a symbioses between experimental results and theoretical modeling. The later, has undergone an enormous boom with the development of relatively inexpensive high performance workstations or PCs, dropping the need for extremely expensive super computers.

Nowadays, the complexity of the materials and mechanisms in the field of physics is sometimes of a staggering complexity that an exact solution it is not always possible to obtain. In these cases the use of approximations is most of the times enough to obtain an reliable solution. Thus, the use of approximations is only a natural alternative but one of the most popular approaches to solve the many-electron problem of a crystal applying density functional theory (DFT)[315,316], which is the foundation behind the computer program Wien2k[317,318]. For example, it has been successfully used to predict superconductive and magnetic properties of solids, and in chemistry, to calculate detailed reaction mechanisms.

In fact, *ab-initio* full potential linearized augmented plane wave (FLAPW) method using the local spin density approximation (LSDA) or the generalized gradient approximation (GGA) has been used for EFG calculations in many studies[319,320].

It has given proofs to be an excellent tool for calculating accurate band structure calculation scheme allowing also the computation of the hyperfine fields in crystalline solids requiring only the lattice constants as input[122,259].

Ab initio density functional theory calculations were carried out using linearised augmented plane wave + local orbitals method (LAPW+lo) as implemented in the Wien2k code[317,318] for the $RCrO_3$ perovskites, which were known to provide accurate results

including the hyperfine parameters[321,322]. Relaxation of the structural parameters by minimization of total energy, charge and calculated forces was performed. These calculations have been performed in close collaboration with Ricardo Teixeira (University of Lisbon).

2.5.1.5 Temperature Dependence of the EFG

The study of the electrical field gradient temperature dependence in solids has been extensively studied. Distinct trends of experimental data on $EFG(T)$ exist, however the most common is the increase of V_{zz} with decreasing temperature. Although, no general description is available there are several contributions for the temperature dependence of V_{zz} and their relative magnitude depend strongly on the details of the studied system.

In a first theory that came forward in an attempt to explain the temperature dependence of V_{zz}, the EFG was assumed to be proportional to the lattice contribution, where the changes in V_{zz} with temperature resulted essentially from thermal expansion of the lattice parameters and thermal motion. In fact, an EFG can vary with temperature due to several reasons: variations of the lattice parameters with temperature (thermal expansion), structural phase transitions with changes on the charge distribution around the probe (*e.g.* change of symmetry), or simply due to the dependence of atomic lattice vibrations on temperature (phonons)[323–326].

This theory explains reasonably well the EFG temperature dependence ionic lattices, however fails for the case of metallic lattices because it lacks a good comprehension of the electronic fluid[xiv] [324,325]. For a ionic crystal, an increase of V_{zz} with decreasing temperature might be observed, resulting from a positive (volume) thermal expansion (V_{zz} depends on the interatomic distances as $1/r^3$). However, in solids, the thermal expansion is very small and rarely can account for the V_{zz} temperature dependence.

Experimentally, *Christiansen et al*[327] found out that in most non-cubic materials the temperature dependence of the EFG follows the so called $T^{3/2}$ law:

$$V_{zz}(T) = V_{zz}(0)\left(1 - \alpha T^{3/2}\right) \ . \tag{2.33}$$

Although several authors tried to get some insight on this EFG trend[306,328–330], there is, up to now, no satisfactory theoretical explanation for the $T^{3/2}$ law and its general validity is still questioned[331].

2.5.1.6 Sample implantation/diffusion

The first step to perform a PAC experiment is to introduce a radioactive isotope, which will act as a probe, inside the material under study. This is generally done either by

[xiv] In metals, the electronic contribution to the EFG temperature dependence is very important since electrons mediate the effect of lattice vibrations on the EFG.

diffusion of a solution containing the desired isotope, via ion implantation or by chemical process (in synthesis stage).

The ^{111m}Cd and ^{111}In isotopes used in this work to perform the local probe measurements by PAC technique were produce in the Isotope Separator On-Line (ISOLDE) CERN Genebra. This facility, situated at the Proton-Synchrotron Booster (PSB) at CERN, is dedicated to the production of a large number of radioactive ion beams for many different experiments in the fields of nuclear, atomic and condensed matter physics and biophysics. ISOLDE produce the isotopes by irradiating an appropriated target with a 1 GeV proton beam delivered by the CERN-PSB. Then isotope ions are accelerated and mass separated to a chamber where the samples are implanted. During the implantation the beam is swept in order to obtain a homogeneous implanted area. The current that emerges from the sample during the implantation process is measured and integrated to dose the isotopes implanted.

The decay scheme of the ^{111}In and ^{111m}Cd isotopes are presented in Fig. 2.11.

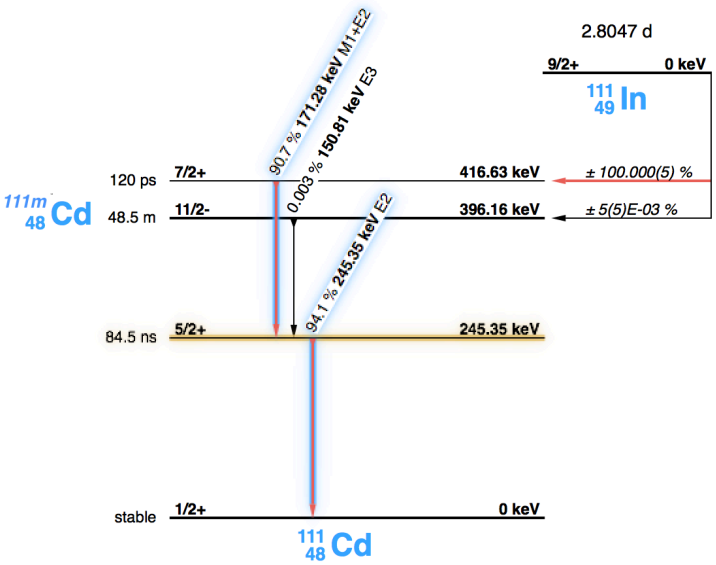

Figure 2.11 – Simplified decay schemes for ^{111}In and ^{111m}Cd nuclei. Intermediate PAC probe state with energy E = 245.4 keV, half life $\tau_{1/2}$ = 84.1 ns and angular momentum I = 5/2. (Adapted from ref. 332)

The ^{111}In probe decays with a half-life $\tau_{1/2}$ of 2.83 days by electron capture to the excited +7/2 state of ^{117}Cd. This state decays by the emission of the 171(γ_1)–245 (γ_2) keV $\gamma-\gamma$ cascade to the +1/2 ground state of ^{111}Cd. The intermediate level +5/2 is characterized by the quadrupole moment Q = 0.77 b, the magnetic moment μ = 0.766 μ_N and the mean life $\tau_{1/2}$ = 84.1 ns. The ^{117}Cd probe decays with a half-life $\tau_{1/2}$ of 2.5 hours by β^- emission to the excited +1/2 state of ^{117}In. This state decays by the emission of the 90(γ_1) – 344 (γ_2) keV $\gamma-\gamma$ cascade to the –1/2 ground state of ^{111}Cd. The intermediate level +3/2 is characterized by the quadrupole moment Q = –0.59 b, the magnetic moment μ = 0.938 μ_N and the mean life $\tau_{1/2}$ = 53.6 ns (adapted from Refs. 332,333).

Table 2.1 – Magnetic dipole, μ, and electrical quadropole, Q, moments for the 245.4 keV state (intermediate state of the ^{111}In$\rightarrow^{111}$Cd cascade).

Isotope	μ (μ_N)	Q (b)	Spin
^{111}In$\rightarrow^{111}$Cd ^{111m}Cd$\rightarrow^{111}$Cd	0.766(3)	0.77(12)	+5/2
^{117}Cd$\rightarrow^{117}$In	0.938(10)	-0.59(1)	+3/2

The ^{111}In isotope was also acquired in the form of a high purity solution of Indium chloride (3 mCi). Initially a pellet shape sample is heated at about 60-80 °C on top of a watch glass that per se was placed in a heating plate. Secondly the sample is wetted with the radioactive solution by placing small quantities of radioactive solution ($\sim \mu$L) at the sample surface. A resting period proceeds it until all the liquid is absorbed. After each drop the sample activity is measured. This procedure is repeated until enough radioactive solution is incorporated into the sample (about 2 KBq). Finally, a high temperature annealing is performed to facilitate the probe diffusion and its placement at regular sites. This diffusion process takes place preferentially trough: point defects, *e.g.* vacancies and interstitial ions, along line and surface defects which include grain boundaries, dislocations, inner and outer surfaces, etc.

After implantation the samples are submitted to a high temperature treatment to recover any damage created by the implantation or to promote diffusion in the case of the wetting process. For that the samples were placed in a alumina crucible inside a quartz tube that by its turn was place inside a tubular furnace. The laboratory for sample preparation includes a tubular furnace allowing the annealing of different samples under different atmospheres (vacuum, gas flux or air). The temperature of the furnaces is electronically controlled and the thermal treatments can be performed up to 1773 K.

The annealing conditions used for the different compounds are summarized in table 2.2.

Table 2.2 – Annealing conditions used in the post-implantation annealing in the different series of compounds.

Sample	Isotope	Atmosphere	Temperature (K)	Dwell time	Type
$CdCr_2S_4$	^{117}Cd ^{111}In	vacuum	793	20 min	Imp.
$CdMn_2O_4$	^{111m}Cd ^{117}Cd ^{111}In	Air	973	20 min 1 hour	Imp. Diff.
$YbCrO_3$	^{111}In ^{111m}Cd	O_2	1273 1073	18 hours 20 min	Diff. Imp.
$ErCrO_3$	^{111}In ^{111m}Cd	Air	1273 973	48 hours 20 min	Diff. Imp.
$YCrO_3$	^{111}In ^{111m}Cd	Air	1273 973	48 hours 20 min	Diff. Imp.
$SmCrO_3$	^{111}In ^{111m}Cd	Air	1273 973	48 hours 20 min	Diff. Imp.

2.5.1.7 $\gamma - \gamma$ PAC set-up

The PAC experiments were carried out using a normal slow-fast setup with four/six detector pac spectrometer equipped with BaF_2 scintillators which have a 650 ps time resolution disposed in an 90° and 180° geometry.

The experimental set-up for pac experiments allows us to measure the time dependence of the $\gamma - \gamma$ cascade emitted when the probe decays from from the excited state to ground state. With 4-detector PAC spectrometer and a set-up of electronic gadgets twelve spectra from the paired combinations, four from detectors at θ = 180^o and eight at θ = 90^o are produced carrying information about their provenance, in the form of counts/versus time. Whereas in the case of six detectors thirty spectra are obtained: six from detectors at θ = 180^o and twenty four at θ = 90^o.

To cover a wide range of physical phenomena, the measurements have been performed in a wide range of temperatures in order to span interesting regions (*e.g.* magnetic and dielectric phase transitions). For low temperature measurements (from 10 K up to room temperature), the samples were attached to the cold finger of a closed-cycle helium refrigerator equipped with a PID temperature controller. For the study of high temperature effects (from room temperature up to 1300 K), a small tubular resistive furnace was used. This system allows the use of different atmospheres such as O_2, N_2 and Ar. Both cryostat and furnace are mounted in such way that the sample is always at the centre of the detector's ensemble.

As a matter of fact, in sequence of the work developed in this thesis on local probing, we were able to play an important role in the creation of a laboratory dedicated to hyperfine interactions using PAC spectroscopy in our facility at IFIMUP-IN. From computer assembly, software installation, electronic rack mounting, wiring connecting to machine calibration help was given, and now a 4 detector machine that can measure from 10 K to 1200 K is fully operational. An in-out and up-down set-up was developed for an easy change between measurements with the cryostat or with the furnace (see Fig. 2.12). Also, new furnaces were developed and build in order to provide an easy assembly of the water refrigeration, gas inlet and outlet and sample change.

2.5.2 Pair Distribution Function - PDF

The atomic pair distribution function method of analysis (PDF) has successfully been used for the study of liquids, glasses and other amorphous materials. This method which takes the information directly from diffraction experiments describes the distribution of the atomic distances in a material[334]. Because, PDF and XRD take information from diffraction experiments, some argue that it should not be applied to periodic structures, like crystals, where with the aid of the Bragg's law the structure can easily be determined, and only should be used where a lack of long-range lattice periodicity exists (*e.g.* liquids or glasses). Furthermore, the PDF obtained by powder diffraction is simply a Fourier-transform of the structure function, $S(Q)$ and thus the PDF carries no less information

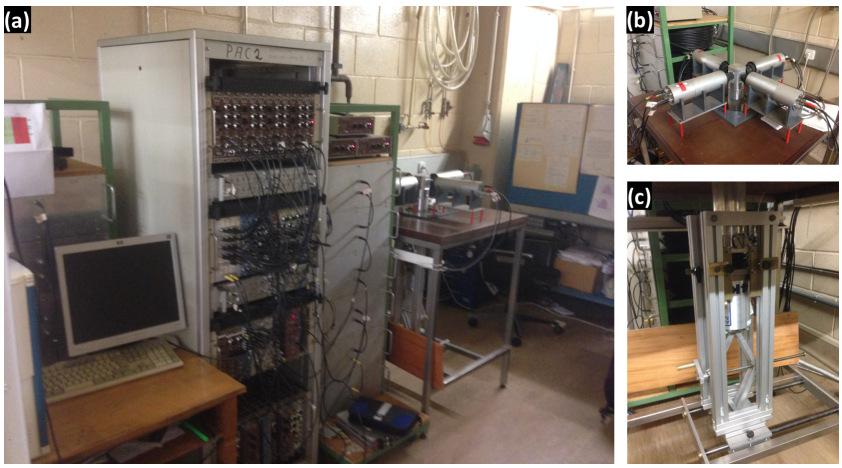

Figure 2.12 – Porto PAC machine. **(a)** Four slow-fast coincidences with BaF_2 detectors set-up in Porto. **(b)** Detailed view of the 4 BaF_2 detectors. **(c)** Detailed view of the in-out lift for the cryostat.

than the powder diffraction pattern[335,336]. Thus, in principle one can say that the real-space PDF analysis is somewhat equivalent to the methods of crystallographic powder diffraction analysis such as the Rietveld refinement that are carried out in the reciprocal space[334,337].

The great advantage of the real-space PDF analysis when comparing it to the conventional crystallographic analysis become obvious when the material under scope has some disorder in the structure. In these cases the former lacks to give the correct information about the structure to some extent. A crystallographic analysis that presumes periodicity will only take the Bragg peaks into account and will ignore the diffuse scattering[338]. Of course, this as a clear impact on the results, because it will only give a spatially averaged picture of the structure, and local variations in the structure will not be correctly represented. Furthermore, if the assumption of perfect periodicity is made, the information regarding the correlation among the local variations is lost. A technique that utilizes diffuse scattering as well as the Bragg scattering, like the real-space PDF method, will be able to describe the disorder in a more accurately way. In this case, if local atomic displacements exists away from the crystallographic sites, they will be reflected in the crystal only in terms of the large thermal, or Debye-Waller, factor, and will not be easily separated from the lattice vibration. As we will see in sections 3.1 and 5.3 in some cases the local structure of a solid is different from the average structure. Here, PDF shows its potential, because it is capable of bringing this difference to light. If we think about it, few materials are perfectly periodic. Even those that are without lattice defects, anharmonicity in the lattice can introduce local collective deviations from perfect periodicity. Many of the materials studied nowadays, which have a technological interest present internal disorder making them complex structural cases of study. Different solid-solutions like in manganese-based perovskite compounds[339,340], lead chalcogenides[341] or even ferroelectrics[342,343] are among those which are inherently disordered at the atomic level. Therefore, in these cases we can profit by the combined

use of the real as well as reciprocal space analysis (which, in fact, are complementary to each other).

The PDF method takes into account data from both the Bragg and diffuse neutron or x-ray scattering signals, hence carrying structural information on different length-scales. We used the PDF method to obtain the precise structure and size information of atomic structure which is based in the scattering-length weighted measure of the probability of finding pairs of atoms in the material at distance r, $G(r)$ (see Fig. 2.13), given by:

$$G(r) = 4\pi r[\rho(r) - \rho_0], \tag{2.34}$$

where $\rho(r)$ is the atomic pair-density and ρ_0 is the average atomic number density.

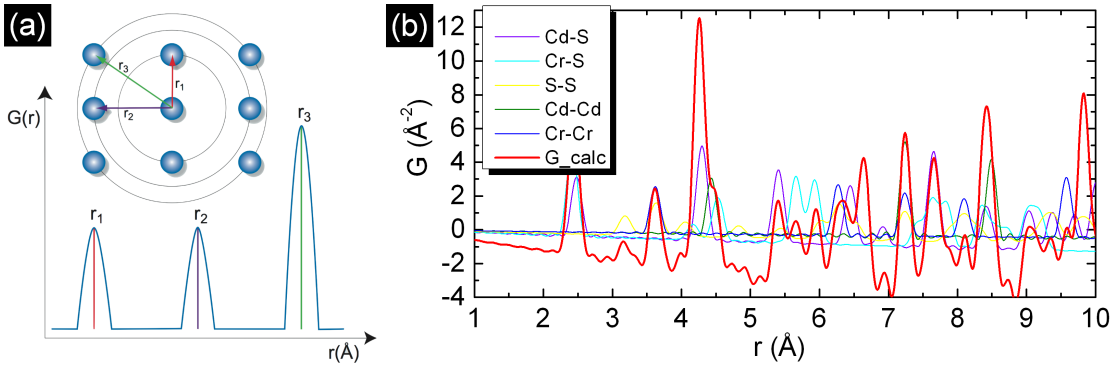

Figure 2.13 – Principle of the PDF. **(a)** A pair correlation function $G(r)$ gives the probability of finding two atoms/particles at a distance r apart, relative to the probability expected for a completely random distribution at the same density. **(b)** Simulated total pair correlation functions for the spinel $CdCr_2S_4$. The individual contributions from the different atoms combination are also shown.

The experimental PDF $G(r)$ or the radial distribution function $4\pi r^2 G(r)$ are directly obtained from the diffraction data by Fourier transforming the reduced total scattering structure function $F(Q)$:

$$G(r) = \frac{2}{\pi}\int_{Q_{min}}^{\infty} F(Q)\sin(Qr)dQ\ , \tag{2.35}$$

where $F(Q)$, being $[S(Q)-1]$ rescaled by Q and averaged over all angles, may be written as:

$$F(Q) = Q[S(Q)-1]\ , \tag{2.36}$$

where $Q = 4\pi(\sin\theta)/\lambda$ is the magnitude of the scattering vector (or momentum transfer) used to obtain the PDF and $S(Q)$ is normalized total structure factor, *i.e.* the measured intensity corrected for background, Compton and multiple scattering, absorption, geometric and other factors[344]. For the calculation of $S(Q)$ and $G(r)$ academic software PDFgetX2 was used[345].

The total scattering experiments allow the same data to be analyzed both in crystallographic mode in reciprocal space using the Rietveld method, which yields the average crystal structure, as well as in the PDF mode in direct space, which yields the local struc-

ture. If a longer length-scale is considered in the PDF, the average crystallographic view is recovered as well.

The scattering experiments for PDF analysis were performed on Beamline 11-ID-C at the Advanced Photon Source at Argonne National Laboratory, over the temperature range 80 – 220 K. 11-ID-C is a fixed, high-energy beamline operating at 105.091 keV. This equipment can be used for diffraction measurements on both crystalline and amorphous materials having a 2D area detection primarily for structural studies or exploration of phase changes where a wide array of additional equipment may be used in a combined mode or individually. To vary temperature, an Oxford Cryosystem was used. The PDFs were modeled using the PDFgui[346] refinement program and the Rietveld refinements used the Fullprof program[347].

Amplitude of the local Cr off-centering, Δr was calculated using the following expression:

$$\Delta r = \sqrt{U_{iso}^{Exp} - U_{iso}^{Theory}}. \tag{2.37}$$

2.6 Studied Materials

2.6.1 Cadmium chromium thiospinel $CdCr_2S_4$

Polycrystalline samples of cadmium chromium sulphide ($CdCr_2S_4$) of the spinel family were first synthesized by *Passerini et al.* in 1931 and later by *Haul and Schöning* (see review on the reactivity of sulphides by *Chaus et al* ref. 348 and references within). In this work, in order to obtain the $CdCr_2S_4$ system, the samples had to be prepared by a variant of solid state reaction method, where the annealing procedure was performed in a double evacuated quartz ampoule. Two major reasons were considered for the necessity of the double evacuated quartz ampoule in the synthesis process. The first one was to avoid oxide formation and thus obtain the desired phase. The second reason was related with safety reasons due to the high partial pressure that sulphur reaches when submitted to the sintering temperatures, which can break the first ampoule. In this way, the use of a second one, conserves the vacuum required in case the first one breaks.

Stoichiometric amounts of cadmium sulphide[xv], chromium[xvi] and sulphur[xvii] were mixed and grinded together until very fine powders were obtained. The powders were then pressed into a pellet of $\sim$ 1 g. Then the pellets were weighted and introduced into a quartz tube and closed in vacuum (10^{-5} Torr) with the help of a burner. This ampoule was then introduced into a larger one that was also filled in vacuum, see Fig. 2.14.

The experimental set-up shown in Fig. 2.14 was developed because the burner could only heat one side of the tube at a time. Thus, collapsing (due to the vacuum inside the

[xv] CdS, metal basis, 99.999% purity, CAS-number:1306 – 23 – 6
[xvi] Cr, -60 mesh metal basis, purity 99.99%,CAS-number:7440 – 47 – 3
[xvii] S, purity 99.98%,CAS-number:7704 – 34 – 9

tube) only the part of the tube that was right in front of the burner. Usually, without our experimental set-up, the sample encapsulation procedure needed to be performed several times until a complete isolation of the tube was achieved. This made the process extremely difficult since most of the times the tube would break or totally collapse opening an hole into the space where the sample was allocated. Therefore, the necessity to rotate the tube and get a relative homogenous heating around the tube arose. With this system we could rotate the tube while heating a certain zone and be able to easily close the tube. Furthermore, allows for a single person to close the quartz ampoule.

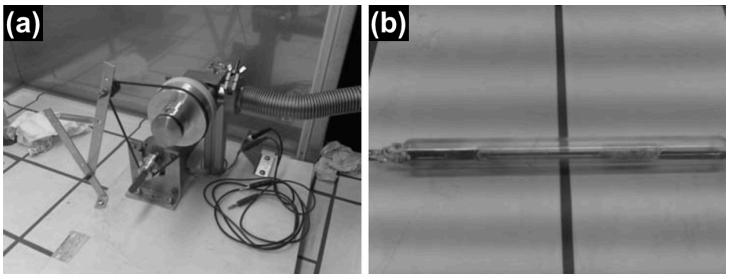

Figure 2.14 – Photos of the synthesis system used for spinel. **(a)** System developed for closing the quartz ampoules in vacuum. **(b)** Double evacuated ampoule with reactants inside.

The double ampoule was placed into an alumina tube for greater protection due to the high temperature that the ampoule was going to endure (sulphur vapor pressure at the temperatures of annealing could break the ampoules and therefore cause the contamination of the furnace).

The firing procedures were performed in several steps (see Fig. 2.15). The furnace was heated up to 400 °C (6.25 °C/min), where it rested for 5 hours and then up to 650 °C (0.1 °C/min). After 5 days at 650 °C the vapor in the ampoule became more transparent indicating that the majority of sulphur had already reacted and thus the oven temperature was increased up to 750 °C (0.1 °C/min). After being at this temperature for 4 days the furnace was slowly cooled to room temperature ($\approx$ 1 °C/min).

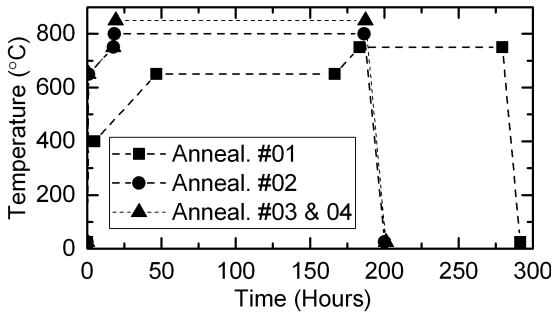

Figure 2.15 – $CdCr_2S_4$ synthesis annealings. Evolution of annealing temperature with time.

After this first heat treatment we could observed that, as expected, a small part of the sulphur did not react remaining in the ampoule wall. After weighting the pellets the mass loss was compensated by adding sulphur. A new grinding, pelletizing and weighing of the pellets was then performed.The heat treatment process was repeated again. This

time a ramp of 10.8 °C/min was used to reach the 650 °C and from there to the 750 °C at 0.1 °C/min rate. Finally the temperature was raised to 800 °C (1.0 °C/min) where it stayed for a week. Again ≈ 1 °C/min rate was used to slowly cool the furnace to room temperature. After this annealing procedure the sample weight was again measured, compensated with sulphur for the mass loss, grinded, pressed into a pellet and was annealed to a maximum temperature of 850 °C. The last process was repeated one more time, in order to obtain homogeneous polycrystalline material with no spurious phases (see Fig. 2.15).

After every step of the synthesis process a XRD pattern was collected allowing to follow the evolution of the diffusion reaction. Its possible to observe in Fig. 2.16, the referred evolution in the XRD pattern after each step and compare the resulting powder with the XRD patterns available in the literature[349]. All patterns are normalized to the more intense peak.

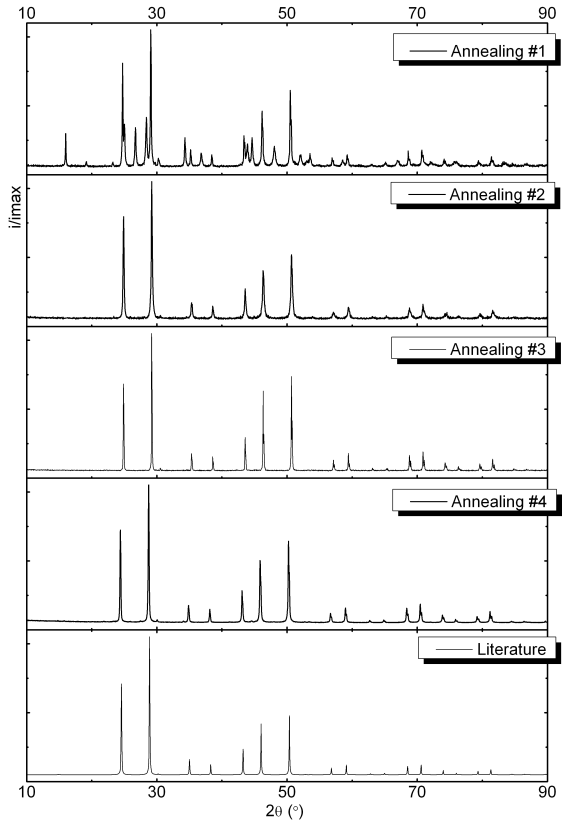

Figure 2.16 – $CdCr_2S_4$ XRD patterns of the different synthesis steps (top) and the reference literature (bottom).

After the first synthesis step the XRD pattern already shows the presence of the desired spinel structure but also the presence of reflections corresponding to the reactants, and to Cr_2S_3. The second heat treatment proved to be very fruitful, because it managed to convert almost all reactants into the final product. The third heat treatment, was enough in order to yield a single phase sample. Nevertheless a fourth treatment was performed in order to ensure that we would obtain a single phase with no spurious

secondary phases. Is also possible to observe that, as desired, the last two treatments improved the sharpness of the peaks, thus increasing grain size.

The preparation of the chalcogenide ($CdCr_2S_4$) was performed following a method kindly provided by Dr. Tsurkan from the Institute of Applied Physics of Moldova University[350].

2.6.2 Cadmium manganese oxyspinel $CdMn_2O_4$

The polycrystalline sample of $CdMn_2O_4$ studied in this thesis has been prepared by a coworker, Tânia Mendonça at CERN during her PhD work. A standard solid-state reaction method was used, where stoichiometric amounts of CdO[xviii] and Mn_2O_3[xix] powders were mixed, grinded, pelletized, and sintered at 900 °C for 6 hours in air in a high-temperature furnace. After sintering, the pellet was crushed, grinded, and pressed to a pellet and sintered again at 900 °C for 20 hours in air. In each cooling and heating process a ramp was used of 5 °C per minute (see Fig. 2.17).

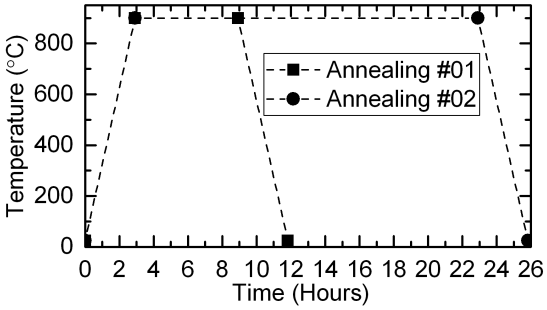

Figure 2.17 – $CdMn_2O_4$ synthesis annealings. Evolution of annealing temperature with time.

In Fig. 2.18 the sample's x-ray powder pattern was collected at room temperature (RT) in a $10 < 2\theta < 74$ range. As can be easily identified by the Bragg reflections (at the bottom of the figure) corresponding to each phase, a major phase corresponding to $CdMn_2O_4$ and a small a small impurity contribution of CdO are present on the XRD spectrum.

2.6.3 Orthorhombic rare-earth chromites $RCrO_3$

The $RCrO_3$ (R=Yb, Er, Y, Sm) polycrystalline samples were prepared by solid state reaction method using high available pure powder component oxides mixed in a stoichiometric ratio and heated supported by high density Al_2O_3 crucibles (usually) in air, with several intermediate grinding and fired at a slow heating rate of 5 °C/min in a three step process ($YbCrO_3$ had an extra step in O_2 flow).

In a first step, appropriate amounts of precursor oxides Cr_2O_3[xx] and R_2O_3 (R= Yb[xxi],

[xviii] Cadmium oxide, purity 99.998%,CAS-number:1306 – 19 – 0
[xix] Manganese (III) oxide, purity 99.9%,CAS-number:1317 – 34 – 6
[xx] Chromium(III) oxide, Puratronic, purity 99.97%,CAS-number:1308-38-9
[xxi] Ytterbium (III) oxide, REacton, purity 99.99%,CAS-number:1314-37-0

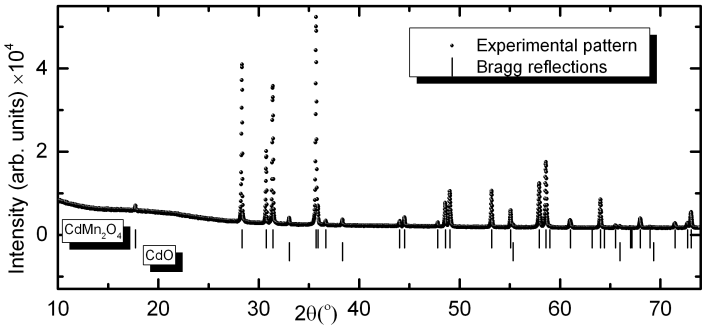

Figure 2.18 – Diffraction pattern output of the spinel $CdMn_2O_4$ structure at room temperature. Bragg reflections for $CdMn_2O_4$ and CdO.

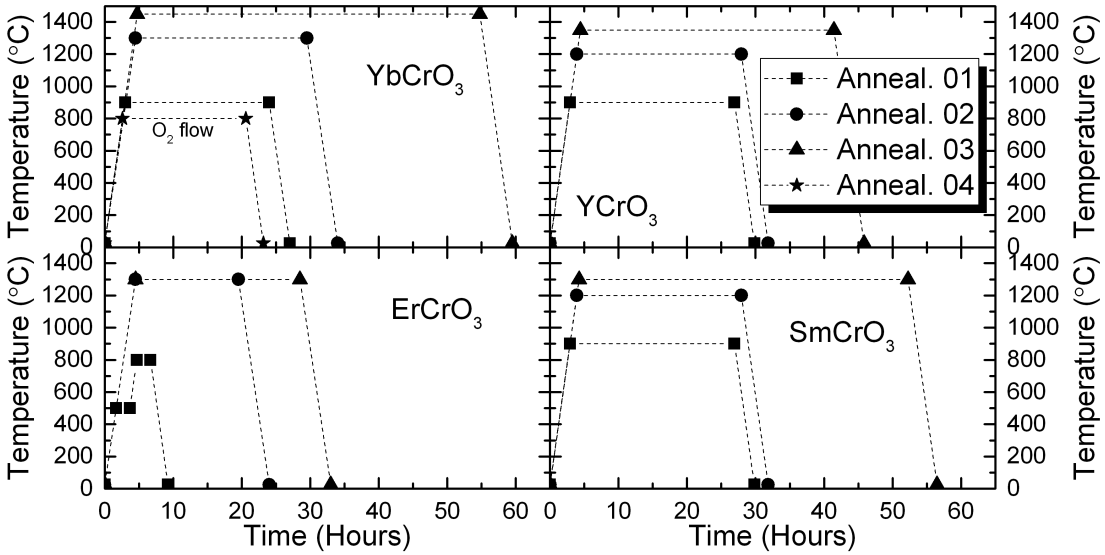

Figure 2.19 – $RCrO_3$ (R=Yb, Er, Y, Sm) synthesis annealings. Evolution of annealing temperature with time.

Er[xxii], Y[xxiii], Sm[xxiv]) were weighed to the nearest milligram in sufficient quantities to give a 1.0 g sample and mixed in an agate mortar until a fine and homogeneous mixture was obtained. The resulting powders were then compacted into pellets and fired in a first heat treatment. This process was repeated two more times until a pure phase was obtained. The temperature evolution with time of each heat treatment for the different samples studied is plotted in Fig. 2.19 and summarized in table 2.3 .

All solid state synthesized $RCrO_3$ powders were confirmed to be single phase by XRD (see Fig. 2.20).

[xxii] Erbium (III) oxide, Reacton, purity 99.99%,CAS-number:7704-34-9
[xxiii] Yttrium(III) oxide, REacton, purity 99.99%,CAS-number:1314-36-9
[xxiv] Samarium (III) oxide, REacton, purity 99.99%,CAS-number:12060-58-1

Table 2.3 – Sintering conditions for polycrystalline chromites $RCrO_3$ (R = Yb, Er, Y, Sm).

$YbCrO_3$	Temperature (°C)	Time (h)	Heating Rate (°C/h)
1st Annealing	900	21	300
2nd Annealing	1300	25	300
3rd Annealing	1450	50	300
4rd Annealing	800	18 (O_2 flow)	300
$ErCrO_3$	Temperature (°C)	Time (h)	Heating Rate (°C/h)
1st Annealing	500/800	2/2	300
2nd Annealing	1300	15	300
3rd Annealing	1300	48	300
$YCrO_3$	Temperature (°C)	Time (h)	Heating Rate (°C/h)
1st Annealing	900	24	300
2nd Annealing	1200	24	300
3rd Annealing	1350	37	300
$SmCrO_3$	Temperature (°C)	Time (h)	Heating Rate (°C/h)
1st Annealing	900	24	300
2nd Annealing	1200	24	300
3rd Annealing	1300	48	300

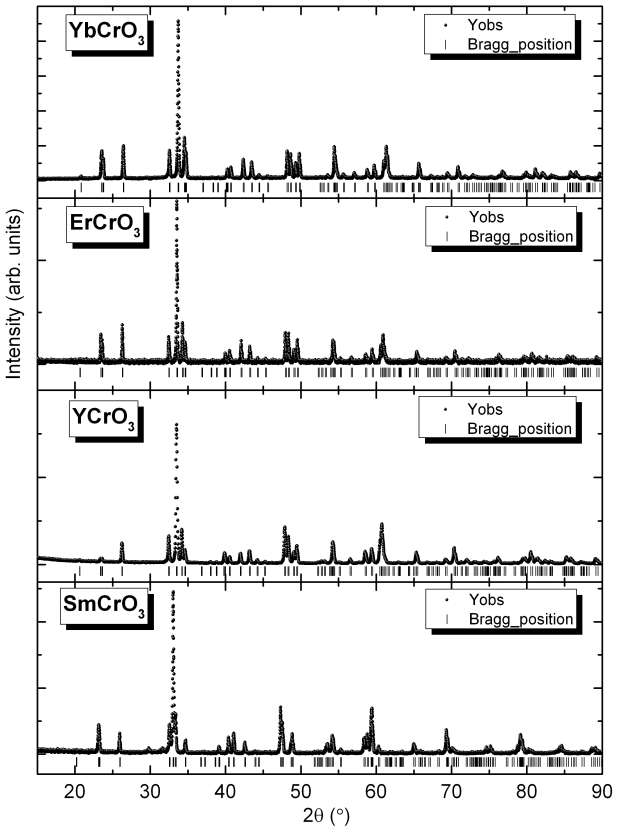

Figure 2.20 – Room temperature powder XRD pattern of $YbCrO_3$, $ErCrO_3$, $YCrO_3$ and $SmCrO_3$ samples after the final heat treatment.

CHAPTER 3

Macroscopic and local scale studies on $CdCr_2S_4$ Spinel

3.1 Dynamic off-centering of Cr^{3+} ions and short-range magneto-electric clusters in $CdCr_2S_4$

The cubic spinel $CdCr_2S_4$ gained recently a vivid interest, given the relevance of relaxor-like dielectric behavior in its paramagnetic phase. By a singular combination of local probe techniques namely Pair Distribution Function (PDF) and Perturbed Angular Correlation (PAC) we firmly establish that the Cr ion plays the central key role on this exotic phenomenon, namely through a dynamic off-centering displacement of its coordination sphere. We further show that this off centering of the magnetic Cr – ion gives rise to a peculiar entanglement between the polar and magnetic degrees of freedom, stabilizing, in the paramagnetic phase, short range magnetic clusters, clearly seen in ultra-low field susceptibility measurements. Moreover, the Landau theory is here used to demonstrate that a linear coupling between the magnetic and polar order parameters is sufficient to justify the appearance of magnetic cluster in paramagnetic phase of this compound. These results give insights on the hotly debated magnetic and polar interaction, setting a step forward in the reinterpretation of the coupling of different physical degrees of freedom. For sake of section completeness we review here again the most important aspects from literature relevant for our analysis. This chapter is based on the published work[169]: G. N. P. Oliveira, A. M. Pereira, A. M. L. Lopes, J. S. Amaral, A. M. dos Santos, Y. Ren, T. M. Mendonça, C. T. Sousa, V. S. Amaral, J. G. Correia, and J. P. Araújo, *Physical Review B* 86, 224418 (2012).

3.1.1 Overview

Materials with multifunctional physical properties are crucial for the modern society, especially those, which display a strong coupling between magnetic and polar degrees of freedom, the so-called magnetoelectrics. This by far unexploited capability promises new paradigm-shift technologies for magnetic data storage, high-frequency magnetic devices, spintronics and micro-electro-mechanical systems[43,351]. However, conventional models and theories cannot explain the strength of this coupling observed in many

examples of multiferroic materials[26,73]. A complete understanding of these macroscopic properties requires a thorough treatment of their atomic-level origins. This coupling is correlated with local distortions, and thus the roles of local polar and magnetic clusters must be determined[352]. Particular interest is currently focused on local distortions in a class of disordered materials, the relaxor-like ferroelectrics, that frequently exhibit a competition/coexistence between short-range and long-range orders[353]. $CdCr_2S_4$ is among these relaxor-like systems and is one of the rare compounds that exhibits four colossal effects (the magnetocapacitive, electrocapacitive, electroresistive and magnetoresistive effects)[159]. $CdCr_2S_4$ crystallizes in the spinel structure, with Cd occupying the tetragonal position in the lattice (A – site) and Cr^{3+} occupying the octahedral site (B – site)[123] (see Fig. 1.11).

The discovery of dielectric relaxational dynamics above the Curie temperature (T_C), which is responsible for the strongly increased dielectric permittivity of $CdCr_2S_4$, has driven an intense debate in the research community[128,160].

Hemberger et al[128] described $CdCr_2S_4$ as a multiferroic relaxor, due to the observed relaxor-like dielectric properties and colossal magnetocapacitance (surpassing 500%). However, *Catalan et al*[160] argued that the observed results could originate from a conductive artifact. They went further, arguing that the polarization hysteresis loops published by *Hemberger et al*[128] had an uncharacteristic ferroelectric shape and that in fact it resembled more those of a lossy dielectric, like in the case of some semiconducting thiospinels. Furthermore, they point out that just the fact that the larger "remanent" polarization in comparison to the pyroelectric one, should suffice to question the validity of the results, because the switchable polarization must always be smaller than the pyroelectric polarization. Here, the observed pyroelectric polarizations were relatively small for any proper ferroelectric (0.05–0.07 $\mu C\,cm^{-2}$), and were in accordance with thermally stimulated discharge of space-charge injected during poling.

Hemberger et al were able to counter point each of these arguments, however the doubt about the ferroelectric character of $CdCr_2S_4$ would linger among the scientific community and the origin for the intrinsic multiferroic behavior still undisclosed.

First-principles calculations excluded softening of the polar modes as a possible origin of the anomalous dielectric behavior[119]. Other models proposed that the spin-driven polar moments originated from the off-centering of the Cr^{3+} ions[128]. *Sun et al*[161] observed a glassy dipolar state near T_C and a ferroelectric ordering near $T_P \sim$ 56 K. The $Fd\bar{3}m$ space group of the overall crystal structure forbids the existence of ferroelectric order, but *Gnezdilov et al.* recently suggested a symmetry reduction below T_C from the $Fd\bar{3}m$ to the $F\bar{4}3m$ non-centrosymmetric space group, which permits the existence of electric dipoles. Interestingly, the discovery of phonon anomalies at $T_F <$ 130 K by means of Raman light scattering suggested that the electronic polarizability was enhanced by the Cr – S distance and respective bond hybridization[163].

Still shrouded is the origin of the strong coupling of magnetization and dielectric permittivity in this compound. As pointed out, the relaxation dynamics of the polar moments

is accelerated below T_C [129], but it remains to be clarified what is the microscopic origin of the detected relaxation dynamics and why the dynamics couples so strongly to the magnetic order parameter. A coupling via exchange-striction, *i.e.*, volume changes arising from the magnetic exchange energy seems possible[129]. The onset of spin order leads to a softening of the lattice thereby reducing the energy barriers against dipolar reorientation and thus enhancing the mean relaxation rate. As an alternative explanation one could also consider a magnetic-field-induced variation of charge-carrier mobility or density. Though much scientific effort has been dedicated to unveil the nature of such effects and to settle multiferroism in this system, the understanding of these phenomena requires an adequate description of the structural, magnetic and charge degrees of freedom.

Several studies on this topic are available, but the origin of this peculiar dynamic dielectric regime above T_C remains unexplained, and detailed local structural characterization and local probe techniques can provide insights into this phenomenon. Herein, we use Pair Distribution Function analysis of x-ray powder diffraction (XRD) data to directly study the local environment of the Cr^{3+} ion. This study is combined with a hyperfine local probe technique, Perturbed Angular Correlation, which examines the properties and dynamics of the atomic-scale distortions. Spin-lattice correlations are evaluated through low-field magnetization measurements and are phenomenologically described using a modified Landau theory model including a magneto-electric coupling term.

3.1.2 Experimental Details

The $CdCr_2S_4$ polycrystalline samples were synthesized by solid state reaction in a double evacuated quartz ampoule. Several firings were required in order to obtain a single crystallographic phase. The sample's crystallographic structure and lattice parameters have been attained. Room temperature X-ray powder diffraction (XRD) using a Rietveld refinement, has confirmed the presence of a single $Fd\bar{3}m$ phase[116,122].

The scattering experiments for PDF analysis were performed on Beamline 11-ID-C at the Advanced Photon Source at Argonne National Laboratory, over the temperature range 80 – 220 K. Fourier transforms (Ft) were computed using PDFgetX2, and the fits were performed using PDFfit2[346]. We used the PDF method to obtain the precise structure and size information of atomic structure which is based on the probability of finding pairs of atoms in the material at distance r, given by $G(r)$ (see Eq. 2.34). $G(r)$ is the scattering-length weight measure of the apart obtained via Fourier transform of the reduced total scattering structure function obtained from the combination of Eq. 2.35 and Eq. 2.36:

$$G(r) = \frac{2}{\pi} \int_{Q_{min}}^{\infty} Q[S(Q) - 1] \sin(Qr) dQ, \tag{3.1}$$

where $S(Q)$ is the structure function obtained after correction and normalization of the

diffracted intensity from the sample and Q is the magnitude of the scattering vector. Δr was calculated using the Eq. 2.37 defined in subsection 2.5.2.

We used PAC technique to study the electrical field gradient (EFG) and magnetic hyperfine field (B_{hf}) at an atomic level, specifically at the Cr and Cd site in this work. The ^{111}In and ^{117}Cd isotopes used were produced in the Isotope Separator On-Line (ISOLDE) CERN Genebra, by ion implantation at 30 keV. To perform the local probe measurements by PAC technique, a six detector spectrometer (BaF_2) in the temperature range from 300 K to 10 K was used. After the implantation an annealing was performed to the samples in an evacuated quartz ampoule with a sulphur excess. The annealing was performed during 20 minutes at a temperature of 500 °C (793 K). These annealing conditions have been previously shown to be ideal to allow the system to recover from the implantation damage and keep the sample properties unchanged[122].

PAC experimental anisotropy function $R(t)$ fit was performed by numerical diagonalization of the interaction Hamiltonian[292,354]. When in the diagonalized form the EFG principal component V_{zz} and the axial symmetry parameter (η) fully characterize the EFG tensor[292]. In case of a static electric quadrupole interaction, considering the relation between the three components of the EFG tensor (see Eq. 2.19) and the asymmetry parameter η (see Eq. 2.20) the perturbation factor for polycrystalline samples can be described as a sum of oscillatory terms and considering the effect of a Lorentzian EFG distribution of relative width δ (defined in Eq. 2.25):

$$G_{kk}(t) = S_{k0} + \sum_n S_{kn} \cos(\omega_n t) e^{-\delta\omega_n t} \,. \tag{3.2}$$

The frequencies represented by ω_n are those of the transition frequencies between the hyperfine levels created when a nuclear state is split by the hyperfine interaction (in the case of ^{111}Cd the intermediate level is characterized by nuclear spin momentum of I = 5/2). The quadrupole interaction splits this level into three sub-levels and thus in the Fts we observe a triplet of frequencies (ω_1, ω_2, $\omega_3 = \omega_1 + \omega_2$) for each non-vanishing EFG distribution present in the system). For a static interaction the anisotropy function obtained experimentally, can be written as

$$R(t) = \sum A_{kk} G_{kk}(t) \tag{3.3}$$

where A_{kk} are the angular correlation coefficients of the nuclear decay cascade and G_{kk} contains the perturbation of the angular correlation. In the case of a dynamic electric quadrupole interaction a different approach is required to characterize the perturbed angular correlation oscillations amplitude. When the characteristic time of the electric field gradient fluctuation is of the same order of magnitude of PAC time scale, the model of random phase approximation is adopted[355]. In this case, considering the additional

term $e^{-\lambda t}$, the perturbation factor for each electric field gradient can be described by:

$$G_{kk}(t) = e^{-\lambda t}\left(S_{k0} + \sum_{n} S_{kn}\cos(\omega_n t)e^{-\delta\omega_n t}\right), \quad (3.4)$$

where λ is related to the EFG fluctuation rate[356].

Low-field DC magnetization measurements were performed using a commercial magnetometer (MPMS from Quantum Design) over the temperature range 5 – 370 K in a field cooling procedure[357] (see section 2.3.2).

3.1.3 Results and Discussion

3.1.3.1 Structure characterization

The high quality XRD pattern of the $CdCr_2S_4$ final sample was analyzed by Le Bail refinement (applying a pseudo-voigt function to fit the peak shape), allowing the determination of the space group and cell parameters. Next the full Rietveld refinement was performed and parameters like the atomic positions, isothermic vibration factor and atomic site occupancy were determined. Figure 3.1 presents the observed pattern (red dots), calculated (black solid line), reflections of the correspondent phases (green tick marks) and fit deviation (blue solid line in the bottom) of the resulting Rietveld refinement. The fit deviation line shows the good quality of the performed refinement.

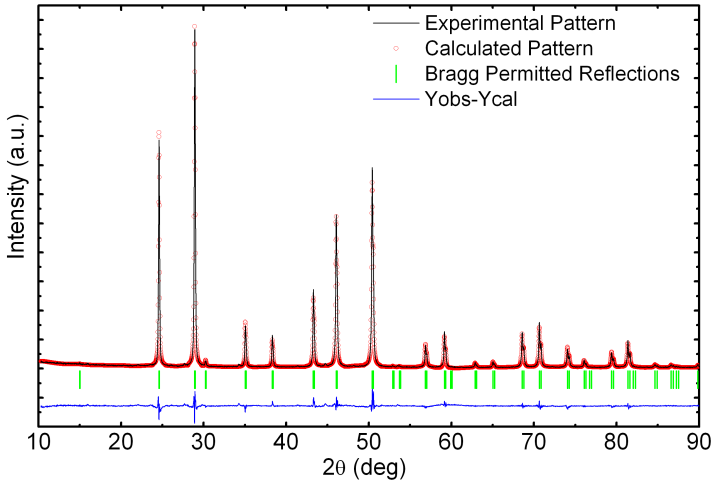

Figure 3.1 – Rietveld fit of XRD pattern of CdCr2S4.

The XRD pattern was fitted with only one phase corresponding to the space group $Fd\bar{3}m$[116,122] expected for the chalcogenide spinel $CdCr_2S_4$. The refinement parameters obtained are summarized in table 4.2.1, allowing to verify the high quality sample, and that the lattice parameters are also in a good agreement in those found in the literature[116,122]. A good way of following and guide a Rietveld profile is by observing the graphical representation given in Fig. 3.1, minimizing the difference between the

experimental and calculated profile. A more quantitative way of doing so is following the reliability factors (R_P; R_{wp}; R_{exp}) follow the evolution of the fit. As can be seen in table 3.1 the profile, the weighted-profile and experimental reliability factors are present. It can be observed by the low value of the χ^2 = 3.51 the goodness of the fit, where $\chi^2 = R_{wp}/R_{exp}$.

Table 3.1 – Summary of obtained structural parameters and atomic positions for $CdCr_2S_4$ system at room temperature.

Space Group			$Fd\bar{3}m$		
Unit Cell			$a = b = c$ =10.23234(17)		
V(Å^3)			1071.334(31)		
Z			8		
N. Points			4993		
Effective 2θ			10-90		
N. Refined Param.			15		
R_P; R_{wp}; R_{exp}			4.54; 4.77; 2.80		
χ^2			3.51		
Atom	x	y	z	B_{iso}	Occ
Cd	0.12500(0)	0.12500(0)	0.12500(0)	1.699(44)	0.233(313)
Cr	0.50000(0)	0.12500(0)	0.12500(0)	1.699(44)	0.233(313)
S	0.26478(16)	0.26478(16)	0.26478(16)	2.081(16)	0.993(99)

Atomic positions: Cd: 8a (⅛, ⅛, ⅛); Cr: 16b (½, ½, ½); S: 32c (x, y, z)

3.1.3.2 Polar nanodomains

Relaxor materials are most of the times identified by a key feature, which is the appearance of a broad temperature (T_M) and frequency dependent maximum of the dielectric permittivity $\epsilon(T, \omega)$, as well as the absence of long-range ferroelectric order in zero field at any temperature[358]. Another relaxor property feature is an extremely slow relaxation below T_M, which indicates the onset of relaxor freezing behavior. The characteristic relaxation time diverges at the freezing temperature T_F according to the well-known Vogel–Fulcher relation:

$$\tau = \tau_0 \exp\left[\frac{E_a}{k\,(T - T_F)}\right] , \tag{3.5}$$

where τ_0 represents the inverse attempt frequency, E_a the activation energy, and T_F the Vogel–Fulcher or freezing temperature. For obvious reasons, Eq. 3.5 only makes sense for $T < T_F$. A typical empirical method used to analyze the dielectric permittivity $\epsilon(T, \omega)$ is to consider the dielectric maximum temperature $T = T_M$ as a function of frequency. One may then define a relaxation time $\tau = 1/\omega$, which is found to satisfy the above Vogel–Fulcher relation[359]. However, in this thesis we used a Vogel–Fulcher law representation of the reciprocal dielectric permittivity maximum peak position as a function of temperature for extracting the freezing temperature. For that we started by measuring the complex dielectric permittivity as a function of temperature and frequency.

The temperature dependence of the complex dielectric permittivity obtained in the 10 K to 300 K temperature range for 500 kHz, 1 and 5 MHz frequencies (applied field 1 V/m) are shown in Fig. 3.2 (a) and 3.2 (b), real and imaginary parts, respectively.

Besides the small increase on the complex dielectric permittivity ϵ at T_C, a broad

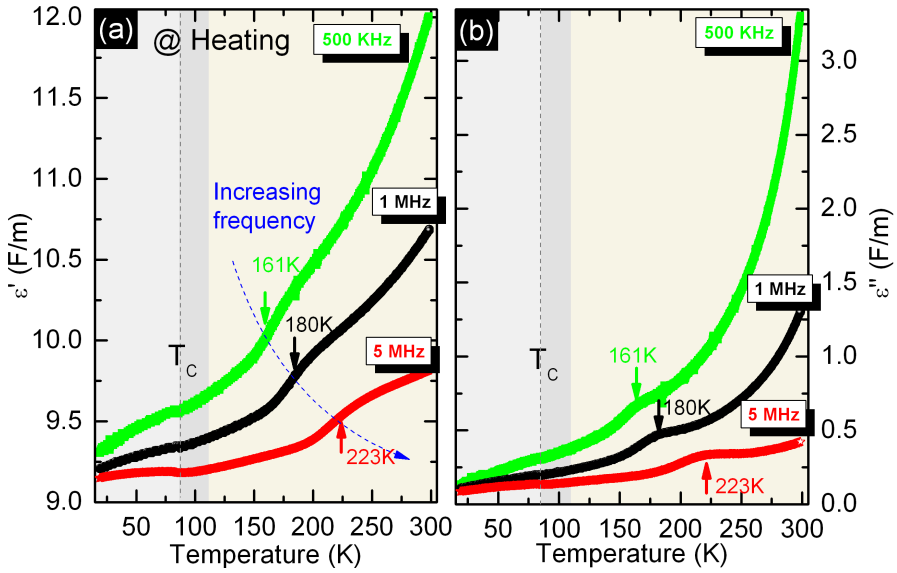

Figure 3.2 – Temperature dependence of real **(a)** and complex **(b)** part of complex dielectric permittivity. The $CdCr_2S_4$ sample was measured to a frequency of 500 kHz, 1 and 5 MHz.

frequency-dependent peak in the temperature-dependent dielectric susceptibility ($\epsilon^{-1} = 4\pi\chi^{-1}$) is observed. This peak shift appears between $T_M \sim 150$ and 250 K which is consistent with a report from literature[128]. In that work a freezing temperature of 150 K was estimate. This behavior was attribute to the controversial presence of ferroelectric relaxor strongly correlated to typical strong dispersion effects that are many times associated with the freezing of ferroelectric clusters[128]. Nevertheless, in the reciprocal $1/\epsilon'$ (not shown), a strong deviation from the expected Curie-Weiss law for paraelectric systems is observed as well as anomalies in the imaginary part (see Fig. 3.2). These features are signatures of a dynamic freezing (at $T = 130$ K) or a glass-like transition in $CdCr_2S_4$ unraveling the presence of polar nanodomains (see Fig. 3.3)[128,129,160].

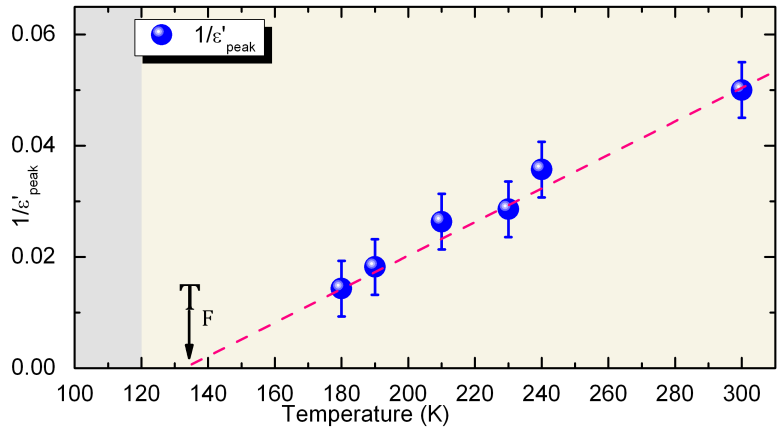

Figure 3.3 – Vogel-Fulcher Law representation of the reciprocal dielectric permittivity maximum peak position as a function of temperature.

3.1.3.3 Off-centering of Cr atoms

A representative experimental PDF of $CdCr_2S_4$, collected at 80 K (blue dots), is depicted in Fig. 3.4 along with the corresponding refinement fit beginning with cubic spinel symmetry ($Fd\bar{3}m$)[349] (red line) and the residual curve (green). For the complete set of temperatures where experimental PDF were collected see Appendix A.

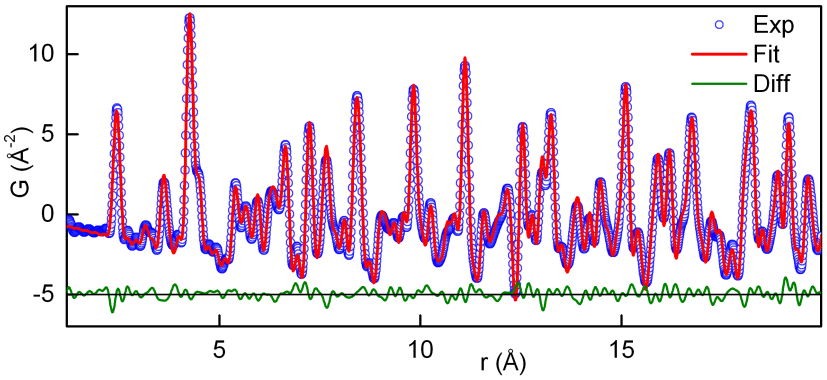

Figure 3.4 – PDF of the spinel $CdCr_2S_4$ structure at 80 K.

Refinements of similar quality were obtained from the data analyses at different temperatures, and the lattice parameters obtained at room temperature are in agreement with findings from previous reports[123]. The T dependences of the lattice parameters, [$a(T)$], obtained from the Rietveld refinement of the PDFs are depicted in Fig. 3.5.

From the date presented in Fig. 3.5, three distinct regimes were observed over the temperature range 80 – 220 K. For $T > 130$ K, $a(T)$ exhibits the conventional linear contraction with cooling as can be observed in Fig. 3.5 (a). This monotonic trend reverses at $T_F \sim 130$ K, where the material begins to exhibit negative thermal expansion, as has been previously observed[123,360]. In 1976, *Göbel*[154] observed that the lattice parameter in $CdCr_2S_4$ expanded anomalous with decreasing temperature, however this was only reported to happen below T_C. This negative thermal expansion regime exists within a narrow temperature range, and the negative coefficient of expansion reaches a maximum at $T_{PM} \sim 115$ K before the material returns to the typical thermal contraction regime at lower temperatures. This anomalous thermal behavior is unequivocally indicative of a local structural distortion[341]. In Fig. 3.5 (b), we present the temperature dependence of the isotropic atomic displacement parameter (ADPs [U_{iso}]) of the Cr^{3+} site and Cd and S [inset of Fig. 3.5 (b)], which were refined from the undistorted model. A linear behavior for the Cd and S atoms was observed over the entire temperature range, and no significant deviations from the Einstein Model (EM) (dashed lines in Fig. 3.5 (b)) were observed in the ADPs (see inset of Fig. 3.5 (b)), whereas for Cr atom it is only observed for $T^* > 160$ K. A deviation from the EM is observed for $T^* < 160$ K and is more pronounced at $T_F = 130$ K. In fact, previous Raman scattering experiments also indicated pronounced anomalies in the intensities and frequencies of optical phonon modes that arose at the same temperature, and these anomalies are consistent with our PDF mea-

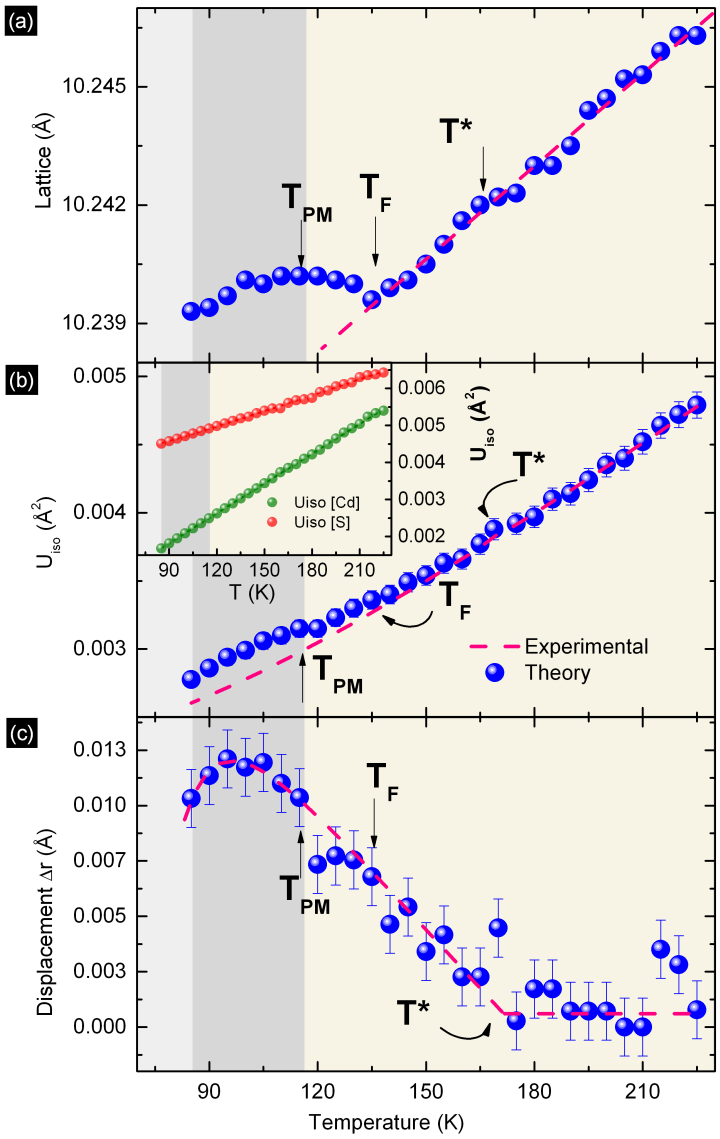

Figure 3.5 – Tendency of PDF output parameters.. **(a)** The temperature-dependent lattice parameters. **(b)** Isotropic ADPs of the Cr atom; inset:Isotropic ADPs of the Cd and S atoms. **(c)** Amplitude of the local Cr off-centering. **(d)** Schematic representation of the local environment of Cr^{3+} as a function of temperature based on our findings.

surements[163]. This finding is consistent with the appearance of random Cr^{3+} off-center displacements that do not break the cubic symmetry at temperatures below T^* [341]. The temperature dependence of the amplitude of the Cr off-centering displacements (Δr) is presented in Fig. 3.5 (c), using Eq. 2.37. A maximum value of 0.012 Å was obtained and is schematically illustrated in Fig. 3.6.

The observed displacement amplitude is one order of magnitude lower than that observed in ferroelectric $BaTiO_3$ [342] (Δr = 0.24 Å and P =~ 30 $\mu C/cm^2$) and the more recently observed value in chalcogenide compounds (PbTe)[341], where off-centering displacements of Pb^{2+} were observed using the same technique. The displacement obtained here is in good agreement with the lower values of polarization observed for

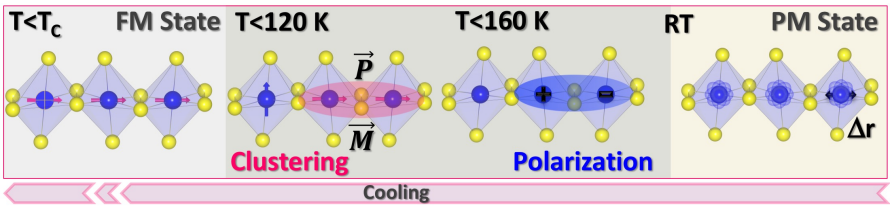

Figure 3.6 – Schematic representation of the local environment of Cr^{3+} as a function of temperature based on this work.

the $CdCr_2S_4$ system (Δr = 0.012 Å and P =~ 0.075 $\mu C/cm^2$)[160].

3.1.3.4 Cr atoms local dynamics

In order to understand the nature of these displacements at the atomic scale we performed PAC measurements, that is an excellent tool to probe and study the phenomena present at a microscopic level.

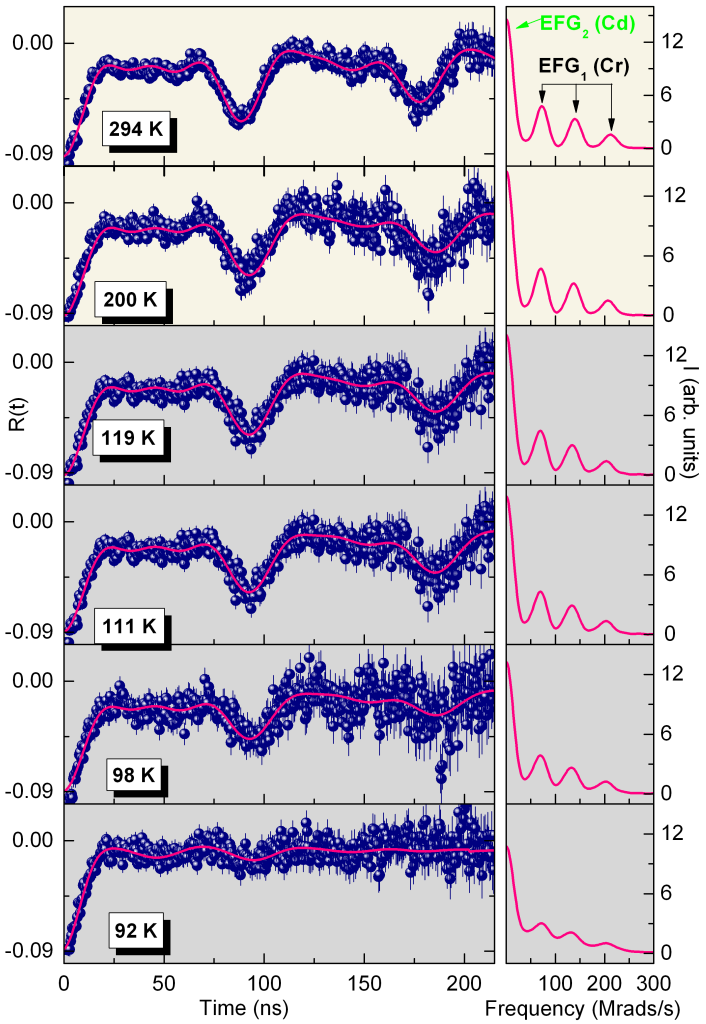

Figure 3.7 – PAC spectra collected at different temperatures.

The experimental $R(t)$ anisotropy function (blue points on the left) and the respective Ft (red lines on the right) as functions of temperature (294 K > T > 92 K) were obtained using the PAC technique and are depicted in Fig. 3.7. Two coexisting local environments were observed from the ^{111}Cd probes at the Cd (30 %) and Cr (70 %) sites (^{111}Cd probe is fed by the ^{111}In radioactive decay [^{111}In$\rightarrow^{111}$Cd]). These results are consistent with a previous work by *Samokhvalov et al.*[122] where the same probes distribution among the Cd and Cr site were obtained. The authors verified that the ratio between the part of probes with non-cubic and with cubic surroundings can be changed by a thermal treatment of the sample. Quenching of the sample in H_2O would freeze the distribution of the probes between two nonequivalent sites (44% A-site and 56% in the Cr-site). However a normal cooling (quench to air) would maximize the percentage of probes in the non-cubic site, *i.e* the Cr site. This was the procedure adopted in our experiments.

The authors, further justify their results based on the comparison between the theoretical (first principles calculations) and experimental electric field gradient and magnetic hyperfine fields values obtained. Additionally, they show the validity of their findings by combining the results of a set of different isotopes. The set of probes have the same PAC intermediate state, therefore giving a sustained background for this claim. In this way, our fits at T > 200 K, included two static EFG distributions. EFG_1 is characterized by an observable frequency, ω_{01} = 68(2) Mrad/s (V_{zz} = 3.6(2)$\times 10^{21}$ V/m^2), and an asymmetry parameter, η = 0.10(5), characteristic of an EFG with a small deviation from axial symmetry as expected for probes at the Cr site[122]. EFG_2 is characterized by an extremely broad frequency distribution with $\omega_{02} \approx 0$ Mrad/s, which is associated with probes at the Cd cubic site. At T < 200 K, the $R(t)$ and Ft plots are visibly altered, particularly between 119 K and 92 K where $R(t)$ becomes increasingly damped as the temperature decreases. This increased damping of the $R(t)$ spectra is attributed to time-dependent interactions[170], *i.e.*, EFG fluctuations within the PAC timescale (1μs> τ > 1 ns; τ - characteristic fluctuation time)[361]. This effect can be modeled by including a dynamic attenuation parameter (λ) in the standard static fit function[361] (as introduced in Eq. 3.4).

Figure 3.8 presents the fit results at different temperatures; the fraction of each EFG, the asymmetry parameter and the fundamental frequency are shown at top, middle and bottom, respectively. Other than the increase of the dynamic attenuation parameter associated with EFG_1 (Cr site), no changes were observed in either EFG.

As shown in Fig. 3.9, the temperature dependence of the natural logarithm of the dynamic attenuation parameter follows an Arrhenius law with an activation energy of E_a = 0.1 eV[362]. The PAC measurements revealed that the Cr site experiences ultra-slow dynamics (τ > 1 ns) in the 92 – 119 K temperature range, while no change was observed in the local environment of the Cd site (the local symmetry remains cubic). These results are in agreement with a model in which the Cr ions hop between equivalent potential energy minima towards an order-disorder-like type phase transition[363] occurring below T_C similarly to what is observed in lead chalcogenides[341]. Additional

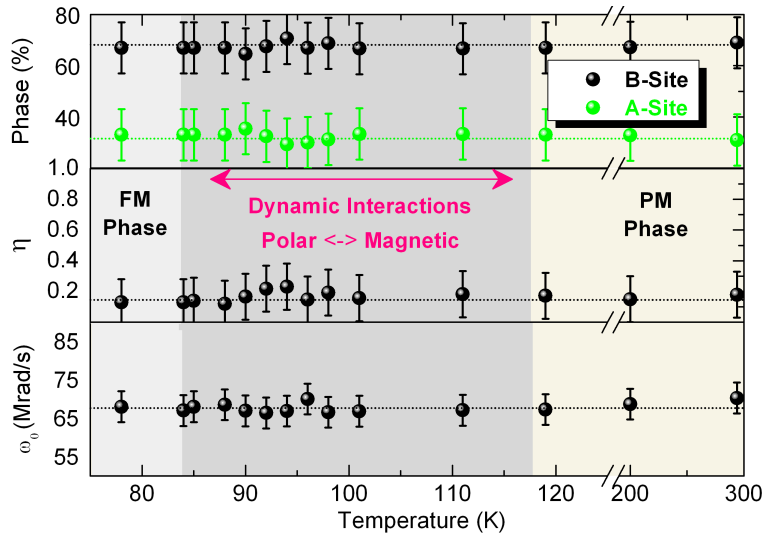

Figure 3.8 – EFG temperature dependent parameters in the $CdCr_2S_4$ system.

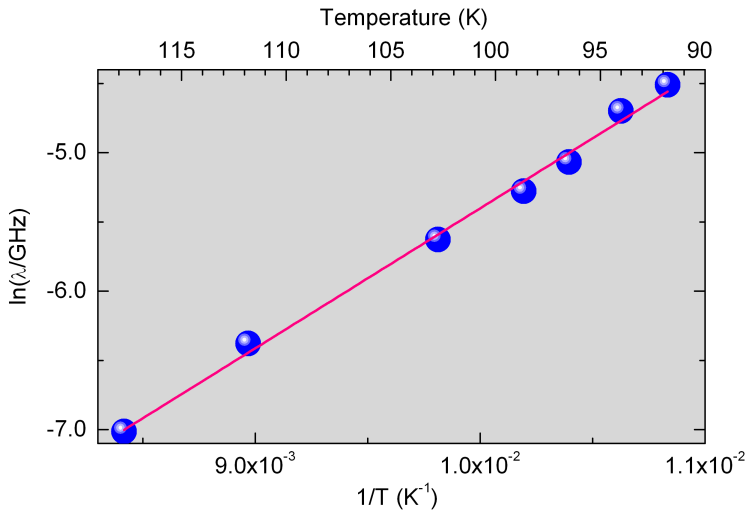

Figure 3.9 – PAC dynamic attenuation parameter characteristic of probes at the Cr site as a function of the inverse temperature.

measurements using the $^{117}Cd \rightarrow ^{117}In$ probe (^{117}Cd probe replaces only the Cd position) corroborate these results (see Fig. 3.10).

Figure 3.10 depicts representative PAC spectra, Fourier transforms and corresponding fits, obtained from RT to 13 K temperature range for the ^{117}Cd probe in the $CdCr_2S_4$ system. Our results (in accordance with previous one[122]) in the 91 K to RT temperature range, paramagnetic state, show only a time independent EFG, characteristic of an A–site substitution. Knowing the A–site has local cubic environment, then a null EFG should be expected. However, experimentally it is common to observe instead a large EFG distribution around zero, like in the present case. Note that, in $T > 91$ K temperature range no changes are observed, in the $R(t)$ spectra. Whereas an "exponential" damping of the $R(t)$ function would be expected if a dynamic interaction was

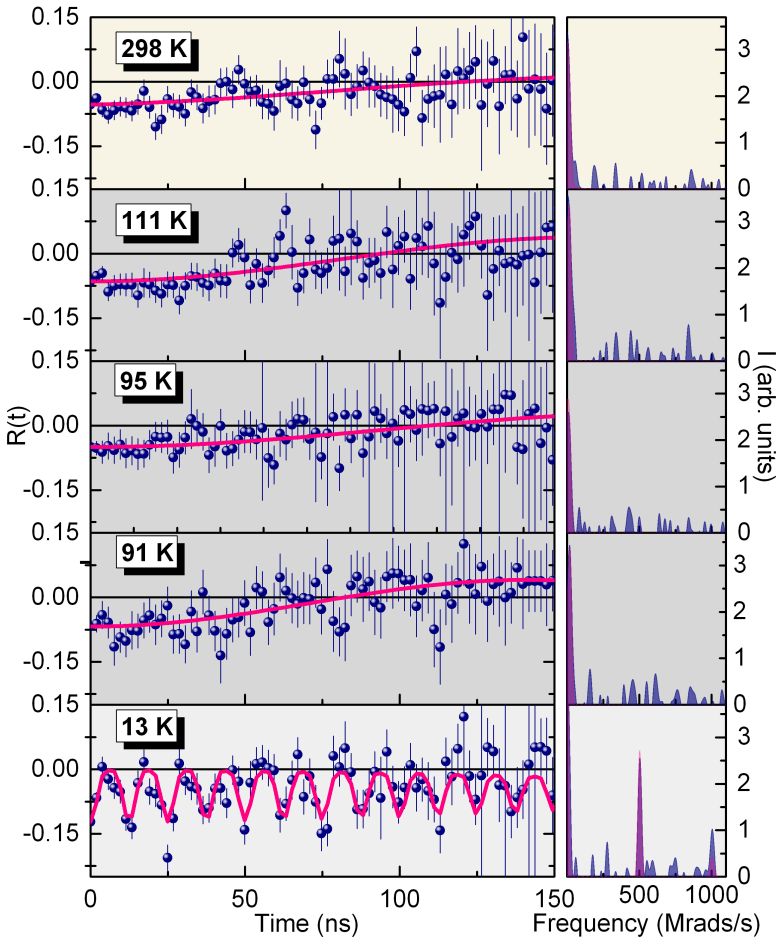

Figure 3.10 – Representative $R(t)$ functions, corresponding fits and respective Fourier transform taken at different temperatures for the ^{117}Cd probe.

present in a certain range of temperatures. Furthermore, the PAC technique is majorly sensitive to nearest neighbors. In this way, Cr and Cd local environment will be mostly affected by the Cr – S and Cd – S bonds respectively. Thus, the absence of changes in the $R(t)$ spectra above T_C points for the fact that no dynamic distortions occur around the Cd site. Therefore, the dynamics distortions observed in the previous results (using the ^{111}In probe) can be exclusively attributed to the B – site. In the ferromagnetic state, as expected[122], the presence of a single magnetic interaction having a high Larmor frequency is observed.

The combined analysis of the PDF and PAC results indicates that the dynamic Cr^{3+} off-center displacements occur well above T_C ($T < T^*$). Furthermore, the average size of the randomly oriented dipoles (formed by the off-centering of the Cr ions) increases as the temperature decreases and saturates at T_{PM} (see Fig. 3.6). The onset of the dynamic slowing-down of these entities is also observed at approximately T_{PM}. These ultra-slow dynamics exhibit the signatures of a phase transition with order-disorder features and eventually result in the recently reported $Fd\bar{3}m$ to non-centrosymmetric $F\bar{4}3m$ phase transition[163]. In fact, a recent LSDA + U calculation suggests that the origin

of the observed relaxor behavior in $CdCr_2S_4$ is distinct from a displacive polar soft mode[119], which was experimentally verified using far-infrared analysis[124].

3.1.3.5 Short Range Magnetic Clusters of Cr atoms

Because the Cr^{3+} ions are magnetic ions, displacements of these atoms should produce macroscopic anomalies in the magnetization properties. In fact, in the very low field measurements (H < 103 Oe), we observed a step-like behavior in the temperature dependence of the reciprocal susceptibility ($\chi^{-1} = H/M$) that has not yet been reported [depicted in Fig. 3.11 (a)]. This step occurs in the temperature range between the ordering temperature $T_C \sim 86$ K and $T_{PM} \sim 116$ K. This feature in the paramagnetic (PM) regime indicates the presence of short-range magnetic clusters (SRMC)[357]. As H increases, $\chi^{-1}(T)$ tends to have only one plateau [see Fig. 3.11 (a)], and the magnetic susceptibility data at $H \geq 100$ Oe shows a trend nearly identical to that of the high-temperature data. Nevertheless, we highlight that even at $T \gg T_C$ and H > 100 Oe, some small curvature in χ^{-1} is still observable, which indicates that a cooperative short-range process is still present up to $T^* \sim 160$ K [see inset in Fig. 3.11 (a)]. These observations are in agreement with the PDF results, which indicate that the Cr atomic displacement seemingly persists up to T^*. Above this temperature, $\chi^{-1}(T)$ enters a nearly linear regime, and an effective paramagnetic moment of $\mu_{eff} = 4.15\ \mu_B$/Cr can be determined [see inset in Fig. 3.11 (a)]. This value is higher than the expected value of 3.87 μ_B/Cr^{3+}(half-filled lower t_{2g} triplet with a spin $S = 3/2$ and $g = 1.984$, as measured by Berzhansky *et al.*[364].), demonstrating the presence of short-range magnetic correlations even at higher temperatures.

In fact, SRMC has been in the origin of exhibited complex magnetic behavior in different materials. *Haines et al.* showed that this was the case in the electronic origin of 3*d* transition metals Fe, Co, and Ni[365]. *Greedan et al.* studying the relatively simple material $LiMnO_2$ observed that crystallographic distortions due to the presence of the Jahn-Teller ion Mn^{3+}, result in a Mn sub-lattice of folded and distorted hexagonal layers that *per se* result in short-range magnetic correlations[366]. $YBaCo_4O_7$, Fe $\gamma - \alpha$ transition, $R_5(Si_xGe_{1-x})_4$ (R = Gd, Tb, Dy, Ho), just to name some, have also shown that SRMO plays an important role in defining their magnetic properties and therefore defining the systems multiferroic properties[367–370].

The observed SRMC are dependent on the magnetic field, which results in different $\chi^{-1}(T)$ slopes that correspond to different magnetic cluster sizes[357]. Applying a Curie-Weiss Law in the $T_C < T < T_{PM}$ region, a $\mu_{eff} = 4.1\ \mu_B$/Cr for H = 103 Oe and 9.4 μ_B/Cr for H = 1 Oe were obtained. This result demonstrates that only a small number of ions are involved in the SRMC, which is in agreement with the correlation length of 5.3 Å obtained from the PDF data (at T = 100 K, where the Cr off-centering has its maximum). This result was obtained by using the method described by *Xiangyun Qiu et al* considering the Cr – Cr(Cd,S) bond lengths[371]. This magnetic effect overcomes the

mysterious behavior previously observed using ESR, for which a polaron-like mechanism was suggested[372]. The atomic displacements of the Cr^{3+} ions lead to correlated polar and magnetic effects in the para-magnetic/electric regime and indicate the presence of a polar-magnetic coupling. Comparing the effect of a magnetic field unveiled by our results and those in ref. 128 (Fig. 2b) one observes that the magnetic and dielectric responses seem to oppose each other, *i.e.* whereas magnetic clustering decreases with the magnetic field, the low-frequency dielectric response is enhanced by it[128]. This result suggests that the Cr ions in a cluster tend to displace towards each other to enhance their coupling at low fields, while larger fields cause the ions to become displaced in a uniform direction, producing an increased dielectric permittivity.

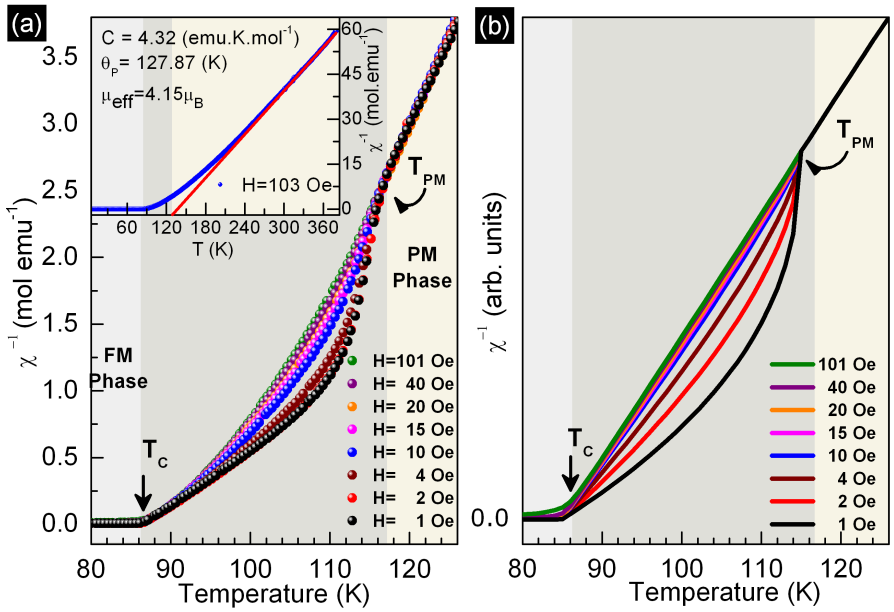

Figure 3.11 – Magnetic reciprocal susceptibility of $CdCr_2S_4$. **(a)** $\chi^{-1}(T)$ at different applied magnetic fields 1 – 101 Oe; **Inset:** $\chi^{-1}(T)$ measured upon heating and with H = 103 Oe. **(b)** $\chi^{-1}(T)$ resulting from theoretical calculations of the phase transitions using the Landau theory, considering a linear magneto-electric coupling.

3.1.3.6 Landau modeling of P-M coupling

In a typical Landau theory free energy expansion (G), (considering the simplest form of magnetoelectric coupling for a multiferroic system with different ordering temperatures for the magnetic (T_C) and electric polarization (T_C') components, under null applied electric field), in powers of magnetization (M) and polarization (P), including magneto-electric coupling terms (αPM) up to the second order (spin-lattice coupling) and ferroic behavior for both order parameters, the free energy is given by:

$$G = \frac{1}{2}A\,(T - T_C)\,M^2 + \frac{1}{4}BM^4 + \frac{1}{2}A'\,(T - T_{PM})\,P^2 + \frac{1}{4}B'P^4 - MH - PE - \alpha PM \qquad (3.6)$$

where A, B, A', B' and α are constants, E is the electric field, T_C is the macroscopic ferromagnetic ordering temperature (86 K) and T_{PM} is the temperature value at which the multiferroic clusters emerge, *i.e.*, the Cr ion distortion is close to its maximum.

By minimizing the free energy in respect to $P(dG/dP = 0)$, we obtain the dependence of the equilibrium value of P on M:

$$P = \frac{\left(27\alpha MB'^2 + \sqrt{108\left(T - T_C'\right)^3 A'^3 B'^3 + 729\alpha^2 M^2 B'^4}\right)^{1/3}}{3 \times 2^{1/3} B'} - \\ - \frac{2^{1/3}(T - T_C')A'}{\left(27\alpha MB'^2 + \sqrt{108\left(T - T_C'\right)^3 A'^3 B'^3 + 729\alpha^2 M^2 B'^4}\right)^{1/3}} . \quad (3.7)$$

Which can then be expressed as an expansion in M, resulting on a modified $-HM$ term,

which acts as an effective magnetic field that is non-zero for $T < T_C'$, resulting in non-zero magnetization values for $T_C < T < T_C'$. This explains the downturn of the inverse susceptibility values at $T \sim T_C'$, which becomes progressively less relevant for increasing external applied magnetic fields. An immediate conclusion from this formulation (Eq. 3.6) is that a non-zero magnetization value for $T_C < T < T_{PM}$ can emerge as a consequence of magneto-electric coupling. The order of the coupling term will affect the general properties of these dependencies, which will be visible in the $\chi^{-1}(T)$ plots when only the terms with a linear dependency on M are considered. Behavior similar to that of the experimental $\chi^{-1}(T)$ is reproduced [see Fig. 3.11 (b)] when simulating with the applied magnetic field values (and $E = 0$). Numerical values for the A and B coefficients were obtained by fitting the Arrott plots of the magnetization data for $H > 1$ kOe. The A' and B' coefficients were chosen to produce ~ 10 μC/cm^2 values of P, as an estimate of the local polarization[128]. The resulting value of the linear magneto-electric coefficient is then $\alpha \sim 1 \times 10^{-2}$ mV/(cm Oe), which is within the typical range of single-phase multiferroics[26]. A similar behavior of the inverse magnetic susceptibility is achieved considering the magnetoelectric coupling term as proportional to P^2M. If the magneto-electric coupling dependence is in higher orders of M, the $-HM$ term of the free energy expansion is unaffected, and so the low-field susceptibility behavior does not reproduce the same characteristic behavior observed in the experimental measurements.

These findings provide evidence for a scenario in which a magneto-electric coupling is present (magnetization↔polarization) and the magnetic and electric anomalies arise from the Cr^{3+} displacement, in accord with our findings. Note that these abnormal reciprocal susceptibility features have also been observed in other compounds that present strong interplay between the lattice and spin degrees of freedom ($R_5[Si, Ge]_4$ and La[Sr, Ca]MO)[357,370,373,374]; thus, a similar analysis may explain these observations.

3.1.4 Conclusions

In summary, our experimental PDF, PAC and $M(T)$ results demonstrate the existence of a dynamic state caused by the presence of simultaneous polar and magnetic nanoclusters, indicating that the system exhibits a birelaxor nature. Our results are consistent with a model in which the effects described in the recent literature arise from atomic displacements of Cr^{3+} ions occurring well above the magnetic ordering temperature. Our combined analysis clearly reveals that the increase in the average size of randomly oriented dipoles saturates at T_{PM}, concomitantly with the onsets of their dynamic slowing and the $Cr^{3+}-Cr^{3+}$ magnetic correlations. Finally, we further demonstrate that an ultra-slow Cr^{3+} displacement dynamics precedes the recently reported $Fd\bar{3}m$ to non-centrosymmetric $F\bar{4}3m$ phase transition, suggesting its order-disorder-type origin. This Cr^{3+} dynamic off-centering is intrinsically entangled with the formation of local dipoles and is also responsible for the observed magnetic correlations between adjacent Cr^{3+} neighbors. We further confirm this coupling of electric and magnetic orders by modeling the peculiar low-field $\chi^{-1}(T)$ measurements using Landau theory with a linear magnetoelectric term. We believe that this is a step forward in understanding the exotic behavior of (bi)relaxor systems and their entanglement with lattice distortions.

3.2 Unveiling the nature of local clusters in $CdCr_2S_4$ through hydrostatic pressure

The results of DC magnetization and X-ray diffraction measurements under hydrostatic pressure are presented for the $CdCr_2S_4$ spinel compound. Magnetization measurements were performed in a polycrystalline sample up to 14 kbar in the $30-220$ K temperature range. At low applied magnetic fields a susceptibility anomalous behavior, associated to magnetic clusters, persists up to 14 kbar. The magnetic transition temperatures T_C and T_{PM} response in the opposite directions but with the same slope, *i.e.* the higher the pressure, the lower the T_C, and the higher the T_{PM}. The x-ray diffraction spectra acquired under pressure show a direct relation between the lattice parameters variation and that of the $Cr-Cr$ distance whereas the angles in the Cr octahedral between Cr and S atoms remain constant. Furthermore, the monotonic X-ray diffraction spectra acquired under pressure reveals the same origin of the observed anomalous susceptibility behavior: an pressure enhanced antiferromagnetic coupling between Cr-Cr. Clearly the $CdCr_2S_4$ magnetic properties are strongly sensitive to pressure variations and the Cr local distortions observed in this compound promote a competition between direct antiferromagnetic and superexchange ferromagnetic interactions within such short-range magnetic clusters. The competition between the superexchange ferromagnetic interaction in the Cr octahedral between Cr and S atoms with the pressure enhanced antiferromagnetism results in the lower T_C under pressure, while the enhanced antiferromagnetic direct exchange in the short-range antiferromagnetic clusters in the

paramagnetic matrix results in the higher T_{PM} (increase of temperature span over which the clusters are observed). For sake of section completeness we review here again the most important aspects from literature relevant for our analysis. This chapter is based on the submitted work: G. N. P. Oliveira, A. M. dos Santos, Z. Gai, G. Halder, J. P. Araújo, A. M. L. Lopes and A. M. Pereira., *Submitted to Applied Physics Letters* (2016).

3.2.1 Overview

Nowadays there is a high demand for materials with multifunctional physical properties. They promise novel applications, especially those which display a strong coupling between magnetic and electric orders, the so-called magnetoelectric.[43,128] A complex interplay between electronic, magnetic, and lattice degrees of freedom is usually at the base of the peculiar properties exhibited by magnetoelectric materials.[128] Consequently promising technologies for magnetic data storage, high-frequency magnetic devices, spintronics, and micro-electromechanical systems are being explored.[43,351]

Among such complex magnetic materials one finds the system ACr_2X_4 spinels (A= Zn, Cd, Hg; X= O, S, Se) with their unique physico-chemical properties.[132,375] In these Cr based systems, the lattice constant increase with the A-site cation radius, leading to a change of the magnetic properties such as a variation Curie-Weiss temperature (θ_{CW}) from negative to positive values due to the enhancement of the ferromagnetic (FM) exchange interactions over the antiferromagnetic (AFM) ones. The same is true when going from the smaller oxides to the larger chalcogenide spinels.[146] This reveals that in ACr_2X_4 family of compounds a strong competition between FM and AFM interactions exist inclusively inducing bond frustration in the oxides.[376,377] Additionally, significant spin-phonon coupling is active in these systems near their magnetic ordering temperatures.[126] For example, in the case of A = Hg and in the AFM state is responsible for the occurrence of a magneto structural transition[146,377]. Finally, a close connection between the local structure and macroscopic electrical polarization is observed for the magnetoelectric members of this family, special for $CdCr_2S_4$.[169,378]

In the ACr_2X_4 spinels, the Cr ion presents a $3d^3$ configuration where the electrons occupy the three lower t_{2g} orbitals in the octahedral site, and an almost complete quench of the orbital angular momentum is observed ($L \approx 0$). Thus, the Cr ion is the only ion that mainly contributes to magnetism. The magnetic properties of these materials result essentially from direct and indirect exchange interactions of Cr^{3+} ions.[121,379] In the case of X = O, the magnetic state at low temperatures is AFM, as the direct overlap of the t_{2g} orbitals dominate (AFM direct Cr^{3+}-Cr^{3+} interaction). Here the superexchange arising from Cr-O-Cr is weak (FM interaction due to 90° between Cr-O-Cr).[376] On the other side the chalcogenide spinels with X=S, where the distance between the Cr^{3+} ions is larger than in the case with X = O, the superexchange interaction becomes stronger, leading to a FM ground state (e.g. $T_C \simeq 84.6$ K in $CdCr_2S_4$).[377]

Hemberger et al discovered a dielectric relaxational dynamics above the Curie tem-

perature (T_C), which was responsible for a strong increase of the dielectric permittivity of $CdCr_2S_4$.[128] Further studies using LSDA+U calculations suggested that the origin of this relaxor behavior was distinct from a displacive polar soft mode,[119] and this assertion was later experimentally verified using far-infrared analysis.[124]

In fact, in our previous work on $CdCr_2S_4$, we found a dynamic off-centering of the Cr^{3+} ions through the combined use of local probe techniques, pair distribution function and perturbed angular correlation. This off-centering fosters the entanglement between the polar and magnetic orders stabilizing, in the paramagnetic phase at $\sim$ 116 K (T_{PM}), in short-range magnetic clusters.[169] These distortions lead to a local symmetry lowering where a local non-centrosymmetric space group sets in ($Fd\bar{3}m$ to $F\bar{4}3m$) supporting a multiferroic behavior. The abnormal thermal expansion behaviour, the broadening of the x-ray peaks and the phonon anomalies at T_F <130 K further suggests that the electronic polarizability is enhanced by the Cr-S bond hybridization and thus supporting this claim.[128,133,159,160,380] More recently *Kitani et al* showed with magnetization under low field and ac susceptibility measurements in the $CdCr_2S_4$ that the ferromagnetic phase showed signs of spin-glass-like behavior, even though it is often regarded as a conventional ferromagnet.[377]

The tight coupling between structural, vibrational, magnetic, and charge degrees of freedom in these materials, makes external pressure an appealing route for tuning $CdCr_2S_4$ physical properties. Measuring the pressure dependence of the magnetic transition temperature will give insights about the ordering mechanism and its relationship to the electronic structure (*e.g.* disordered local moments coupled with frustration mechanisms).[381] In fact, external pressure is an efficient method to control the material's structure and consequently overlap between electron orbitals. A shift and/or split of the energy levels and changes in exchange interaction strength in response to pressure variations does occur.[382] When compared to chemical pressure (sequence of chemical substitutions) external pressure, is a cleaner tool as it avoid substitutional induced disorder and spurious effects due to the use of multiple samples of different compositions. Indeed, several studies report structural and electronic transitions under pressure for various Cr-based spinels.[146,379,382–384] Nevertheless, to the best of our knowledge, studies on the relaxor-like temperature regime are not yet reported.

In this framework, the present study will focus on the pressure effects on the relaxor properties and T_C, correlating the magnetic and lattice degrees of freedom contributing to a comprehensive knowledge of this system properties and in particular on those of the short-range magnetic clusters.

3.2.2 Experimental Details

The $CdCr_2S_4$ polycrystalline sample studied in this work was synthesized using a solid-state reaction in a double evacuated quartz ampoule and its structural and magnetic characterization at ambient pressure was reported in detail in the previous section[169]

(see section 3.1).

The magnetization measurements under pressure up to 14 kbar were performed, while heating, using a clamp-style high pressure cell (BeCu) with a commercial MPMS Superconducting Quantum Interference Device (SQUID). The zero-pressure measurement could not be performed in the pressure cell since a residual pressure has to be applied at all times in order to seal it. Therefore the data used for the zero-pressure was obtained using a sample in the standard loading, in a gel capsule.

The pressure values were determined by measuring the shift of the superconducting transition temperature (in the range of 5 to 7.2 K) of a small piece of lead (Pb) loaded together with the sample. Silicon oil was used as pressure-transmitting medium. One should note that the medium presents a much smaller diamagnetic moment when compared to the sample, and that it is constant with temperature, thus not interfering with the main conclusions of the present work.

The work is focused on the relative variation of the Curie (T_C) and polar-magnetic interaction (T_{PM}) temperatures induced by the external pressure. In order to determine the T_C temperature we have taken the minimum of the temperature derivative of the magnetic susceptibility ($\frac{\partial \chi}{\partial T}$), by fitting the obtained curve with a lorenztian function. In the case of T_{PM}, the second temperature derivative of magnetization was employed to achieve the same purpose. A constant magnetic field of 3 Oe, was applied during all the measurements, and after an initial quenching of the superconducting coils.

The room-temperature high-pressure synchrotron powder diffraction measurements were carried out at beamline 17-BM at the Advanced Photon Source using a 100 μm monochromated x-ray beam at a wavelength of λ=0.727750 Å. Variable pressure diffraction data were collected in situ using a Perkin Elmer amorphous-Si flat panel detector centered on the x-ray beam. The sample-to-detector distance was nominally set at 300 mm, yielding an available 2θ scattering angle of 27.5°, corresponding to access of Bragg reflections with d spacing as low as 1.52 Å. The diffractometer geometrical parameters (such as precise sample-to-detector distance and tilt of the detector) were optimized with respect to a NIST [i] a LaB_6 (660a) standard.

The $CdCr_2S_4$ powdered sample was loaded in a membrane-driven diamond anvil cell fitted with a pair of 800 μm culet diamonds. Gold was added to the sample as a pressure manometer and silicone oil was used as pressure-transmitting medium.

The pressure values were determined by fitting the measured gold unit cell volume to a third-order Birch-Murnaghan equation of state using the parameters V_0 =67.850 $Å^3$, B_{0T} =167 GPa, and B'_{0T} =5.77, where V_0 is the Au primitive cell volume at ambient conditions, B_{0T} is the bulk modulus, and B' is its first pressure derivative.[385,386]

Rietveld refinement using Fullprof software package[347] of the X-ray powder diffraction were performed to determine the sample's crystallographic structure and lattice parameters under applied pressure.

[i] National Institute of Standards and Technology.

3.2.3 Results and Discussion

3.2.3.1 Pressure effects on T_C and T_{PM}

The magnetization over magnetic field curves as a function of temperature ($\frac{M}{H}(T)$ curves) under different applied hydrostatic pressures (ranging from 0.0 to 14 kbar) are displayed in Fig. 3.12. These curves measured under high pressures exhibit the similar behavior to those measured at ambient pressure, as they all show two features, one consistent with the FM transition, and at higher temperature the deviation from the CW curve that is ascribed to the cluster formation at T_{PM}. For zero pressure, at $\sim$ 85 K the system undergoes a second order transition from a paramagnetic (PM) into a ferromagnetic (FM) state. When analyzing the pressure effect, one can clearly identify two main features: a decrease of T_C and a decrease of magnetization magnitude ($\frac{M}{H}(T)$) with increasing pressure.

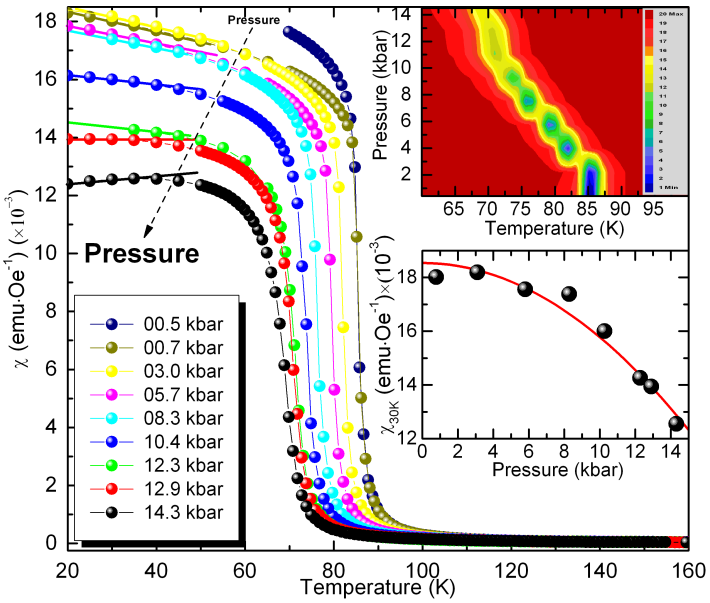

Figure 3.12 – Magnetic susceptibility curves at different applied pressures. Solid lines between 20 and 50 K are guides for the eyes. Upper inset: Contour plot of temperature derivative of susceptibility ($\frac{\partial \chi}{\partial T}$). Lower inset: Magnetization at 30 K at different applied pressures (The continuous line represent a $\chi_{30K} = \alpha[1 - |P/P_0|^2]$ fit to the data points, with α = 0.019(2) emu Oe^{-1} and P_0 = 26(1) k bar).

The evolution of T_C, towards low temperatures with pressure increase is well patent in the contour plot representation of the first derivative of the magnetization data (see Fig. 3.12 upper inset).

Portrayed on the lower inset of Fig. 3.12 is the $\frac{M}{H}$ value taken at 30 K for the different applied pressures. A magnetization significant reduction of about 33% can be observed when reaching a pressure of about 14 kbar. Since the magnetic field was kept constant for all measurements, the magnetization loss is an intrinsic magnetic effect and not an artifact due to the experimental procedure (H = *const* during all measurements). Additionally we observe that below T_C, specifically between 20 and 50 K, the $\frac{M}{H}(T)$ curves

slope varies from negative to positive, with increasing pressures. The negative slope (characteristic of FM) is observed for pressures $\lesssim$12.5 kbar, whereas a change to a positive one (characteristic of AFM) is observed for pressures $\gtrsim$12.9 kbar. Due to the pressure rating of this cell we were not able to further increase pressure to further verify this trend.

A possible explanation for the observed results near T_C can be given by considering the exchange interactions responsible for the magnetic behavior in spinels, in particular, the competition between FM/AFM interactions. Indeed, in the cases where two different interactions are present, T_C can be defined as:[387]

$$T_C = \frac{2}{3}\frac{S(S+1)}{k_B}\left(z_2 J_{FM} - z_1 J_{AFM}\right) \ , \tag{3.8}$$

where S is the spin, k_B the Boltzman constant and z_i the number of corresponding neighbors. Thus, increasing pressure, J_{AFM} will increase or/and J_{FM} will decrease leading to a decrease of T_C as observed. Previous experimental high-pressure magnetic studies on spinels (*e.g.* $HgCr_2S_4$), showed strong competition between FM and AFM exchange.[146,379] This is further supported, by several studies in other spinels ACr_2X_4 (A= Zn, Cd, Hg; X= O, S, Se) showing that strong competition between FM/AFM interactions is responsible for the evolution of θ_{CW}/T_C values. These studies also set a strict relation to the cell parameters evolution (A, X atomic sizes).[121,133,146,379,388]

In fact, the strength of the magnetic interactions can be followed by studying the evolution of the Curie-Weiss temperature with pressure extracted from $\frac{H}{M}(T)$ (see Fig. 3.13). Extrapolating from these data, it can be seen that, above 16 kbar one can expect an inversion sign of θ_{CW}, consistent with the AFM interaction, thus being in accordance with the slop change below T_C in the $\frac{H}{M}(T)$ data.

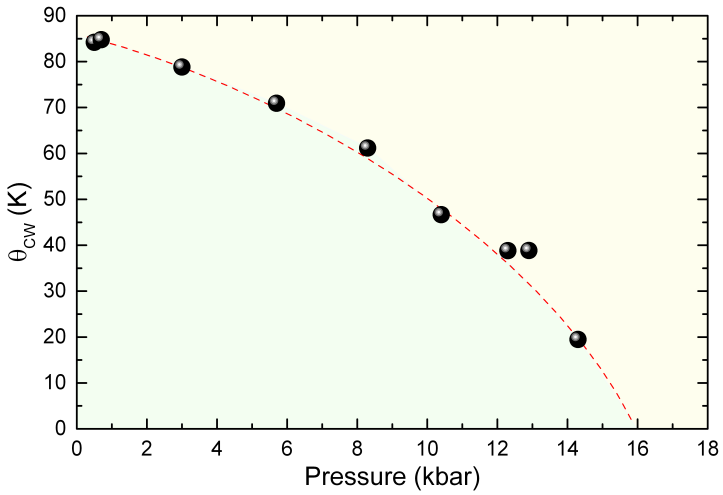

Figure 3.13 – Curie-Weiss temperature as a function of pressure. Dashed line is a guideline for the eyes.

Regarding the anomalous behavior in the magnetic reciprocal susceptibility around

116 K, arising from Cr^{3+} local displacements,[169] the magnetic measurements under applied pressure still exhibit similar anomalous behavior near T_{PM} (step-like behavior), as at ambient pressure (see Fig. 5a of ref. 169).

T_{PM} value and its broadening is best observed by analysis of the second derivative of magnetic susceptibility (see Fig. 3.14).

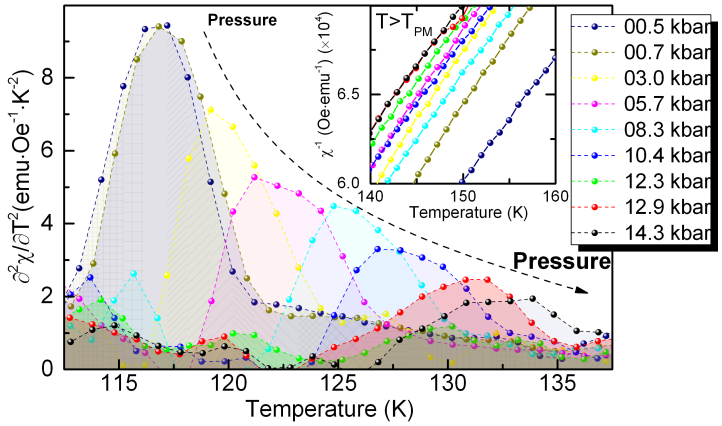

Figure 3.14 – Second temperature derivate of magnetic susceptibility as a function of temperature. inset) Reciprocal susceptibility under selected values of pressure.

A decrease of $\frac{\partial^2 M/H}{\partial T^2}$ magnitude and a shift of its peak (T_{PM}) towards high temperatures is evident as the pressure value increases in contrast with T_C. In the previous section (see section 3.1), we have shown that this step like behavior was due to short-range magnetic clusters[169] that were present at very low magnetic field, but are undetectable by the application of even moderate ones (> 100 Oe), while T_{PM} remained constant. With pressure the T_{PM} value changes evidencing that a different mechanism is in place. The present results, seems to indicate that pressure is tuning the magnetic correlations within the clusters.

Based on these observations a phase diagram can be assembled and is depicted in Fig. 3.15. When increasing the pressure a linear decrease in T_C value is accompanied by a linear increase in the value of T_{PM}.

The pressure derivative of the Curie temperature ($\frac{\partial T_C}{\partial P}$) was found to be negative, with a value of -1.15 $Kkbar^{-1}$. This value is in agreement with the one previously reported in literature (-0.83 $Kkbar^{-1}$) both in signal (negative, characteristic of ferromagnets) as in magnitude.[121,384,389]

Furthermore, it is interesting to note that T_C and T_{PM} change at approximately the same rate ($\left|\frac{\partial T_C}{\partial P}\right|$ =1.15 $K\,kbar^{-1}$ $\approx$ $\left|\frac{\partial T_{PM}}{\partial P}\right|$ =1.13 $K\,kbar^{-1}$, supporting the idea that the same mechanism is responsible for both phenomena. That being the case, that would mean that a strengthening of the J_{AFM} is behind this inverse evolution of these characteristic temperatures, contributing in a similar manner.

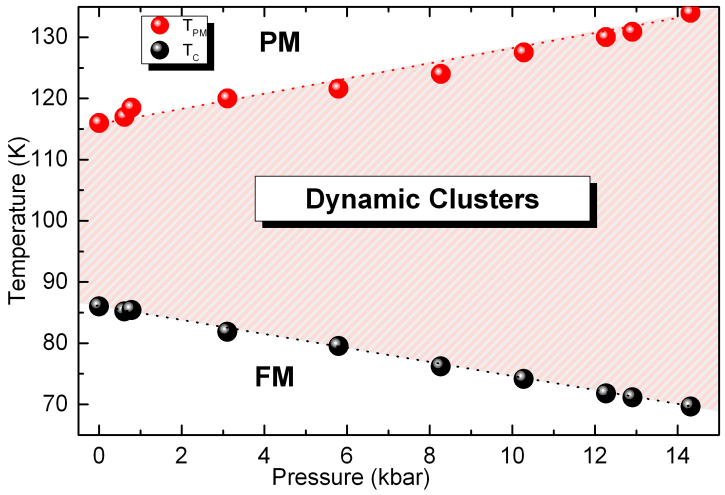

Figure 3.15 – Phase diagram for T_C and T_{PM} as a function of pressure. PM, DC, FM stands for paramagnetic, dynamic clusters and ferromagnetic, respectively.

3.2.3.2 Pressure effects on structure

Since the clusters arise from the Cr displacement[169], our results suggest that the magnetic interactions between Cr – Cr within the clusters are governed by J_{AFM} being reinforced with the pressure. Thus the presence of such clusters is observed at higher temperatures with pressure increase. In order to support this scenario, pressure dependent X-ray diffraction data was acquired at room temperature.

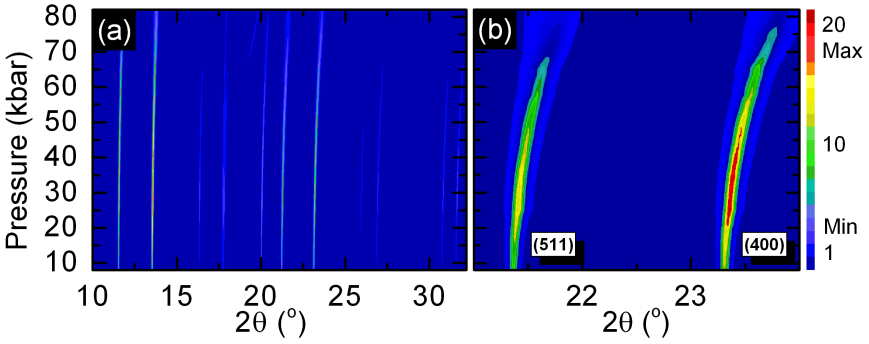

Figure 3.16 – **(a)**: Contour plot of the x-ray diffraction data as a function of pressure. **(b)**: Detailed 2θ from 21 to 24°of the X-ray diffraction data.

A contour plot representation of the X-ray diffraction spectra as a function of pressure in the $10^o < 2\theta < 32^o$ range is represented in Fig. 3.16 (a). In a first inspection of the results a shift of the peaks towards higher angles with increasing pressure is clearly evident (as expected due to the reduction of the cell parameter). As an example this evolution can be better observed in Fig. 3.16 (b) where the peaks corresponding to the (511) and (400) reflections are plotted in more detail.

The synchrotron high resolution X-ray diffraction pattern measured at room temperature and zero applied pressure revealed that the sample crystallizes as a cubic $Fd\bar{3}m$ spinel with a lattice constant of a_0 = 10.2425(5) Å (spectrum not shown). This result was

used as a starting point to the Rietveld refinement which was performed in all spectra obtained under applied pressure.

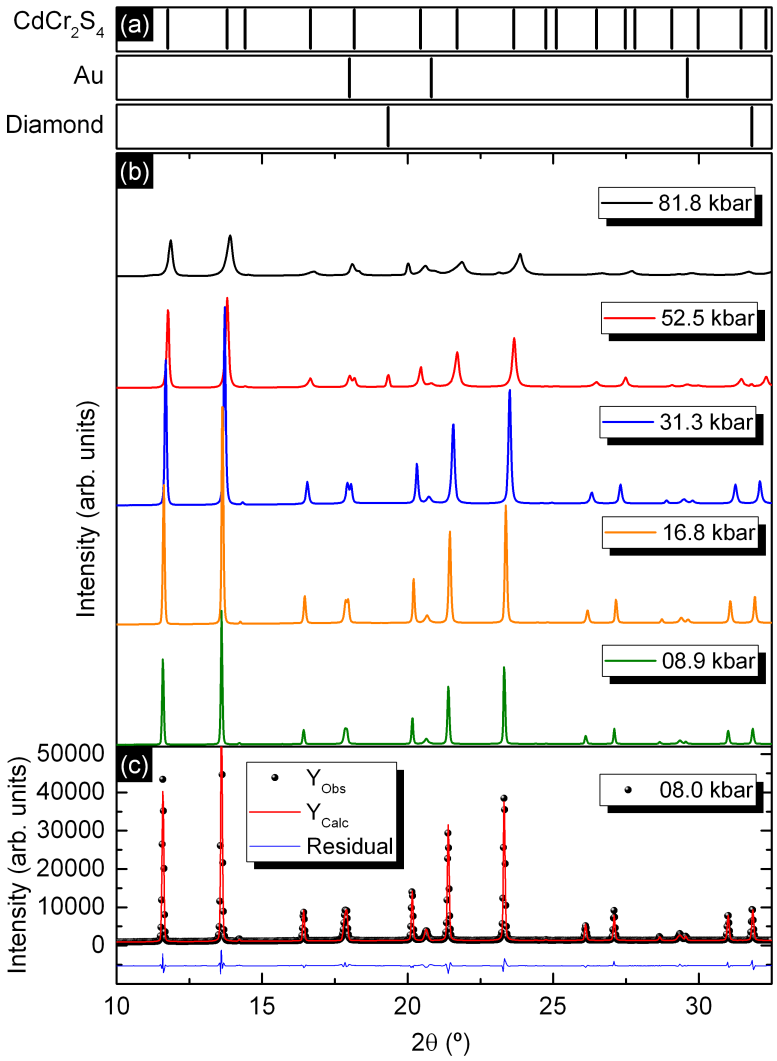

Figure 3.17 – **(a)** Bragg reflections for $CdCr_2S_4$, Au and Diamond phases, respectively. x-ray diffraction spectra acquired at 81.8, 52.5, 31.3, 16.8 and 8.9 kbar. **(b)** x-ray diffraction Rietveld refinement output of the spectrum at room temperature and 8.0 kbar with spinel $CdCr_2S_4$, Au and Diamond structures. **(c)** Experimental pattern (•), fit curve (_) and residual difference (_).

In Fig. 3.17 (a) are represented the Bragg reflections corresponding to the different phases present in (or near) the sample. Note that the diamond anvil cell (111) single crystal reflection appears only at the highest pressures. In Fig. 3.17 (b) are represented illustrative x-ray diffraction spectra obtained under applied pressure. In Fig. 3.17 (c) is represented the Rietveld fit output for the spectrum measured at 8.0 kbar.

The Rietveld profile fitting results of the spectrum in the studied range of applied pressures, showed that while the expected unit cell volume reduction is clearly observed, no space group change is detected (Fig. 3.18 (b) left scale). The obtained parameters from the structural refinements (Rietveld refinement fits) are summarized in table 3.2.

To verify the system symmetry constrains, we have studied the lattice parameter (*a*),

Table 3.2 – Summary of obtained structural parameters and atomic positions for $CdCr_2S_4$ system at room temperature at selected pressures.

Pressure (kbar)		0	8.0	31.3	81.8
Space Group			$Fd\bar{3}m$		
a (Å)		10.2425(5)	10.2100(6)	10.1319(1)	9.9995(8)
V (Å^3)		1074.54(3)	1064.35(1)	1040.09(7)	999.87(5)
ρ (g/cm^3)		4.196	4.284	4.299	4.342
$d_{Cr...Cr}$		3.621(9)	3.609(8)	3.582(2)	3.535(3)
S-Cr-S (1) (^{o})		97.270	97.266	97.075	96.340
S-Cr-S (2) (^{o})		82.73	82.24	82.45	83.28
Cd	Biso (Å^2)	0.942	1.658	1.253	0.714
	Occ	0.041	0.041	0.041	0.043
Cr	Biso (Å^2)	0.670	1.042	0.404	0.268
	Occ	0.080	0.079	0.077	0.078
S	x, y, z	0.2645(6)	0.2654(7)	0.2650(7)	0.2635(3)
	Biso (Å^2)	0.875	1.918	0.902	0.826
	Occ	0.166	0.166	0.164	0.160
χ^2 (%)		4.15	8.38	18.8	42.6
N^o Reflections		151	22	22	30

Atomic positions: Cd: 8a (⅛, ⅛, ⅛); Cr: 16b (½, ½, ½); S: 32c (x, y, z)

distances between adjacent Cr atoms and angles between S – Cr – S as a function of applied pressure, which are plotted in Fig. 3.18, left and right scale and inset respectively.

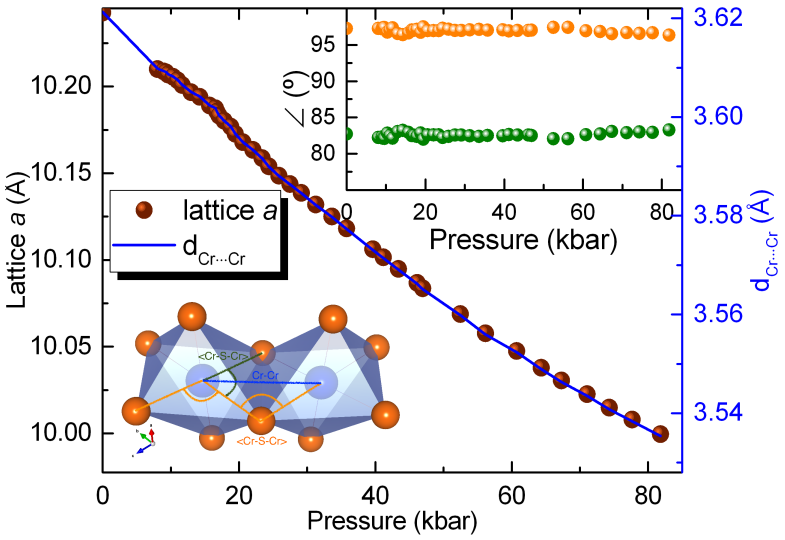

Figure 3.18 – Lattice parameter a (left scale), distances between adjacent Cr atoms (right scale) and the ∠S – Cr – S inside the Cr octahedral environment (inset) as a function of pressure obtained from the XRD pattern fit.

Since no change in symmetry is observed, the Cr – Cr distance follows monotonically the lattice contraction, with the bond angle remaining unchanged. These findings are consistent with the picture where the observed changes in the magnetization data are due to the strengthening of the AFM, within the AFM/FM competition, as the crystallographic analyses show no changes in the ∠CrSCr angle and a Cr – Cr distance reduction with pressure increase.

Assuming that no symmetry breaking is induced with pressure, the applied pressure would lead to a shortening in the Cr – Cr distances, conserving the ∼90° superexchange

interaction Cr^{3+}-X^{2-}-Cr^{3+} angle leading to a strengthening of J_{AFM}.

One can comprehend the effect if we consider that for large distances between Cr^{3+} ions, a strong FM behavior is observed, governed by a dominant 90° Cr^{3+}-X^{2-}-Cr^{3+} ferromagnetic superexchange interaction (J_{FM}). Conversely, when the distance between the Cr^{3+} ions decreases, the overlap of t_{2g} bands from Cr-Cr becomes considerably stronger and the AFM behavior is enhanced.

In a first approach our results point to a similar picture where AFM correlations are strengthened when compared to the FM ones.

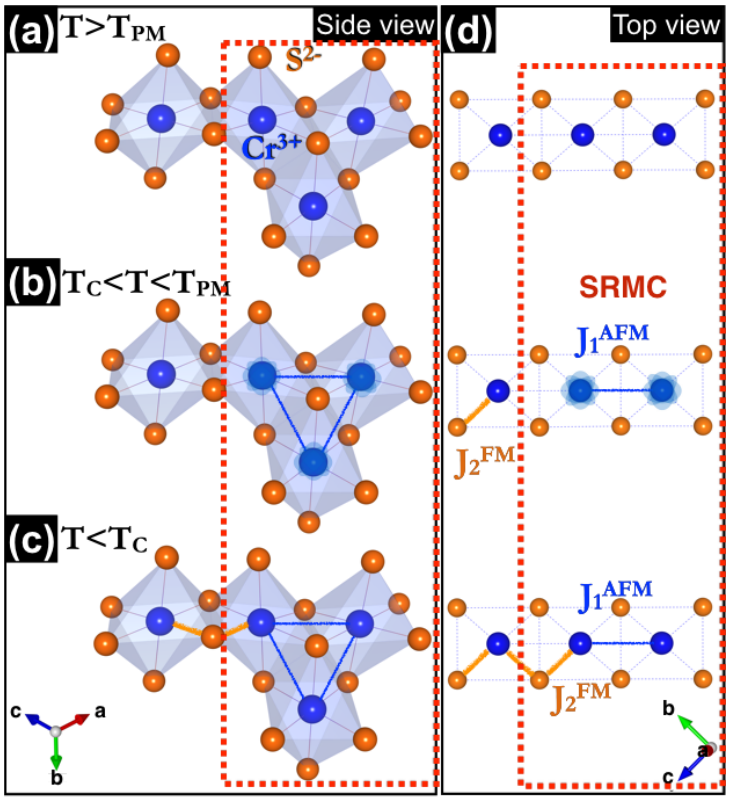

Figure 3.19 – Detailed schematic representation of the CrO_6 octahedra, where the important exchange interactions between Cr^{3+} are evidenced in the different temperature ranges. Above T_{PM} the sample is in the paramagnetic state. Between T_{PM} and T_C the antiferromagnetic interactions inside the magnetic clusters. Below T_C, both J_{FM} and J_{AFM} interactions. Direct antiferromagnetic exchange J_{AFM} (blue lines) and ferromagnetic superexchange J_{FM} (orange lines)

This competition induces a temperature shift of the magnetic order *i.e.*, a reduction in the T_C value. In Fig. 3.19 a schematic representation illustrates the possible evolution of the exchange interactions with temperature herein discussed. Our x-ray diffraction data taken under pressure, show that a small variation of volume (~ 1%) corresponding to a variation of the $d_{Cr–Cr}$ distance ($\Delta d_{Cr\text{-}Cr}$ =0.0131~0.3%) is enough to enhance the AFM interactions as the ones driven by direct proximity.

3.2.4 Conclusions

In conclusion, our results suggest that the magnetic properties of $CdCr_2S_4$ can be tuned by the application of pressure resulting in an enhancement of J_{AFM}. Despite the opposite response in T_C and T_{PM} the underlying operating mechanism seems to be correlated. We believe that the magnetic clusters in this compound develop from J_{AFM} interactions among Cr^{3+} spins. Approaching T_{PM} from a higher temperature, the Cr^{3+} displacement promotes the formation of short range magnetic clusters which are antiferromagnetic in a paramagnetic matrix. With pressure increase the distances between the Cr ions are reduced and the antiferromagnetic direct exchange increases and T_{PM} shifts toward higher temperatures. Between T_{PM} and T_C we observe an competition between J_{AFM} and J_{FM}, in which J_{FM} overcomes the J_{AFM} at T_C.

Thus, in order to have an overall picture of the mechanism that are playing rule here, measurements of pressure diffraction patterns for low temperature and transport properties under applied pressure should be performed to fully understand also the electronic mechanism. These studies are envisaged for a future opportunity. However, in this chapter we were able to demonstrate that spin-lattice coupling in $CdCr_2S_4$ is strong which is an important factor to the multiferroic properties and strong magnetoresistance observed in this material.

CHAPTER 4

Local Symmetry Lowering in $CdMn_2O_4$ spinel

In this chapter it is presented an atomic scale study of the electric field gradient (EFG) in the tetragonally distorted $CdMn_2O_4$ spinel manganite. The EFG temperature dependence at the Cd and Mn sites was followed via perturbed angular correlation measurements with the ^{111}In and ^{111m}Cd probes, from 873 down to 12 K at Isolde-CERN. The results show that in the 12 – 600 K temperature range a single Jahn-Teller distorted local phase exists. However above 100 K, a dynamic lattice distortion, evidenced by time dependent EFG fluctuations sets in, suggesting a structural instability. Above 600 K a local MnO_6 octahedra with relaxed Jahn-Teller distortions emerge and grow in the low temperature matrix, although no macroscopic tetragonal to cubic phase transition was observed. For sake of chapter completeness we review here again the most important aspects from literature relevant for our analysis. This chapter is based on the published work[390]: G. N. P. Oliveira, R. Teixeira, T. M. Mendonça, M. R. Silva, J. G. Correia, A. M. L. Lopes, and J. P. Araújo, *Journal of Applied Physics* 116, 223907 (2014).

4.1 Overview

A substantial research effort has been employed in order to understand the physical properties of the 3*d* transition-metal oxides, in particular those of the spinel type (*e.g.* spinel oxides AB_2O_4)[165]. The continuous scientific and technological interest which has been devoted to them has resulted in many important applications in electronics, optics, magnetic, catalysis, energy storage and conversion[166].

Alongside with the interesting applicability, these materials provide a fertile playground for fundamental physics where (the potential) frustration, local distortions, local range order and dynamic mechanisms are yet to be fully understood (*e.g.* in $CdCr_2O_4$, $CdCr_2S_4$, Sr_2RuO_4)[132,167–170]. Moreover, the distribution and valencies of the metal ions in the spinels are of great importance, therefore under the spotlight, for the interpretation of the magnetic, electric, and crystallographic properties of these materials[167,168].

In particular, manganite spinels AMn_2O_4 represent such multifunctional materials

in which the tuning of the quantity and the chemical identity of A^{2+} permits to reach a wide range of properties[171]. These spinels belong to a family of compounds which are isomorphous with the mineral hausmannite (Mn_3O_4), characterized by a full replacement of the Mn^{2+} ions on the tetrahedral sites by Zn^{2+}, Mg^{2+} or Cd^{2+} ions accompanied by large tetragonal distortions[172].

More particularly yet, $CdMn_2O_4$ spinel was found to be an excellent candidate for being used as an active component in highly sensitive mixed potential electrochemical sensors of oxygenic gases such as NO_x[174–178].

The $CdMn_2O_4$ crystal structure can be described as a tetragonal spinel with only diamagnetic cations (Cd^{2+}) on tetrahedral A–sites and magnetic Mn^{3+} cations on the distorted octahedrally coordinated B–sites (normal spinel) with space group $I4_1/amd$ and $c/a \sim 1.6$ [Fig. 4.1 (a)][185].

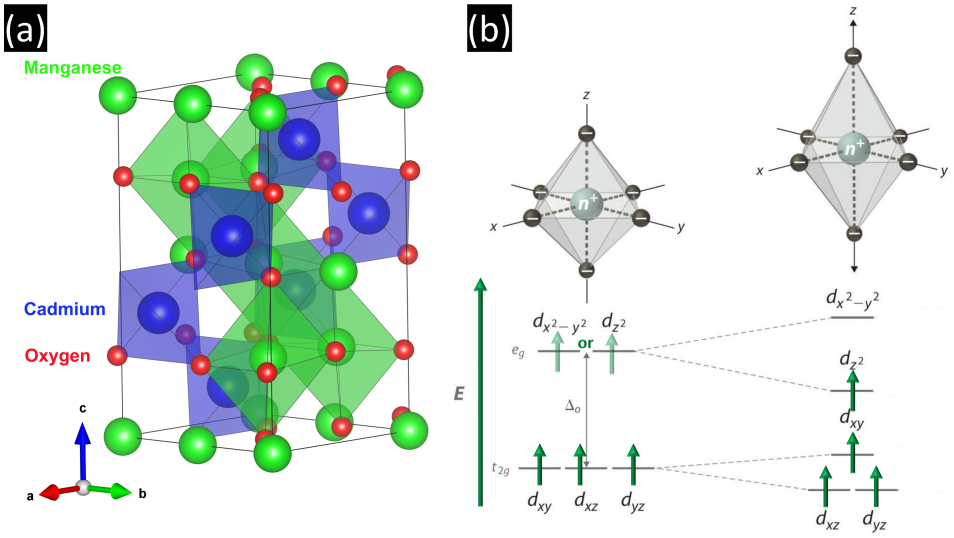

Figure 4.1 – **(a)** Polyhedron model of the $CdMn_2O_4$ structure. **(b)** Illustration of tetragonal distortion (elongation) for an octahedral complex.

The tetragonal distortions are caused by the Jahn-Teller (JT) instability of the Mn^{3+} (d^4) ions[165]. Whereas the divalent A–site cation has a fully filled shell and, thus, it is JT inactive, the trivalent B–site (Mn^{3+} cation), is not. The Mn^{3+} cation has four d electrons and since they are surrounded by six oxygen atoms in the center of the octahedral sub-lattice, the five degenerate 3d orbitals split into three t_{2g} orbitals and two e_g orbitals. Three electrons out of these four occupy the three t_{2g} orbitals with spin up, respectively. As result of the effective exchange energy (J_{eff}) being larger than the crystal field strength, the fourth electron occupies one of two e_g orbitals with spin up. Since the e_g levels are partially filled, the system can lower its energy if the degenerate levels are split by lattice distortions making the Mn ion JT active. In this way, the system will lower the crystal symmetry from cubic to tetragonal, in order to compensate the energy gain equal to one-half of the JT splitting energy (see Fig. 4.1 (b)). However, the energy splitting of t_{2g} orbitals, does not contribute to the energy gain in d^4 systems because the

center of gravity is conserved.

In the majority of the cases, the structural distortion can be controlled in some extent by suitable parameters, *e.g.*, the substitution of A or B site cations,[173] and it is known that the JT effect increases with increasing size of the A – site cation[165].

In the last decade many studies have been dedicated to deepen the understanding of the JT effect and its role in the distortion effect in spinel manganites.

These studies included the measurement of the *JT* splitting by X-ray absorption spectroscopy (XAS)[165] in AMn_2O_4 (A =Zn,Mg, and Cd) as well as the suppression of Jahn-Teller distortion in the case of the $LiMn_2O_4$ particles[179]. In addition, high pressures have been used to study the parallelism between lowering the temperature and increasing the pressure and their effect in inducing a transition to another tetragonal phase, as a consequence of the increase of the Mn occupation at tetragonal sites[180]. The importance of these phenomena is highlighted in recent literature[181,182].

The work of *S. K. Dey et al.*[183] opened already a pathway in comprehending the physical properties observed in $CdMn_2O_4$. Two important aspects found between 600 – 700 K were evidenced in that work: a broad discontinuous peak on differential thermal analysis curves and a deviation from linearity on the magnetic susceptibility measurements. These reported anomalies were, in a final way, ascribed to a crystallographic phase change.

The literature shows several spinel families where it is possible to observe a high temperature phase transition, which is usually connected to the sample's oxygen stoichiometry change[186–192]. However, this has not been observed in $CdMn_2O_4$. In $MgMn_2O_4$ and $ZnMn_2O_4$ systems[193,194] a JT- distortion and a cubic to tetragonal transition was reported at high temperatures (> 1000 K). Also, in some spinel, it was observed a local symmetry lowering at high temperatures. Here the point symmetry of some sites is subjected to modifications and these local structural instabilities can be observed in the form of anomalies in macroscopic properties[169,170,195].

Considering these ideas, it becomes desirable to carry out additional investigations, specially with the help of nanoscale characterization techniques, to further examine locally the crystallographic, magnetic and electric structure properties of these spinel systems. In this context, hyperfine methods such as perturbed angular correlation (PAC) spectroscopy are of the highest relevance. In fact, information on structural properties such as lattice transformation and/or distortion can be extracted by studying the electric field gradient (EFG) tensor obtained from the nuclear quadrupole hyperfine interaction. The EFG in the vicinity of the probe atom, which is due to asymmetries on the local charge distribution, allows to reconstruct the atomic and electronic environment of the atomic probe in the material. Furthermore, PAC has given proofs to be a valuable technique to study this kind of local anomalies[169,170,352].

The aim in this chapter, is to provide new data, which will assist in clarifying the nature of the previously observed anomalies and relate them with the magnetization behavior, Jahn-Teller distortion and the possible structural phase transformation observed in the

$CdMn_2O_4$ system[165,172,183,185].

4.2 Experimental Details

The polycrystalline sample of $CdMn_2O_4$ studied in this work has been prepared by a standard solid-state reaction method where stoichiometric amounts of CdO and Mn_2O_3 powders were mixed, grinded, pelletized and sintered at 1173 K for 20 hours in air. In order to check the sample properties, structural and magnetic characterization was performed after the sample preparation. The x-ray powder diffraction pattern was collected using a Bruker D8 Discovery diffractometer with Cu Kα radiation at room temperature (RT) and 820 K in a $10^\circ < 2\theta < 74^\circ$ range. Magnetic susceptibility measurements in the 5 – 350 K temperature range, carried out using a commercial superconducting quantum interference device (SQUID) magnetometer, were performed under an applied magnetic field, H = 100 Oe, using the zero-field-cooling (ZFC) and field-cooling (FC) procedures (see section 2.3.2).

PAC spectroscopy has been applied to study the atomic scale properties of this compound. To perform the EFG measurements, meaning $\gamma-\gamma$ PAC measurements[292], the sample was implanted with ^{111m}Cd ions [^{111m}Cd$\rightarrow{}^{111}$Cd, $t_{1/2}$= 49 minutes] or ^{111}In ions [^{111}In$\rightarrow{}^{111}$Cd, $t_{1/2}$ = 2.8 days] (same PAC probe state with I = 5/2 and Q = 0.77(12) b) with a small dose of 10^{11} atoms/cm^2 (dose lower than 1 ppm of the Cd/Mn concentration) and 30 keV energy at the Isolde-CERN facility.

In both cases the measurements were performed using the same intermediate nuclear state of the PAC probe (245 keV ^{111}Cd state) fed either by the 396.2 keV ^{111m}Cd or 416.6 keV ^{111}In decay. In the ^{111}In particular case this process occurs through electron capture (EC) of an electron from the probe K shell. An electron-shell recombination follows the EC decay and leaves the probe in a highly ionized state.

Normally, the inner electron shells are filled in a very short time (t < 10^{-14} s) leaving the PAC spectra unaffected[391]. Nevertheless, in some specific cases as in insulators and wide band gap semiconductors, the recovery rates of the outer shells and their nearest neighbor ions towards the equilibrium electronic configuration can be of the same order of the PAC time scale (10^{-9} – 10^{-6} ns). This slow re-arrangement of the probe and neighborhood atom's to a final stable configuration (so-called after-effects, AF) can, sometimes, affect the experimental PAC function. Due to delayed electron-shell recombination transient EFG's might then be observed in the PAC spectra and this situation could be described by time-dependent hyperfine interactions, in particular, described by a unidirectional relaxation process[391,392]. In this case, a stochastic transition from an initial "unfilled" state to a final stable one after electron recombination would be expected. The initial state would be described by a strongly damped EFG distribution whereas the final one by an unperturbed EFG. This would lead to a reduction of the PAC spectra amplitude for times longer than a few ns. Slow relaxation of trapped

electronic defects have been observed in La_2O_3, Cr_2O_3, ZnO[391,393–395] and other wide band gap semiconductors ($\Delta E > 3$ eV) due to low availability of charge carriers in the host matrix[395].

To exclude the existence of after-effects in our $^{111}In \rightarrow ^{111}Cd$ spectra measurements using ^{111m}Cd probe were performed. After-effects cannot be observed in ^{111m}Cd PAC spectra due to this probe metastable nature.

In the case of the studies with the ^{111}In parent probe, the results were also complemented by measurements performed in Lisbon at CFNUL where the ^{111}In was introduced in the sample by diffusion process. The process was carried out by wetting the sample in a ^{111}In activated solution. To fully recover from implantation damage the sample was annealed for 20 min at 973 K in air (in the case of the implantation process) and 1 hour at 973 K in air (in the case of the diffusion process). PAC measurements performed in the 873 – 12 K temperature range were carried out on a 6-BaF_2 detector spectrometer[294] or in a 4-BaF_2 detector spectrometer (in the case of the diffusion procedure).

In this way, PAC experimental anisotropy function $R(t)$ is measured, containing information about the EFG tensor at the Cd and Mn sites, which can be fitted by performing a numerical diagonalization of the interaction Hamiltonian. A more detailed description has already been given in subsections 2.5.1 and 3.1.2 or can be further pursued in Refs. 292,352,354,396.

4.3 Results and Discussion

4.3.1 Crystal Structure of $CdMn_2O_4$

The sample's crystallographic structure and lattice parameters have been fully checked and refined by means of x-ray powder diffraction (XRD) taken at RT (300 K) and 820 K. A Rietveld refinement of the spectra using Fullprof software[347] was performed. The resulting normalized spectra are presented in Fig. 4.2.

The fit solutions shows that the sample, more specifically the $Mn^{3+}O_6$ octahedra, is strongly tetragonally distorted from spinel structure (as reported in refs. 185,397,398) with a, b = 5.811(1), c = 9.794(1) and c/a = 1.685 in the space group $I4_1/amd$. A small impurity contribution of CdO was also found on the XRD spectrum ($\sim$ 5(2)%). The XRD spectrum acquired at 820 K was refined with similar parameters (space group, lattice parameters, atomic positions, *etc.*) to those of room temperature and only a slight increase in the lattice, atomic vibration parameters and CdO (200) plane reflection was observed. The increase in those parameters is attributed to temperature effects. No macroscopic phase transition could be observed. However, we cannot rule out the possibility of local symmetry change from tetrahedral to cubic with no collective effect[169] or even the existence of a JT distortion relaxation[181]. Albeit, a JT distortion was observed by means of soft X-ray absorption spectroscopy (XAS) investigation.[165] A Mn-K edge

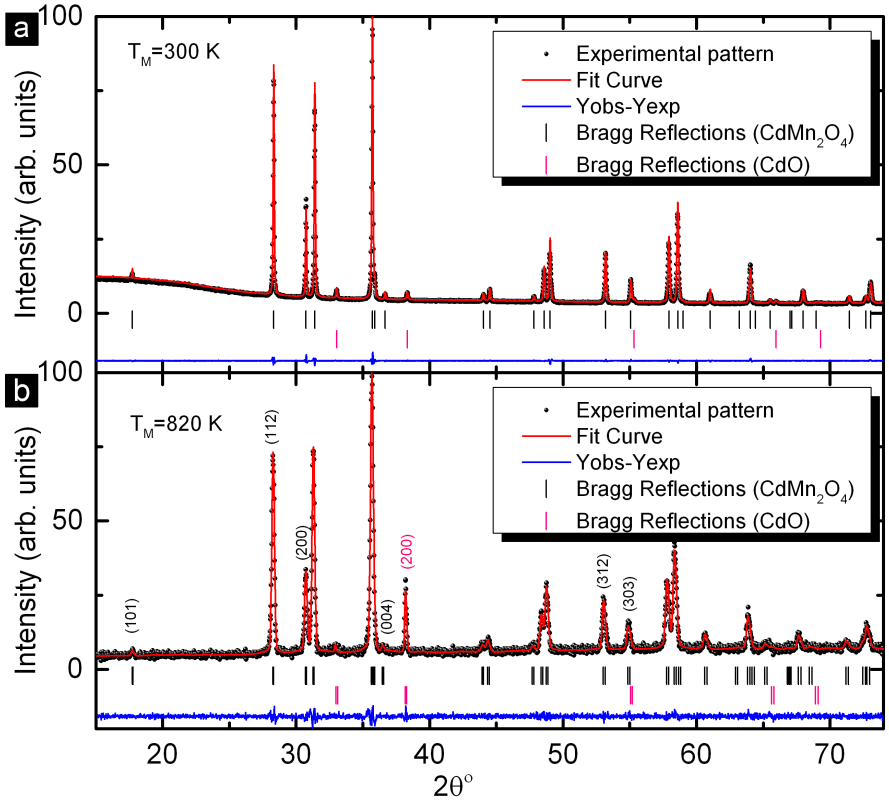

Figure 4.2 – XRD Rietveld refinement output of the spinel $CdMn_2O_4$ structure at room temperature (**a)**) and at 820 K (**b)**). Experimental pattern (•), Fit curve (_), Residual difference (_), Bragg reflections for $CdMn_2O_4$ (|) and CdO (|).

XAS investigation on this system[195] pointed out the presence of Mn(II) in the $CdMn_2O_4$ tetrahedral sites of the spinel structure, when prepared with a cadmium defect, which is not the case of this work. The same authors showed that the presence of small quantities of $Cd^t_{1-x}Mn(II)^t_xMn(III)^o_2O_4$ could be regarded as local inhomogeneities, where the average should appear as the normal spinel compound[195]. *Sinha et al*[185] have observed stable hybridized bond orbitals in the cadmium manganese oxide spinels pointing out that the existence of disorder is unlikely and even if present it is very difficult to be observe.

Table 4.1 – Structural parameters for $CdMn_2O_4$ and CdO systems.

Phase	$CdMn_2O_4$		CdO	
Space group	$I4_1/amd$		$Fm3m$	
Parameters	300 K	800 K	300 K	800 K
χ^2	2.4(2)	2.9(3)	2.4(2)	2.9(3)
a (Å)	5.814(9)	5.834(8)	4.691(9)	4.720(7)
b (Å)				
c (Å)	9.801(2)	9.871(9)		
Phase(%)	96(2)	96(3)	4(2)	4(3)
Density (g/cm^3)	5.754	6.045	7.510	11.208
Volume (Å^3)	331(1)	336(1)	103(1)	105(1)

In our work, considering the family of compounds $(Cd_{1-x}Mn_x)Mn_2O_4$, the values obtained are typical for a sample in which the total substitution of the A-site by the Cd

atoms is present ($CdMn_2O_4$). On the opposite end member (isostructural Mn_3O_4) the distortion is less pronounced (c/a = 1.16) [185]. Also, when considering the intensity of the XRD peaks, we observe that the 101 reflection is very weak, which is characteristic of normal spinel type (note that for the cases of inverted or random spinel type, a strong or medium 101 reflection respectively, should appear). Additionally, the 112 reflection is very strong, whereas in the case of inverted type spinel should be weaker than the 101. Furthermore *Irani et al.* [186] also describe the expected ratios of some reflections intensities which are characteristic of the different type of spinels. For example, the I_{200}/I_{004} (normal 1 : 7, random 1 : 2 and inverted 1 : 1) and I_{312}/I_{303} (normal 1 : 3, random 1 : 5 and inverted 1 : 1) ratios, when compared to our results (1 : 10 and 1 : 2 respectively), points also to a spinel with normal distribution.

The surface morphology and composition of the sample was checked by SEM and EDS. Some micrographs taken with secondary electrons (SE) are presented in Fig. 4.3 (a) and 4.3 (b).

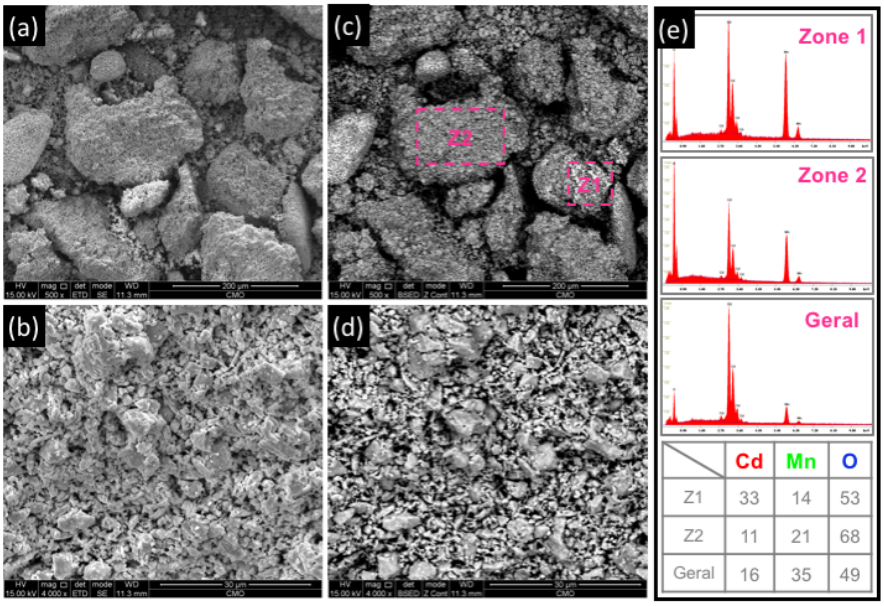

Figure 4.3 – Scanning electron microscope photographs performed in $CdMn_2O_4$ sample using secondary electrons (SE) and backscattered electrons (BSE). With a magnification: **(a)** 500× (SE), **(b)** 4000× (SE), **(c)** 500× (BSE) and **(d)** 4000× (BSE) . **(e)** EDS results of 3 different zones.

According to the results the sample surface topography seems to be composed of relative large agglomerate of grains ($\sim$ 100 – 200 μm). Upon a closer inspection (see 4000 magnification on Fig. 4.3 (b)) we can observe that these agglomerates are in fact composed by smaller grains with a large size distribution. As seen in Fig. 4.3 (c) and 4.3 (d) some bright spots seem to be scattered in the surface of some agglomerates (a contrast between lighter and darker areas). Therefore, the grains were analyzed to obtain the corresponding elemental composition, using EDS analysis of X-rays. The analysis was performed in different agglomerates for acquiring information about the elements present at different points of the samples (see Fig. 4.3 (c)) and the results are

sumarized in graphs and table in Fig. 4.3 (e).

For Zone 1, the areas where the bright spots were observed, an anormal proportion of the Cd and Mn is observed. We believe that this areas are richer in the spurious phase CdO observed by XRD data. Zone 2 a proportion of 1 : 2 is observed between the Cd and Mn atoms, characteristic of the $CdMn_2O_4$ phase. In the analysis of the general area the proportion between the atoms is also in accordance (inside the experimental error).

4.3.2 Magnetic Characterization

In Fig. 4.4 (a) the molar magnetic susceptibility as a function of temperature for the ZFC and FC measurements is shown. Comparing the two curves no major differences can be observed, *i.e.*, a complete overlap between them is observed, thus assuring the system reversibility as a function of temperature. Isothermal magnetization at 5 K acquired with sweeping of the magnetic field from 5 T to -5 T is represented in Fig. 4.4 (b). Accordingly, the $M(H)$ curve shows no hysteresis and no saturation up to 5 T.

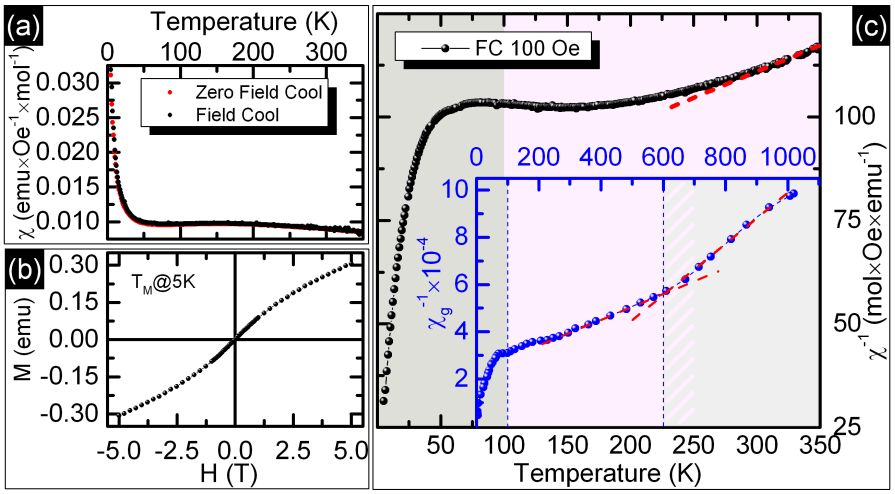

Figure 4.4 – Magnetic susceptibility as a function of temperature measured at H = 100 Oe, in ZFC (●) and FC (●) modes. **c)** Isothermal magnetization at 5 K acquired with sweeping the magnetic field from 5 T to –5 T. **d)** Reciprocal susceptibility as a function of temperature measured at H = 100 Oe , in FC mode. **inset:** Mass reciprocal susceptibility as a function of temperature (data taken from ref. 183). Dashed lines are guides for the eyes.

The reciprocal magnetic susceptibility of the cadmium manganite as a function of temperature shows a Curie-Weiss behavior above RT with a very broad short range ordering of the spins that begins around 230 K, see Fig. 4.4 (c)). Below this temperature the spin arrangement on the octahedral sites gives rise to a temperature independent antiferromagnetic (TIP) susceptibility, which has been explained as if all the spins would order antiferromagnetically in low-anisotropy planes[183,184].

Approximately at 70 K the antiferromagnetic interaction of the Mn^{3+} ions becomes dominant and a magnetic phase transition can be observed. The works of *Azzoni et al.* and *Troyanchuk et al.* suggest that $CdMn_2O_4$ exhibits only a single magnetic sub-lattice of antiferromagnetically interacting Mn^{3+} ions, possibly with a spin glass-

type behavior[115,173,183]. In another work by *Dey et al*[183,184] on the study of antiferromagnetic $CdMn_2O_4$, it is argued that since the A-site ion has no magnetic moment and, in the absence of any appreciable long-range order, the magnetic configuration of the B sites may be compared to groups of four magnetic ions, which are exchange-coupled amongst themselves but are isolated in a diamagnetic matrix, if neglecting super-superexchange[183]. According to the authors only local structures are involved rather than a cooperative phenomenon among many ions. Furthermore, if the local structures exhibit weak net magnetization, behaving like canted or spiral antiferromagnets below the transition temperature[183], it is possible that an applied field can align the spins to produce a net spontaneous magnetization (see Fig. 4.4 (c) inset)[183].

4.3.3 Probing Local Instabilities

The hyperfine technique, PAC, as pointed out previously (see section 2.5.1), has a great potential in probing at a local scale, and therefore, was employed aiming to clarify the anomalous phenomena observed in this system. In a first stage, these properties were studied using ^{117}In probe (^{117}In probe fed by the ^{117}Cd radioactive decay [^{117}Ag$\rightarrow$ ^{117}Cd$\rightarrow$ ^{117}In]). Fig. 4.5 depicts the experimental R(t) anisotropy function (left) together with the Fts (right) as a function of temperature (297, 293, 80 and 12 K) obtained in the $CdMn_2O_4$ system. The fits to the R(t) functions are shown by the continuous lines in the spectra.

A single local environment was observed with the ^{117}In probe and assigned to the Cd lattice site (A – site). This assignment was based in the chemical properties of the probe and those of the lattice elements together with point charge model calculations [V_{zz}^{PCM}(Cd site) $\sim$ 65.6 V/Å^2 with $\eta \approx 0$ and V_{zz}^{PCM}(Mn site) $\sim$ 85.4 V/Å^2 with $\eta \approx 1$].

Therefore, our fits included one static EFG distribution in all temperature range. This EFG is characterized by an observable frequency ω_0 = 248(1) Mrad/s (V_{zz} = 55(1) V/Å^2) and an asymmetry parameter η = 0.08(5), which is characteristic of an EFG with a small deviation from axial symmetry (see Fig. 4.8 (b) and 4.8 (c)).

After these first results, the local properties were studied using ^{111}Cd probe (^{111}Cd probe fed by the ^{111m}Cd radioactive decay [^{111m}Cd$\rightarrow$ ^{111}Cd]). Figure 4.6 depicts the experimental R(t) anisotropy function (left) together with the Fts (right) as a function of temperature (529 K > T > 279 K) obtained in the $CdMn_2O_4$ system. The fits to the R(t) functions are shown by the continuous lines in the spectra. As in the case of the ^{117}In probe, a single local environment was observed with the ^{111m}Cd probe and was also assigned to the Cd lattice site (A – site). The assignment was based in the same principles used for the previous isotope probe. Therefore, our fits included one static EFG distribution in all temperature range. This EFG is characterized by an observable frequency ω_0 = 95(2) Mrad/s (V_{zz} = 54(1) V/Å^2) and an asymmetry parameter η = 0.10(5), which is also characteristic of an EFG with a small deviation from axial symmetry (see Fig. 4.8 (b) and 4.8 (c)).

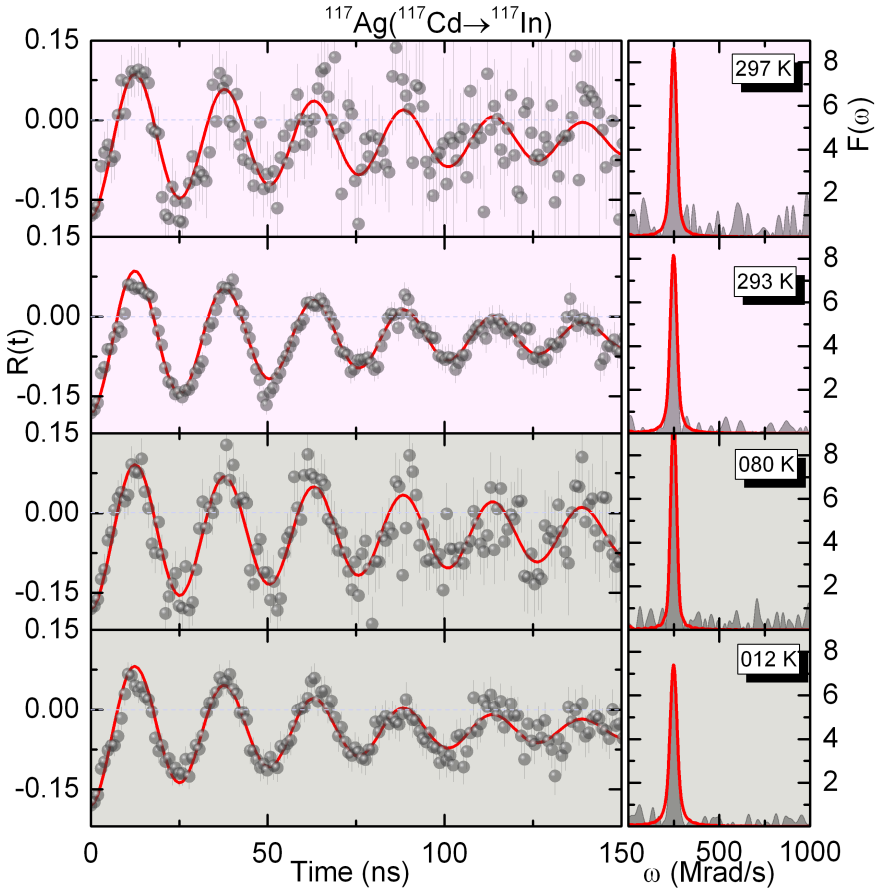

Figure 4.5 – Representative R(t) functions, corresponding fits, and respective Fourier transforms taken at different temperatures using the ^{117}Cd probe.

The A – site for spinels with cubic crystallographic symmetry is expected to be cubic also *i.e.*, null EFG at A – site[169]. The present results show that the $CdMn_2O_4$ material does not have a regular tetrahedral A – site, as expected for the tetragonally distorted manganese spinels. This comes in agreement with the results obtained by XRD diffraction data. The tetragonal crystallographic phase due to JT distortions of the octahedral B – site leads to changes in the lattice in a way that also the A – sites are altered.

Finally, apart from a damping visible in the temperature evolution of the R(t) spectra, no other changes are present, and the EFG parameters show a constant thermal dependence behavior. The observed damping in the R(t) spectra on Fig. 4.6 (more evident if we compare the evolution of the R(t) spectra, at T = 529 K and at $T \leq 293$ K), can be caused by a static EFG distribution and/or dynamic fluctuation of the EFG. However, the model that best fitted the results (better χ^2) was the one considering a larger static distribution, *i.e.*, larger distribution of the EFG components (which arise from random inhomogeneities in the local environment of the Cd probe nucleus).

The $V_{zz}^{lattice}$ values derived for ^{117}In and ^{111}Cd are remarkably similar to each other, *i.e.*, $1.8(3) \times 10^{20}$ V/m^2 and $2.2(2) \times 10^{20}$ V/m^2, respectively, meaning that the In and Cd ions are in the same lattice environment.

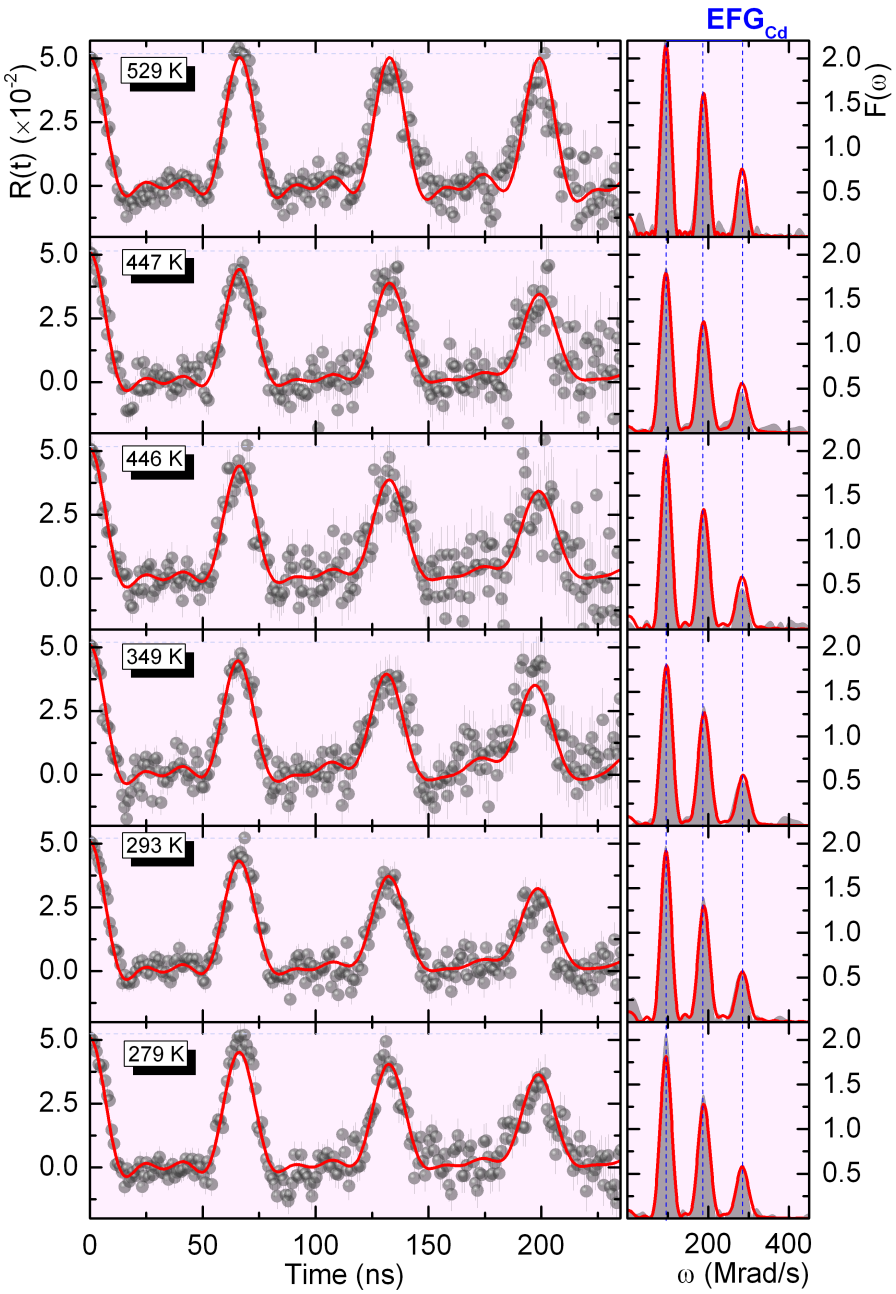

Figure 4.6 – Representative R(t) functions, corresponding fits, and respective Fourier transforms taken at different temperatures using the ^{111m}Cd probe.

In order to better understand these results, additional measurements were performed using the same I = 5/2 ^{111}Cd intermediate level, but in this case fed by the ^{111}In radioactive decay (^{111}In→^{111}Cd). Figure 4.7 depicts representative PAC spectra, Fourier transforms, and corresponding fits, obtained from 873 K to 12 K temperature range in the $CdMn_2O_4$ system.

The final fit solutions were obtained after careful consideration of the different tested models, choosing the one that gave the best χ^2 and consistent temperature dependence tendency. In the end we could observe that our results showed three distinct regions in

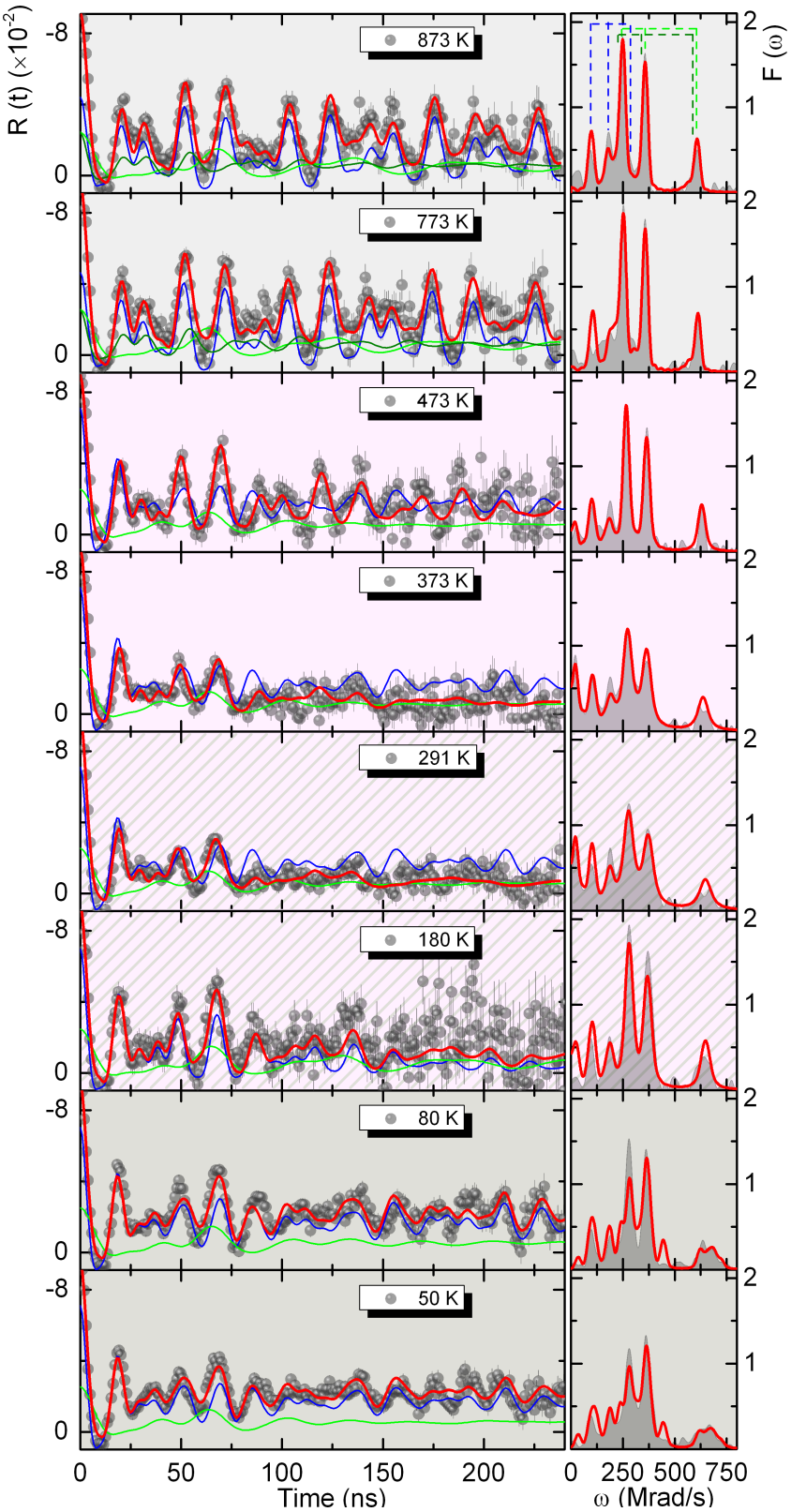

Figure 4.7 – Representative R(t) functions, corresponding fits (Partial fits, corresponding to each individual EFG, are represented in blue and green and sum in red) and respective Fourier transform taken at different temperatures using the ^{111}In probe.

the temperature range from 873 K to 12 K. The first one from the highest temperature down to ≈ 600 K, where three frequency triplets corresponding to three coexisting local environments (three EFG) can be observed (see Fts in Fig. 4.7); the second from ≈ 600 K to ≈ 100 K, where only two coexisting local environments exist with only electric quadrupole interactions. A third region below 100 K where combined hyperfine interactions, electric quadrupole and magnetic dipolar interactions coexist, within the same two local environments. Additionally, one can realize, by simple picture inspection, that below ∼ 600 K the R(t) become increasingly damped as the temperature decreases.

The probe site distribution was determined taking into account the EFG results obtained with the ^{111m}Cd isotope, PCM calculations, previous results in spinel materials[399–402] and considering that the ^{111m}Cd and ^{111}In probes have the same PAC intermediate state, therefore giving a sustained background for our claim.

In the first region, the fits to the R(t) experimental data were performed considering three static EFG distribution assumed to be Lorentzian-like. At T_{max} = 873 K, the probes sites were settled in the following manner: EFG_{Cd} site (26(5)%), EFG_{Mn_1} site (49(5)%) and EFG_{Mn_2} site (25(5)%). The ratio between probes at Cd and Mn sites was set as Cd/Mn=25/75 and maintained constant in the whole temperature range.

In this way, the spectrum obtained at high temperature (873 K) revealed an EFG_{Cd} characterized by an observable frequency ω_0^{Cd} = 90(1) Mrad/s [V_{zz}^{Cd} = 51(1) V/Å^2] with an asymmetry parameter η_{Cd} = 0.27(3), characteristic of an EFG with a small deviation from axial symmetry as expected for probes at the Cd site. Two EFG_{Mn} associated with the Mn – site are characterized by an observable frequency $\omega_0^{Mn_1}$ = 190(1) Mrad/s($V_{zz}^{Mn_1}$ = 108(1) V/Å^2) with an asymmetry parameter η_{Mn_1} = 0.60(2) and $\omega_0^{Mn_2}$ = 182(1) Mrad/s [$V_{zz}^{Mn_2}$ = 104(1) V/Å^2] with an asymmetry parameter η_{Mn_2} = 0.50(2) characteristic of EFG's with a non axial symmetry as expected for probes at the Mn site.

The thermal dependence of the EFG's parameters (V_{zz}, η and probe distribution site) obtained by our fits for the ^{111}Cd [^{111}In→^{111}Cd] probe are depicted in Fig. 4.8 (a) and 4.8 (b). One should bring to attention that the error associated with EFG_{Cd} and EFG_{Mn_2} is greater due to a lower percentage of probes in these sites and a much larger static frequency distribution when considering those of EFG_{Mn_1}. This phenomenon can be observed as well in the case of ^{111m}Cd, with both implantation or diffusion process therefore excluding any influence of the preparation method.

The EFG attributed to probes substituting Cd sites in the lattice (EFG_{Cd}) shows a slight monotonic increase in the EFG principal component (V_{zz}) when decreasing the temperature, whereas the asymmetry parameter (η) and percentage of probe at this local site show an almost constant value in the entire temperature range.

The two EFGs attributed to probes substituting Mn sites in the lattice (EFG_{Mn}), show that the EFG_{Mn_2} principal component and asymmetry parameter increases towards EFG_{Mn_1}, merging completely one into another below ∼ 600 K. EFG_{Mn_1} shows a slight increase on both parameters, V_{zz} and η when lowering the temperature.

As mentioned, in the two local environments observed in the entire temperature

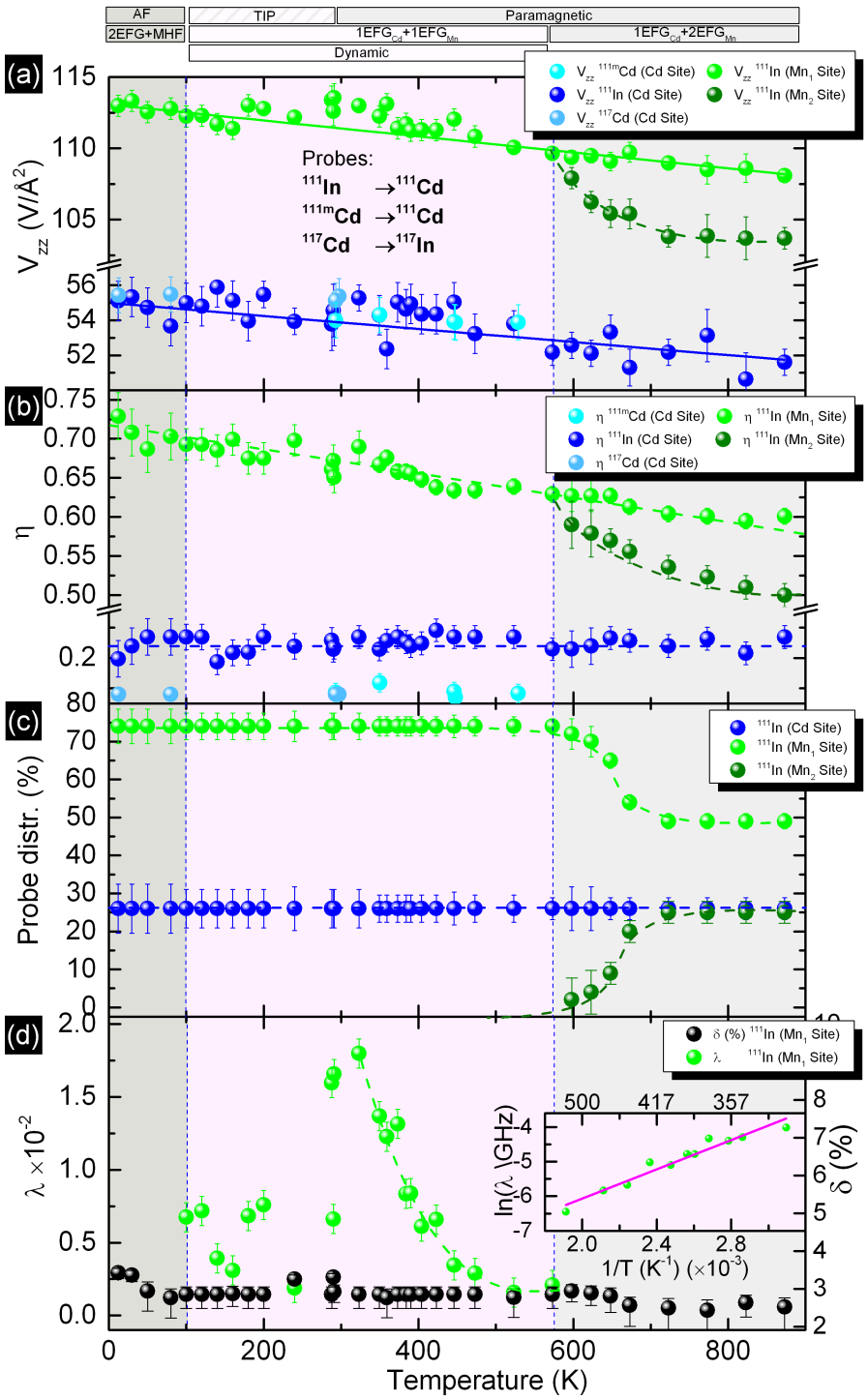

Figure 4.8 – **a:** Experimental electric field gradient principal component (dots). The continuous lines represent a least-squares fit of the function $V_{zz}(T) = V_{zz}(0)[1 + \alpha T^{\kappa}]$ to the data points. **b:** Asymmetry parameter. **c:** Local probe distribution in the lattice sites. **d:** Dynamic (left scale) and static (right scale) attenuation parameters of EFG_{Mn_1}. **(inset)** Natural logarithm of the dynamic attenuation parameter of EFG_{Mn_1}. Continuous lines are fits to the data and dashed lines are guides for the eye.

range, EFG_{Mn_1} and EFG_{Cd}, an increase of the V_{zz} is observed when decreasing the temperature. It is known that the temperature dependence of the V_{zz} is governed by

the atomic vibrations in the vicinity of the probe atom. Therefore, as the sample temperature is decreased, the quadrupole interaction frequency of the system will increase monotonically, which could be least-squares fitted according to:

$$V_{zz} = V_{zz}(0)(1 + \alpha T^{\kappa}) \,, \tag{4.1}$$

with $\kappa = 1$[182]. The obtained coefficients for Cd and Mn are respectively, $\alpha_{Cd} = -6.8(1) \times 10^{-5}$ K^{-1} and $\alpha_{Mn} = -4.9(1) \times 10^{-5}$ K^{-1} and are associated to thermal lattice expansion and atomic vibrations (see solid lines in Fig. 4.8 (a). This V_{zz} trend is similar to those presented by manganites with perovskite structures, albeit the values of α are one order of magnitude lower (2.9×10^{-4} K^{-1})[182].

Between 600 and 100 K a small deviation from this linear trend is observed for V_{zz}^{Mn}. Indeed, this deviation is attributed to the attenuation observed in the R(t) spectra, which is caused by EFG fluctuations within the PAC time scale, as referred before. The model that best fit the data in that temperature range (600 K–100 K) considers time-dependent interactions[170], *i.e.*, EFG fluctuations within the PAC time scale (1 μs > τ > 1 ns; τ is characteristic fluctuation time), associated to the EFG$_{Mn}$[169,361]. This effect can be modeled by including a dynamic attenuation parameter (λ) in the standard static fit function[361] (as introduced in Eq. 2.26). The temperature dependence of the dynamic attenuation parameter (λ) is shown in Fig. 4.8 (d). An exponential increase can be observed below $\approx$ 600 K, reaching a maximum just above RT (323 K).

The $\lambda(T)$ follows an Arrhenius type behavior with:

$$\lambda(T) = \lambda e^{\frac{E_a}{K_B T}} \,, \tag{4.2}$$

where E_a denotes the activation energy, which can be extracted from the slope of the linear plot between $\log(\lambda)$ and $1/T$. This is shown in the inset of Fig. 4.8 (d), where the temperature dependence of the natural logarithm of the dynamic attenuation parameter allowed to determine an activation energy of $E_a = 0.21(2)$ eV[169,362].

The PAC measurements revealed that the Mn site senses an ultraslow dynamics (τ > 1 ns) in the 600 – 100 K temperature range. In fact, the dynamic effect is not only observed in the Mn – site, since using ^{111}Cd probe (^{111m}Cd$\rightarrow$ ^{111}Cd), an increasing attenuation is also observed in the Cd – site in this temperature region. However, in this case, the effect is not so pronounced and thus, as mentioned before, we opted to perform the fit considering a static attenuation parameter mimicking the dynamic effect.[403,404]

The increase of the attenuation observed in the PAC spectra measured using the ^{111m}Cd probe rules out after-effects related time-dependent interactions when using the ^{111}In probe. In fact the observed EFG fluctuations seem to be present in 600 – 100 K temperature range independently of the used PAC probe. As mentioned above after-effects are usually observed in insulators and wide band gap semiconductors. AMn_2O_4 manganite spinels are typically narrow band gap-semiconductors with relatively high

charge mobility and charge carrier availability[405]. The observed time dependent hyperfine interactions are thus a consequence of a material´s intrinsic effect.

One can observe in Fig. 4.7 a strong damping in the R(t) spectra below T_N (100 K). This feature in the R(t) spectra and the frequencies splitting in the FT transforms reveal that the probes interact now with a magnetic hyperfine field, in addition to the EFG. Accordingly, the fits were performed considering a magnetic hyperfine field below T_N. The obtained magnetic hyperfine field (MHF) at 80 K was B_{hf}^{Cd} = 2.5(3) T and B_{hf}^{Mn} = 10.0(2) T, for probes substituting the Cd and Mn sites respectively. At 12 K the values increase slightly: B_{hf}^{Cd} = 3.8(4) T and B_{hf}^{Mn} = 10.8(2) T. The angle between the magnetic hyperfine field and the principal component of the EFG was found to be β^{Cd} = 107(4)° and β^{Mn} = 85(4)°. These values were found to be constant in all temperatures below T_N within error bars.

Face to our XRD results, one cannot ascertain for a cubic to tetragonal phase transition occurring concomitantly with the magnetic anomaly around 650 K, as suggested in the literature. However, a local structural instability might occur in this system and it might justify the magnetization and differential thermal analysis data.

In fact our PAC results show an emerging second EFG along with the reciprocal susceptibility curve slope change. A second EFG at high temperatures is compatible with the existence of local inhomogeneities within the tetragonal matrix. This new local environment with lower and decreasing axial asymmetry may be related with a JT distortion relaxation of some MnO_6 octahedra towards the cubic symmetry. Note that in a cubic space group (*e.g.* $Fd\bar{3}m$) a regular octahedra around Mn^{3+} ion (equal Mn – O bonds) should be expected and no JT distortion should be observed. Consistently, above 700 K we observe a continuous increase of the number of sites with a more regular MnO_6 octahedra in detriment of the number of sites within the distorted low temperature matrix. We can speculate that with further temperature increasing, the relaxed JT octahedra phase will continue to increase and eventually will become the dominant one[193,194]. Similar behavior has been reported in the orthorhombic-rhombohedric (O – R) phase transition region for $LaMnO_3$[406,407] and $LaMnO_{3.12}$[181] by means of local probing. In fact a phase coexistence of fully JT distorted Mn^{3+} and regular octahedra persist well above the O – R transition in those systems.

The mentioned local structural instability might also be at the origin of the dynamic lattice distortion, evidenced by the time dependent EFG fluctuations with its onset below $\sim$ 600 K. These EFG fluctuations are observed in the temperature region spanning from 100 K to 600 K where EFG_{Mn_1}, with JT distorted MnO_6 octahedra, is the solo phase. Note that at such temperatures, especially at room temperature and below, it is very unlikely that the EFG fluctuations arise as a consequence of Cd/O and/or defects diffusion. Also one should rule out the hypothesis of these time-dependent effects arising due to the electron capture decay of the ^{111}In isotope, as EFG fluctuations seem to be present also in the measurements with the metastable ^{111m}Cd isotope. Thus the observed EFG fluctuations should be an intrinsic effect of the system and might have its grounds on

local instabilities of the JT MnO_6 octahedra. Also here a correlation between the electric and magnetic degrees of freedom might be present. One should note that the dynamic effect seems to halt around 100 K where the complete magnetic ordering into an antiferromagnetic state is observed. These results point to a lattice-spin coupling as observed in other spinel systems. In fact in Sr_2RuO_4 the local dynamic effects were presented as a pre mechanism of a spin ordered state[170].

Although dynamic effects have been observed in perovskites manganites[408] or spinel systems[169,170] the actual nature of the dynamic lattice distortion observed in $CdMn_2O_4$ needs further investigation with complementary techniques.

4.3.4 Conclusions

The local lattice properties of $CdMn_2O_4$ have been studied by means of Perturbed Angular Correlations. The EFG measurements at the Cd and Mn sites in the 12 – 600 K temperature region clearly demonstrate that a single Jahn-Teller distorted local phase, compatible with the long-range tetragonal average structure, exists. Above the magnetic phase transition, T_C = 100 K, and up to 600 K a dynamic lattice distortion, related with a local structural instability, is observed.

In the high temperature region, *i.e.* above 600 K, a second EFG emerges along with the reciprocal susceptibility curve slope change. The existence of local inhomogeneities within the tetragonal matrix, also signed by the magnetic anomaly, is however not followed by a tetragonal to cubic phase transition. Instead, a phase segregation in two distinct Jahn-Teller distorted local phases was found. In this high temperature region a relaxed Jahn-Teller distorted octahedral phase grows in the low temperature tetragonal matrix. In order to assertively understand the origin of the dynamic effects observed in this compound, additional studies with complementary local probe techniques are necessary.

Nevertheless this work gives insides on the $CdMn_2O_4$ local lattice structure that might contribute to AMn_2O_4 spinels better understanding.

CHAPTER 5

On the properties of Perovskites $RCrO_3$

5.1 Magnetocaloric effect and refrigerant capacity in polycrystalline $YCrO_3$ (non magnetic R ion)

Rare earth orthochromites ($RCrO_3$) have attracted much interest in recent years due to their physical properties which arise from the orthorhombically distorted perovskite structure. They also show great potential application as multifunctional materials. In this work we present the results of structural, DC magnetization measurements and magnetocaloric properties for $YCrO_3$ hard magnet. The magnetocaloric effect was investigated by means of field dependence magnetisation measurements in a temperature range from 98 K to 182 K. The magnetic entropy change, $-\Delta S_M$ = 0.36 J kg^{-1}K^{-1}, and the refrigerant capacity, R_C = 7.1 J kg^{-1}, was obtained near the transition temperature T_N = 140 K, for applied fields up to 50 kOe. For sake of section completeness we review here again the most important aspects from literature relevant for our analysis. This section is based on the published work[409]: G. N. P. Oliveira, P. Machado, A. L. Pires, A. M Pereira, J. P. Araújo and A. M. L. Lopes, *Journal of Physics and Chemistry of Solids* 91, 182-188 (2016).

5.1.1 Overview

Magnetic refrigeration (MR) based in the magnetocaloric effect (MCE) has given giant steps in recent years and nowadays promises to become a cooling tool for both cryogenic and room temperature applications[83,91]. Alongside with a lower noise and higher efficiency it shows a great ecological advantage compared to conventional refrigeration systems, since this type of MR does not require the use of freon gases[90,91,94].

On magnetic refrigeration technology, apart from the magnetic field source, the magnetocaloric material is a crucial issue since its efficiency scales directly with the generated entropy change[94]. Therefore, the development of new MR systems is accompanied by the search for materials presenting large MCE at moderate magnetic fields.

Research in this area, has already highlighted potential magnetocaloric materials based on La(Fe, Si)$_{13}$ and (La, Ca, Sr)MnO_3[410] which have been tested in magnetic cooling systems with very good results[83,91,411]. Beside these examples, many

other materials show promising properties valuable for new technologies (*e.g.*: $R_5(Si, Ge)_4$ [90], $(Fe, Rh)_1$ [412], Ni-Mn-In(Co)[413] and MnAs[97] based alloys). Besides all these systems that show a potential application near room temperature, some new materials can be explored to be applied to MR near liquid nitrogen temperature.

In fact, almost a decade ago, *Sahu et al* found that rare earth orthochromites with the formula $RCrO_3$ (R=Ho, Er, Yb, Lu or Y) exhibit rich and varying physical properties, including octahedral distortions, relaxor-like behavior, spin-phonon coupling, ferroelectric and multiferroic properties[208,218,230,414].

As a typical pervoskite-like compound these materials have a canted antiferromagnetic (AFM) transition (113 – 140 K range) and exhibit different types of field induced spin reorientation wherein the weak ferromagnetic component becomes parallel to the direction of the applied magnetic field[415,416]. Additionally, this family of compounds is believed to be multiferroic with a claimed ferroelectric (FE) transition in the 472 – 516 K temperature range.

Of particular interest is the $YCrO_3$ perovskite which below T_N = 140 K presents a canted AFM order (G type-AFM) with an additional weak ferromagnetic component, a reported FE transition at T_E = 410 K and a octahedra tilting, which may have a geometric, electronic and/or magnetic origin[417].

Given the $YCrO_3$ complex nature where several kinds of order parameters coexist, and therefore are likely to offer new kinds of functionalities, it is worthwhile to study the effect of the magnetic entropy change[418]. Hard magnetic materials like $YCrO_3$ have been left at bay in preference for soft magnetic ones, at least in what concerns the MCE[419]. Thus, we will show that despite these materials show hysteresis and therefore have losses by the form of heat, no significant effect will be observed in the magnetic entropy change[289]. In this work, we present the results of structural, DC magnetization measurements and MCE properties for polycrystalline $YCrO_3$.

5.1.2 Experimental Details

A polycrystalline sample of $YCrO_3$ was prepared using a conventional solid state reaction method. The sample was synthesized from high purity Y_2O_3 (99.99%) and Cr_2O_3 (99.9%) powders, mixed in a stoichiometric ratio and heated in air up to 1173 °K (5 $Kmin^{-1}$) in high density Al_2O_3 crucibles in the final heat treatment.

The structural properties of the powder sample were evaluated from the x-ray diffraction patterns (XRD) recorded at room temperature using a Panalytical, X'Pert Pro diffractometer with a CuK_α radiation and λ = 1.54056 Å at 50 kV and 40 mA. The crystallographic structure was determined by Rietveld refinement of the XRD spectrum using the Fullprof software package[347].

The magnetic properties measurements were carried out in a commercial (MPMS Quantum Design) Superconducting Quantum Interference Device (SQUID) magnetometer in the 5 – 370 K temperature range. The isofield $M(T)$ curves were measured under

an applied field of 0.1 kOe and the isotherms $M(H)$ curves were measure between 0 and 50 kOe from 98 K to 182 K. Afterwards, the magnetic entropy change $[-\Delta S_M(T)]$ was estimated using the Maxwell relations as report in ref. 289.

5.1.3 Results and Discussion

5.1.3.1 Crystalographic characterization

Figure 5.1 (a) presents the graphical output of the rietveld refinement performed to the XRD pattern of the $YCrO_3$ sample after the final annealing treatment.

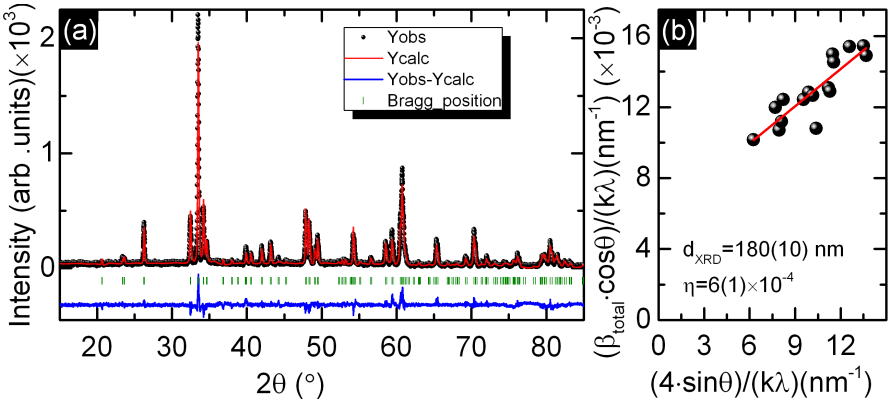

Figure 5.1 – **a:** XRD Rietveld refinement output of the perovskite $YCrO_3$ structure at room temperature. Experimental pattern (•), Fit curve (_), Residual difference (_) and Bragg reflections (|). **b:** Linear fit using the Williamson–Hall relation. (the slope represents the mean strain and the line interception gives the inverse particle size).

The values obtained in the last refinement cycle are summarized in table 5.1.

Table 5.1 – Structural parameters and atomic positions for $YCrO_3$ system at room temperature.

SG:*Pnma*	***a*** (Å) 5.5157(4)	***b*** (Å) 7.5308(5)	***c*** (Å) 5.2419(2)		
Atom	*x*	*y*	*z*	U_{iso}(Å^2)	*Occ*
Y: 4*c* (*x*, 0.25, *z*)	0.0654	0.25	-0.0179	0.2148	0.7314
Cr: 4*b* (0, 0, 0.5)	0	0	0.5	0.2630	0.7398
O(1): 4*c* (*x*, 0.25, *z*)	0.4721	0.25	0.1026	0.0796	0.7386
O(2): 8*d* (*x*, *y*, *z*)	0.2996	0.0542	-0.31144	1.26675	1.6382
Cr-O1-Cr=146.9°	R_{wp} = 16.6	R_p = 18.6	R_{exp} = 16.2	χ^2 = 1.24	

All the diffraction peaks were indexed within the orthorhombic perovskite structure (single phase pattern) that belong to the space group *Pnma*[238]. The obtained values are in good agreement with those reported in the literature evidencing the good quality of the sample[420]. Furthermore, the pattern is characterized by sharp and well defined peaks that reveal high crystallinity.

The average crystallite size of the $YCrO_3$ particles (d_{XRD}) was calculated using the Williamson–Hall relationship in order to consider the possible contribution from the in-

ternal strain[421–423]:

$$\beta_{total} = \beta_{size} + \beta_{strain} = \frac{k\lambda}{d_{XRD}\cos\theta} + 4\eta\tan\theta\ , \tag{5.1}$$

where β_{total} is the full width at half-maximum (fwhm) of the XRD peak (combination of both instrument and sample dependent effects), k is the Debye-Scherrer constant ($\sim$ 0.94 for spherical crystallites), λ is the incident x-ray wavelength, θ is the diffraction angle, and η is the microstrain parameter. For all samples, the microstrain can be considered negligible (η < 0.1%) and therefore does not play a significant role in the main physical properties of the bulk sample. Figure 5.1 (b) shows a plot of $\frac{\beta_{total}\cos\theta}{k\lambda}$ vs. $\frac{4\sin\theta}{k\lambda}$, where an approximation to the average crystallite size of the particles, d_{XRD} = 180(10) nm was extracted.

5.1.3.2 Magnetic characterization

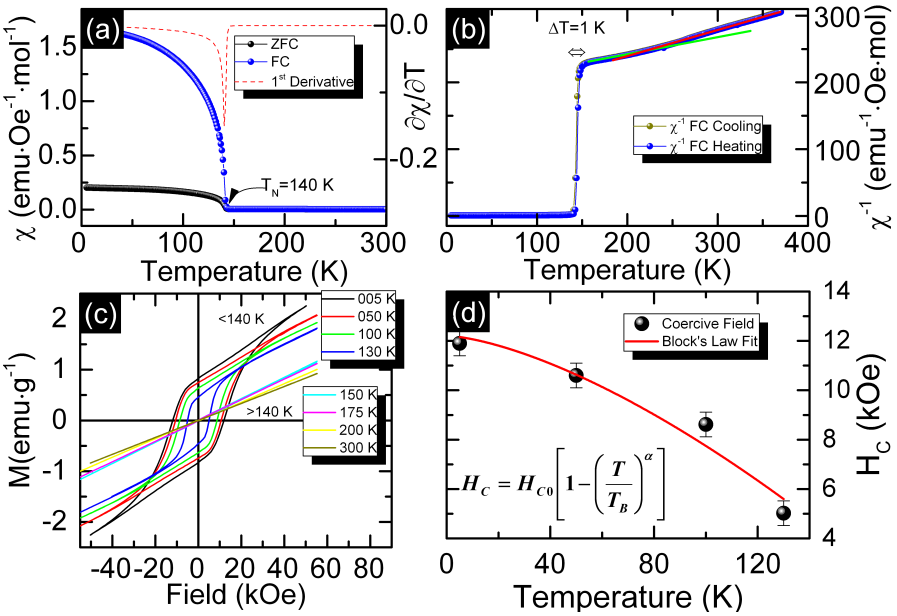

Figure 5.2 – **a:** $\chi(T)$ measured at H = 0.1 kOe, in ZFC (•) and FC (•) modes (Red dashed line (–) depicts $\partial\chi/\partial T$ curve.). **b:** $\chi^{-1}(T)$ measured at H = 0.1 kOe, in FC mode while cooling and heating. **c:** Isothermal $M(H)$ curves at 5 and 300 K. (**Inset:** χT as a function of temperature.) **d:** Magnetic coercive field as a function of T.

The molar magnetic susceptibility as a function of temperature for the ZFC and FC measurements are shown in Fig. 5.2 (a). A single sharp transition is observed at 140 K, for both ZFC and FC modes, which is associated with the ordering of the Cr^{3+} magnetic sub-lattice from a high temperature paramagnetic state to a canted antiferromagnetic (CAFM) order with a weak ferromagnetic contribution at low temperature[415]. The transition temperature value (T_N^{Cr}) was extracted by the inflection point in $\partial\chi/\partial T$ (see red line in Fig. 5.2 (a)). Below T_N^{Cr} a splitting of the curves is observed and the magnetisation increases until it saturates at different values at very low temperatures. The suscep-

tibility value at 5 K in FC mode is almost ten times greater than that for ZFC mode. Weak ferromagnetism was pointed out as a plausible explanation to the origin of this observation[415].

The temperature dependency of the inverse magnetic susceptibility $\chi^{-1}(T)$ for FC while cooling and heating modes are plotted on Fig. 5.2 (b). Firstly, a slight variation of the onset of magnetic ordering ($\Delta T_N \sim 1$ K) has been verified to increase in the FC heating compared to the FC cooling measurements. *Udagawa et al* pointed that this thermal hysteresis was due to a change in the unit cell volume near the magnetic transition (change in exchange interaction energy)[424]. Secondly, it is observed that $\chi^{-1}(T)$ curve does not follow a perfect linear behavior characteristic of a material in a paramagnetic regime, where the Curie–Weiss (CW) law could be applied. In fact, two different slopes can be identified in the paramagnetic regime. A first one above $\sim$ 220 K (red line), with an estimated moment μ_{eff} = 4.56 μ_B (from the C-W fit), which is in agreement with those reported in literature[204,415] but higher then the theoretical one. A theoretical value of μ_{eff} = 3.87 μ_B is expected for Hund's rule ground state of the Cr^{3+} when the orbital moments are quenched due to crystal field effects as expected for a d^3 ion in octahedral environment. Additionally, a negative Curie-Weiss constant Θ = –452 K was observed for $YCrO_3$, indicating the predominance of antiferromagnetic interactions in the chromium perovskite[230,415,425,426]. A second linear regime exists below $\sim$ 220 K, down to T_N^{Cr} (green line), where a value of μ_{eff} = 5.3 μ_B was obtained.

Actuality, this behavior was also reported by Durán et al[427] by specific heat measurements and attributed to spin fluctuations, *i.e.*, the observed difference seems to be the build-up of magnetic correlations preceding the transition to the long-range antiferromagnetic ordering (*i.e.* development of a short-range order above T_N). This is further supported by pair distribution function results which showed that local noncentrosymmetic regions appear below 470 K[219]. The correlation between the change in local symmetry and anomalous behavior in $\chi^{-1}(T)$ has also been observed in other systems[169].

In order to better understand the magnetic behavior, several magnetization isotherms were acquired between 5 and 300 K sweeping the magnetic field from 50 kOe to –50 kOe (see inset in Fig. 5.2 (c)). As expected, for the magnetization isotherm above 140 K there is no loop opening since the sample is in its paramagnetic state. However, below 140 K the $M(H)$ curve shows hysteresis and no saturation up to 50 kOe. The hysteresis plot is symmetric with field and magnetization axes and thus, there is no indication of exchange bias effect in this sample. This type of magnetization loop is attributed to the existence of weak ferromagnetism where DC magnetization increases linearly in the larger magnetic field region and the magnetization evolves as $M(H) = \chi_{AF}H + M_S$; where $\chi_{AF}H$ is the antiferromagnetic contribution and M_S is the saturation magnetization of the weak ferromagnetism (see ref. 427). The FM contribution for $YCrO_3$ can be obtained by subtracting the AFM contribution from the total magnetization curve. The saturation magnetization is then obtained by the extrapolation of the linear part of $M(H)$

curve to zero ($M_S \approx 0.91$ emug^{-1}). The high coercive field (11.4 kOe) and the remanent magnetization ($\sim$ 0.84 emug^{-1}) are also indicative of the extent of the ferromagnetic component[428].

From the temperature dependence of the magnetic coercive field (H_C) extracted from the $M(H)$ curves (acquired below T_N) the blocking temperature of the magnetic domains (T_B) can be estimated using the Bloch's relation:

$$H_C = H_{C0}\left[1 - \left(\frac{T}{T_B}\right)^{\alpha}\right], \tag{5.2}$$

where H_{C0} is the coercive field at T = 0 K and α is the Bloch's exponent for bulk materials (α = 3/2)[429] The fit of H_C vs T (Fig. 5.2 (d)) reveals a good agreement with the temperature dependence regime where H_{C0} could be estimated to be $\sim$ 12 kOe and $T_B \sim 196$ K.

Interestingly, an electron paramagnetic resonance (EPR) study in $YCrO_3$ showed that I_{EPR} increases continuously with the temperature decrease (starting from room temperature), exhibiting an inflection point at T = 220 K and a maximum at T = 182 K. The inflection point indicates the presence of additional absorption process, and was proposed to be originated by magnetic fluctuations at those temperatures. Measurements of specific heat[430] also suggest this process, where the magnetic specific heat contribution begins to dominate the phonon specific heat contribution at temperatures below $\sim$ 225 K. With further temperature decrease, I_{EPR} rapidly diminishes until T_N^{Cr} = 139 K (in this region the quantity of absorbing centers diminishes considerably due to the process of antiparallel spin alignment)[426]. This comes in good agreement with the $\chi^{-1}(T)$ data in the paramagnetic region where it is observed a slope change around 220 K and with the extrapolated domain blocking temperature of 196 K, further supporting the development of short-range order preceding the antiferromagnetic transition.

5.1.3.3 The magnetocaloric effect

Setting the nature of the magnetic properties of $YCrO_3$ one can proceed to the study of its MCE through the study of the variation of the magnetic entropy. The MCE of a certain material, *i.e.*, the isothermal magnetic entropy change ($-\Delta S_M(T)$) can be quantified by performing isothermal measurements and then applying the Maxwell relation as reported in ref. 289.

In our experiments, the $M(H)$ curves were measured as follows: First, the sample was cooled-down to the lowest temperature to be measured. After stabilizing the temperature the measurement was performed varying the field from 0 up to 50 kOe (in 40 steps). At each step the magnetization was measured at a fixed temperature and field ($H\uparrow$). After the maximum field was reached the measurement was performed decreasing the field ($H\downarrow$). Once back at initial field (0 kOe) the sample was heated up all the way into the paramagnetic region (T = 190 K $\gg T_N$). Only then the sample is cooled

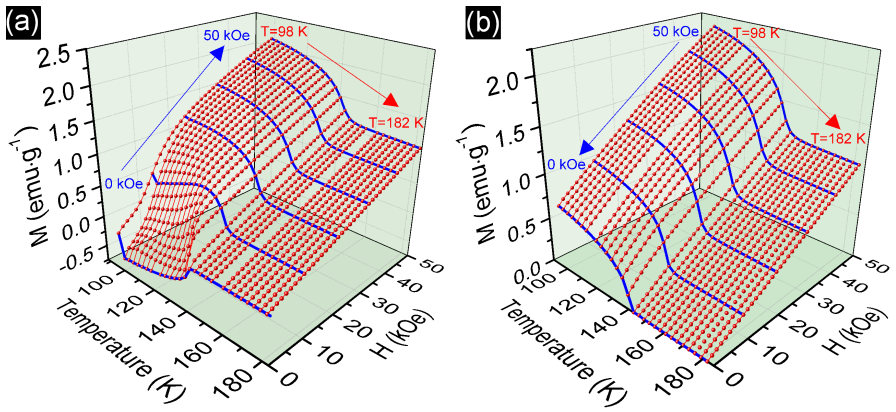

Figure 5.3 – Isothermal $M(H)$ curves at different temperatures from 98 K to 182 K with an interval of 3 K measured while (**a**) increasing [$H \uparrow$] and (**b**) decreasing [$H \downarrow$] the magnetic field between 0 kOe to 50 kOe (red lines). Isofield $M(T)$ curves obtained from $M(H)$ curves (blue).

to a new measurement temperature above the previous one. This was repeated over a temperature range of 98 – 182 K (ΔT = 3 K) (Fig. 5.3 (a) [$H \uparrow$] and 5.3 (b) [$H \downarrow$])[289].

In a first inspection of the results, one can identify, an abnormal behavior of the isothermal curves in increasing field mode, negative magnetization values for low fields, which was related to the presence of a negative remanent field. However this does not invalidate the nature of our findings. Thus, we focus our calculations into the measurements in decreasing field mode where this type of influence is minimized.

The approximate temperature dependence of isothermal magnetic entropy change ΔS_M, corresponding to a magnetic field change ΔH starting from zero field (or from H_{max}), can be numerically calculated from the discrete magnetization data by means of the expression obtained from the Maxwell relationship:

$$\Delta S_M(T,H) = S(T,H) - S(T,0) = \int_0^H \left(\frac{\partial M}{\partial T}\right)_H dH \,. \tag{5.3}$$

Magnetic entropy change versus temperature for different magnetic field changes is shown in Fig. 5.4 (a) [$H \uparrow$] and 5.4 (b) [$H \downarrow$]. The positive sign of $-\Delta S_M$ and the curves shape, at a first glance indicates the FM nature and a conventional magnetic cooling effect by adiabatic demagnetization in the present compound[431]. Also, no distinct temperature alteration of the peak position of $-\Delta S_M$ vs T curves under variable magnetic field is observed showing its second order nature.

The maxima in $-\Delta S_M(T)$ for different maximum variations of the applied magnetic field H_{max}, are peaked close to 140 K, which marks the onset of the antiferromagnetic phase transition (T_N = 140 K). It is interesting to note that above the antiferromagnetic ordering, under small applied magnetic field which doesn't disturb the $YCrO_3$ ground state, a small positive entropy change is observed confirming the presence of the weak ferromagnetic interactions due to anisotropy in the system (Dzialoshinski–Moriya type antisymmetric exchange interaction of $Cr^{3+} - Cr^{3+}$ ions)[428]. Additionally, in Fig. 5.4, when comparing the $-\Delta S_M(T)$ for H_{max} = 50 kOe varying the field in increasing or de-

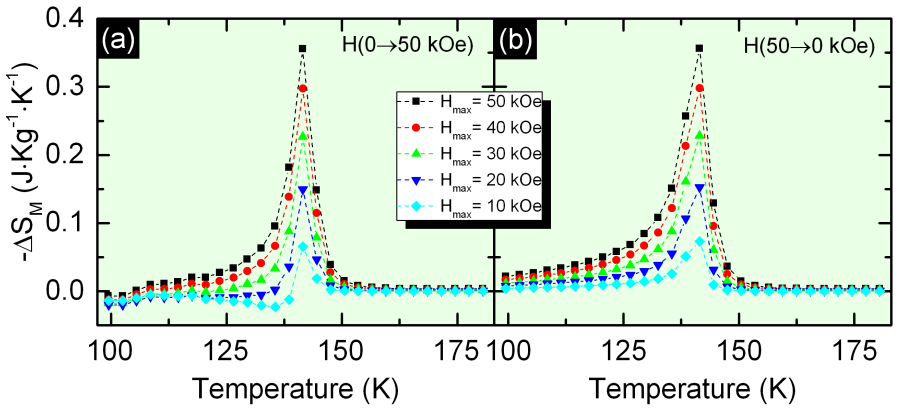

Figure 5.4 – Magnetic entropy changes with respect to temperature at different field changes for $YCrO_3$ sample.

creasing mode, the same maximum value and an overlap of the curves is observed above T_N. However, below T_N a difference between the two curves is evident. A possible explanation for this observation lies on the fact that the ordering temperature of Cr^{3+} is sensitive to the thermal cycling history of the sample when an external field is applied. The difference observed near T_N is, as referred before, due to the competition between weak ferromagnetic and antiferromagnetic interactions[413,415].

Curiously, as pointed out previously the same $-\Delta S_M^{max}$ was observed in the cases of $H\downarrow$ and $H\uparrow$. One should stress that each isothermal measurement was made after the sample is heated, with no applied field, up to the paramagnetic region (well above T_N). Thus, the available thermal energy simply overcomes the interaction energy between the spins. This is an indication that a big variation of M due to the presence of magnetic domains does not affect the magnitude of $-\Delta S_M$ but will affect its shape for $T < T_N$. Furthermore, we observed that the nature of the magnetic material (hard/soft), in which usually hard magnets were preferred, does not have a large influence in the MCE. Therefore, new pathways can be pursuit using the coupling of soft and hard magnets in different applications fields, without the concern of losses under the form of heat in systems showing hysteresis[419].

The calculated $-\Delta S_M$ was found to be positive in almost all temperature span. An increase with field of the maximum value is observed, reaching a value as high as 0.36 $J\,kg^{-1}K^{-1}$ for a field change of 50 kOe. This value is significantly larger than that obtained for a similar perovskite $LaCrO_3$ (T_N^{Cr} = 285 K), where $-\Delta S_M$ = 0.067 $J\ kg^{-1}K^{-1}$ for the same magnetic field H_{max} = 50 kOe[212]. In both $YCrO_3$ and $LaCrO_3$ the A-site cation has a zero magnetic moment (J = 0), same spin value for B-site ($J_{Cr^{3+}}$ = 3/2) and have the same elements ratio and therefore for a higher T_N a lower $-\Delta S_M$ is expected[100,432]. On the other hand $DyCrO_3$, which belongs also to the $RCrO_3$ family, has a $-\Delta S_M$ = 8.4 $J\,kg^{-1}K^{-1}$ (H_{max} = 40 kOe) calculated near the spin reorientation temperature ($T_{SR}^{DyCrO_3} \sim 15$ K)[433]. Though a direct $-\Delta S_M$ comparison for $DyCrO_3$ and $YCrO_3$ cannot be made, a higher ΔS_M value is expected for $DyCrO_3$ due to the rare

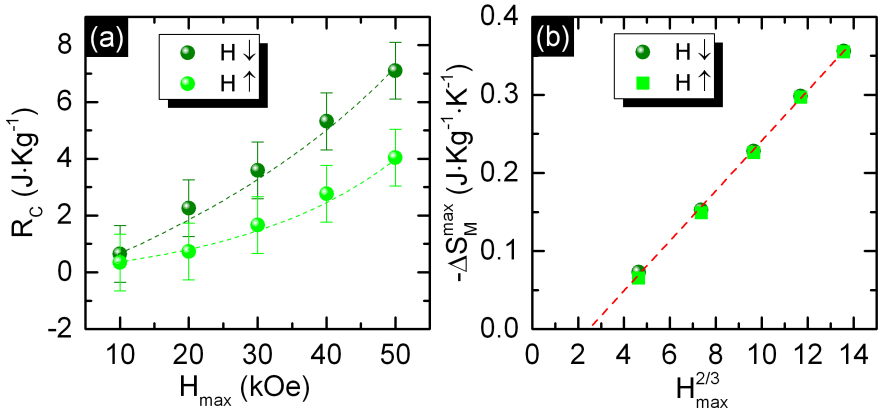

Figure 5.5 – (**a**) R_C evaluated for different fields at different temperature. (**b**) Maximum magnetic entropy change versus maximum field variation two thirds power. (Dashed lines are guidelines for the eyes.)

earth magnetic ion contribution to the system entropy.

In the cases where $-\Delta S_M^{max} \propto H_{max}^{2/3}$ we should expect that the magnetization properties can be explained by a mean field theory. Figure 5.5 (b) pictures that dependency, where by a simple inspection a linear dependency seems to be present. This seems to hint that a mean field theory approach should suffice to explain the $YCrO_3$ magnetic behavior for high fields. However, nowadays a more comprehensive expression and a complete field dependence of $-\Delta S_M^{max}$ is known, where the implications for the use of the $H^{2/3}$ model are further discussed[434]. Having this in mind it should be interesting for a future work a detailed study on the critical exponents.

5.1.3.4 The relative cooling power

A further parameter used in magnetocaloric materials is the refrigerant capacity (R_C), which can be used to determine the interest of a material for a real application and represents the amount of heat transferred in one thermodynamic cycle. For a given magnetic refrigerant, the optimum refrigeration cycle occurs when the R_C has a maximum value. R_C is represented by the expression:

$$R_C(H) = \int_{T_1}^{T_2} \Delta S_M(T,H)\mathrm{d}T\,. \tag{5.4}$$

It can be also estimated for each value of field variation by the product of the maximum magnitude of $|-\Delta S_M^{max}|$ and its full width at half maximum (δT_{fwhm}), plotted in Fig. 5.5 (a). An estimated R_C = 7.1 J kg^{-1} for bulk $YCrO_3$ was achieved near the transition temperature at 140 K for ΔH = 50 kOe[83,212,433].

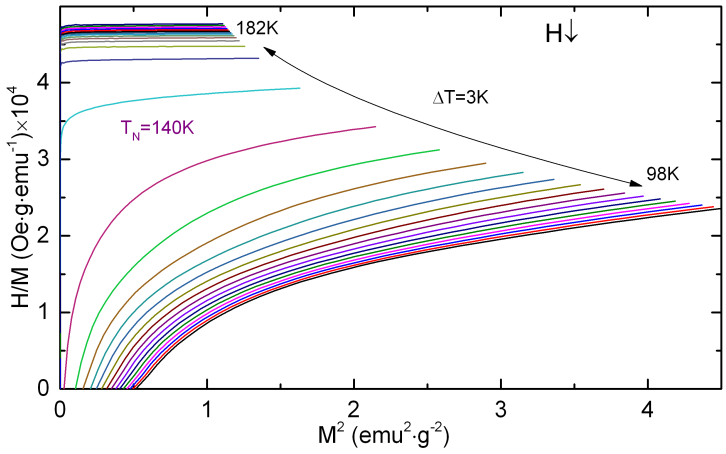

Figure 5.6 – Belov-Arrott plots at different temperatures for bulk $YCrO_3$ sample.

5.1.3.5 Arrott-plot representation

According to Banerjee criterion[435], it is possible estimate the order parameter of the field-induced magnetic transition by the presence of positive/negative slope in Arrott plots. Negative for a first-order magnetic phase transition and positive when the transition is of second order. Therefore, we have constructed Arrott plots for $YCrO_3$, which are shown in Fig. 5.6. Observing the figure, neither an inflection point nor a negative slope is observed, therefore evidencing the occurrence of a second-order magnetic transition further confirming the above statement concerning the $-\Delta S_M$ peak invariability.

While ΔS_M change is smaller than that observed in some other magnetocaloric materials, including Gd metal[83], understanding the mechanisms producing the MCE in $YCrO_3$ may lead to better materials in the future. Furthermore these materials can be used to operate in different temperature intervals like near the liquid nitrogen temperature. One can point out that the magnitude of the MCE depends strongly on the sample magnetization, therefore if one would increase the weak ferromagnetic moment by tuning the $Cr-O_1-Cr$ bond angle an increase of ΔS_M in the system would be expected[415,427]. In fact, modifying this bond angle may also increase the magnetic transition temperature, which is desirable to many applications. This interplay of the transition temperature and magnitude of the MCE will require a careful control of the bond angles in $YCrO_3$. Possibly the doping with magnetic rare earth ions would optimise the properties of the system for magnetocaloric applications.

5.1.4 Conclusions

We have synthesized polycrystalline $YCrO_3$ and confirmed an orthorhombic structure with the *Pnma* space group using structure refinement. Magnetization measurements reveal an antiferromagnetic transition with weak ferromagnetism below $T_N \sim 140$ K. The magnetocaloric effect was calculated by measuring the isothermal magnetic en-

tropy change, which shows a maximum of 0.36 $J\,kg^{-1}K^{-1}$ for a field of 50 kOe and a refrigerant capacity R_C = 7.1 $J\,kg^{-1}$. No difference in the magnitude of the MCE was observed for increasing and decreasing field modes, reinforcing the idea that hard magnets should also be included in the search for new MCE materials. The positive slope of the Arrott plots at all high fields implies that the field-induced magnetic transition in $YCrO_3$ is second-order in nature.

$YCrO_3$, a canted antiferromagnetic system with weak ferromagnetism, possessing rich physics due to the complex coupling among different degree of freedoms, is a model of chromium perovskites and may provide further information to possible applications in MR in liquid nitrogen temperature range.

5.2 Effect of Chemical Pressure on the magnetocaloric effect of $RCrO_3$ perovskites (R=Yb, Er, Sm and Y)

A comparative study of the magnetocaloric effect and refrigerant capacity properties of orthorhombic perovskite-like isostructural compounds $RCrO_3$ (R:Yb, Er, Sm and Y) was carried out. A comparison between the magnetocaloric effect in the different samples is discussed considering the effect of using R cations with and without a nill magnetic moment and different cation size (R = Yb, Er, Y and Sm). It is shown that the magnetocaloric effect is higher near the rare earth ion ordering temperature than that at the Cr ordering temperature. Two scales of values can be observed at the Cr^{3+} and R^{3+} ordering temperatures. The first one with values ranging $-\Delta S_M(T_N^{Cr})$ = [0.15; 0.72] and the second one ranging $-\Delta S_M(T_N^{R})$ = [–0.2; 12.5]. An inverse magnetocaloric effect was observed at T_N^R for Sm. The evolution of $-\Delta S_M$ with R^{3+} ion radius increase and with total paramagnetic system moment are also discussed. For sake of section completeness we review here again the most important aspects from literature relevant for our analysis.

5.2.1 Overview

Magnetic refrigeration based in the magnetocaloric effect (MCE) has given giant steps in recent years and nowadays promises to become a cooling tool for both cryogenic and room temperature applications[26,83,91]. Apart from the explicit advantages of using this type of technology at room temperature, there is also great interest in the applications to cryogenic temperatures where the current dominant technology is helium based. Facing the decline of the global amount of helium, its liquefaction cost is only expected to increase. Thus, leading to a more costly technology based on it (*e.g.* scientific and medical instrumentation based in superconducting magnets)[433,436].

Here, the high energy efficiency walks alongside with a great ecological advantage since this application is not based in freon gases (*i.e.*, as conventional refrigeration systems)[90,91,94,100]. However, this technology requires the search for promising materials

which can then be used in suitable applications. Ideally, these materials might present a coexistence of several types of orders and thus are more likely to offer new kinds of functionalities[419]. In this respect, one can find those which are very appealing due to the coupling between ferroelectric and ferromagnetic orders (magnetoelectric multiferroics) giving the capacity to control them electrical and magnetically[26,437]. Among multiferroic we can find those in which the ordering temperatures and the polarization values are usually very high but the magnetoelectric coupling is rather weak. In these materials, type-I multiferroics, ferroelectricity and magnetism have different origins and different ordering temperatures. On the other, a second group of multiferroics in where ferroelectricity appears as a consequence of the magnetic order. Here, a strong magnetoelectric coupling is observed but the ordering temperatures and polarization values are typically very low.

In the last years, there has been a few reports on rare-earth orthochromites ($RCrO_3$) suggesting them as potential magnetoelectric multiferroic materials[218,230]. Still under debate are the ferroelectric transition temperature and its origin. The $RCrO_3$ magnetic properties have been described as G-type antiferromagnetic (AFM)[433], more especifically as having a canted AFM transition and a claimed ferroelectric (FE) transition in the 113–140 K and 472–516 K temperature range, respectively. The magnetic properties of these compounds arise from the different possible magnetic spin interactions (exchange interactions), namely: Cr^{3+}-Cr^{3+}, Cr^{3+}-R^{3+}, and R^{3+}-R^{3+}, which are isotropic, symmetric, and antisymmetric anisotropic, respectively. In these compounds the antissimetric Dzialoshinski-Moriya (D-M) interaction might also act on the Cr^{3+} spins originating a weak ferrimagnetic component[265]. In this way, the $RCrO_3$ exhibit three important transitions: the antiferromagnetic Neél temperature T_N^{Cr} for Cr^{3+} sub-lattice ordering, T_{SR} due to spin reorientation and finally T_N^R for R^{3+} sub-lattice ordering. These characteristic temperatures tend to shift towards higher values with the increase of the R cationic radius. By its turn, these increase are associated with the decreasing of the lattice distortions and increasing Cr^{3+}-O^{2-}-Cr^{3+} bond angles approaching the ideal 180°.

In general, $RCrO_3$ perovskite-type oxides are very fascinating materials for both fundamental physics and applied related issues. Together with their capacity to adopt a variety of different structural distortions, which can be driven by external parameters like temperature, pressure or chemical composition makes them an interesting object of study[207]. Additionally, the different ferroic orders that these multiferroic perovskites may exhibit, such as ferromagnetism, ferroelectricity, and/or ferroelasticity, adds a large contribute to this interest[26,91].

In the present work, we report the MCE studies of rare-earth orthochromites $RCrO_3$ with magnetic A-site ions (Er, Sm, Yb) and compare with previous works with magnetic (Gd and Dy)[433,438] and non magnetic (Y, La) R ions[212,409]. Thus, exemplifying the role of rare-earth magnetism in the MCE in these materials.

We show that $ErCrO_3$ presents a significant magnetic entropy change, $-\Delta S_M$ = 13 $Jkg^{-1}K^{-1}$ while $SmCrO_3$ has an inverse MCE effect of –0.3 $Jkg^{-1}K^{-1}$. The refrig-

erant capacity, R_C calculated near the transition temperature of the R^{3+} ion for applied fields up to 50 kOe varies between 0.2 and 75 Jkg^{-1}.

5.2.2 Experimental Details

Polycrystalline samples of $RCrO_3$ (R = Yb, Er, Y and Sm) were prepared by solid state reaction of stoichiometric quantities of R_2O_3 and Cr_2O_3 at 1173 K for several hours followed by two more grinding and heating steps. Phase purity was confirmed by Rietveld refinement on the x-ray powder diffraction data collected with a Panalytical X'Pert Pro diffractometer (and analyzed with the Fullprof software package[347]). The magnetic properties measurements, isothermal magnetization curves $M(H)$ were carried out in a commercial (MPMS Quantum Design) Superconducting Quantum Interference Device (SQUID) magnetometer in several temperature spans, depending on the sample. $M(H)$ isotherms were obtained by varying the field between 50 to 0 kOe for all samples. Previous to the measurement and in order to minimize any remanent field present in the superconducting coils and destroy any previous field effect on the sample, at room temperature, the field was set to 10 kOe and then to 0 in an oscillating mode. The sample was then cooled-down to the lowest temperature to be measured. After stabilizing the temperature, the measurement was performed varying the field from 50 down to 0 kOe (in 40 steps). At each step the magnetization was measured at a fixed temperature and field. Once back at initial field (0 kOe) the sample was heated up all the way into the paramagnetic region ($T \gg T_N^{Cr}$). Only then the sample was cooled to a new measurement temperature above the previous one (loop preocess)[289]. The temperature range was adjusted in order to span over the ordering temperatures of the Cr^{3+} and R^{3+} sublattices. Afterwards, the magnetic entropy change $[-\Delta S_M(T)]$ was calculated using the first quadrant isothermal $M(H)$ curves.

The refrigerant capacity (R_C), an important parameter to evaluate magnetocaloric materials is determined for each value of field, by the magnitude of $-\Delta S_M$ and its full width at half maximum (δT_{fwhm}). The values of the magnitude of $-\Delta S_M$ and its full width at half maximum were obtained by fitting the $-\Delta S_M(T)$ with a Lorentzian peak function.

5.2.3 Results and Discussion

5.2.3.1 Crystalographic characterization

The crystallographic propertied were investigated using XRD analysis. The resulting XRD pattern were analyzed using Fullproof software and all chromites samples $RCrO_3$ (R = Yb, Er, Y, Sm) presented an orthorhombic perovskite structure, that belong to the space group *Pnma*. The results are summarized in table 5.2.

All solid state synthesized $RCrO_3$ powders were confirmed to be single phase by XRD. The obtained parameters from the structural refinements (Rietveld refinement fits) are summarized in table 5.2. The results are ordered by ionic radius size increase,

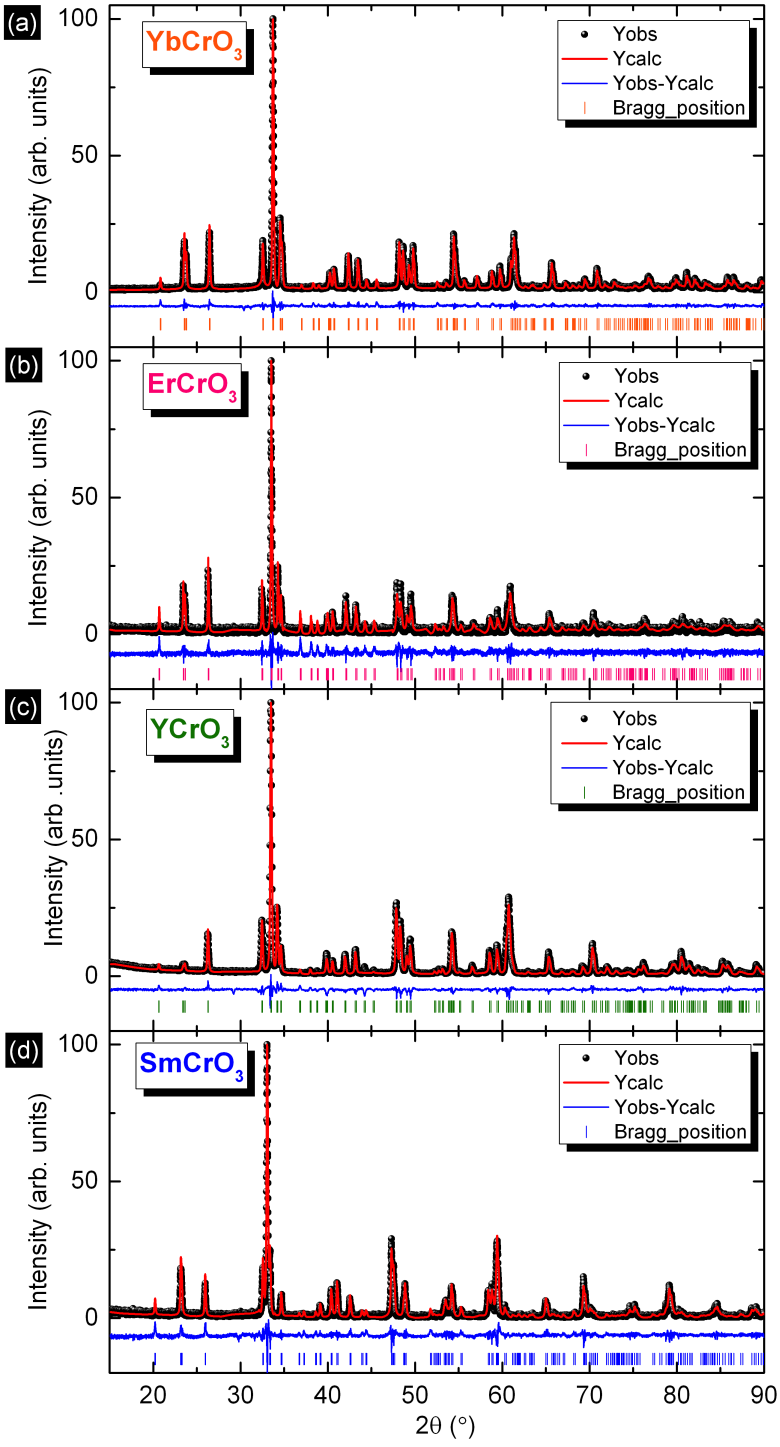

Figure 5.7 – Room temperature of Rietveld refined powder XRD pattern of $YbCrO_3$, $ErCrO_3$, $YCrO_3$ and $SmCrO_3$ samples after the final treatment.

Yb→Er→Y→Sm, where it was considered a trivalent positive charge and an eight-fold coordinated site, obtaining the values 1.042, 1.060, 1.075 and 1.133 Å respectively.

Table 5.2 – Summary of obtained structural parameters and atomic positions for $RCrO_3$ system at room temperature and magnetic transition temperatures.

R=		Yb	Er	Y	Sm
Ionic radius ()		0.985	1.004	1.019	1.079
a ()		5.4991	5.5091	5.5157	5.4970
b ()		7.4847	7.5212	7.5309	7.6436
c ()		5.1918	5.2275	5.2419	5.3670
$V(^3)$		213.7	216.6	217.7	225.5
ρ (g/cm^3)		8.190	9.316	5.902	8.166
Cr-O1-Cr		143.27	146.60	146.89	153.14
R	*x*	0.0676	0.0669	0.0654	0.0525
	z	-0.0221	-0.0151	-0.0179	-0.0141
	Biso (^{2})	0.49	0.03	0.22	0.60
	Occ	0.84	0.77	0.74	0.54
Cr	Biso (^{2})	0.56	0.94	2.83	0.08
	Occ	0.82	0.88	0.60	0.56
O (1)	*x*	0.4507	0.47838	0.4721	0.48822
	z	0.1078	0.1055	0.1026	0.0842
	Biso (^{2})	0.78	1.38	0.08	0.89
	Occ	0.62	1.17	0.74	0.72
O (2)	*x*	0.2998	0.2961	0.2996	0.2916
	y	0.0404	0.0568	0.0542	0.0465
	z	-0.2821	-0.3124	-0.31144	-0.2954
	Biso (^{2})	0.31	2.74	1.27	2.17
	Occ	1.45	2.53	1.64	1.74
χ^2 (%)		1.54	2.45	1.24	1.37
$T_N^{Cr^{3+}}$ (K)		118	134	141	193
T_{SR} (K)		12	22	–	34
$T_N^{R^{3+}}$ (K)		3 [265]	6.5	–	20

Atomic positions: R: 4c (x, ¼, z); Cr: 4b (0, 0, ½); O (1): 4c (x, ¼, z) and O (2): 8d (x, y, z)

The distorted perovskite structure with orthorhombic symmetry [space group *Pnma* (Nº 62)] was confirmed to all $RCrO_3$ chromites[265]. The unit cell volume increase with the ionic radius due to the linear increase of *b* and *c* parameters and an almost constant value of *a* cell parameter. We should point out that in the case of R = Sm a reduction of the lattice *a* parameter is observed. Nevertheless the volume increase is still observed. The decrease of the lattice parameter *a* is compensated with a larger increase of the *b* and *c* parameters. Simultaneously with the increase of the R cationic radius size (Yb→Sm:Δ = +0.094) a decrease of the octahedral tilting of the perovskite cell (distortion of the structure from the ideal RBO_3 cubic perovskite) is observed. The significant increase of the average $Cr-O_1-Cr$ bond angle from 143° to around 153° towards the ideal 180° of non distorted perovskites (Yb→Sm:$\Delta\theta$ = +10°) trends with an increase of T_N^{Cr}.

5.2.3.2 Magnetic characterization

Concomitantly with the increase in the octahedral tilting angle, towards that of the undistorted perovskite, an increase of the antiferromagnetic ordering temperature T_N^{Cr} (118 K → 193 K) is verified. This rise is due to the increase of the Cr^{3+}-Cr^{3+} exchange interaction which determines the magnetic properties of the system above about 100 K. Below this temperature the influence of the Cr^{3+}-R^{3+} interaction becomes increasingly impor-

tant and at the temperatures in the liquid helium range, where the R sub-lattice orders at T_N^R, the R^{3+}-R^{3+} interaction enters into consideration.

The characteristic magnetic transition temperatures obtained for these compounds are also summarized at the bottom of table 5.2 and are in good conformity with data present in the literature[208,248,439].

In Fig. 5.8 (c) are represented the $M(T)$ curves taken from 5 to 350 K with an applied field of 0.1 kOe for the $RCrO_3$ perovskites studied in this work. The effective paramagnetic moments of the magnetic atoms is depicted in the same figure.

As one can observe the magnetization curves shape of these perovskites exhibit different behaviors depending on the R-ion and in the thermal history of the sample (cooled with an applied magnetic field or not). In a general way, the Cr^{3+} spins in the $RCrO_3$ perovskites systems order antiferromagnetically below T_N^{Cr}. A weak ferromagnetic moment also arises due to the canting of the Cr atoms. One should point out that when R ion presents a non zero magnetic moment, two spin lattices are present in the system, which can be uncoupled or not. In the case of a zero field cooled mode, the Cr and R substructures are uncoupled and experience the same external applied field and thus contribute independently to the total magnetization. Whereas, in the FC measuring mode, when the Cr sub-lattice moments order at T_N^{Cr} a local field will be impose over the R moments. Hence, the R sub-lattice experiences a local field, which is the sum of the internal field due to the Cr sub-lattice and the external field. The resulting magnetization depends on the relative contribution of the sub-lattices and their temperature dependent magnetic behaviors.

For example, in the case of $YbCrO_3$ (the system with the smaller R radius in the Yb→Er→Y→Sm series) the canted Cr moments are coupled antiferromagnetically with Yb, leading to an antiparallel polarization of the Yb magnetic moments with respect to the ferromagnetic component of the Cr spins. As the temperature decreases the Yb moments eventually align with the internal field of the chromium moments. At the compensation temperature the Yb sub-lattice contribution equals that resulting from the Cr sub-lattice. Below that temperature a negative net magnetization is observed as the Cr sub-lattice component is overcome by the Yb moments polarization[248].

Successive isothermal magnetization measurements $M(H)$ (and respective isofield $M(T)$ curves obtained from those measurements), as shown in Figure 5.8 ((a), (b), (d) and (e)), $YbCrO_3$, $ErCrO_3$, $YCrO_3$ and $SmCrO_3$, were used to extract further information on the effect of the R ion substitution on the magnetocaloric behavior. On the left side of Fig. 5.8 are the curves centered on T_N^R and on the right side centered on T_N^{Cr}. As expected for R=Y, which has a zero magnetic moment no low temperature R-ordering exists and so no measurements were made in that temperature range for $YCrO_3$.

As we can observe, the difference of R-site cations has a clear impact on the magnetic susceptibility temperature behavior. All samples exhibit a paramagnetic behavior at room temperature and undergo several magnetic transitions upon cooling (see table 5.2). The characteristics magnetic transitions are easily identified by a simple figure

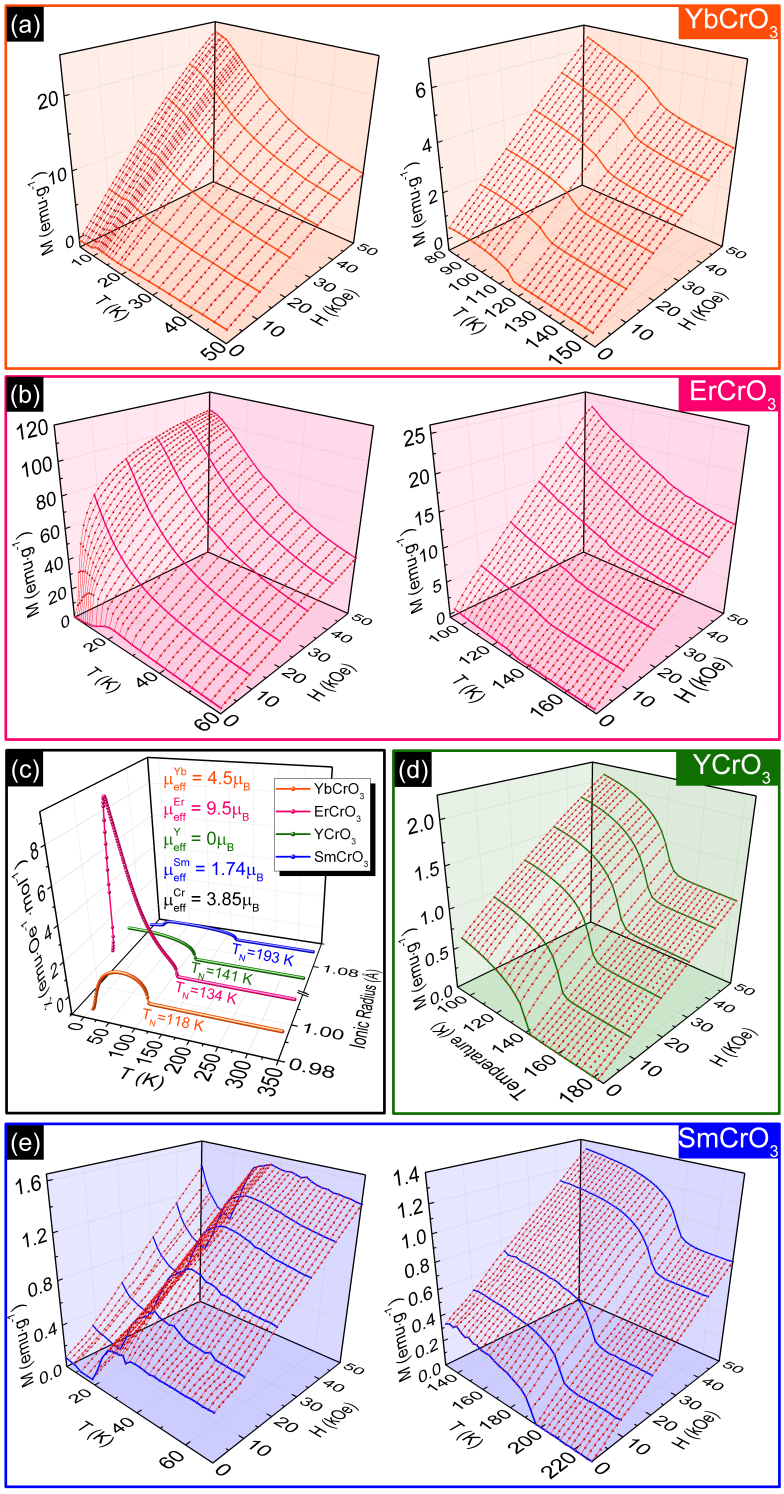

Figure 5.8 – Isothermal [M(H)] and isofield [M(T)] curves at different temperatures ranges (around the R^{3+} and Cr^{3+} sub-lattices ordering temperatures) while decreasing the magnetic field from 50 to 0 kOe for the $YbCrO_3$, $ErCrO_3$, $YCrO_3$ and $SmCrO_3$ (**a**,**b**,**d** and **e** respectively). (**c**) Isofield [*M*(*T*)] curves for the different systems taken with an applied field of 0.1 kOe.

inspection (colored lines). As mentioned above, T_N^{Cr} evolves towards high temperatures with the increase of the ionic radius, while T_N^R and and T_{SR}, do not seem to to follow an obvious trend (see bottom of table 5.2). Due to the low values of T_N^R and their proximity with T_{SR} hereafter we will refer the low temperature transition observed in the $M(H)$ curves simply as T_N^R.

Above T_N^{Cr} the $M(T)$ curves behaves linearly, indicating a non correlated spin behavior. Upon T_N^{Cr}, where the system goes from a paramagnetic to a canted antiferromagnetic state, the $M(T)$ curves show an increase in the magnetization value. Below that temperature the magnetization seems to saturate with the exception of $ErCrO_3$. This magnetization trend is observed for the measurements performed in all range of applied magnetic fields. Furthermore, the Cr^{3+} ordering temperature of each system (magnetization step increase) seems to be independent of the applied field.

In the case of the measurements at lower temperatures (left side of Fig. 5.8), a small bump around T_N^R is observed for the lowest applied magnetic field for $YbCrO_3$ and $ErCrO_3$. The bump maximum shifts towards lower temperatures and is accompanied by its broadening when going for the largest applied field. The $SmCrO_3$ sample shows an almost field independent behavior with a step decrease in the magnetization value at T_N^R. At low fields, the magnetization increase, that is observed since below T_N^{Cr}, alts at T_N^R and a decrease in magnetization is in place below this temperature. For higher applied magnetic fields this inversion in the magnetization increase ceases to manifest and only a continuous increase is observed. This seems to hint that with lower applied magnetic fields, a certain degree of uncoupling of the two magnetic sub-lattices is still present, similarly to what happens to the isofield zero field cooled measurements.

The highest magnetization values were recorded in the low temperature transition (T_N^{Er}) in $ErCrO_3$ (110 emu g^{-1}) while the lowest value was recorded for $SmCrO_3$ ($\sim$ 1.35 emu g^{-1}) for the high temperature magnetic transition (T_N^{Cr}). This comes in good agreement when considering the magnetic moment variation of the cations of this systems, 4.53, 9.59, 0.85 and 3.87 μ_B for Yb, Er, Sm and Cr respectively (see Fig. 5.8 (c)).

The coercive field ($H_C = (H_\downarrow - H_\uparrow)/2$, where $H_\downarrow$ and $H_\uparrow$ are the left and right coercive fields), described as field necessary to reduce the magnetization to zero, can be a source of information about the intrinsic mechanism of a system ordering. By overlapping the coercive field and magnetic susceptibility information additional knowledge concerning the system ordering intrinsic mechanism can be achieved. Figure 5.9 shows the normalized coercive field and Isofield [$M(T)$] curves as a function of temperature for the different materials.

The $YCrO_3$ results presents the more simple interpretation for the reason that it has only one magnetic ion in its formula. Here, the coercive field mimics the behavior of the magnetic susceptibility. In the paramagnetic regime a zero value is observed, which increases below T_N^{Cr} reaching an almost temperature independent stage at the lowest temperature measured.

For the cases of $SmCrO_3$ and $YbCrO_3$ we observe a concomitantly increase of the

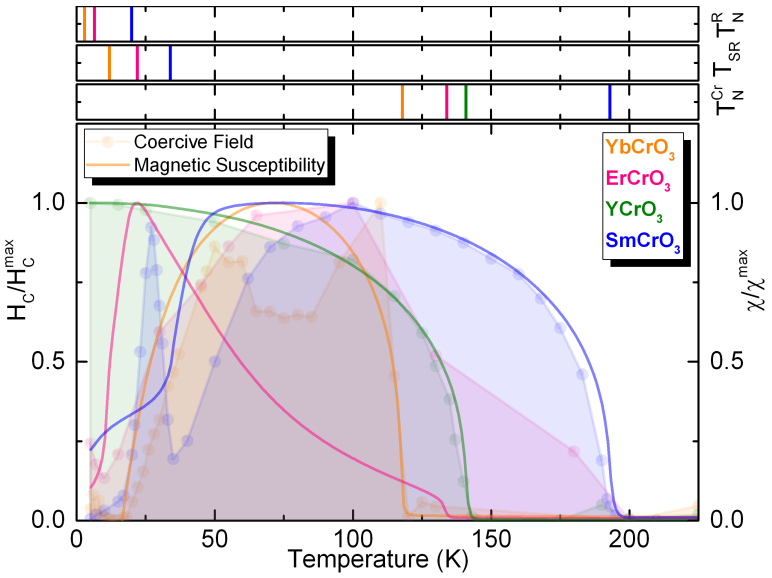

Figure 5.9 – Normalized coercive field and isofield [$M(T)$] curves for the $YbCrO_3$, $ErCrO_3$, $YCrO_3$ and $SmCrO_3$.

magnetization susceptibility with the increase of the coercive field below T_N^{Cr}.

Furthermore, the coercive field temperature variation seems to follow the magnetic susceptibility curve almost down to the spin reorientation temperature. Here, the decrease in the magnetic susceptibility is preceded by a decrease in the coercive field. Decreasing further the temperature the coercive field increases, showing a maximum before the T_N^R. This sudden increase in H_C results from the development of an exchange anisotropy due to the reorientation of the R^{3+} moments with respect to the canted Cr^{3+} components. Further down, the decrease in coercivity suggest a strong AFM contribution from R^{3+} ions that dominates at low temperature, giving rise to a complex behavior at low temperatures. For the case of $ErCrO_3$ the presence of a coercive field is already perceived at a much higher T than T_N^{Cr}. This seems to hint to a different mechanism present in this compound in the paramagnetic regime. For lower temperatures the H_C seems to go accordingly to the other systems.

5.2.3.3 Magnetocaloric effect

Magnetic entropy change versus temperature was calculated applying Eq. 1.9 to the $M(H)$ curves of Fig. 5.8 for different magnetic field changes and for the different systems in study are shown in Fig. 5.10.

The maxima in isothermal magnetic entropy change versus temperature [$\Delta S_M(T)$] for different maximum variations of the applied magnetic field (H_{max}), are peaked close to T_N^R and T_N^{Cr}, left and right side of figure respectively. The $-\Delta S_M$ plots show a sharper peak near T_N^{Cr} than near T_N^R (or T_{SR}) for all systems. It is at T_N^{Cr} in $SmCrO_3$ that the smallest value of the full width at half maximum (δ_{fwhm}) is obtained. This behavior is expected because it is in $SmCrO_3$ and at T_N^{Cr} that the transition spans over the narrowest

temperature range. Furthermore, the transitions at T_{SR} and T_N^R are very close to one another resulting in a variation of the magnetization in a larger temperature range and therefore a broader peak in $-\Delta S_M$.

The entropy change due to the MCE is related to the slope of the temperature dependence of the magnetization. Thus $ErCrO_3$ is the sample studied in this work showing the greatest greatest magnetic entropy change 0.75 $JK^{-1}kg^{-1}$ for a H_{max} = 50 kOe (see table in Fig. 5.10 (c)). Furthermore, the ordering of large magnetic moments, such as the 9.5 μ_B of the Er^{3+} ion, can cause a large change in magnetization, and is therefore expected to have a large MCE.

Literature shows that $SmCrO_3$ shows a peculiar magnetic behavior due to the competition between the external field, thermal activation energy and antiparallel $Sm^{3+} - Cr^{3+}$ spin interaction[245] which leads to the observation of a magnetization reversal and exchange bias. The R^{3+} sub-lattice orders antiferromagnetically to the Cr^{3+} sub-lattice causing a decrease in the magnetization. As a result, the magnetocaloric effect should be larger at a transition which involves the larger portion of the available magnetic entropy. Generally, one would expect that the splitting of the total available magnetic entropy would decrease $-\Delta S_M$ near the two successive transformations. Additionally, the Cr^{3+} ordering at T_N^{Cr} results in a small $-\Delta S_M$. Therefore, a Cr^{3+} spin-reorientation transition is not likely to cause a significant $-\Delta S_M$[433]. The magnetic field can decrease the antiferromagnetic order and finally convert it to the ferromagnetic one. This process is accompanied by a field-induced MCE (and $-\Delta S_M$) sign change[440] *i.e.*., the $SmCrO_3$ sample possesses both inverse (positive) and normal (negative) MCE in the low temperature regime. The presence of two successive MCE peaks in this temperature range leads to a large operating temperature window ($\sim$ 47 K) with one thermodynamic cycle.

In all samples and in both temperature ranges, an increase of the intensity of the magnetic entropy change with the increase of the maximum magnetic applied field is also observed.

The evolution of $-\Delta S_M$ considering the ionic radius and the total effective paramagnetic moments in the $RCrO_3$ samples are plotted in Fig. 5.11 (a) and Fig. 5.11 (b), respectively. From these figures we can observe that two scales of values are present, one for $-\Delta S_M$ at T_N^R and one for $-\Delta S_M$ at T_N^R. All systems present larger $-\Delta S_M$ (in module) at T_N^R. This is not unusual because in the higher temperature transition almost only the $Cr^{3+} - Cr^{3+}$ interactions contributes to the sample magnetism. While at lower temperatures we have the full contribution of all magnetic ions to the system magnetization.

Furthermore, $-\Delta S_M$ at T_N^{Cr} was found to monotonically decrease with the ionic radius increase, with the exception of $ErCrO_3$ (purple zone) where the largest value was obtained ($-\Delta S_M$ = 13 $Jkg^{-1}K^{-1}$). The values R = La, Gd, Dy from literature, were also included[212]. For the values obtained near T_N^R, a maximum is evident[433]. The same is true at T_N^R when studying $-\Delta S_M$ with the evolution of the total effective paramagnetic moment. In the case of the values obtained at T_N^{Cr} a monotonic increase seems to be

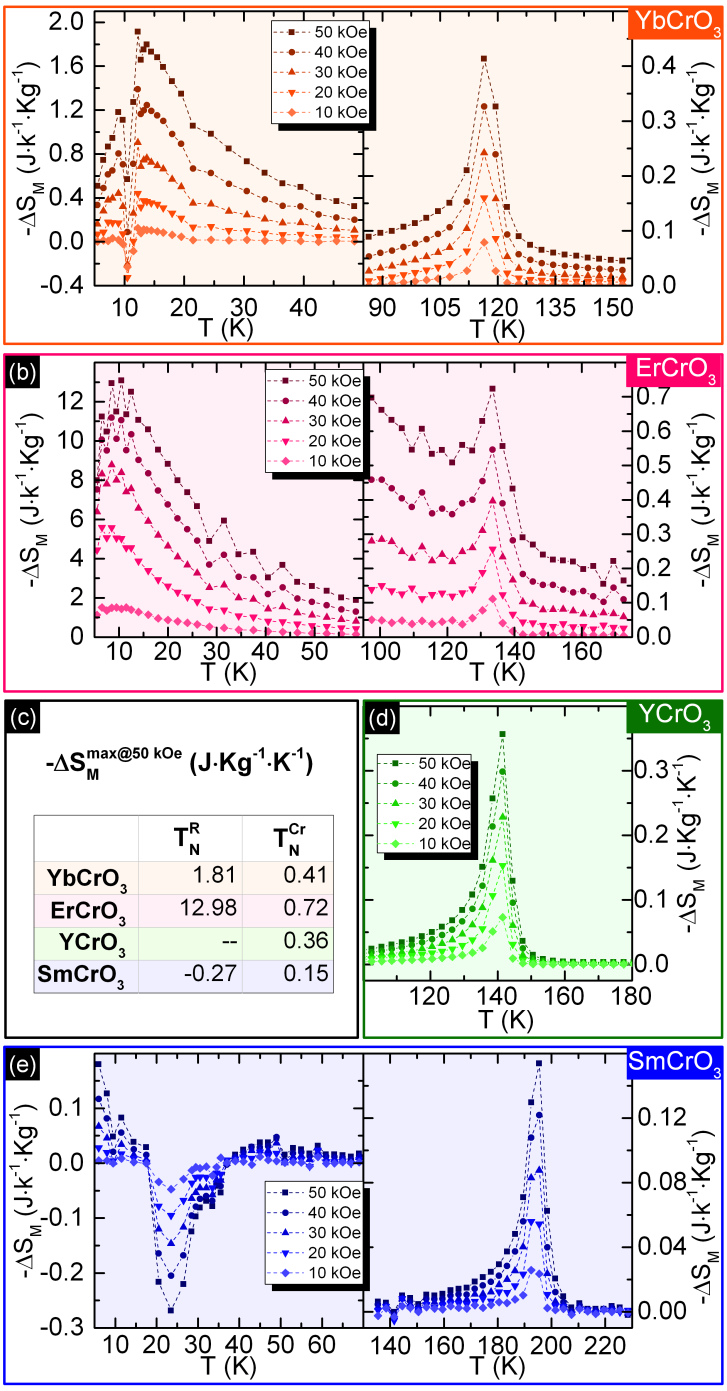

	T_N^R	T_N^{Cr}
$YbCrO_3$	1.81	0.41
$ErCrO_3$	12.98	0.72
$YCrO_3$	--	0.36
$SmCrO_3$	-0.27	0.15

Figure 5.10 – Magnetic entropy changes with respect to temperature at different field changes for $YbCrO_3$, $ErCrO_3$ $YCrO_3$ and $SmCrO_3$, near T_N^R (left) and T_N^{Cr} (right), from top to bottom respectively.

in place, with the increase of the total paramagnetic moment[i] and decrease with R ion radius decrease.

Finally we see in Fig. 5.11 (b) that the use of a R magnetic ion helps to enhance the magnetic entropy variation near T_N^{Cr}, *i.e.* the highest $-\Delta S_M$ are observed for samples with the highest μ_{eff}. This clearly shows that already at this temperature, where the Cr magnetic sub-lattice orders, the system, or more specifically the Cr ions interactions are already influenced by the magnetic R ions.

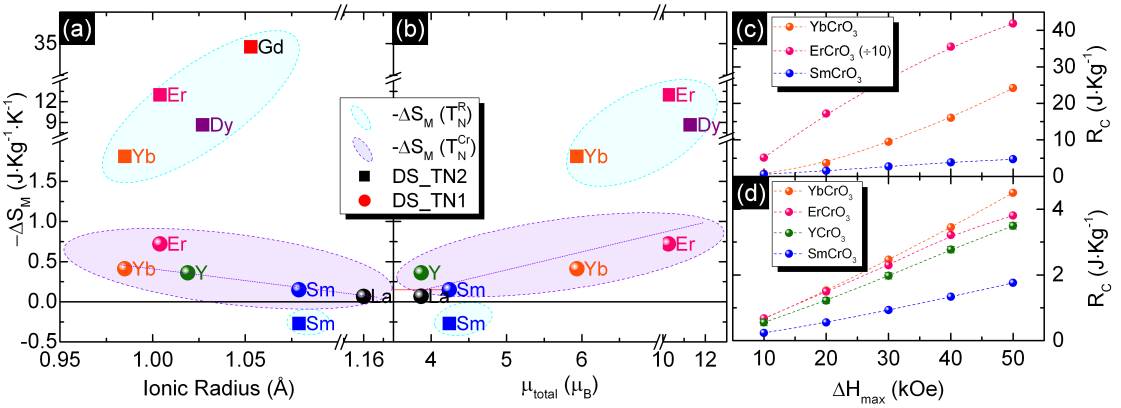

Figure 5.11 – Magnetic entropy changes with respect to the different R^{3+} ions (**a**) and to total effective paramagnetic moment μ_{total} (**b**) for a field variation of 5 T. (**c**) and (**d**) show the refrigerant cooling power for the different systems near T_N^{Cr} and T_N^R, respectively.

5.2.3.4 Refrigerant cooling power

An estimation of the refrigerant cooling power (R_C) value for bulk $RCrO_3$ samples was performed. The results are depicted in Fig. 5.11 (c) and Fig. 5.11 (d) near T_N^R and near T_N^{Cr}, respectively. As expected from the previous results, $ErCrO_3$ presents the largest capacity to be applied as a material for magnetic refrigeration (at both ordering temperatures). Also, an almost linear increase is observed with the increase of ΔH_{max}.

Note that these values are an approximation since in some of the results the extraction of $-\Delta S_M^{max}$ and δ_{fwhm} is not straight forward and is prone to large errors.

Furthermore, the results show a lesser difference between all systems for the calculations near T_N^R than for T_N^{Cr} where a larger distribution of values are observed. For T_N^R the values range from 0.2 with an applied field of 10 kOe to a maximum of almost 75 for an applied field of 50 kOe. No major difference between the other systems is evident. All systems shows an increase of R_C with applied field, where $YbCrO_3$ shows the largest increase[83].

We foresee that mix cations systems or even doping with other ions may be a good approach to enhance the observed effect[83,433,438]. This would provide a more in depth

[i] $\mu_{total} = \sqrt{\left(\mu_{eff}R^{3+}\right)^2 + \left(\mu_{eff}Cr^{3+}\right)^2}$

knowledge of these systems and could pave the way to the applications of materials in magneto refrigeration system.

While this systems present smaller values than those observed in some other magnetocaloric materials, including Gd metal[83], understanding the mechanisms producing the MCE in $RCrO_3$ may lead to better materials in the future.

5.2.4 Conclusions

In conclusion, a comparative study of the magnetization, magnetocaloric effect and refrigerant capacity properties of orthorhombic $RCrO_3$ compounds was carried out. The R ions radius increase was found to slightly increase the Cr^{3+} ordering temperature.

The magnetic entropy change due to the magnetocaloric effect was calculated from the isothermal magnetization measurements, and was found to increase with the total paramagnetic moment increase. The use of a R magnetic ion helps to enhance the magnetic entropy variation at T_N^{Cr}.

We show that $ErCrO_3$ presents a significant magnetic entropy change, $-\Delta S_M$ = 13 $Jkg^{-1}K^{-1}$ while $SmCrO_3$ has an inverse $-\Delta S_M$ of –0.3 $Jkg^{-1}K^{-1}$. The refrigerant capacity, calculated near the transition temperature of the R^{3+} ion for applied fields up to 50 kOe varies $R_C = [0.2 - 75]$ Jkg^{-1}.

5.3 Local Probing $RCrO_3$ perovskites

This work presents an atomic scale study of the electric field gradient (EFG) in the rare earth orthochromites $RCrO_3$ (with R= Yb, Er, Y and Sm) with perovskite structure. The EFG temperature dependence at the R site was followed via perturbed angular correlation measurements with the ^{111}In and ^{111m}Cd probes. The results are compared with *ab-initio* calculations performed to obtain the EFG at the R site in the $RCrO_3$ system with different rare-earth elements. For each compound the EFG was studied in the 1000 K to 10 K temperature range in order to obtain information across the systems phase transitions. In particular, $ErCrO_3$ sample shows an EFG change from a slightly distorted axial symmetry to a EFG with axial symmetry, providing a microscopic evidence that the local point symmetry of the crystal has changed. $YCrO_3$ PAC results are compatible with the appearance of local $P2_1$ symmetry observed by PDF. Our data on $SmCrO_3$ show that a distortion of the high temperature local environment start to develop below 300 K within the paramagnetic phase. The emergent distorted local environment is compatible with the structure change from *Pbnm*[ii] to $Pna2_1$. Although our data might be compatible with the most recent reports, where polar octahedral rotations and/or cation displacements are at the origin of a polar order in the paramagnetic state, remarkably, they point to a

[ii] In some publications, a *Pnma* or a pseudo-cubic lattice are introduced for $RCrO_3$ perovskites. There is a 45°rotation between the *Pbnm* and the pseudo-cubic indexing. Axes are switched between the *Pbnm* and *Pnma* indexing.

more subtle scenario, where locally an inhomogeneous state emerges. In this new state regular and distorted environments (most probably polar and non polar states) coexist.

For sake of section completeness we review here again the most important aspects from literature relevant for our analysis.

5.3.1 Overview

Almost a decade ago, it was found that rare earth orthochromites with the formula $RCrO_3$ (*e.g.* R=Yb, Er, Y, Lu and Sm) exhibit rich and varying physical properties, including magnetic, semiconducting, ferroelectric, multiferroic properties and so on. Thus, making $RCrO_3$ perovskite-type oxides an interesting and meaningful object of study, for both fundamental physics (either in theory or experimental point of view) and applied related issues. The development of any suitable application is, obviously, dependent on the fundamental understanding of the material properties[59,441].

$RCrO_3$ compounds originate from an ideal cubic structure, however, due to the sizes of the ions, they crystallize in the orthorhombic $GdFeO_3$-type perovskite structure (space group *Pnma*)[218,219]. Here, the larger atoms R are located at the center of a cube, the Cr atoms are on 8 vertices and oxygen atoms occupy 12 positions in the middle of each side of the cube. Different structural distortions are present in these compounds (from cubic to orthorhombic or rhombrohedric symmetry)[203–206], which can be driven by external parameters like temperature, pressure or chemical composition. Additionally, distortions in this structure may lead to new magnetic and electrical properties, with great scientific and technological interest[207,208]. Furthermore, the different ferroic orders that these multiferroic perovskites may exhibit, such as ferromagnetism, ferroelectricity, and/or ferroelasticity, adds a large contribute to this interest[26,91,212].

Canted antiferromagnets with a weak ferromagnetic component, their Néel magnetic transition temperature (T_N) decreases with decreasing radius of the R^{3+} ions (*e.g.*, T_N = 288 K in $LaCrO_3$ and T_N = 112 K in $LuCrO_3$). Some $RCrO_3$ compounds with R=Nd, Sm, Gd, Er show Cr^{3+} spin-reorientation transitions at lower temperatures[245,261]. At very low temperatures, spins of R^{3+} ions undergo antiferromagnetic (AFM) ordering. Some members of the $RCrO_3$ family show magnetization reversal (or negative magnetization) phenomena[245–248].

Rare-earth orthochromites of the formula $RCrO_3$ are currently at the center of great controversy regarding ferroelectricity. When R=Dy, Pr, Ho, Yb, Er, Y, Lu, Sm they are claimed to be ferroelectric while when $R = La, Nd$ are not[218,219,230,253]. While dielectric permittivity anomalies near 400-500 K in the heavier rare-earth chromites were associated with non-centrosymmetry others claim that the polarization observed in these systems is due to the combined effect of the poling-field that breaks the R ion local symmetry and the exchange-field on the R ion from the Cr sub-lattice[208]. Accordingly, no spontaneous ferroelectric polar-order exists in these systems and the presence of a magnetic R-ion is essential to induce a metastable ferroelectric state. Contrarily, the appearance

of ferroelectricity without any correlation to the magnetic order, arising from polar octahedral rotations and/or cation displacements, was recently claimed[259]. Although these systems have been claimed as potential magnetoelectric materials additional efforts are needed to definitely validate this claim. In fact, ferroelectricity in $RCrO_3$ (R=Ho-Lu and Y) have not yet been demonstrated in contrast to the $La_{1-x}Bi_xCrO_3$ system where ferroelectric hysteresis loops were observed[442].

Since these properties might arise from local structural features that are not well described by methods based on long-range average structural models, the use of local probe studies is essential[205,218,245,259,427].

In this context, hyperfine methods, such as perturbed angular correlation (PAC) spectroscopy, might provide relevant additional knowledge. Considering these ideas, it becomes desirable to carry out additional investigations, specially with the help of nanoscale characterization techniques, to further examine locally the crystallographic, magnetic and electric structure properties of these perovskite systems. In this context, hyperfine methods such as perturbed angular correlation (PAC) spectroscopy are of the highest relevance. In fact, information on structural properties such as lattice transformation and/or distortion can be extracted by studying the electric field gradient (EFG) tensor obtained from the nuclear quadrupole hyperfine interaction. The EFG in the vicinity of the probe atom, which is due to asymmetries on the local charge distribution, allows to reconstruct the atomic and electronic environment of the atomic probe in the material. Furthermore, PAC has given proofs to be a valuable technique to study local anomalies[169,170,352].

Information on local lattice properties can be extracted by studying the electric field gradient and can assist in clarifying the validity of the claimed ferroelectricity[441] in $RCrO_3$.

In this work $RCrO_3$ (R = Yb, Er, Y, Sm) compounds (also known as orthochromites) were studied. The samples were produced by means of solid state method and analyzed by X-Ray Diffraction. The temperature dependent EFG study, using the $^{111}In \rightarrow {}^{111}Cd$ and $^{111m}Cd \rightarrow {}^{111}Cd$ PAC probe, was performed in a temperature range which comprehend the important magnetic and claimed electric phase transitions.The probe nuclei were introduced in the samples by diffusion or implantation method.

5.3.2 Experimental Details

Polycrystalline samples of $RCrO_3$ (R = Yb, Er, Y and Sm) were prepared by solid state reaction of stoichiometric quantities of R_2O_3 and Cr_2O_3 at 1173 K for several hours followed by two more grinding and heating steps (see section 2.6.3).

Phase purity was confirmed by Rietveld refinement on the x-ray powder diffraction data collected with a Panalytical X'Pert Pro diffractometer and analyzed with the Fullprof software package[347] (see section 5.2.3.1).

The magnetic properties measurements, isofield and isothermic magnetization curves

were carried out in a commercial (MPMS Quantum Design) Superconducting Quantum Interference Device (SQUID) magnetometer in several temperature spans, depending on the sample (see section 5.2.3.2).

PAC spectroscopy has been applied to study the atomic scale properties of this compound. To perform the EFG measurements, meaning $\gamma-\gamma$ PAC measurements[292], the systems were implanted with ^{111m}Cd ions [^{111m}Cd$\rightarrow^{111}$Cd, $t_{1/2}$= 49 minutes] with a small dose of 10^{11} atoms/cm^2 (dose lower than 1 ppm of the R/Cr concentration) 30 keV energy at the Isolde-CERN facility, with ^{111}In ions [^{111}In$\rightarrow^{111}$Cd, $t_{1/2}$ = 2.8 days] (same PAC probe state with I = 5/2 and Q = 0.77(12) barn) or the ^{111}In ions were introduced in the sample by diffusion process at C2TN-CFNUL and at Isolde-CERN. The process was carried out by wetting the sample in a ^{111}In activated solution. An annealing was performed to all samples, to recover from implantation damage or to facilitate diffusion process (see section 5.3.3.1).

PAC measurements were carried out on a 6-BaF_2 detector spectrometer[294] or in a 4-BaF_2 detector spectrometer (in the case of the diffusion procedure performed in Lisbon). For further experimental details see Refs. 352 and 354.

5.3.3 Results and Discussion

The hyperfine technique, PAC, as pointed out previously (see 2.5.1), has a great potential in probing at a local scale, and therefore, could be a good source of information for clarifying the validity of the claimed ferroelectricity in these systems along with probe possible local phenomena that could be in its origin.

In an ideal PAC experiment it is aimed that all the radioactive probes go to substitutional lattice sites. Usually that can be accomplished with an after implantation or diffusion annealing . Here some important factors have to be taken into consideration: annealing temperature, time and cooling method (slow cooling or quenched). In this way, in a first stage, several annealing testes were performed in order to determine the proper annealing conditions.

5.3.3.1 Post-implantation annealing

A study of the dependence of the EFG parameters and probe distribution as a function of annealing temperature and time was performed in order to achieve the best results possible. Thus, several PAC experiments have been performed by diffusing the ^{111}In isotope into the $RCrO_3$ perovskite (R=Yb, Er, Y and Sm), followed by different annealing conditions in order to help their diffusion into regular lattice sites. The post-diffusion annealings performed during this work took into consideration the stoichiometry of the different samples and the sintering conditions that were required to obtained them (temperature and atmosphere). Here we will focus our attention on the $YCrO_3$ results. Nevertheless, similar studies were also performed in the R = Yb, Er, Sm systems. The annealing conditions tested are summarized in table 5.3.

Table 5.3 – Annealing conditions used in the post-diffusion annealing in the $YCrO_3$ compound with the diffusion of ^{111}In parent probe isotope .

Sample	Atmosphere		Temperature (°C)	Dwell Time (h)	EFG parameters ω_0	η	δ (%)	Fraction (%)
YCO-1	Air		800	24	142(1) 158(3)	0.05(5) 0.6(1)	2.1(5) 32(4)	14(10) 86(10)
YCO-2	Air		900	1	142(1) 158(3)	0.07(5) 0.76(8)	6.1(5) 24(5)	15(5) 85(5)
YCO-3		+	900	13	142(1) 158(3)	0.07(5) 0.72(6)	6.1(4) 31(5)	26(5) 74(5)
YCO-4		+	1000	14	142(1) 158(2)	0.07(1) 0.72(5)	2.4(4) 26(5)	27(6) 73(6)
YCO-5		+	1000	14	142(1) 158(3)	0.1(1) 0.75(5)	2.1(4) 33(4)	25(5) 75(5)
YCO-6	Air		1000	24	141(1) 159(3)	0.09(3) 0.67(5)	1.4(3) 32(4)	22(3) 78(3)
YCO-7	Air	+	1000 1100	24 48	142(1) 158(1)	0.05(4) 0.74(4)	0.9(6) 39(9)	28(2) 72(2)
YCO-8	Air		1000	48	140(1)	0.05(1)	1.6(2)	100

Samples YCO-1 to YCO-7 where quenched after the annealing, rapid cooling in air from the annealing temperature to room temperature. Sample YCO-8 experienced a slower cooling.

The sample identified by YCO-2 to YCO-5 was submitted to several incremental annealings, at the end of each annealing a R(t) spectrum was collected. In the case of sample YCO-7 the annealing was processed in two stages, a first one at 1000 °C during 24 hours and a second one where the furnace temperature was increased to 1100 °C for more 48 hours coming from 1000°C. Apart from sample YCO-8, all the samples were quenched after the annealing, rapid cooling in air from the annealing temperature to room temperature. In the case of sample YCO-8, after being removed from the furnace it rested a couple of minutes inside the crucible and quartz tube in which the annealing was performed. As indicated previously the conditions are summarized in table 5.3.

After the annealing, the experimental $R(t)$ spectra were measured at room temperature and some representative examples are depicted in Fig. 5.12 (experimental $R(t)$ anisotropy function on the left and the Fts on the right). The information about the last annealing performed to the sample before the spectrum acquisition is also shown in the graph. The fits to the $R(t)$ functions are shown by the continuous lines in the spectra. Also in the spectra are represented the individual contributions of each fraction (local environment) to the total fit line (red line).

The fits to each experimental PAC spectrum were calculated numerically by taking into account the hamiltonian for the nuclear quadrupole interaction[396]. The final fit solutions were obtained after careful consideration of the different tested models, choosing the one that gave the best χ^2. In the end, the best fit to each spectrum was obtained considering that the ^{111}Cd probes interact with two EFG distributions (named EFG^{R_1} and EFG^{R_2}), which were assumed as Lorentzian-like.

In this way, the spectrum obtained at the lowest annealing temperature revealed an EFG^{R_1}, given by a smaller fraction of probe atoms ~14(10)% interacting with an EFG characterized by $V_{ZZ}^{R_1} \sim 81(1)$ V/Å^2 ($\omega_0^{R_1} \sim 142$ Mrad/s) and $\eta^{R_1} \sim 0.05(5)$ characteristic

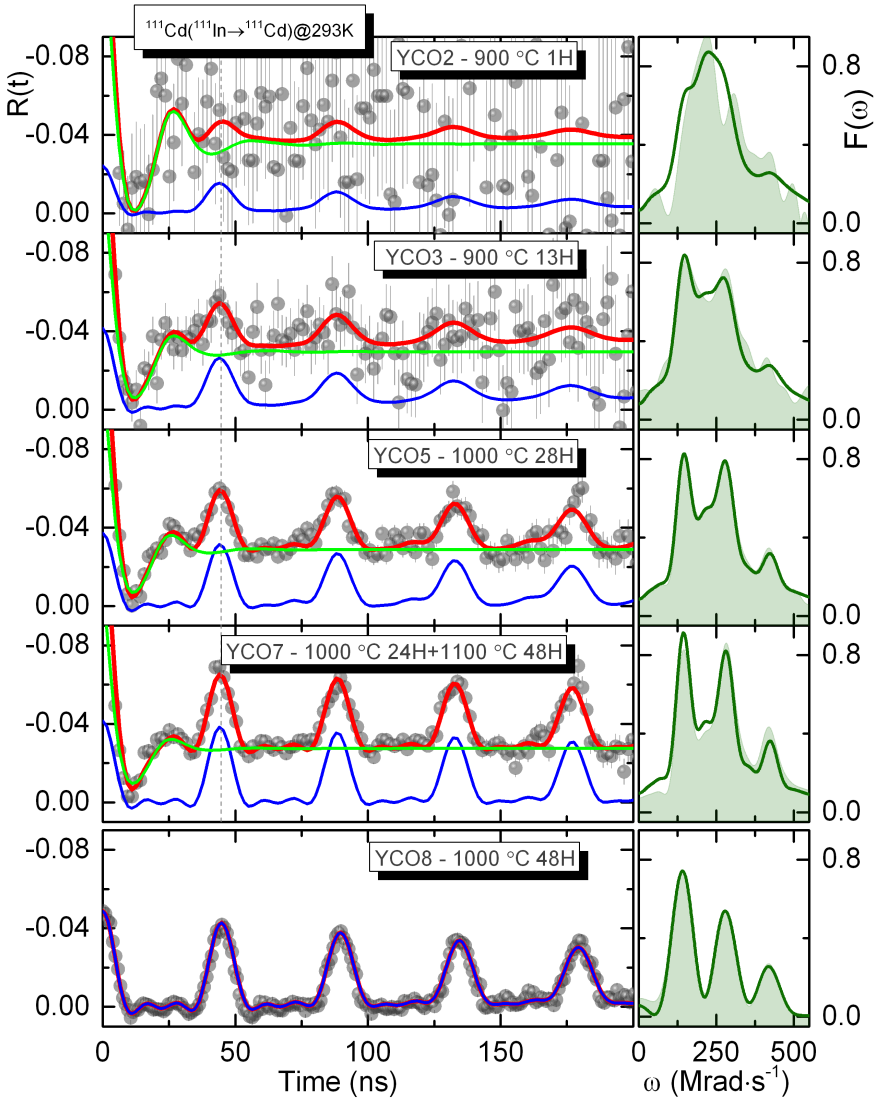

Figure 5.12 – Representative R(t) functions, corresponding fits (partial fits, corresponding to each individual EFG, are represented in blue and green) and respective Fourier transform taken at different annealing temperatures and dwell times for the ^{111}In probe on $YCrO_3$. The bottom $R(t)$ spectrum correspond to sample YCO-8 which experienced a slower cooling after the annealing.

of an EFG with a small deviation from axial symmetry[443]. The other EFG distribution observed (EFG^{R_2}) is given by ~86(10)% of the probe atoms interacting with it (majority phase) and it is characterized by $V_{ZZ}^{R_2} \sim 90(2)$ V/Å^2 ($\omega_0^{R_2} \sim 158$ Mrad/s) and an $\eta^{R_2} \sim 0.6(5)$. This EFG is extremely more attenuated than the previous one ($\delta^{R_1} \sim 2$ % and $\delta^{R_2} \sim 32$ %).

The EFG parameters obtained in the fits are also summarized in table 5.3. Notwithstanding, for a better visualization of the parameters evolution with different annealing conditions they are also plotted in Fig. 5.13. We should call to the attention that in order to avoid the overlap of points that correspond to annealings that have the same final temperature, an horizontal offset of ±10 K was employed. Also, to help its identifica-

tion we have denoted in the graph by strong dashed lines the sample that underwent successive annealings.

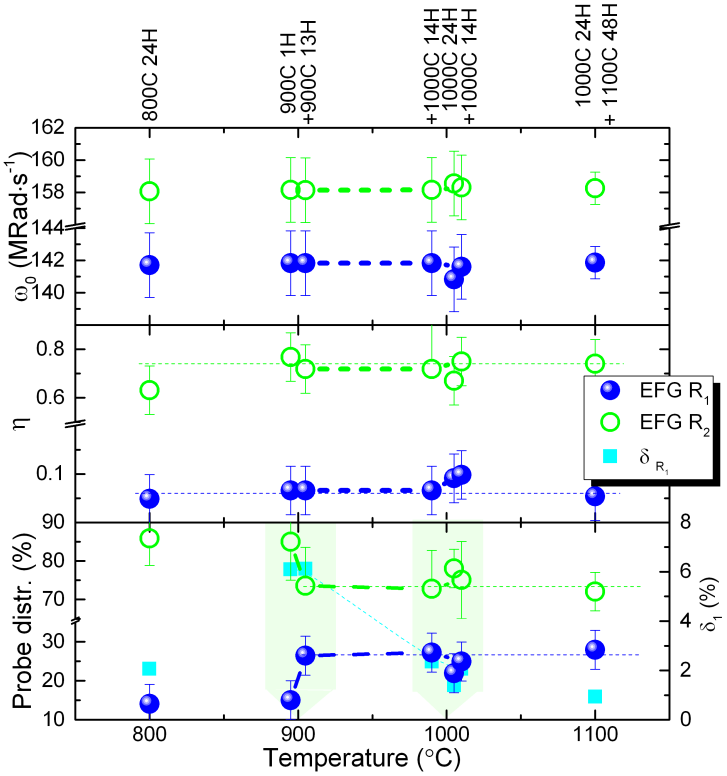

Figure 5.13 – Experimental electric field gradient fundamental frequency, asymmetry parameter and local probe distribution in the lattice sites, from top to bottom. Static attenuation parameter for EFG^{R_1} is represented in bottom right scale. (Thin dashed lines are guidelines for the eyes.)

Studying the evolution of the experimental $R(t)$ spectra depicted in Fig. 5.12, a clear difference with the increase of the annealing temperature and dwelling time can be observed, *i.e.*, a reduction of the $R(t)$ attenuation (static attenuation δ). When increasing the annealing temperature and dwelling time an increase of the number of probes sensing EFG^{R_1} is achieved. The number of probes interacting with EFG^{R_1} duplicates already with an annealing of 900 °C during 13 hours. As can be seen in the graph one hour does not seem to be sufficient. Furthermore, with further temperature increase and dwelling time another change (subtle) can be observed, this time in the in the static attenuation parameter of EFG^{R_1} (δ^{R_1}). Namely, for annealings with at least 1000 °C during 24 hours, δ^{R_1} trends to the lowest values observed. This result does not seem to be affected by the fact that the annealing was performed in one continuous or two cumulative firings. Furthermore, for all annealing conditions the room temperature ω_0 and asymmetry parameters for both EFGs remains constant.

The majority of the measurements presented in this work were performed quenching the sample after the annealing. However, in a later stage of our study further tests were conducted with ^{111}In isotopes incorporated into the sample by diffusion method with a slow cooling after the annealing. Here, we were able to achieve a R(t) spectra with

a single EFG (EFG^{R_1}) characterized by $V_{ZZ}^{R_1} \sim 79(1)$ V/Å^2 ($\omega_0^{R_1} \sim 140$ Mrad/s) and $\eta^{R_1} \sim 0.05(5)$, sample YCO-8. In sum, removing the sample from the furnace after the annealing, instead of rapidly cool it down, a slower cooling rate gives better results. Unfortunately, it was not possible to repeat all measurements with these conditions. It should be noticed that when using the ^{111m}Cd parent probe, the presence of two EFG was also observed. However, in this case different probe distribution between EFG^{R_1} and EFG^{R_2} was observed, 70–80% and 20–30% respectively. As before the increase of temperature and annealing time seems to improve the quality of the spectra by reducing the fraction of the more attenuated EFG environment.

In literature we can find local probing studies with the PAC technique in similar orthorhombically distorted perovskites (*e.g.* $LaCrO_3$, $LaFeO_3$, $LaMnO_3$, $LaCoO_3$) where the existence of this second EFG, EFG^{R_2}, is also observed[444,445].

Studies with $^{140}La \rightarrow ^{140}Ce$ in $LaMnO_3$ or with $^{111}In \rightarrow ^{111}Cd$ in $LaCoO_3$ showed a similar second EFG, with an unknown origin. However, the authors related this EFG to the presence of different La sites in the lattice arising due: to a structural defect; to oxygen vacancies[446]; to a minor structural phase change not detected by normal x-ray measurements[445]. These PAC studies hint that for these sites, where EFG^{R_2} is observed, a larger CoO_6 octahedra distortion is present, when compared to the observed EFG^{R_1} of the normal Co sites.

Furthermore, it has been reported that the diffusion and trapping of defects near the PAC probes (especially ^{111}In[447]) and their influence on the perturbation functions is still unclear[448]. This is not only a consequence of the fact that there is little information on defects (oxygen vacancies, charge transfers) in the perovskites, but also differences may arise depending on the method of preparation of the samples[449,450]. A more detailed study on this matter should be pursued in the future, for example PAC studies on single-crystal samples where such measurements may shed some light onto the so-far unexplained. Meanwhile in this work, we will focus our attention on EFG^{R_1}.

5.3.3.2 EFG dependence on the rare-earth ionic radius

In this section a systematic study of the dependence of the electric field gradients (EFG) properties were studied using the $^{111}In \rightarrow ^{111}Cd$ and $^{111m}Cd \rightarrow ^{111}Cd$ PAC probes at room temperature as a function of the rare-earth ionic radius (R^{3+}) is presented. The perturbed angular correlations (PAC) experiments have been performed by implanting the orthorhombic $RCrO_3$ (R= Yb, Er, Y and Sm) with ^{111m}Cd or diffusing the ^{111}In into the sample, following the procedure described in chapter 2. Afterwards the samples were annealed between 973 and 1173 K in air (or O_2 in the case of $YbCrO_3$) for 20 minutes to recover from implantation damage or annealed at 1273 K in air for 48 hours to diffuse the ions. After the annealing, the experimental $R(t)$ spectra were measured at room temperature [293-297] K. Presented on Fig. 5.14 are some selected experimental perturbation functions $R(t)$ and corresponding Fourier transforms. On the right the spectra

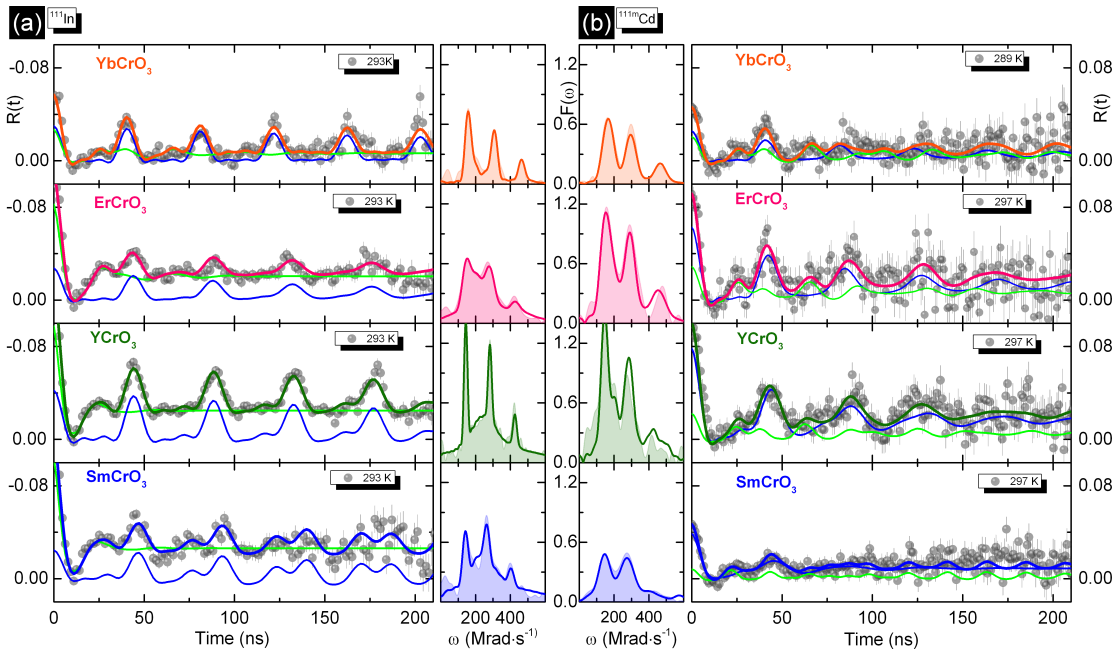

Figure 5.14 – Representative $R(t)$ functions, corresponding fits (represented as thicker lines over the R(t) spectra) and respective Fourier transform taken at room temperature for the **(a)** ^{111}In and **(b)** ^{111m}Cd probe.

measured with the ^{111}In probe and on the left the one measured with the ^{111m}Cd, from the largest ionic radius on top to the lowest on the bottom. The fits to each experimental PAC spectrum (continuous lines over $R(t)$) were calculated numerically by taking into account the hamiltonian for the nuclear quadrupole interaction[292,396]. The best fit to each spectrum was obtained considering that the radioactive probes interact with two different EFG distributions, which were assumed as Lorentzian-like.

Globally, the experimental R(t) spectra depicted in Fig. 5.14 are quite similar and the small differences found on the Fourier transforms are due to the different rare-earth substitution. These spectra are characterized by the coexistence of two EFG distributions (named EFG^{R_1} and EFG^{R_2}), which have been found in all compounds as mentioned before. A list of the EFG parameters obtained in these fits is summarized in table 5.4.

Table 5.4 – Summary of obtained fit parameters of the R(t) functions for $RCrO_3$ system at room temperature with the ^{111}In and ^{111m}Cd parent probe isotope. The indexes R_1 and R_2 refer to the two EFG distributions obtained from the fitting procedure.

R= Ionic radius (Å)		YbCrO3 0.985		ErCrO3 1.004		YCrO3 1.019		SmCrO3 1.079	
		^{111}In	^{111m}Cd	^{111}In	^{111m}Cd	^{111}In	^{111m}Cd	^{111}In	^{111m}Cd
EFG^{R_1}	ω_0 (Mrad/s)	147(1)	154(3)	142(1)	152(2)	142(1)	140(1)	133(1)	132(2)
	η	0.06	0.01	0.10	0.01	0.12	0.20	0.23	0.31
	δ(%)	1.0	4.8	3.4	10.3	1.4	8.4	0.8	15.1
	Probe(%)	55	56	25	78	30	78	19	82
EFG^{R_2}	ω_0 (Mrad/s)	148	150(3)	170(3)	163(3)	158(3)	157(3)	155(2)	170(3)
	η	0.50	0.53	0.60	0.82	0.54	0.55	0.64	0.84
	δ(%)	12.0	3.1	20.8	4.1	30.0	4.2	31.8	1.0
	Probe(%)	45	44	75	22	70	22	81	18

In order to extract maximum information and to fully understand the probes local-

ization in PAC experimental results, *ab−initio* calculations of the hyperfine parameters in the R and Cr sites on the orthorhombic lattice were performed in the framework of this study. Density functional theory calculations were carried out using linearized augmented plane wave + local orbitals method (LAPW+lo) as implemented in the WIEN2k code[317,318] which enable the interpretation of the experimental data (see section 2.5.1.4).

The calculations were performed in pure orthorhombic compounds using a set of lattice parameters taken from the literature[265], to have the best precision on the atomic positions. The relaxation of internal atomic positions has been also implemented to make a more accurate description of the EFG parameters (minimizing the atomic forces to values less than 5 mRy/a.u.). The iteration halted when the difference charge, energy and force were less than 0.001 e, 0.0001 Ry and 1 mRy/a.u. respectively for all compounds.

The muffin-tin radius R_{MT} for each compound are summarized in table 5.5:

Table 5.5 – Muffin-tin radius R_{MT} for the $RCrO_3$ (R=Yb, Er, Y, Sm, Gd, Nd, La) compounds

Sample	R_{MT}(R) (a.u.)	R_{MT}(Cr) (a.u.)	R_{MT}(O) (a.u.)
$YbCrO_3$	2.23	1.89	1.71
$ErCrO_3$	2.24	1.90	1.72
$YCrO_3$	2.16	1.91	1.72
$SmCrO_3$	2.32	1.89	1.71
$GdCrO_3$	2.27	1.89	1.71
$NdCrO_3$	2.31	1.88	1.70
$LaCrO_3$	2.38	1.85	1.68

The cutoff energy, which defines the separation between valence and core states was chosen to be –6 *Ry*. Inside the atomic spheres, the partial waves were expanded up to l_{max} = 10. Several *k*-points grids and maximum wave numbers for the plane waves were tested in order to reach a good convergence of the V_{ZZ} and η parameters. In this way, the number of plane waves was limited by a cutoff $R_{MT}K_{max}$ = 7.5 and a *k*-mesh of 120 K points in the irreducible Brillouin zone was used. The plane wave cutoff also known as magnitude of largest vector in charge density Fourier expansion is G_{max} = 12.

The exchange correlation potential was calculated using a Perdew-Becke-Erzenhof generalized gradient approximation (PBE)-GGA[320] following the work of *Ong et al.*[310] in which it was shown that a chromite $LaCrO_3$ should not be considered an highly correlated material, therefore GGA approximation was sufficient to describe the distorted Cr – O polyhedron.

A ferromagnetic configuration is considered for simplicity since the temperature range in which we will measure the hyperfine parameters and compare with calculations results, the sample should be paramagnetic. This approach has proven to show good results[321,322].

The results of the calculated EFG principal component at the R and Cr lattice sites and respective asymmetry parameters are presented in Fig. 5.15. Also in Fig. 5.15 are presented the experimental values obtained from the measurements using the ^{111}In and ^{111m}Cd probe isotopes together with data on $(Gd, Nd, La)CrO_3$ using ^{181}Hf parent probe

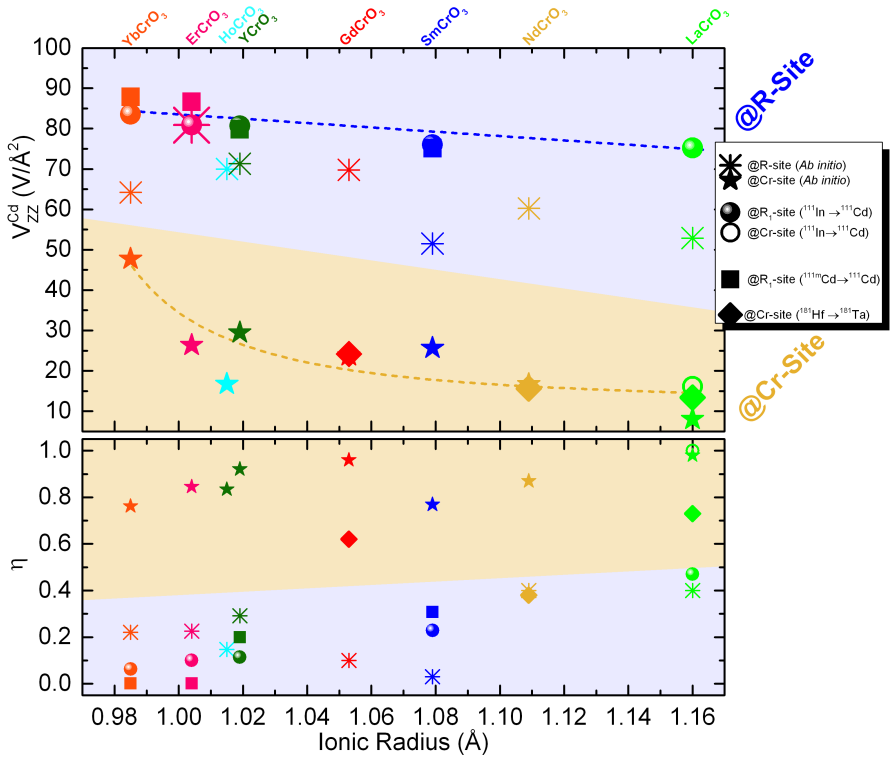

Figure 5.15 – Linearized augmented plane wave + local orbitals method EFG parameters in the rare-earth and chromium sites for the orthorhombic $RCrO_3$. Data on (Gd, Nd, La)CrO_3 using ^{181}Hf parent probe was taken from Refs 451 and 452. The dashed lines are guidelines to the eyes.

taken from literature[451,452].

In order to compare the calculated with the experimental values, the contribution originating from the core deformation of the probe under the presence of the lattice EFG has to be considered. This contribution can be computed using the Sternheimer anti-shielding factor (γ_∞)[iii] of the probe atom or of the native structure ion. The sum of this contribution and V_{zz}^{latt} is called the 'ionic contribution', and the EFG can be written as given by Eq. 2.29. Thus, the values obtained from the *ab−initio* calculations which are presented in Fig. 5.15 are in fact:

$$V_{zz}^{Cd} = \frac{V_{zz}^{R/Cr}}{\left(1-\gamma_\infty^{R/Cr}\right)}\left(1-\gamma_\infty^{Cd}\right) , \tag{5.5}$$

where V_{zz}^{Cd} is the calculated V_{zz} in the lattice sites of the rare-earth or the chromium, as measured with a ^{111}Cd probe.

The results of the *ab-initio* calculations show that we should expect a greater V_{zz} value for the rare-earth site, and a smaller one for the Cr site ($V_{zz}^{R} \sim 4V_{zz}^{Cr}$), while in the case of the asymmetry parameter a lower value (low distortion from axial symmetry) should be expected for the R site and a larger value (lack of axial symmetry) for the case of the Cr site. We should call to attention that these calculations were performed in a

[iii] $\gamma_\infty^{Cd} = -29.3$, $\gamma_\infty^{Cr} = -8.81$, $\gamma_\infty^{Yb} = -58.49$, $\gamma_\infty^{Er} = -59.18$, $\gamma_\infty^{Y} = -31.02$ and $\gamma_\infty^{Sm} = -61.94$

lattice without the substitution of the regular lattice site with the ^{111}Cd probe. Therefore, in the future the calculated V_{zz} and η values should be improved by taken into account the influence of the ^{111}Cd probe in the lattice to better validate our findings.

Nevertheless, when we compare our experimental results (V_{zz} and asymmetry parameter η) with the *ab-initio* calculations a reasonably good agreement is found for all compounds, clearly evidencing that EFG^{R_1} is related with probes substituting the rare earth site.

Furthermore, a clear tendency of these two parameter is also present, as evidenced by the guidelines in Fig. 5.15, where a decrease of V_{zz} and an increase of η with the increase of the R ionic radius is present. In fact, *Rearick et al.* observed in orthoferrites that in the heavier rare-earth system, the rare-earth-site EFGs are nearly axially symmetric and, as the rare-earth atomic number decreases, the EFG asymmetry η increases[443] and the EFG component V_{ZZ} decreases slowly.

In literature, the works of *Junqueira et al.*, *Dogra et al.* or *Carbonari et al.* present similar results to ours. In $LaCoO_3$ and $La(Cr, Fe)O_3$ where the $^{111}In \rightarrow ^{111}Cd$ probe was introduced in the samples by a chemical process, two *EFG* interactions are observed and associated with two non-equivalent crystallographic sites, one associated to the rare earth site and the other to the Cr, Fe site. *Rearick et al.* reported that for perovskites systems with heavier R ions, the ^{111}Cd probe substitute primarily the rare-earth sites while in systems with lighter R (larger ionic radius) it can substitute into both the B(Fe, Cr) and the rare-earth sites[443]. Similar findings were obtained in the work of *Dogra et al.*, were only the R site substitution was observed in $LaCoO_3$, while for $LaCrO_3$ and $(La, Lu, Ho, Eu, Y, Yb)FeO_3$ both sites were possible[443,444]. In these works, similar values of V_{zz} and η are observed in systems with a different rare-earth atom[444,445,451,452].

In our results we cannot observe any *EFG* corresponding to probes at the Cr site. We believe that the chemical process used by those authors for introducing the ^{111}In into the samples allows a distribution of the probes by the two lattice sites, whereas by implantation or by diffusion method does not.

The same authors present a similar PAC study using $^{181}Hf \rightarrow ^{181}Ta$ in $(Gd, Nd, La)CrO_3$ where only one EFG associated with probes at the B = Fe, Cr site was observed[451,452]. These values are plotted in Fig. 5.15 for a better visualization of the V_{zz} trend as a function of the rare-earth ionic radius.

In the following sections we will focus our attention on the EFG parameters of the main local environment of the rare-earth site EFG^{R_1}, hereafter denoted as EFG^R.

5.3.3.3 EFG temperature dependence

Representative samples of the orthorhombic $RCrO_3$ series (R=Yb, Er, Y, Sm) have been selected to study in detail the temperature dependence of the EFGs. The $^{111m}Cd \rightarrow ^{111}Cd$ PAC probe results have been complemented with measurements using $^{111}In \rightarrow ^{111}Cd$ diffused probes. Due to its half-life (2.8 days), ^{111}In probe is very suitable to perform

several measurements at different temperatures within a single implantation or diffusion.

As referred in the previous section, the majority of the PAC spectra have an unknown EFG most probably due to defects trapped near the substitutional lattice site or incomplete annealing. Nevertheless, $R(t)$ spectra will show all the partial fractions and the total fit result.

The PAC experimental results will be presented separately for each sample in the following subsections.

5.3.3.4 EFG dependence on temperature - $YbCrO_3$

In this subsection, the study of the EFG behavior in$YbCrO_3$ as function of temperature is presented. To perform the PAC experiments, the orthorhombically distorted antiferromagnetic $YbCrO_3$ sample was implanted with ^{111m}Cd or diffused with ^{111}In. The introduction of the isotopes into the sample followed the standard procedure described in section 2.5.1.6.

The implantation of ^{111m}Cd was proceeded by an 20 minutes annealing at 1073 K whereas the diffusion of ^{111}In was proceeded by an 18 hours annealing at 1273 K both in an O_2 dynamic atmosphere.

Figure 5.16 depicts the experimental $R(t)$ anisotropy function (left) together with the Fts (right) obtained in the $YbCrO_3$ system. The global fits to the $R(t)$ functions are shown by the continuous thicker orange lines in the spectra. In the case of ^{111m}Cd, data was collected between 650 K > T > 150 K, a temperature range that includes the reported ferroelectric transition (T_{FE}^{Yb} = 515 K)[218]) (see Fig. 5.16 (b)). The study using ^{111}In was initiated and a room temperature spectrum was acquired (see Fig. 5.16 (a)).

As presented in section 5.3.3.2, the spectra obtained at room temperature using the different probes reveal similar results, two EFGs, *i.e.*, two probe local environments, exists. We will only focus our attention in only one EFG, the one corresponding to the probes substituting the Yb lattice site. Nevertheless we show the second *EFG* distribution, EFG^{R_2}, that was included to account for the attenuation observed in all spectra and thus to improve the quality of the fits. This EFG^{R_2} is believed to be due to defects trapped near the substitutional lattice site or incomplete annealing in the $YbCrO_3$ samples (see section 5.3.3.2).

In this way, using ^{111}In we observe an EFG with a small deviation from axial symmetry, characterized by a fundamental frequency $\omega_0^{Yb_1}$ = 147(1) Mrad/s (V_{zz}^R = 84(2) V/Å^2) and $\eta^R \sim 0.06$ (δ^R = 5(2)%). Whereas in the case of ^{111m}Cd the observed EFG is characterized by by a fundamental frequency $\omega_0^{Yb_1}$ = 154(1) Mrad/s (V_{zz}^R = 88(2) V/Å^2) and $\eta^R \sim 0.01$ (δ^R = 15(4)%).

The thermal dependence of the EFGs main parameters (V_{zz} and η) obtained by our fits for both probes is depicted in Fig. 5.17 (a) and (b) respectively. The presented V_{zz} value correspond to the value obtained with a Cd probe at the rare earth-site.

The magnitude of EFG principal component decrease with the increase of tempera-

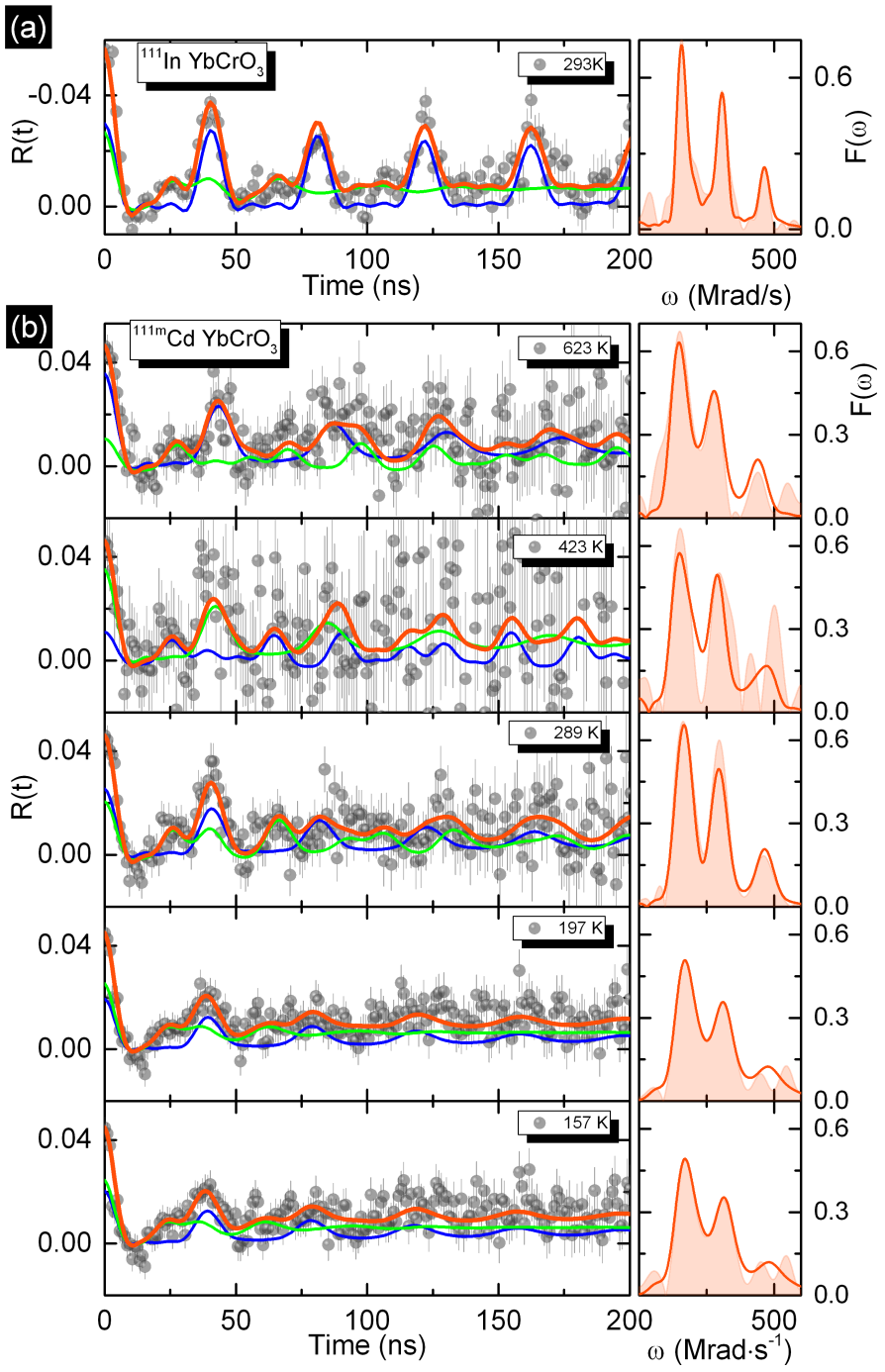

Figure 5.16 – Representative R(t) functions, corresponding fits and respective Fourier transform taken at different temperatures for the ^{111}In probes in $YbCrO_3$.

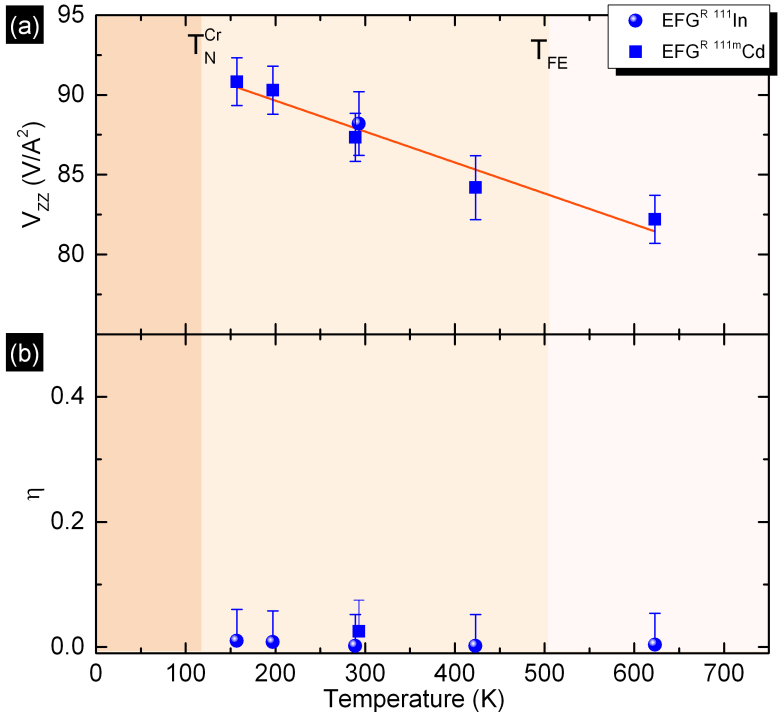

Figure 5.17 – **(a)** Experimental electric field gradient principal component. The continuous line represents a least-squares fit of the function $V_{zz}(T) = V_{zz}(0)[1 + \alpha T^k]$ to the data points. **(b)** Asymmetry parameter.

ture. It is known that the temperature dependence of the V_{zz} is governed by the atomic vibrations in the vicinity of the probe atom, which can be least-squares fitted according to Eq. 2.33. This trend is common for perovskite structures and is frequently associated with the increase of the atomic vibrations and (volume) thermal expansion, when increasing temperature[293]. The obtained coefficient for the rare earth site is then $\alpha_{Yb} = -2.1 \times 10^{-4}$ K^{-1}. However, the V_{zz} temperature dependence cannot be attributed exclusively to a thermal expansion because its coefficient is usually one order of magnitude smaller. Nevertheless, this temperature dependence V_{zz} coefficient is similar to those presented by manganites with perovskite structures, with the same order of magnitude (-2.9×10^{-4} K^{-1})[182] and one order of magnitude higher than in manganites with spinel structure (see chapter 4).

Other than the linear increase of V_{zz} as a function of temperature, no other changes were observed in EFG^{Yb}. Thus, we cannot provide further insights in the appearance of ferroelectricity in this system. Further PAC studies in this system should be pursued, specially near the claimed FE transition.

5.3.3.5 EFG dependence on temperature - $ErCrO_3$

In this subsection, the study of the EFG behavior in $ErCrO_3$ as function of temperature is presented. To perform the PAC experiments, the orthorhombically distorted antiferromagnetic $ErCrO_3$ sample was implanted with ^{111m}Cd or diffused with ^{111}In. The intro-

duction of the isotopes into the sample followed the standard procedure described in section 2.5.1.6.

The implantation of ^{111m}Cd was proceeded by an 20 minutes annealing at 973 K whereas the diffusion of ^{111}In was proceeded by an 48 hours annealing at 1273 K, both in air.

In the case of ^{111}In a study was made as a function of temperature (723 K > T > 27 K), a temperature range that spans over the reported ferroelectric transition and the magnetic ordering of Cr atoms sub-lattice.

Figure 5.18 depicts the experimental $R(t)$ anisotropy function (left) together with the Fts (right) obtained in the $ErCrO_3$ system using the diffused ^{111}In probe. The global fits to the $R(t)$ functions are shown by the continuous pink lines (thicker ones) in the spectra. Also, together with the $R(t)$ spectra are represented the lines corresponding to the individual fractions used to perform the fit (Please see Appendix B for the complete set of results).

The spectrum obtained at 723 K revealed an EFG characterized by a fundamental frequency of $\omega_0^{Er_1}$ = 136(1) Mrad/s ($V_{zz}^{Er_1}$ = 77(1) V/Å^2) and an asymmetry parameter η^{Er_1} = 0.14(5) which are in good agreement with similar systems (see section 5.3.3.2). A second EFG was used to improve the global fit (origin of this second EFG explained in previous section), characterized by a higher fundamental frequency, $\omega_0^{Er_2}$ = 171(4) Mrad/s ($V_{zz}^{Er_2}$ = 75(4) V/Å^2) and an asymmetry parameter η^{Er_2} = 0.56(9).

Below T = 473 K the $R(t)$ spectra was fitted with the same EFG^{Er_1} but with a slighter lower asymmetry parameter η^{Er_2} = 0.04(3).

Below 250 K in order to be able to perform reasonable fits we had to consider the scenario where the probes interact now with a magnetic hyperfine field, in addition to the EFG. Accordingly, the fits were performed considering a magnetic hyperfine field (combined interactions (EFG+MHF)), even if with a weak one. At 250 K the MHF parameters associated with EFG^{Er_1} are characterized by a Larmor frequency ω_L = 2.0 Mrad/s (B_{hf} = 0.1 T) and orientated at an angle $\beta \approx 60°$ with EFG^{Er_1} principal component V_{zz}. These values increase only marginally with decrease of temperature, and at 125 K we have ω_L = 9.4 Mrad/s (B_{hf} = 0.6 T) with the same β. Only well below T_N^{Cr} the strength of the magnetic interaction becomes considerable. In this way, at the lowest temperatures measured, at 75 K and 27 K, the $R(t)$ spectra fit were performed accordingly. EFG^{Er_1} is thus characterized by a fundamental frequency of $\omega_0^{Er_1}$ = 161(2) Mrad/s ($V_{zz}^{Er_1}$ = 92(2) V/Å^2) and an asymmetry parameter η^{Er_1} = 0.45(8). The MHF parameters associated with EFG^{Er_1} are characterized by a Larmor frequency ω_L = 44 Mrad/s (B_{hf} = 3.0 T) and orientated at an angle $\beta \approx 60°$ with EFG^{Er_1} principal component V_{zz} (for both temperatures).

The data below 250 K, *i.e.* the presence of an MHF above the magnetic order transition, is rather in line with our magnetization measurements as a relative strong coercive field was observed in this sample well above the Cr sub-lattice ordering temperature (see Fig. 5.9).

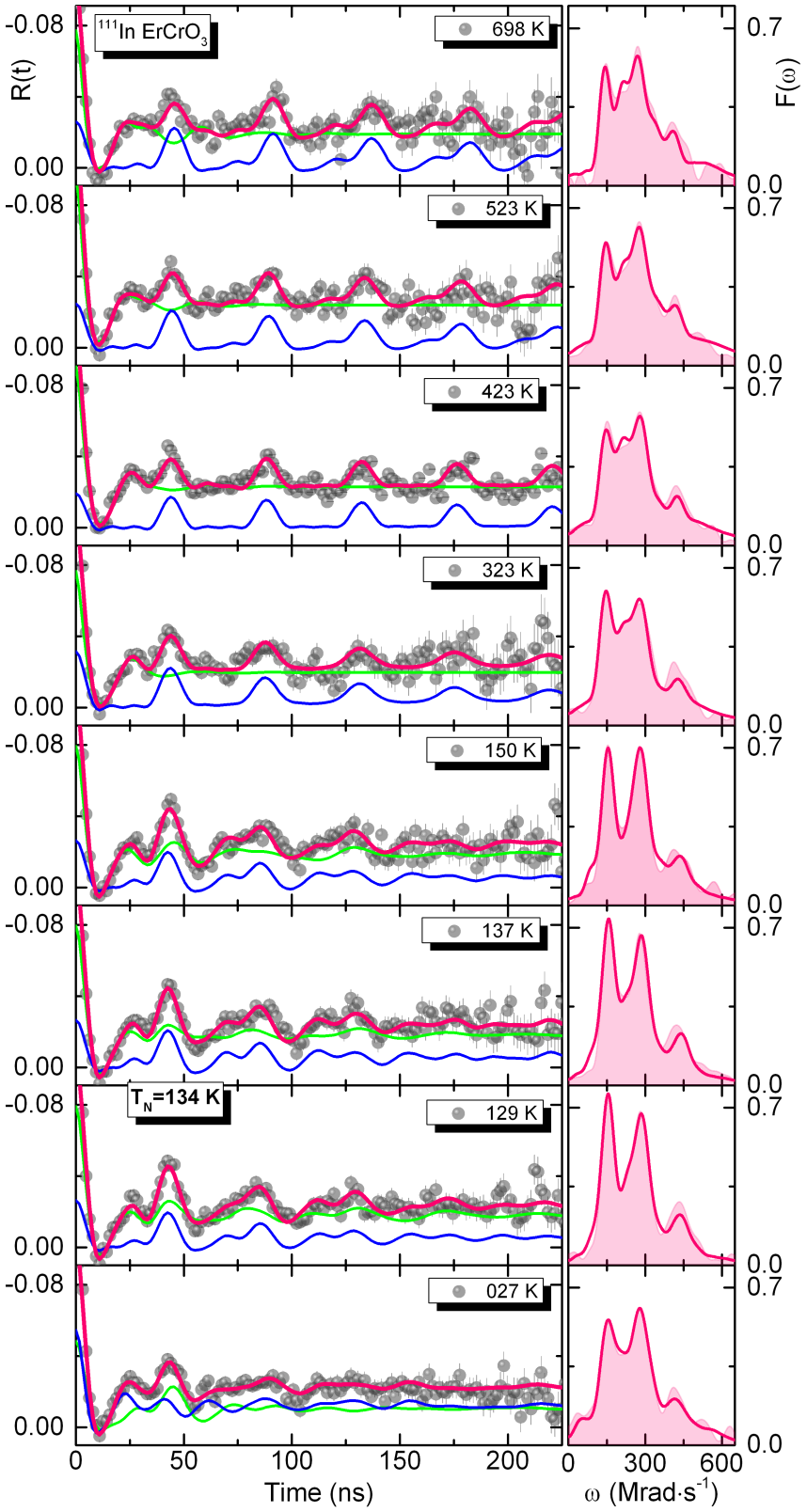

Figure 5.18 – Representative R(t) functions, corresponding fits and respective Fourier transform taken at different temperatures for the ^{111}In probe in $ErCrO_3$.

Figure 5.19 depicts the experimental $R(t)$ anisotropy function (left) together with the Fts (right) obtained in the $ErCrO_3$ system using the implanted ^{111m}Cd probe. The global fits to the $R(t)$ functions are shown by the continuous pink lines (thicker ones) in the spectra. Also in the $R(t)$ spectra are represented the lines corresponding lines of the individual fractions used.

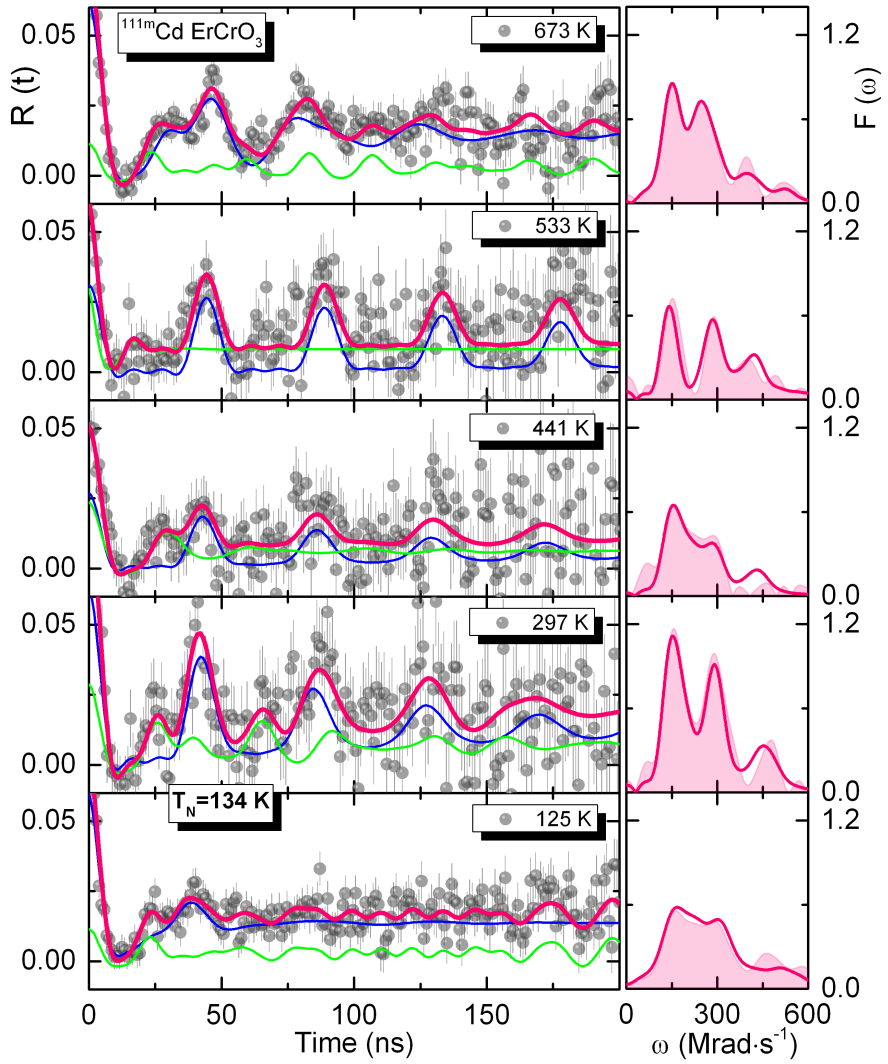

Figure 5.19 – R(t) functions, corresponding fits and respective Fourier transform taken at different temperatures for the ^{111m}Cd probe in $ErCrO_3$.

The PAC results using the ^{111m}Cd probe, show similar EFGs to those using the ^{111}In parent probe. Above T = 473 K the $R(t)$ spectra was fitted with the same EFG^{Er_1} but with higher attenuation parameter. Thus, the parameters obtained are $\omega_0^{Er_1}$ = 135(5) Mrad/s ($V_{zz}^{Er_1}$ = 77(4) V/Å^2) and an asymmetry parameter η^{Er_1} = 0.3(1). In the region between T_N^{Cr} and T_{FE}^{Er} the observed EFG is characterized by $\omega_0^{Er_1}$ = 146(5) Mrad/s ($V_{zz}^{Er_1}$ = 84(5) V/Å^2) and an asymmetry parameter η^{Er_1} = 0.01(5).

Below T_N^{Cr} the $R(t)$ spectrum shows a strong damping. The final fit solutions were obtained after careful consideration of the different tested models, choosing the one that

gave the best χ^2 and consistent temperature dependence tendency. In the end, the adopted model was the one considering that the probes interact now with a magnetic hyperfine field, in addition to the EFG. Accordingly, the fits were performed considering a magnetic hyperfine field below T_N (combined interactions (EFG+MHF)). Therefore, at 125 K the spectrum obtained revealed an EFG characterized by a fundamental frequency of $\omega_0^{Er_1}$ = 157 Mrad/s ($V_{zz}^{Er_1}$ = 89 V/Å^2) and an asymmetry parameter η^{Er_1} = 0.25 and a magnetic part ω_L = 13 Mrad/s (B_{hf} = 0.8 T).

The magnetic hyperfine field, measured with ^{111}In or with ^{111m}Cd, is very small. This is not unexpected because we are probing the rare earth site above its ordering temperature. PAC on similar chromium perovskites reported in literature (*e.g.* $(Gd, Nd)CrO_3$) also sustain this observation[451].

In the cases of $GdCrO_3$ and $NdCrO_3$, both Gd^{3+} and Nd^{3+} ions have incomplete 4*f*-shell and in principle should contribute to the hyperfine magnetic field. However, in $GdCrO_3$ and $NdCrO_3$ perovskites measured with ^{181}Ta the observed B_{hf} values are similar but much smaller than the corresponding value for $LaCrO_3$ where La^{3+} has no 4*f*-electrons[444,452]. The difference in values observed for these systems may be understood by considering the local magnetic moments of Cr and rare earth ions both contributing to hyperfine fields in these compounds.

Let us consider the spin-only value for Cr^{3+} ($3d^3$, μ_{eff} = 3.87 μB) for the purpose of illustration as the orbital contribution is expected to be largely quenched. In the cases of $RCrO_3$, where R has a zero magnetic moment, only Cr^{3+} moments contribute to the hyperfine field. However in the case of $RCrO_3$ where R = Nd, Gd, Yb, Er, Sm the net effective moment has contributions from the rare-earth moments in addition to Cr^{3+} moment and these must be properly taken in to account. The effective moments in these compounds are however considerably reduced because Cr^{3+} moments are oriented anti-parallel to those of R resulting in lower hyperfine fields. It is therefore important to consider the relative importance of Cr – R interactions in addition to Cr – Cr interactions in determining the hyperfine fields in these compounds. The R – R interactions are important only at very low temperatures.

The thermal dependence of the EFGs main parameters (V_{zz} and η) obtained using ^{111}In and ^{111m}Cd probes is depicted in Fig. 5.20 (a) and (b) respectively.

The *EFG* attributed to probes substituting Er sites in the lattice measured with ^{111m}Cd and ^{111}In show a slight monotonic increase in the *EFG* principal component (V_{zz}) when decreasing the temperature down to T_N^{Cr}. The obtained coefficient for the rare earth site when fitting V_{zz} with Eq. 2.33 is α_{Er} = –1.1 × 10^{-4} K^{-1} and is associated with thermal lattice expansion and atomic vibrations (see solid line in Fig. 5.20 (a)). However in this temperature span the asymmetry parameter associated with EFG^{Er_1}, seems to present three distinct regimes. The first one above the T_{FE}^{Er} with $\eta \sim 0.17$, a second between this temperature and 293 K where an apparent decrease of the value is present ($\eta \sim 0.01$) and a third region where a monotonic increase is present down to the lowest measured temperature. No evident change is observed in the η trend when crossing T_N^{Cr}.

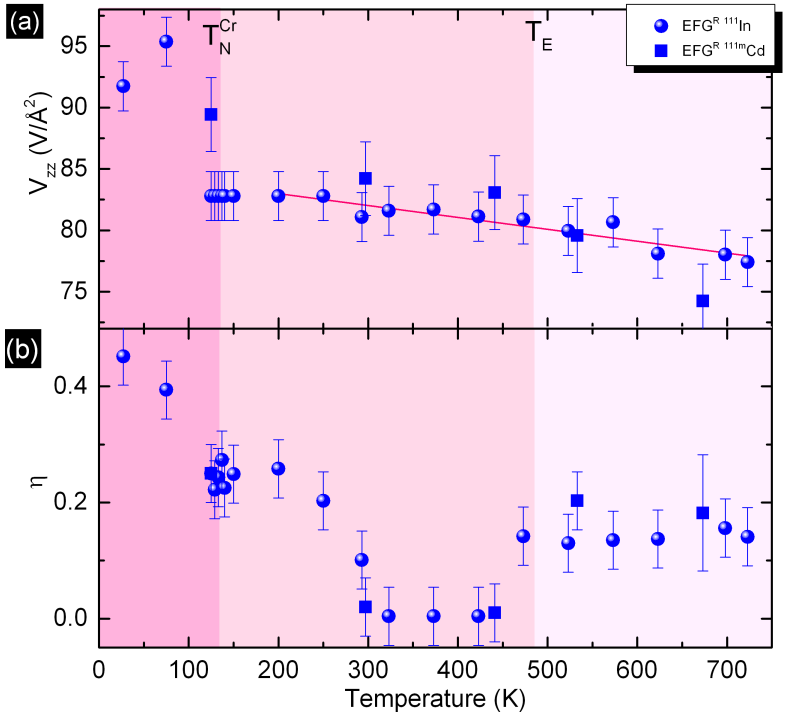

Figure 5.20 – **(a)** Experimental electric field gradient principal component with ^{111}In and ^{111m}Cd probes for the $ErCrO_3$ sample. The continuous line represents a least-squares fit of the function $V_{zz}(T) = V_{zz}(0)(1 + \alpha T^k)$ to the data points. **(b)** Asymmetry parameter.

Summarizing, through the EFG temperature evolution we observe two clear signals of local environment changes, one at T_{FE} and the other close below 250 K. At the claimed ferroelectric phase transition[444] the EFG change from a slightly distorted axial symmetric to an EFG with axial symmetry. Naturally, we cannot appoint these changes as correlated with a ferroelectric phase transition but certainly they providing microscopic evidence that the local point symmetry of the crystal might have changed. At temperatures around 250 K we observe the development of an MHF and a change in the EFG to an axial slightly distorted one. These observations are rather in line with our magnetization measurements as a relative strong coercive field was observed well above the Cr sub-lattice ordering temperature.

5.3.3.6 EFG dependence on temperature - $YCrO_3$

In this subsection, the study of the EFG behavior in$YCrO_3$ as function of temperature is presented. To perform the PAC experiments, the orthorhombically distorted antiferromagnetic $YCrO_3$ sample was implanted with ^{111m}Cd or diffused with ^{111}In. The introduction of the isotopes into the sample followed the standard procedure described in section 2.5.1.6.

The implantation of ^{111m}Cd was proceeded by an 20 minutes annealing at 973 K whereas the diffusion of ^{111}In was proceeded by an 48 hours annealing at 1273 K both in air.

In the case of ^{111}In a study was made as a function of temperature (723 K > T > 27 K, a temperature range that spans over the reported ferroelectric transition (T_{FE} = 485 K) and the magnetic ordering of Cr atoms (T_N^{Cr} = 133 K).

PAC spectra and corresponding fits (continuous lines over the $R(t)$) obtained for the sample $YCrO_3$ system using the diffused ^{111}In probes are depicted in Fig. 5.21. In the same figure, the Fourier Transforms of the $R(t)$ functions are presented. (Please see Appendix C for the complete set of results)

As demonstrated in section 5.3.3.2 the $R(t)$ spectra can exhibit one or two EFG depending on the cooling method in the post-diffusion annealing. Nevertheless there is one EFG, EFG^{Y_1} that is common in both cases, rapid cooling and slow cooling annealing. Thus, we consider that the vanishing EFG, EFG^{Y_2}, to be related to defects trapped near the substitutional lattice site or incomplete annealing in the $YCrO_3$ samples (see section 5.3.3.2). In this way, in the interpretation of the PAC results we will only consider the common static EFG distribution. This effect can clearly be observed in Fig. 5.21 where below room temperature we selected to show only the spectra that showed a single EFG. The fit to each experimental PAC spectrum was obtained considering one static EFG distribution that was assumed to be Lorentzian-like. The frequency triplet correspondent to the EFG from the probes substituting the Y site can be clearly viewed in the Fourier transforms of the R(t) functions below room temperature. This triplet is also visible in the other spectra but with the contribution of EFG^{Y_2}

The spectrum obtained at room temperature revealed that all the ^{111}In nuclei interact with a single almost axially symmetric EFG, characterized by $\omega_0^{Y_1}$ = 141(1) Mrad/s ($V_{zz}^{Y_1}$ = 80(1) V/Å^2) and an asymmetry parameter η^{Y_1} = 0.11(2) as expected for probes at the Y site.

The final fit solutions were obtained after careful consideration of the different tested models, choosing the one that gave the best χ^2 and consistent temperature dependence tendency. Furthermore, for the fits as a function of temperature we took into account the results obtained in the $R(t)$ with only one EFG, as guidelines for fitting the spectra showing the second EFG.

In the case of ^{111m}Cd a study was made in the temperature range of 673 K > T > 12 K. PAC spectra and corresponding fits (continuous lines over the $R(t)$) obtained for the sample $YCrO_3$ system using ^{111m}Cd probes are depicted in Fig. 5.22. In the same figure, the Fourier Transforms of the $R(t)$ functions are presented.

The preliminary PAC results using the ^{111m}Cd probe, show similar EFGs than those using the ^{111}In parent probe. Above T = 485 K the $R(t)$ spectra was fitted with the same EFG^{Y_1} but with higher attenuation parameter. The EFG obtained from the $R(t)$ spectrum at the highest temperature is characterized by the parameters $\omega_0^{Y_1}$ = 134(5) Mrad/s ($V_{zz}^{Y_1}$ = 76(4) V/Å^2) and an asymmetry parameter η^{Y_1} = 0.07(1). In the region between T_N^{Cr} and T_{FE}^{Y} the observed EFG is characterized by $\omega_0^{Y_1}$ = 142(5) Mrad/s ($V_{zz}^{Y_1}$ = 81(5) V/Å^2) and an asymmetry parameter η^{Y_1} = 0.10(4).

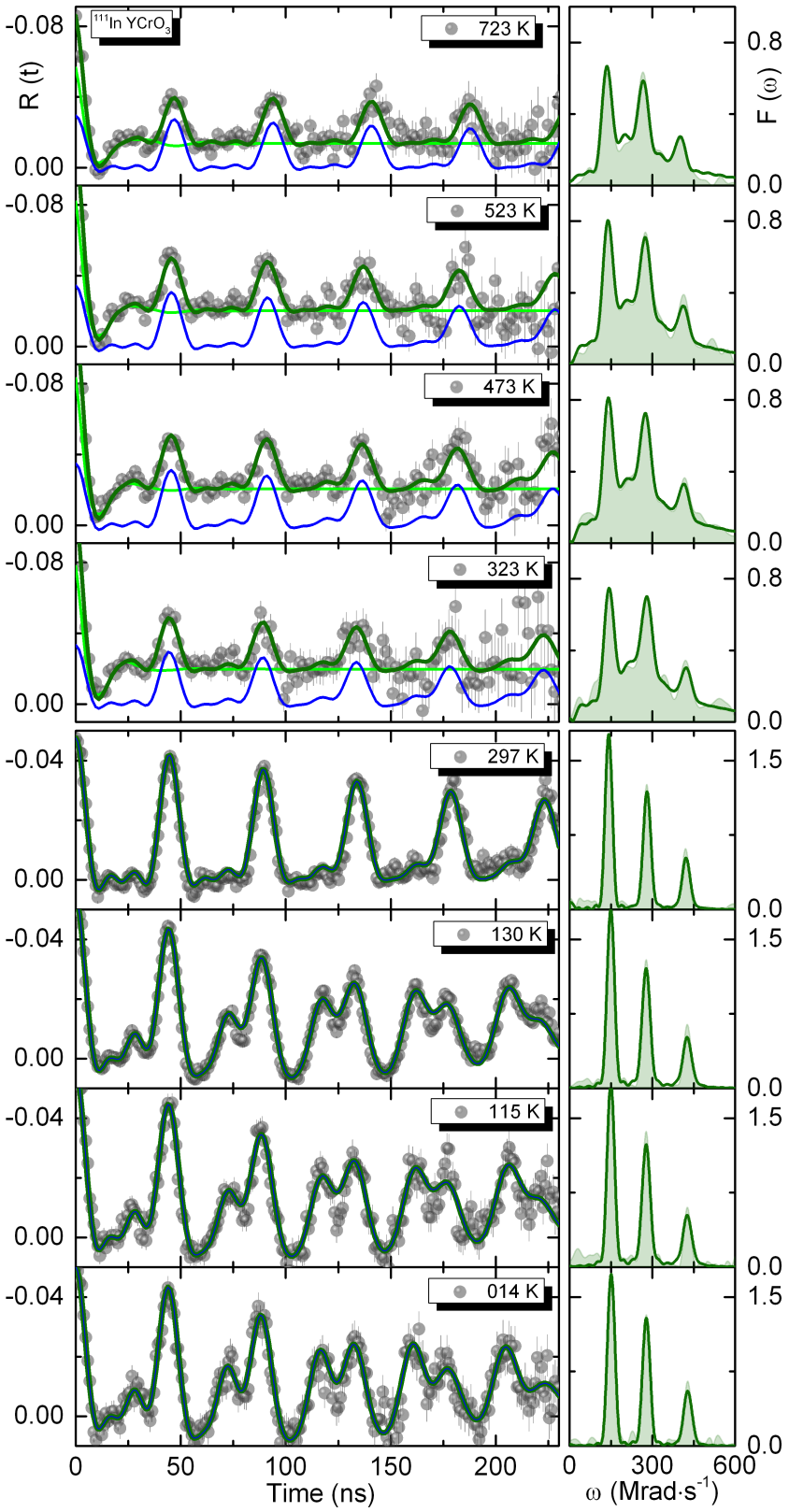

Figure 5.21 – Representative R(t) functions, corresponding fits and respective Fourier transform taken at different temperatures for the ^{111}In probe in $YCrO_3$.

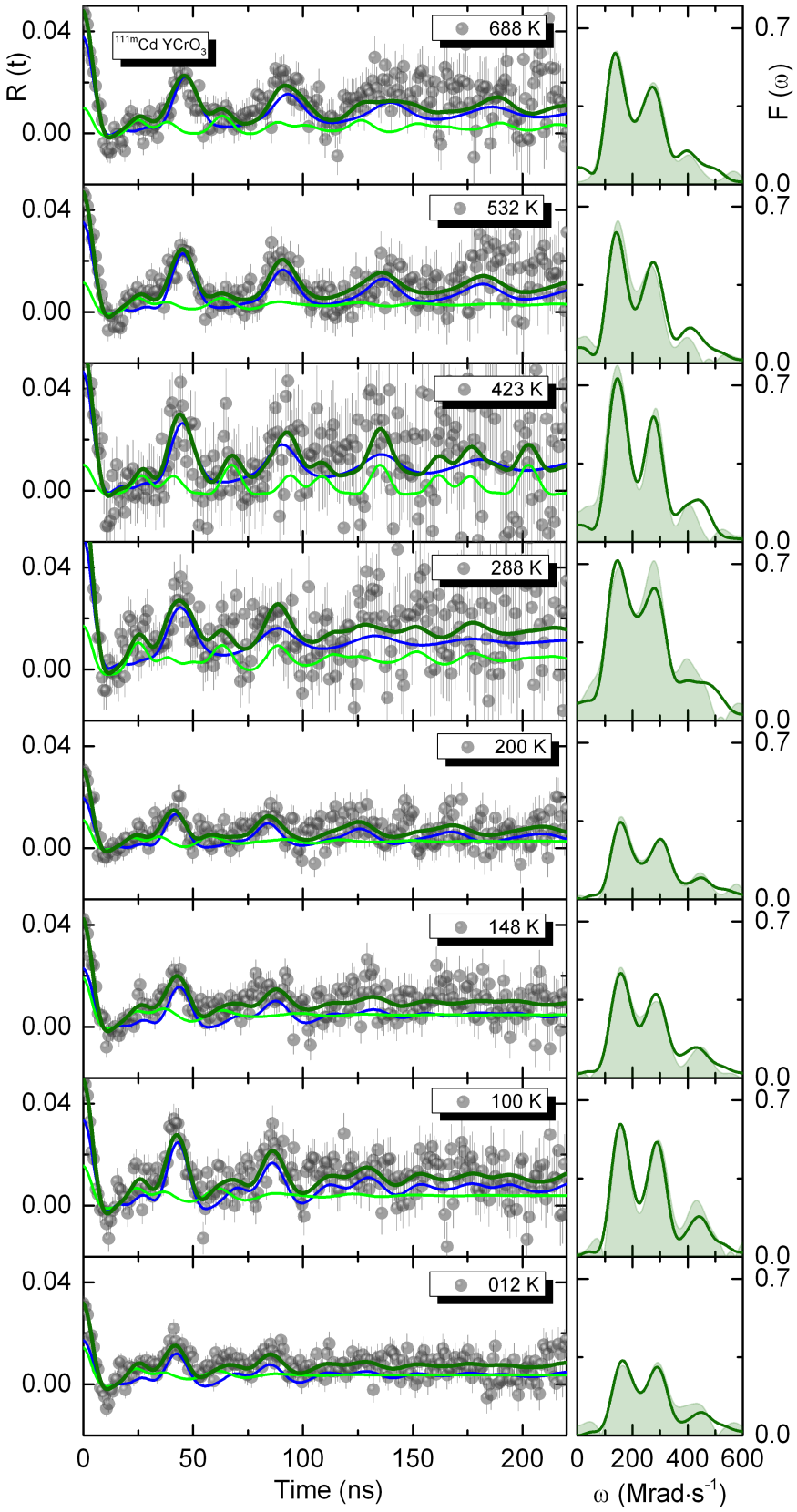

Figure 5.22 – R(t) functions, corresponding fits and respective Fourier transform taken at different temperatures for the ^{111m}Cd probe in $YCrO_3$.

At the lowest measured temperature (T = 12 K) using the ^{111m}Cd probe, the EFG^{Y_1} is characterized by $\omega_0^{Y_1}$ = 146(5) Mrad/s ($V_{zz}^{Y_1}$ = 83(4) V/Å^2) and an asymmetry parameter η^{Y_1} = 0.24(5) interacting with a small MHF (B_{hf} = 0.4 T and $\beta \approx 0°$).

The thermal dependence of the EFGs main parameters (V_{zz} and η) obtained with our fits for both probes are depicted in Fig. 5.23 (a) and (b) respectively.

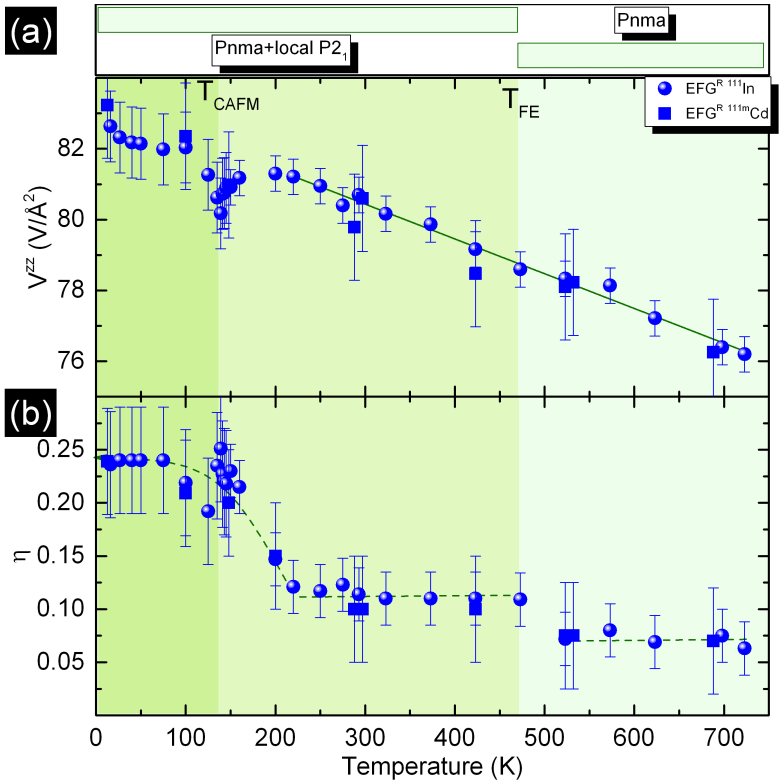

Figure 5.23 – **(a)** Experimental electric field gradient principal component with ^{111}In and ^{111m}Cd for the $YCrO_3$ sample. The continuous line represents a least-squares fit of the function $V_{zz}(T) = V_{zz}(0)(1 + \alpha T^k)$ to the data points. **(b)** Asymmetry parameter.

As can be seen, the EFG principal component as a function of temperature increases slightly as the temperature decreases toward T_N^{Cr} = 133 K. However, at T_N the values seem to drop only to resume the high temperature trend below.

The V_{zz} thermal dependance coefficient for the rare earth site when a least-squares fit of the function given by Eq. 2.33 was performed, gave $\alpha_Y = -1.2 \times 10^{-4}$ K^{-1}, represented by the solid line in Fig. 5.23 (a)). The $YCrO_3$ thermal expansion value is two orders of magnitude smaller (7.8×10^{-6} K^{-1}) and alone cannot account for the V_{zz} temperature dependence in accordance to the behavior of the other perovskites studied in this work and with those reported in literature[293,453].

The thermal dependence of the asymmetry parameter shows an interesting trend. Instead of the monotonic increase that is observed in the V_{zz} parameter, three stages are observed. In the first stage, above T_{FE} = 485 K, we observe an almost zero and constant value characteristic of an EFG with axial symmetry. In the second stage, 223 K < T < 485 K, the value of η^{Y_1} is observed to be also constant but slightly higher.

This seems to indicate that a loss of axial symmetry takes place at $T \sim 500$ K. Here, we should stress that these results agree well with the work reported by *Ramesha et al.*[219] where using high-resolution neutron powder diffraction measurement reveal an average centrosymmetric structure for $YCrO_3$ with space group *Pnma* both above and below the dielectric transition temperature. However, using neutron pair distribution function analysis the authors found that, in the low-temperature ferroelectric-like state, $YCrO_3$ is locally non-centrosymmetric, characterized with a Cr off-centering displacement of the order of 0.01 Å along the *z* direction that seemed to be temperature independent.

The small value of the Cr off-centering displacement and the local character of the non-centrosymmetry nature in $YCrO_3$ could explain the small value of the polarization observed in this material (2 μCcm^{-2} at 300 K for $YCrO_3$ compared to $\sim$ 30 μCcm^{-2} in $BaTiO_3$ for Δr = 0.24 Å)[342]. In fact, we showed in chapter 3.1 a similar picture in the cubic spinel $CdCr_2S_4$[169] , where an Δr = 0.012 Å could give rise to a polarization of $\sim$ 0.075 μCcm^{-2}. It is likely that the same type of local non-centrosymmetry may give rise to ferroelectricity and related phenomena in other materials as well.

In the last stage, we observe an increase of the asymmetry parameter preceding the anti-ferromagnetic transition, similarly as observed in the $ErCrO_3$ system. This increase seems to halt below T_N where a constant value is observed down to the lowest temperature measured.

5.3.3.7 EFG dependence on temperature - $SmCrO_3$

In this subsection, the study of the EFG behavior in $SmCrO_3$ as function of temperature is presented. To perform the PAC experiments, the distorted perovskite $SmCrO_3$ sample was diffused with ^{111}In. Studies with implanted ^{111m}Cd were initialized (see section 5.3.3.2). The introduction of the isotopes into the sample followed the standard procedure described in section 2.5.1.6.

The implantation of ^{111m}Cd was proceeded by an 20 minutes annealing at 973 K whereas the diffusion of ^{111}In by an 48 hours annealing at 1273 K both in air.

The $SmCrO_3$ sample was studied as a function of temperature (723 K > T > 16 K, a temperature range that spans over the important transition temperatures, the reported ferroelectric transition (T_{FE} = 220 K), the magnetic ordering of Cr atoms sub-lattice (T_N^{Cr} = 197 K), the spin reorientation (T_{SR} = 40 K) and magnetic ordering of Sm atoms sub-lattice (T_N^{Sm} = 20 K).

Figure 5.24 depicts the experimental $R(t)$ anisotropy function (left) together with the Fts (right) for the $SmCrO_3$ system using the diffused ^{111}In probe. The global fits to the $R(t)$ functions are shown by the thick continuous blue lines in the spectra. (Please see Appendix D for the complete set of results)

At high temperatures, T > 300 K, a frequency triplet (ω_1, ω_2, and ω_3 with $\omega_2 \sim 2\omega_1$ and $\omega_3 \sim 3\omega_1$) corresponding to a single EFG can be clearly observed. By a simple picture inspection one can realize that in this temperature range no significant changes occur

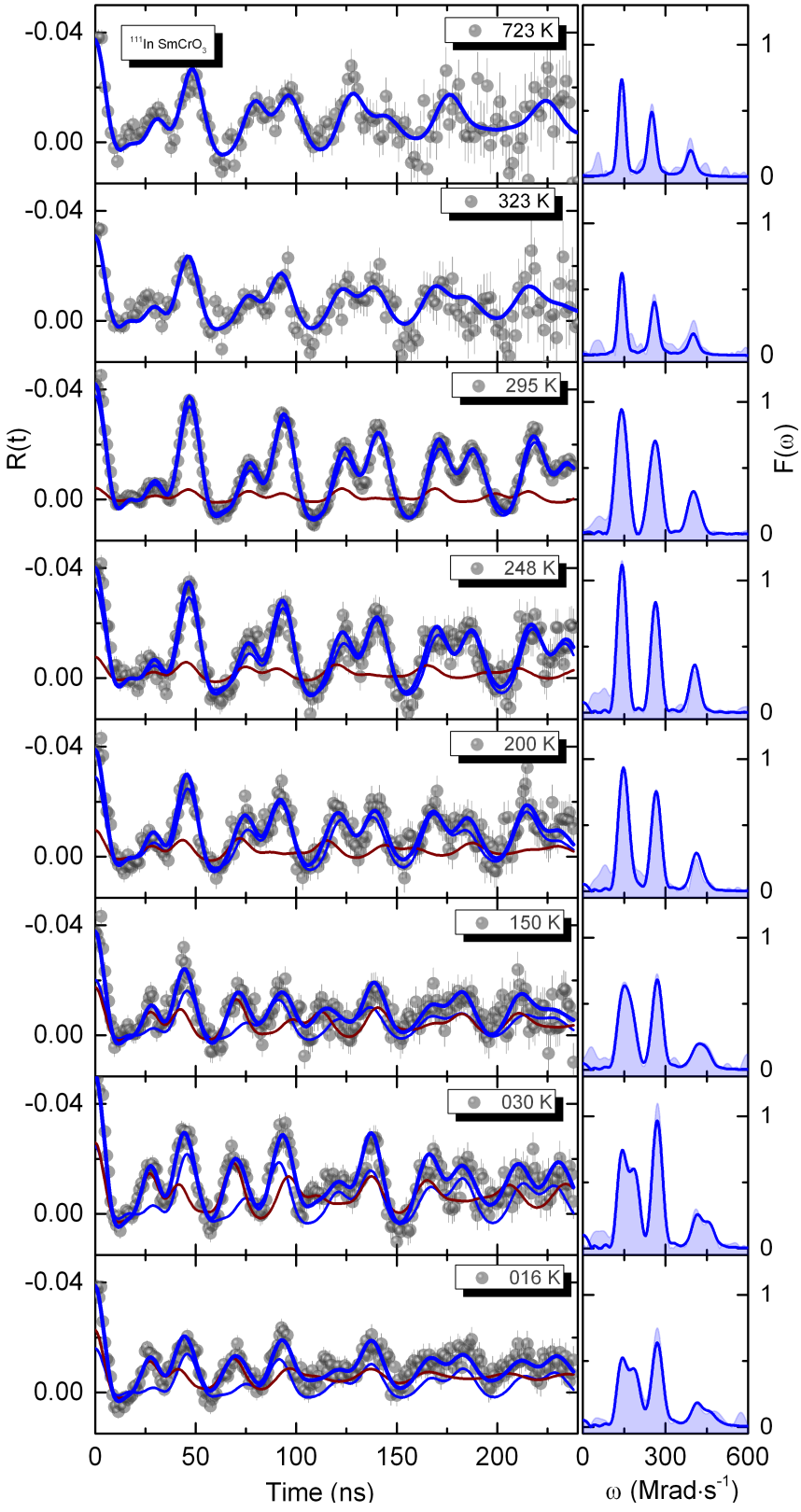

Figure 5.24 – Representative R(t) functions, corresponding fits and respective Fourier transform taken at different temperatures for the ^{111}In probe in $SmCrO_3$.

in the spectra when the temperature is lowered and only one EFG, *i.e.*, one probe local environment, exists. One should point out that the samples that endured a fast cooling after the recovery annealing showed the presence of a second highly attenuated *EFG*, whereas with a slower cooling only the first one was present (see section 5.3.3.1). In fact, at room temperature we have collected two $R(t)$ spectra, one after a fast cooling and another with a slower cooling. The fast cooled sample showed two *EFG*s, the first one for the substituting probes at the Sm site while the second one attributed to defects trapped near the substitutional lattice site or to an incomplete annealing. The slow cooled sample showed the presence of only one EFG (arising from the substitutional Sm site - EFG^{Sm_1}). Not withstanding, for a better visualization of the parameters evolution with temperature and to not confuse the analysis of the results we have subtracted this fraction of the spectra when it was present. Furthermore, as we will discuss further on, at lower temperature another *EFG*, different from these appears. This should not be confused with the highly attenuated fraction observed in some of the $R(t)$ spectra, above and below 300 K. Hereafter, in order to avoid confusion in notations, the two relevant EFGs observed in the slow cooled sample will be denoted as EFG^{Sm_1} (thin blue color on $R(t)$) and EFG^{Sm_2} (thin brick color on $R(t)$).

A very interesting aspect in our $SmCrO_3$ PAC results is revealed below 300 K where visible changes can be observed in the perturbation function ($R(t)$) data and in the corresponding Fourier transforms. In detail, a second EFG emerges and its relative abundance increases with decreasing temperature. Accordingly, the fits to the R(t) experimental data were performed considering only one static regular EFG distribution, which was assumed to be Lorentzian-like, for $T > 300$ K while two EFG distributions had to be considered to account for the features that emerge below that temperature.

The spectrum obtained at high temperatures revealed an EFG characterized by a fundamental frequency of $\omega_0^{Sm_1} = 132(2)$ Mrad/s^{-1} ($V_{zz}^{Sm_1} = 75.5$ V/m^2) and an asymmetry parameter $\eta = 0.23(3)$ in good agreement with the other system series studied in this work. The second EFG that emerges below 300 K is characterized by a similar fundamental frequency, $\omega_0^{Sm_2} = 132(3)$ Mrad/s^{-1} ($V_{zz}^{Sm_2} = 75.5$ V/m^2) and an asymmetry parameter slightly higher $\eta = 0.37(3)$.

The thermal dependence of the EFGs main parameters ($V_{zz}^{Sm_1,Sm_2}$, η^{Sm_1,Sm_2}) obtained by our fits are depicted in Fig. 5.25 (a) and (b) respectively.

The EFG principal component of both EFG^{Sm_1} and EFG^{Sm_2} increase slightly as the temperature decreases halting below $\sim$ 150 K where the value remains constant. The asymmetry parameter for both EFGs show an inverse trend to each other. While the asymmetry parameter of EFG^{Sm_1}, η^{Sm_1}, slowly decreases in the entire measured temperature range, the asymmetry parameter of EFG^{Sm_2}, η^{Sm_2}, increases since it appears below 300 K, down to the lowest measured temperature. Curiously, between $T_{FE} = 220$ K and $T_N^{Cr} = 197$ K a bump in η^{Sm_1} and a step in the η^{Sm_2} trends are observed. One should also mention that the relative widths of the EFG distributions are nearly temperature independent ($\delta^{Sm_1} \approx 2$ Mrad/s and $\delta^{Sm_2} \approx 3$ Mrad/s).

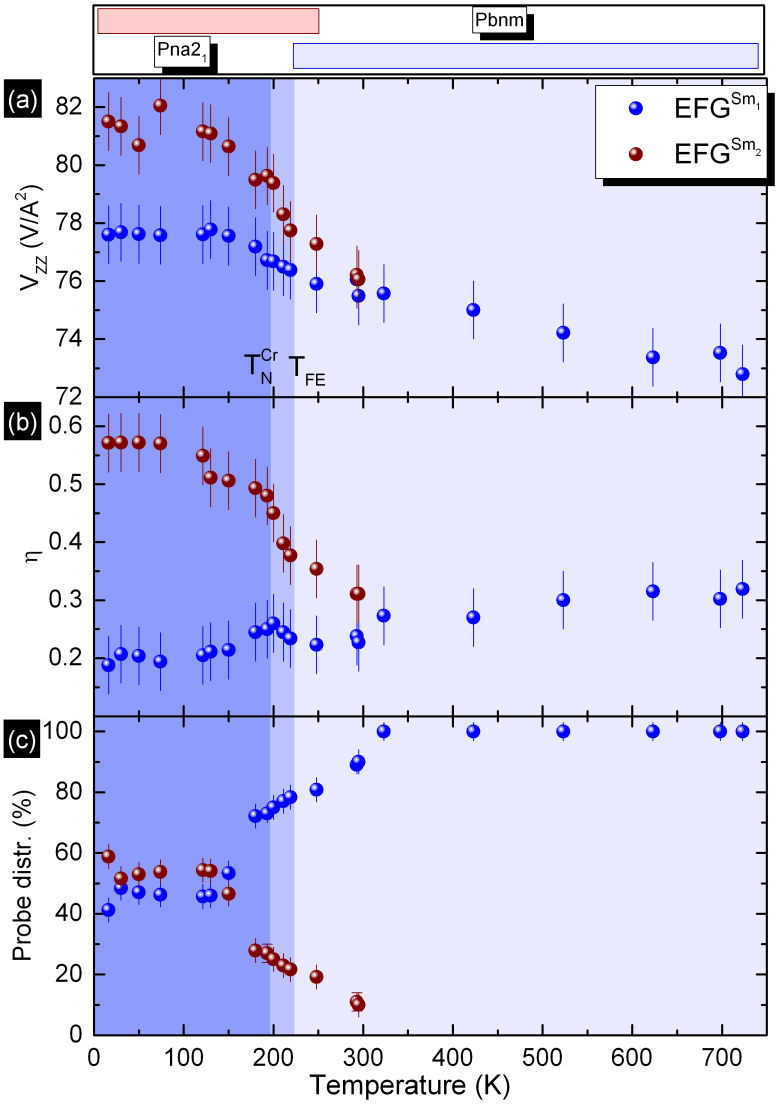

Figure 5.25 – **(a)** Experimental electric field gradient principal component with ^{111}In for the $SmCrO_3$ sample. **(b)** Asymmetry parameter. **(c)** Probe distribution.

Figure 5.25 (c) presents the temperature evolution of the fraction of probes interacting with each EFG, *i.e.*, the relative abundance of each local environment (LE): f^{Sm_1} and f^{Sm_2}. As introduced previously, at high temperatures all the probes interact with EFG^{Sm_1}. On decreasing temperature and below 300 K, a second EFG, EFG^{Sm_2}, becomes apparent. Below that temperature f^{Sm_1} decreases sharply and seems to halt for temperatures below 150 K with approximately $f^{Sm_1} \approx f^{Sm_2} \approx 50(5)\%$.

As discussed before, EFG^{Sm_1} is only compatible with probes substituting the trivalent rare earth site, *i.e.* the Sm site. An unlikely scenario to the appearance of a second EFG would be to consider that at temperatures below 300 K the probes were changing their location (*e.g.*, probe ions diffusion), thus EFG^{Sm_1} – EFG^{Sm_2} can only be associated with modifications to the Sm/probe local environment. Comparing these two local environments one realizes that the most relevant difference is their asymmetry param-

eter. While EFG^{Sm_1} presents an η characteristic of a slightly distorted axial symmetric, $\eta^{Sm_1} \approx 0.21(2)$, EFG^{Sm_2} is a non axial symmetric local environment, $\eta^{Sm_2} \approx 0.56(5)$. As a consequence, while part of the system (associated with EFG^{Sm_1}) maintain its local orthorhombic symmetry, the remaining part, associated with EFG^{Sm_2}, appears as a distortion of the first, with axial symmetry breaking.

The ^{111}Cd probe state when fed by the ^{111}In radioactive decay, occurs through electron capture (EC) of an electron from the probe *K* shell. In some cases where the sample has an insulator character, the existence of spectra features due to after effects is a concern. In fact, $SmCrO_3$ shows insulator properties when measured, particularly at low temperatures, however conventional band theories predicts that it will conduct electricity [259], supporting in this way why after effects should be excluded on these experiments. Furthermore, the main effect expected on the PAC spectra would be a situation described by time-dependent hyperfine interactions, in particular, described by a unidirectional relaxation process[391,395]. This leads mainly to a constant reduction of the PAC spectra amplitude, for times longer then a few ns, but with unchanged features apart from that reduction (unchanged quadrupole parameters). Other dynamics effects, such intrinsic or extrinsic equilibrium EFG fluctuations, should also be excluded from the interpretation since no exponential damping growth is observed at any temperature[354,393]. Such is not the case of the present data and in reality, a phenomenology consistent with the material's intrinsic properties exists.

The fits below T_N^{Cr} have been perfectly performed without the inclusion of typical combined interactions (EFG+MHF). In fact, PAC studies in the $RCrO_3$ show that down to the ordering temperature of Sm no (or almost nill) MHF is observed[444,445,451,452]. The $R(t)$ spectrum at T = 16 K, *i.e.* below T_N^{Sm}, was fitted considering combined interaction (electric and magnetic hyperfine interaction). Thus below T_N^{Sm} the $R(t)$ experimental data also show the presence of hyperfine fields due to the antiferromagnetic ordering of the Sm magnetic sub-lattice. However, even at this temperature the magnetic hyperfine field interaction is much weaker than the electric quadrupole one, only a frequency broadening/splitting is observed. Nevertheless, it was verified that the magnetic hyperfine field was too small to resolve the two distinct MHFs, their magnitude being approximately the same ($B_{hf}^{Sm_1} \approx B_{hf}^{Sm_2}$). The final $R(t)$ spectra fit was performed accordingly, with a small value around B_{hf} = 0.3(1) T and an angle between the B_{hf} and V_{zz} of 1(1)° (which can be treated as zero).

Summarizing, in recent reports on this system, local distortions have been theoretically predicted and experimentally observed where polar oxygen octahedral rotations associated with Sm displacement are proposed to be correlated with the development of polar order below 250 K (still in the paramagnetic state)[259]. Although our data might be compatible with these reports, remarkably, our results point to a more subtle scenario, where locally an inhomogeneous state emerges. In this new sate regular and distorted environments (most probably polar and non polar states) coexist.

5.3.4 Conclusions

In this chapter we performed a systematic local probe study using PAC in the $RCrO_3$ (R=Yb, Er, Y, Sm) system. The study of the dependence of the EFG parameters and probe distribution as a function of annealing temperature and time showed that the post implantation/diffusion annealing improves with higher times and higher temperatures, but above a certain value their influence is minimal to the system. As important as those parameters is the cooling rate after the annealing, making the difference between all probes substituting a single, well defined, lattice site or the mix of probes in different sites and/or the trapping of defects near the PAC probes. Furthermore, the experimental results are in good agreement with initial *ab-initio* calculations, where a higher V_{zz} and an axial symmetric environment is expected for probe substituting the rare-earth site. We also observe a decrease of the V_{zz} and an axial symmetry parameter increase with the increase of the rare-earth ionic radii.

The EFG temperature evolution study in $ErCrO_3$ shows two clear signals of local environment changes, one at the reported T_{FE} and the other close below 250 K. At the claimed ferroelectric phase transition the EFG change from a slightly distorted axial symmetric to an EFG with axial symmetry. Naturally, we cannot appoint these changes as correlated with a ferroelectric phase transition but certainly they providing microscopic evidence that the local point symmetry of the crystal might have changed. At temperatures around 250 K we observe the development of an MHF and a change in the EFG to an axial slightly distorted one. These observations are rather in line with our magnetization measurements as a relative strong coercive field was observed well above the Cr sub-lattice ordering temperature.

In the case of $YCrO_3$, the thermal dependence of the EFG asymmetry parameter show three stages of values when a monotonic increase ofV_{zz} parameter is observed. In the first stage, above the reported T_{FE} = 485 K the observed EFG has axial symmetry, between 223 K < T < 485 K a loss of axial symmetry takes place and finally preceding the anti-ferromagnetic transition the asymmetry parameter increases, and seems to halt below below T_N^{Cr}. Our results agree well with reports on $YCrO_3$ where locally a non-centrosymmetric environment was claimed below the low-temperature ferroelectric-like state while an average centrosymmetric structure was measured in all range of temperatures. In fact, we showed in chapter 3.1 a similar picture in the cubic spinel $CdCr_2S_4$, where a small Cr off-centering could give rise to a polarization. It is likely that the same type of local non-centrosymmetry may give rise to ferroelectricity and related phenomena in other materials as well.

Finally, in the case of $SmCrO_3$, we observed that a distortion of the high temperature local environment start to develop below 300 K within the paramagnetic phase. Although our data might be compatible with the most recent reports, where polar octahedral rotations and/or cation displacements are at the origin of a polar order in the paramagnetic state, remarkably, our results point to a more subtle scenario, where locally

an inhomogeneous state emerges. In this new sate regular and distorted environments (most probably polar and non polar states) coexist.

In summary, our experimental PAC results demonstrate the aptitude of this technique to probe local phenomena. Apart from the $YbCrO_3$ system where an EFG with axial symmetry is observed in all temperature range, our data is compatible with a scenario where local distortions, altering the local symmetry permits the installment of a ferroelectric order in these systems. We believe that this is a step forward in understanding the exotic behavior of the orthochromites with perovskite structure and their entanglement with lattice distortions.

CHAPTER 6

Conclusions and Perspectives

In this chapter we summarize the main conclusions and achievements accomplished in this thesis during these last four years. First we will focus on the novel results achieved, presenting the most important conclusions regarding our main results published, submitted or in preparation for publication, in international journals. Subsequently, we will give an outlook for future perspectives.

6.1 Conclusions

In the $CdCr_2S_4$ spinel type multiferroic material, with a unique combination of techniques, we demonstrated the existence of a dynamic state caused by the presence of simultaneous polar and magnetic nanoclusters, indicative of a system exhibiting a birelaxor nature. Our results are consistent with a model in which the effects described in the recent literature arise from atomic displacements of Cr^{3+} ions occurring well above the magnetic ordering temperature in the form of short range magnetic clusters. Our combined analysis clearly reveals that the increase in the average size of randomly oriented dipoles saturates at T_{PM}, concomitantly with the onset of their dynamic slow-down and the emergence of $Cr^{3+} - Cr^{3+}$ magnetic correlations. Finally, we further demonstrate that an ultra-slow Cr^{3+} displacement dynamics precedes the recently reported $Fd\bar{3}m$ to non-centrosymmetric $F\bar{4}3m$ phase transition, suggesting its order-disorder-type origin. This Cr^{3+} dynamic off-centering is intrinsically entangled with the formation of local dipoles and is also responsible for the observed magnetic correlations between adjacent Cr^{3+} neighbors. We further confirmed that this coupling between electric and magnetic orders by modeling the peculiar low-field $\chi^{-1}(T)$ measurements using Landau theory with a linear magneto-electric term. We believe that this is a step forward in understanding the exotic behavior of (bi)relaxor systems and their entanglement with lattice distortions.

At this point we were curious to understand the nature of the observed short range magnetic clusters. Thus, we continued our quest in studying the response of these material to external stimuli, namely by the application of an external pressure and observed the effects in its properties. We observed that the magnetic properties of $CdCr_2S_4$ can be tuned by the application of pressure resulting in an enhancement of J_{AFM}. Despite the opposite response in T_C and T_{PM} the underlying operating mechanism was found

to be the same. We unveil that the magnetic clusters in this compound arise from J_{AFM} interactions among Cr^{3+} spins (increase of the T_{PM}). Approaching T_{PM} from a higher temperature, the Cr^{3+} displacement promotes the formation of short range magnetic clusters which are antiferromagnetic in a paramagnetic matrix. With pressure increase the distances between the Cr ions are reduced and the antiferromagnetic direct exchange increases and T_{PM} shits toward higher temperatures. Between T_{PM} and T_C we observe a competition between J_{AFM} and J_{FM}, in which J_{FM} overcomes the J_{AFM} at T_C.

Thus, with the combination of these studies, we advanced the understanding and offer a way to tune the AB_2X_4 spinels magnetic properties.

We also undertook a study in another type of spinel material, but this time an oxide with manganese in its composition. Besides the potential that these materials present to be applied in multifunctional devices, a better understanding of the effect of Jahn-Teller distortions and how it relates to this material properties was envisaged.

The local lattice properties of $CdMn_2O_4$ were studied by means of PAC. The EFG measurements at the Cd and Mn sites in the 12 – 600 K temperature range clearly demonstrated that a single Jahn-Teller distorted local phase, compatible with the long-range tetragonal average structure, exists. Above the magnetic phase transition, T_C = 100 K, and up to 600 K a dynamic lattice distortion, related with a local structural instability, is observed.

In the high temperature region, *i.e.* above 600 K, a second EFG emerges along with a reciprocal susceptibility curve slope change. The existence of local inhomogeneities within the tetragonal matrix, also signed by the magnetic anomaly, is however not followed by a tetragonal to cubic phase transition. Instead, a phase segregation in two distinct Jahn-Teller distorted local phases was found. In this high temperature region a relaxed Jahn-Teller distorted octahedral phase grows in the low temperature tetragonal matrix. In order to assertively understand the origin of the dynamic effects observed in this compound, additional studies with complementary local probe techniques are necessary.

Nevertheless this work gives insights about $CdMn_2O_4$ local lattice structure which can contribute to a better understanding of AMn_2O_4 spinels .

Orthochromites oxides with perovskite structure have been much debated lately in the multiferroic community. However, before they can be considered with potential to be applied in multifunctional devices, the claimed ferroelectricity of these compounds has to be settle. Furthermore, other properties like the magnetocaloric effect and ways of maximizing it have to be studied.

In this way, we have synthesized polycrystalline $YCrO_3$ and confirmed an orthorhombic structure with the *Pbnm* space group using structure refinement. Magnetization measurements reveal an antiferromagnetic transition with weak ferromagnetism below $T_N \sim 140$ K. The magnetocaloric effect was calculated by measuring the isothermal magnetic entropy change, which shows a maximum of 0.36 $J\,kg^{-1}K^{-1}$ for a field of 50 kOe and a refrigerant capacity R_C = 7.1 $J\,kg^{-1}$. No difference in the magnitude of

the MCE was observed for increasing and decreasing field modes, reinforcing the idea that hard magnets should also be included in the search for new MCE materials. The positive slope of the Arrott plots at all high fields implies that the field-induced magnetic transition in $YCrO_3$ is second-order in nature.

$YCrO_3$, a canted antiferromagnetic system with weak ferromagnetism, possessing rich physics due to the complex coupling among different degree of freedoms, is a model of chromium perovskites and may provide further information to possible applications in magnetic refrigeration in liquid nitrogen temperature range.

After settling the properties of $YCrO_3$, we advanced into checking the effects on those properties with chemical pressure, *i.e.* by changing the R ion. Furthermore, changing from a non magnetic ion to a magnetic one, enabled us to also study their influence in the evolution of the different magnetic properties like the MCE effect.

The R ions radius increase was found to slightly increase the Cr^{3+} ordering temperature. The entropy change due to the magnetocaloric effect was calculated from the isothermal magnetization measurements, and was found to monotonically decrease with R ionic radius increase. However, it showed an increase with the total paramagnetic moment increase. The use of a R magnetic ion helps to enhance the magnetic entropy variation at T_N^{Cr}.

We have showed that $ErCrO_3$ presents a significant magnetic entropy change, $-\Delta S_M$ = 13 $Jkg^{-1}K^{-1}$ while $SmCrO_3$ has an inverse $-\Delta S_M$ of –0.3 $Jkg^{-1}K^{-1}$. The refrigerant capacity, calculated near the transition temperature of the R^{3+} ion for applied fields up to 50 kOe varies $R_C = [0.2 - 75]$ Jkg^{-1}. The magnetocaloric entropy change observed in $RCrO_3$ and its ability to be tuned by R substitution signifies that this material system is promising for future solid-state refrigeration devices.

Furthermore, we performed a systematic local probe study using PAC in the $RCrO_3$ (R=Yb, Er, Y, Sm) system. The study of the dependence of the EFG parameters and probe distribution as a function of annealing temperature and time showed that the post implantation/diffusion annealing improves with higher times, higher temperatures and slower cooling. Initial *Ab-initio* calculations are in good agreement with the experimental results, where a higher V_{zz} and a more axial symmetric environment is expected for probe substituting the rare-earth site. We also observe a decrease of the V_{zz} and a decrease of the axial symmetry with the increase of the rare-earth ionic radii.

Our experimental PAC results demonstrate the aptitude of this technique to probe local phenomena. Apart from the $YbCrO_3$ system where the PAC study needs to be further pursued, our data is compatible with a scenario local distortions altering the local symmetry permits the installment of a ferroelectric order in these systems. In particular, in $SmCrO_3$ we observed that a distortion of the high temperature local environment start to develop below 300 K within the paramagnetic phase. Thus our data is compatible with the most recent reports, where polar octahedral rotations and/or cation displacements are claimed to be at the origin of a polar order in the paramagnetic state. Nevertheless, our results point to a more subtle scenario, where locally an inhomogeneous state

emerges. In this new sate regular and distorted environments (most probably polar and non polar states) coexist. We believe that this is a step forward in understanding the exotic behavior of the orthochromites with perovskite structure and their entanglement with lattice distortions.

6.2 Perspectives

The work performed in this thesis is a good example that sometimes an answer to a question raises new questions. Although, in our opinion, important steps were given towards understanding the physics underlying the properties of the studied systems, new questions arised that we hope to give an answer in the future.

Firstly, in the spinel $CdCr_2S_4$ system, in order to have an overall picture of the mechanism that is playing the role, some studies are envisaged, namely, measurements of diffraction patterns under pressure and lower temperatures. Additionally, in order to study how pressure affects the antiferromagnetic direct exchange interaction, magnetic measurements under higher applied pressures are also envisioned.

The magnetic entropy variation study on $YCrO_3$ pointed to a linear dependence of $-\Delta S_M^{max} \propto H_{max}^{2/3}$ and so, one can expect that the magnetization properties can be explained by a mean field theory. However, as we discussed previously, nowadays a more comprehensive expression and a complete field dependence of $-\Delta S_M^{max}$ is known. Having this in mind we wish in a future work to perform a detailed study of the critical exponents in the $YCrO_3$ system as well as in the other perovskite systems here studied.

The local scale studies performed in $RCrO_3$ (Yb, Er, Y, Sm) systems showed promising results that we hope to complement them with further measurements at different temperatures in order to encompass all important phase transitions with different isotopes *e.g.* with ^{48}Cr to probe the Cr lattice site. Additionally, the PAC studies showed the importance of the cooling rate after the annealing on the lattice probe distribution. We will further pursuit this matter in order to achieve probes substituting only the R or Cr site and avoiding possible trapping of defects near the PAC probes. We hope also to perform PAC studies on single-crystal samples which may shed some light onto the so-far unexplained results and learn about the electrical filed gradient and magnetic hyperfine filed directions in the crystal.

The results of the *ab-initio* calculations were performed in a lattice without the substitution of the regular lattice site with the ^{111}Cd probe. Therefore, in the future we will calculate the V_{zz} and η values by taken into account the influence of the ^{111}Cd probe in the lattice to better validate our findings.

Besides those studies, one can foreseen new promising research already initiated in magnetic frustrated materials. Frustrated magnetism arising from geometric frustration is a peculiar phenomenon resulting from intrinsic incompatibilities between some fundamental interactions and the underlying lattice geometry (especially in prototypi-

cal frustrated network as triangular, Kagomé, fcc or pyrochlore lattices)[454]. Geometric frustration has claimed the appearance of fascinating effects such as the formation of exotic states like spin ice, spin liquids and spin glasses[454]. Although geometric frustration in magnetic systems has been under the scope for the past two decades, still we observe a myriad of proposed mechanisms in order to understand how frustration is lifted. Moreover, frustrated magnets seem to be the long sought goal for materials where control of electric properties by magnetic fields is possible, namely in the perovskites $RMnO_3$, RMn_2O_5 (R: rare earths) or $Ni_3V_2O_8$ [455].

In this area of research we have already begun similar studies to those presented in this thesis. A series of frustrated materials of the general formula AB_2O_4 (A=Ba, Ca, Cd, Hg, Mg, Mn, Sr, Zn and B=Cr) has been prepared by solid state synthesis or sol-gel methods. For A=Cd, Mg, Zn structural and magnetic results were already obtained and the study has proceeded to a next stage. The remaining systems, showed only the partial formation of the desired phase and further work is required. A further development and optimization of the synthesis in these materials will be thus pursued.

Local probe studies in high quality prepared systems has already begun and the results are being analyzed.

Additional studies with complementary local probe techniques are envisaged for the presented systems, either spinels or perovskites together with further theoretical calculations.

Publications related to the PhD work

Several contributions were made to the scientific community, directly related to the work developed in the present thesis, including 9 oral communications, 10 poster presentations, and the several publications. This thesis is based on the following publications:

1. G.N.P. Oliveira, P. Machado, A.L. Pires, A.M. Pereira, J.P. Araújo, A.M.L. Lopes, Magnetocaloric effect and refrigerant capacity in polycrystalline $YCrO_3$, J. Phys. Chem. Solids **91**, 182-188 (2016)

2. G.N.P. Oliveira, R. Teixeira, T.M. Mendonça, M.R. Silva, J.G. Correia, A.M.L. Lopes, and J.P. Araújo, Local symmetry lowering in $CdMn_2O_4$ spinel, J. Appl. Phys. **116**, 223907 (2014).

3. G.N.P. Oliveira, A.M. Pereira, A.M.L. Lopes, J.S. Amaral, A.M. dos Santos, Y. Ren, T.M. Mendonça, C.T. Sousa, V.S. Amaral, J.G. Correia, and J.P. Araújo, Dynamic off-centering of Cr^{3+} ions and short-range magneto-electric clusters in $CdCr_2S_4$, Phys. Rev. B **86**, 224418 (2012).

4. G. N. P. Oliveira, A. M. dos Santos, Z. Gai, G. Halder, J. P. Araújo, A. M. L. Lopes and A. M. Pereira, Unveiling the nature of local clusters in $CdCr_2S_4$ through hydrostatic pressure, *Submitted to Applied Physics Letters* (2016).

5. G.N.P. Oliveira, A. Pires, P. Machado, A.M. Pereira, L. Fernandes, P.B. Tavares, J.P. Araújo, and A.M.L. Lopes, Effect of Chemical Pressure on the magnetocaloric effect of perovskites $RCrO_3$ (R-Yb, Er, Sm and Y), *In preparation*.

6. G.N.P. Oliveira, R. Teixeira, J.G. Correia, J.P. Araújo, and A.M.L. Lopes, Probing the local structure in Multiferroic $SmCrO_3$, *In preparation*.

Nevertheless, several collaborations also took place, resulting in 6 oral communications, 12 poster presentations, and the following publications:

1. A. Apolinário, C.T. Sousa, G. N. Oliveira, A. M. L. Lopes, J. Ventura, L. Andrade, A. M.Mendes and J. P. Araújo, Effects of different organic solvent's electrolyte on the morphology of anodic hafnium oxide, *In preparation*.

2. A. Apolinário, C. T. Sousa, A. M. Pereira, M. P. Fernandez, G. Oliveira, J. Azevedo, J. Ventura, L. Andrade, A. M. Mendes and J. P. Araújo, Anodic iron oxide nanotubes: unveiling their rich magnetic and structural behavior, *In preparation*.

3. A.L. Pires, J.H. Belo, J. Turcaud, G.N.P. Oliveira, J.P. Araújo, A. Berenov, L.F. Cohen, A.M.L. Lopes, A.M. Pereira, Influence of short time milling in $R_5(Si, Ge)_4$, R = Gd and Tb, magnetocaloric materials, Materials and Design 85, 32-38 (2015).

4. I. Soares, A. Moleirinho, G.N.P. Oliveira , A. Amorim, DivStat: A User-Friendly Tool for Single Nucleotide Polymorphism Analysis of Genomic Diversity, PLoS ONE 10(3): e0119851 (2015).

5. A. Ghosh, A. Pasko, S.N. Kane, M. Satalkar, R. Prasad, R. Diwedi, S. Ladole, A.S. Aswar, G.N.P. Oliveira, A. Apolinário, C.T. Sousa, J.P. Araujo, and F. Mazaleyrat, Influence of Mn addition on magnetic and structural properties of barium hexaferrite, AIP Conf. Proc. 1536, 961 (2013).

6. A.M.L. Lopes, G.N.P. Oliveira, S. Ferdov, Mild hydrothermal synthesis, isomorphous substitution, crystal structure characterization and magnetic properties of $BaMP_2O_7$ (M=Mn, Cu), Solid State Sciences 26, 59e64 (2013).

7. S. Pinto, R. Krishna, C. Dias, G. Pimentel, G.N.P. Oliveira, J.M. Teixeira, P. Aguiar, E. Titus, J. Gracio, J. Ventura, and J.P. Araújo, Resistive switching and activity-dependent modifications in Ni-doped graphene oxide thin films, Applied Physics Letters 101, 063104 (2012).

8. J.H. Belo, A.M. Pereira, J. Ventura, G.N.P. Oliveira, J.P. Araújo, P.B. Tavares, L. Fernandes, P.A. Algarabel, C. Magen, L. Morellon, M.R. Ibarra, Phase control studies in $Gd_5Si_2Ge_2$ giant magnetocaloric compound, Journal of Alloys and Compounds 529, 89-95 (2012).

9. S. Pinto, R. Krishna, C. Dias, G. Pimentel, G.N.P. Oliveira, J.M. Teixeira, P. Aguiar, E. Titus, J. Gracio, J. Ventura, J. P. Araujo, Switching and learning in Ni-doped graphene oxide thin films, Nature Conference “Frontiers in Electronic Materials” 586-587 (2012).

10. M.P. Fernández-Garcia, J. Agostinho Moreira, A.M. Pereira, G.N.P. Oliveira, J. Oliveira, M.R.Chaves, J.C.A.M. Azevedo, C.T. Sousa, J.M. Teixeira, A.M.L. Lopes, M.M.R Costa, J. Amaral, T.M. Mendonça, V.A. Khonchenko, V.H. Rodrigues, P.B. Tavares, A. Mendes, J.G. Correia, V. Amaral, A. Almeida, J.B. Sousa, J.P. Araújo, Synchrotron radiation experiments on multiferroic, magnetocaloric and magnetic nanostructured materials, Ciência & Tecnologia dos Materiais, vol 24, no 3-4 pp 128-133 (2012).

11. A.M.L. Lopes, G.N.P. Oliveira, T.M. Mendonça, J. Agostinho Moreira, A. Almeida, J.P. Araújo, V.S. Amaral, J.G. Correia, Local Distortions in multiferroic $AgCrO_2$ Triangular spin Lattice, Physical Review B 84, 014434 (2011).

Bibliography

[1] K. F. Wang, J. M. Liu, Z. F. Ren, Multiferroicity: The coupling between magnetic and polarization orders, Advances in Physics **58** (4) (2009) 321–448. doi:10.1080/00018730902920554.

[2] J. E. Mark, Physical Properties of Polymers Handbook, Springer, New York, NY, 2007. doi:10.1007/978-0-387-69002-5.

[3] M. Peplow, March of the machines, Nature **525** (7567) (2015) 18–21. doi:10.1038/525018a.

[4] K. Salonitis, J. Pandremenos, J. Paralikas, G. Chryssolouris, Multifunctional materials: engineering applications and processing challenges, The International Journal of Advanced Manufacturing Technology **49** (5-8) (2009) 803–826. doi:10.1007s00170-009-2428-6.

[5] L. Christodoulou, J. D. Venables, Multifunctional material systems: The first generation, The Journal of The Minerals, Metals & Materials Society **55** (12) (2003) 39–45. doi:10.1007/s11837-003-0008-z.

[6] P. mcMullen, Fibre/resin composites for aircraft primary structures: a short history, 1936–1984, Composites **15** (3) (1984) 222–230. doi:10.1016/0010-4361(84)90279-9.

[7] J. Delmonte, Metal/Polymer Composites, Springer Science+Business Media, LLC, Boston, MA, 1990. doi:10.1007/978-1-4684-1446-2.

[8] D. Son, J. Lee, S. Qiao, R. Ghaffari, J. Kim, J. E. Lee, C. Song, S. J. Kim, D. J. Lee, S. W. Jun, S. Yang, M. Park, J. Shin, K. Do, M. Lee, K. Kang, C. S. Hwang, N. Lu, T. Hyeon, D.-H. Kim, Multifunctional wearable devices for diagnosis and therapy of movement disorders, Nature Nanotechnology **9** (2014) 397–404. doi:10.1038/nnano.2014.38.

[9] C. M. Friend, Smart materials and structures: The emerging technology, Interdisciplinary Science Reviews **21** (3) (1996) 195–198. doi:10.1179/isr.1996.21.3.195.

[10] D. L. Polla, L. F. Francis, Processing and characterization of piezoelectric materials and integration into microelectromechanical systems, Annual Review of Materials Science **28** (1) (1998) 563–597. doi:10.1146/annurev.matsci.28.1.563.

[11] D. M. Elzey, A. Y. N. Sofla, H. N. G. Wadley, A shape memory-based multifunctional structural actuator panel, International Journal of Solids and Structures **42** (7) (2005) 1943–1955. doi:10.1016/j.ijsolstr.2004.05.034.

[12] C. M. Lampert, Chromogenic smart materials, Materials Today **7** (3) (2004) 28–35. doi:10.1016/S1369-7021(04)00123-3.

[13] C.-W. Nan, M. I. Bichurin, S. Dong, D. Viehland, G. Srinivasan, Multiferroic magnetoelectric composites: Historical perspective, status, and future directions, Journal of Applied Physics **103** (3) (2008) 031101–36. doi:10.1063/1.2836410.

[14] Y. Wang, Y. Xia, Bottom-Up and Top-Down Approaches to the Synthesis of Monodispersed Spherical Colloids of Low Melting-Point Metals, Nano Letters **4** (10) (2004) 2047–2050. doi:10.1021/nl048689j.

[15] M. Shaarbaf, M. R. Toroghinejad, Nano-grained copper strip produced by accumulative roll bonding process, Materials Science and Engineering: A **473** (1-2) (2008) 28–33. doi:10.1016/j.msea.2007.03.065.

[16] M. E. Lines, A. M. Glass, Principles and Applications of Ferroelectrics and Related Materials, Oxford University Press, 1977. doi:10.1093/acprof:oso/9780198507789.001.0001.

[17] C. Morón, C. Cabrera, A. Morón, A. García, M. González, Magnetic Sensors Based on Amorphous Ferromagnetic Materials: A Review, Sensors **15** (11) (2015) 28340–28366. doi:10.3390/s151128340.

[18] Y. Tokura, S. Seki, Multiferroics with Spiral Spin Orders, Advanced Materials **22** (14) (2009) 1554–1565. doi:10.1002/adma.200901961.

[19] M. N. Baibich, J. M. Broto, A. Fert, F. N. Van Dau, F. Petroff, P. Etienne, G. Creuzet, A. Friederich, J. Chazelas, Giant Magnetoresistance of (001)Fe/(001)Cr Magnetic Superlattices, Physical Review Letters **61** (21) (1988) 2472–2475. doi:10.1103/PhysRevLett.61.2472.

[20] I. Žutić, J. Fabian, S. Das Sarma, Spintronics: Fundamentals and applications, Reviews of Modern Physics **76** (2) (2004) 323–410. doi:10.1103/RevModPhys.76.323.

[21] J. F. Scott, Ferroelectric Memories, Vol. 3 of Springer Series in Advanced Microelectronics, Springer Berlin Heidelberg, Berlin, Heidelberg, 2000. doi:10.1007/978-3-662-04307-3.

[22] Y. H. Chu, L. W. Martin, M. B. Holcomb, R. Ramesh, Controlling magnetism with multiferroics, Materials Today **10** (10) (2007) 16–23. doi:10.1016/s1369-7021(07)70241-9.

[23] D. I. Khomskii, Multiferroics: Different ways to combine magnetism and ferroelectricity, Journal of Magnetism and Magnetic Materials **306** (1) (2006) 1–8. doi:10.1016/j.jmmm.2006.01.238.

[24] Y. Tokura, Multiferroics-toward strong coupling between magnetization and polarization in a solid, Journal of Magnetism and Magnetic Materials **310** (2) (2007) 1145–1150. doi:10.1016/j.jmmm.2006.11.198.

[25] A. K. Zvezdin, A. M. Kadomtseva, S. S. Krotov, A. P. Pyatakov, Y. F. Popov, G. P. Vorob'ev, Magnetoelectric interaction and magnetic field control of electric polarization in multiferroics, Journal of Magnetism and Magnetic Materials **300** (1) (2006) 224–228. doi:10.1016/j.jmmm.2005.10.068.

[26] W. Eerenstein, N. D. Mathur, J. F. Scott, Multiferroic and magnetoelectric materials, Nature **442** (7104) (2006) 759–765. doi:10.1038/nature05023.

[27] N. A. Spaldin, M. Fiebig, Materials science. The renaissance of magnetoelectric multiferroics., Science **309** (5733) (2005) 391–392. doi:10.1126/science.1113357.

[28] L. E. Fuentes-Cobas, J. A. Matutes-Aquino, M. E. Botello-Zubiate, A. González-Vázquez, M. E. Fuentes-Montero, D. Chateigner, Advances in Magnetoelectric Materials and Their Application, Vol. 24, Elsevier Ltd, 2015. doi:10.1016/bs.hmm.2015.10.001.

[29] N. A. Hill, Why Are There so Few Magnetic Ferroelectrics?, Journal of Physical Chemistry

B **104** (29) (2000) 6694–6709. doi:10.1021/jp000114x.

[30] S. Dong, J.-M. Liu, S.-W. Cheong, Z. Ren, Multiferroic materials and magnetoelectric physics: symmetry, entanglement, excitation, and topology, Advances in Physics **64** (5-6) (2015) 519–626. doi:10.1080/00018732.2015.1114338.

[31] S. Picozzi, A. Stroppa, Advances in ab-initio theory of multiferroics, The European Physical Journal B **85** (7) (2012) 240. doi:10.1140/epjb/e2012-30124-1.

[32] J. F. Scott, R. Blinc, Multiferroic magnetoelectric fluorides: why are there so many magnetic ferroelectrics?, Journal of Physics: Condensed Matter **23** (11) (2011) 113202. doi:10.1088/0953-8984/23/11/113202.

[33] H. Schmid, Some symmetry aspects of ferroics and single phase multiferroics*, Journal of Physics: Condensed Matter **20** (43) (2008) 434201. doi:10.1088/0953-8984/20/43/434201.

[34] A. P. Pyatakov, A. K. Zvezdin, Magnetoelectric and multiferroic media, Physics - Uspekhi **55** (6) (2012) 557–581. doi:10.3367/UFNe.0182.201206b.0593.

[35] S. Fusil, V. Garcia, A. Barthelemy, M. Bibes, Magnetoelectric Devices for Spintronics, Annual Review of Materials Research **44** (1) (2014) 91–116. doi:10.1146/annurev-matsci-070813-113315.

[36] M. Fiebig, Revival of the magnetoelectric effect, Journal of Physics D: Applied Physics **38** (8) (2005) R123–R152. doi:10.1088/0022-3727/38/8/R01.

[37] S. Picozzi, C. Ederer, First principles studies of multiferroic materials, Journal of Physics: Condensed Matter **21** (30) (2009) 303201–19. doi:10.1088/0953-8984/21/30/303201.

[38] G. T. Rado, V. J. Folen, Observation of the Magnetically Induced Magnetoelectric Effect and Evidence for Antiferromagnetic Domains, Physical Review Letters **7** (8) (1961) 310–311. doi:10.1103/PhysRevLett.7.310.

[39] W. Eerenstein, M. Wiora, J. L. Prieto, J. F. Scott, N. D. Mathur, Giant sharp and persistent converse magnetoelectric effects in multiferroic epitaxial heterostructures, Nature Materials **6** (5) (2007) 348–351. doi:10.1038/nmat1886.

[40] I. E. Dzyaloshinskii, On the magneto-electrical effect in antiferromagnets, Journal of Experimental and Theoretical Physics **10** (3) (1960) 928–629.

[41] V. J. Folen, G. T. Rado, E. W. Stalder, Anisotropy of the Magnetoelectric Effect in Cr_2O_3, Physical Review Letters **6** (11) (1961) 607.

[42] Y. Wang, J. Hu, Y. Lin, C.-W. Nan, Multiferroic magnetoelectric composite nanostructures, NPG Asia Materials **2** (2) (2010) 61–68. doi:10.1038/asiamat.2010.32.

[43] T. Kimura, T. Goto, H. Shintani, K. Ishizaka, T.-h. Arima, Y. Tokura, Magnetic control of ferroelectric polarization, Nature **426** (6962) (2003) 55–58. doi:10.1038/nature02018.

[44] D. Lebeugle, D. Colson, A. Forget, M. Viret, A. M. Bataille, A. Gukasov, Electric-Field-Induced Spin Flop in $BiFeO_3$ Single Crystals at Room Temperature, Physical Review Letters **100** (22) (2008) 227602.

[45] C. N. R. Rao, A. Sundaresan, R. Saha, Multiferroic and Magnetoelectric Oxides: The Emerging Scenario, The Journal of Physical Chemistry Letters **3** (16) (2012) 2237–2246. doi:10.1021/jz300688b.

[46] Y. W. Yin, J. D. Burton, Y.-M. Kim, A. Y. Borisevich, S. J. Pennycook, S. M. Yang, T. W. Noh, A. Gruverman, X. G. Li, E. Y. Tsymbal, Q. Li, Enhanced tunnelling electroresistance effect due to a ferroelectrically induced phase transition at a magnetic complex oxide interface., Nature Materials **12** (5) (2013) 397–402. doi:10.1038/nmat3564.

[47] T. Zhao, A. Scholl, F. Zavaliche, K. Lee, M. Barry, A. Doran, M. P. Cruz, Y. H. Chu, C. Ederer, N. A. Spaldin, R. R. Das, D. M. Kim, S. H. Baek, C. B. Eom, R. Ramesh, Electrical control of antiferromagnetic domains in multiferroic $BiFeO_3$ films at room temperature, Nature Materials **5** (10) (2006) 823–829. doi:10.1038/nmat1731.

[48] B. B. Van Aken, T. T. M. Palstra, A. Filippetti, N. A. Spaldin, The origin of ferroelectricity in magnetoelectric $YMnO_3$, Nature Materials **3** (3) (2004) 164–170. doi:10.1038/nmat1080.

[49] Y. S. Oh, X. Luo, F.-T. Huang, Y. Wang, S.-W. Cheong, Experimental demonstration of hybrid improper ferroelectricity and the presence of abundant charged walls in $(Ca,Sr)_3Ti_2O_7$ crystals, Nature Materials **14** (4) (2015) 407–413. doi:10.1038/nmat4168.

[50] Y. S. Oh, S. Artyukhin, J. J. Yang, V. Zapf, J. W. Kim, D. Vanderbilt, S.-W. Cheong, Non-hysteretic colossal magnetoelectricity in a collinear antiferromagnet, Nature Communications **5** (2014) 3201–3201. doi:10.1038/ncomms4201.

[51] W. Prellier, M. P. Singh, P. Murugavel, The single-phase multiferroic oxides: from bulk to thin film, Journal of Physics: Condensed Matter **17** (30) (2005) R803–R832. doi:10.1088/0953-8984/17/30/R01.

[52] Y. Tokura, Multiferroics as Quantum Electromagnets, Science **312** (5779) (2006) 1481–1482. doi:10.1126/science.1125227.

[53] R. Ramesh, N. A. Spaldin, Multiferroics: progress and prospects in thin films, Nature Materials **6** (1) (2007) 21–29. doi:10.1038/nmat1805.

[54] T. Kimura, Spiral Magnets as Magnetoelectrics, Annual Review of Materials Research **37** (1) (2007) 387–413. doi:10.1146/annurev.matsci.37.052506.084259.

[55] Y. Tokura, S. Seki, N. Nagaosa, Multiferroics of spin origin, Reports on Progress in Physics **77** (7) (2014) 076501–46. doi:10.1088/0034-4885/77/7/076501.

[56] S.-W. Cheong, M. Mostovoy, Multiferroics: a magnetic twist for ferroelectricity, Nature Materials **6** (1) (2007) 13–20. doi:10.1038/nmat1804.

[57] A. Stroppa, P. Barone, P. Jain, J. M. Perez-Mato, S. Picozzi, Hybrid improper ferroelectricity in a multiferroic and magnetoelectric metal-organic framework, Advanced Materials **25** (16) (2013) 2284–2290. doi:10.1002/adma.201204738.

[58] D. Khomskii, Classifying multiferroics: Mechanisms and effects, Physics **2** (2009) 20–28. doi:10.1103/Physics.2.20.

[59] K. R. S. P. Meher, C. Martin, V. Caignaert, F. Damay, A. Maignan, Multiferroics and Magnetoelectrics: A Comparison between Some Chromites and Cobaltites, Chemistry of Materials **26** (1) (2014) 830–836. doi:10.1021/cm4020546.

[60] N. A. Spaldin, S.-W. Cheong, R. Ramesh, Multiferroics: Past, present, and future, Physics Today **63** (10) (2010) 38–43. doi:10.1063/1.3502547.

[61] L. W. Martin, Y. H. Chu, R. Ramesh, Advances in the growth and characterization of magnetic, ferroelectric, and multiferroic oxide thin films, Materials Science & Engineering

R **68** (4-6) (2010) 89–133. doi:10.1016/j.mser.2010.03.001.

[62] J. P. Velev, S. S. Jaswal, E. Y. Tsymbal, Multi-ferroic and magnetoelectric materials and interfaces, Philosophical transactions. Series A, Mathematical, physical, and engineering sciences **369** (1948) (2011) 3069–3097. doi:10.1098/rsta.2010.0344.

[63] T. Kimura, Magnetoelectric Hexaferrites, Annual Review of Condensed Matter Physics **3** (1) (2012) 93–110. doi:10.1146/annurev-conmatphys-020911-125101.

[64] S. Dong, J.-M. Liu, Recent Progress Of Multiferroic Perovskite Manganites, Modern Physics Letters B **26** (09) (2012) 1230004–26. doi:10.1142/S0217984912300049.

[65] C. A. F. Vaz, Electric field control of magnetism in multiferroic heterostructures, Journal of Physics: Condensed Matter **24** (33) (2012) 333201. doi:10.1088/0953-8984/24/33/333201.

[66] P. Yu, Y. H. Chu, R. Ramesh, Emergent phenomena at multiferroic heterointerfaces., Philosophical transactions. Series A, Mathematical, physical, and engineering sciences **370** (1977) (2012) 4856–4871. doi:10.1098/rsta.2012.0199.

[67] X. Huang, S. Dong, Ferroelectric control of magnetism and transport in oxide heterostructures, Modern Physics Letters B **28** (23) (2014) 1430010–25. doi:10.1142/S0217984914300105.

[68] C. Lu, W. Hu, Y. Tian, T. Wu, Multiferroic oxide thin films and heterostructures, Applied Physics Reviews **2** (2) (2015) 021304–19. doi:10.1063/1.4921545.

[69] L. W. Martin, D. G. Schlom, Advanced synthesis techniques and routes to new single-phase multiferroics, Current Opinion in Solid State & Materials Science **16** (5) (2012) 199–215. doi:10.1016/j.cossms.2012.03.001.

[70] R. D. Johnson, P. G. Radaelli, Diffraction Studies of Multiferroics, Annual Review of Materials Research **44** (1) (2014) 269–298. doi:10.1146/annurev-matsci-070813-113524.

[71] F. Matsukura, Y. Tokura, H. Ohno, Control of magnetism by electric fields, Nature Nanotechnology **10** (3) (2015) 209–220. doi:10.1038/nnano.2015.22.

[72] N. Ortega, A. Kumar, J. F. Scott, R. S. Katiyar, Multifunctional magnetoelectric materials for device applications, Journal of Physics: Condensed Matter **27** (2015) 1–23. doi:10.1088/0953-8984/27/50/504002.

[73] Y. H. Chu, L. W. Martin, M. B. Holcomb, M. Gajek, S.-J. Han, Q. He, N. Balke, C.-H. Yang, D. Lee, W. Hu, Q. Zhan, P.-L. Yang, A. Fraile-rodriguez, A. Scholl, S. X. Wang, R. Ramesh, Electric-field control of local ferromagnetism using a magnetoelectric multiferroic, Nature Materials **7** (6) (2008) 478–482. doi:10.1038/nmat2184.

[74] A. K. Kundu, Magnetic Perovskites: Synthesis, Structure and Physical Properties, Springer, New Delhi, 2016. doi:10.1007/978-81-322-2761-8.

[75] D. K. Pradhan, V. S. Puli, S. Kumari, S. Sahoo, P. T. Das, K. Pradhan, D. K. Pradhan, J. F. Scott, R. S. Katiyar, Studies of Phase Transitions and Magnetoelectric Coupling in PFN-CZFO Multiferroic Composites, The Journal of Physical Chemistry C **120** (3) (2016) 1936–1944. doi:10.1021/acs.jpcc.5b10422.

[76] B. Koteswararao, K. Yoo, F. C. Chou, K. H. Kim, Observation of magnetoelectric effects in a S=1/2 frustrated spin chain magnet $SrCuTe_2O_6$, APL Materials **4** (3) (2016) 036101.

doi:10.1063/1.4943012.

[77] G. J. M. Velders, A. R. Ravishankara, M. K. Miller, M. J. Molina, J. Alcamo, J. S. Daniel, D. W. Fahey, S. A. Montzka, S. Reimann, Preserving Montreal Protocol Climate Benefits by Limiting HFCs, Science **335** (6071) (2012) 922–923. doi:10.1126/science.1216414.

[78] E. Warburg, Magnetische Untersuchungen, Annalen der Physik **249** (5) (1881) 141–164. doi:10.1002/andp.18812490510.

[79] P. Debye, Einige Bemerkungen zur Magnetisierung bei tiefer Temperatur, Annalen der Physik **386** (25) (1926) 1154–1160. doi:10.1002/andp.19263862517.

[80] W. F. Giauque, A Thermodynamic Treatment of certain magnetic effects. A proposed method of producing temperatures considerably below 1º absolute, Journal of the American Ceramic Society **49** (8) (1927) 1864–1870. doi:10.1021/ja01407a003.

[81] W. F. Giauque, D. P. MacDougall, Attainment of Temperatures Below 1° Absolute by Demagnetization of $Gd_2(SO_4)_3 \cdot 8H_2O$, Physical Review **43** (9) (1933) 768–768. doi:10.1103/PhysRev.43.768.

[82] W. Goetzler, R. Zogg, H. Lisle, J. Burgos, Ground-Source Heat Pumps. Overview of Market Status, Barriers to Adoption, and Options for Overcoming Barriers, Tech. rep., EERE Publication and Product Library (Feb. 2009). doi:10.2172/1219308.
URL http://www.osti.gov/servlets/purl/1219308/

[83] A. M. Tishin, Y. I. Spichkin, The Magnetocaloric Effect and its Applications, IOP Publishing Ltd, 2003. doi:10.1887/0750309229.

[84] J. S. Amaral, V. S. Amaral, The effect of magnetic irreversibility on estimating the magnetocaloric effect from magnetization measurements, Applied Physics Letters **94** (4) (2009) 042506. doi:10.1063/1.3075851.

[85] E. Brück, Magnetocaloric Refrigeration at Ambient Temperature, Proceedings of the th Brazilian Congress of Thermal Sciences and Engineering. doi:10.1016/S1567-2719(07)17004-9.

[86] X. Moya, L. Mañosa, A. Planes, S. Aksoy, M. Acet, E. F. Wassermann, T. Krenke, Cooling and heating by adiabatic magnetization in the $Ni_{50}Mn_{34}In_{16}$magnetic shape-memory alloy **75** (18) (2007) 184412. doi:10.1103/PhysRevB.75.184412.

[87] G. J. Liu, J. R. Sun, J. Shen, B. Gao, H. W. Zhang, F.-x. Hu, B. G. Shen, Determination of the entropy changes in the compounds with a first-order magnetic transition, Applied Physics Letters **90** (3) (2007) 032507. doi:10.1063/1.2425033.

[88] J. S. Amaral, N. J. O. Silva, V. S. Amaral, A mean-field scaling method for first- and second-order phase transition ferromagnets and its application in magnetocaloric studies, Applied Physics Letters **91** (17) (2007) 172503. doi:10.1063/1.2801692.

[89] C. Zimm, A. Jastrab, A. Sternberg, V. Pecharsky, K. Gschneidner, M. Osborne, I. Anderson, Description and Performance of a Near-Room Temperature Magnetic Refrigerator, Advances in Cryogenic Engineering **43** (1998) 1759–1766. doi:10.1007/978-1-4757-9047-4_222.

[90] V. K. Pecharsky, J. K A Gschneidner, Giant Magnetocaloric Effect in $Gd_5(Si_2Ge_2)$, Physical Review Letters **78** (23) (1997) 4494–4497. doi:10.1103/PhysRevLett.78.4494.

[91] B. F. Yu, Q. Gao, B. Zhang, X. Z. Meng, Z. Chen, Review on research of room temperature magnetic refrigeration, International Journal of Refrigeration **26** (6) (2003) 622–636. doi:10.1016/S0140-7007(03)00048-3.

[92] K. A. Gschneidner, V. K. Pecharsky, Recent developments in magnetocaloric materials, Reports on Progress in Physics **68** (2005) 1479–1539. doi:10.1088/0034-4885/68/6/R04.

[93] J. R. Gómez, R. F. Garcia, A. De Miguel Catoira, M. R. Gómez, Magnetocaloric effect A review of the thermodynamic cycles in magnetic refrigeration, Renewable and Sustainable Energy Reviews **17** (C) (2013) 74–82. doi:10.1016/j.rser.2012.09.027.

[94] V. K. Pecharsky, K. A. Gschneidner Jr, Magnetocaloric Effect and Magnetic Refrigeration, Journal of Magnetism and Magnetic Materials **200** (1) (1999) 44–56. doi:10.1016/S0304-8853(99)00397-2.

[95] K. A. Gschneidner, V. K. Pecharsky, Mgnetocaloric Materials, Annual Review of Materials Science **30** (1) (2000) 387–429. doi:10.1146/annurev.matsci.30.1.387.

[96] K. Matsumoto, T. Kouen, R. Nishida, S. Abe, K. Kamiya, T. Numazawa, Magnetocaloric Effect of RCo_2 (R: Er, Ho, Dy) Compounds for Regenerative Magnetic Refrigeration, Low Temperature Physics International Conference on low Temperature Physics **850** (2006) 1581–1582. doi:10.1063/1.2355310.

[97] H. Wada, Y. Tanabe, Giant Magnetocaloric Effect of $MnAs_{1-x}Sb_x$, Applied Physics Letters **79** (2) (2001) 3302. doi:10.1063/1.1419048.

[98] R. Bjørk, C. R. H. Bahl, M. Katter, Magnetocaloric properties of $LaFe_{13-x-y}Co_xSi_y$ and commercial grade Gd, Journal of Magnetism and Magnetic Materials **322** (24) (2010) 3882–3888. doi:10.1016/j.jmmm.2010.08.013.

[99] M. P. Annaorazov, S. A. Nikitin, A. L. Tyurin, K. A. Asatryan, A. K. Dovletov, Anomalously high entropy change in FeRh alloy, Journal of Applied Physics **79** (3) (1996) 1689–8. doi:10.1063/1.360955.

[100] J. H. Belo, J. S. Amaral, A. M. Pereira, V. S. Amaral, J. P. Araújo, On the Curie temperature dependency of the magnetocaloric effect, Applied Physics Letters **100** (2) (2012) 242407. doi:10.1063/1.4726110.

[101] L. J. Love, J. F. Jansen, T. McKnight, Y. Roh, T. J. Phelps, A Magnetocaloric Pump for Microfluidic Applications, IEEE Transactions on Nanobioscience **3** (2) (2004) 101–110. doi:10.1109/TNB.2004.828265.

[102] D. Baldomir, J. Rivas, D. Serantes, M. Pereiro, J. E. Arias, M. C. Buján-Núñez, C. Vázquez-Vázquez, Magnetocaloric effects in magnetic nanoparticle systems: A Monte Carlo study, Journal of Non-Crystalline Solids **353** (8-10) (2007) 790–792. doi:10.1016/j.jnoncrysol.2006.12.041.

[103] K. A. Gschneidner Jr, V. K. Pecharsky, Rare Earths and Magnetic Refrigeration, Journal of Rare Earths **24** (6) (2006) 641–647. doi:10.1016/S1002-0721(07)60001-5.

[104] K. A. Gschneidner, V. K. Pecharsky, Thirty years of near room temperature magnetic cooling: Where we are today and future prospects, International Journal of Refrigeration **31** (6) (2008) 945–961. doi:10.1016/j.ijrefrig.2008.01.004.

[105] S. Zhang, Electric-Field Control of Magnetization and Electronic Transport in Ferro-

magnetic/Ferroelectric Heterostructures, Springer Berlin Heidelberg, Berlin, Heidelberg (2014). doi:10.1007/978-3-642-54839-0.
URL http://link.springer.com/10.1007/978-3-642-54839-0

[106] S. Anthony. GE develops high-tech fridge magnets that could save the world billions of dollars in energy costs | ExtremeTech [online] (Feb. 2014).

[107] Cooltech Applications. Premiere of Revolutionary Medical Refrigerator with Cooltech Applications at Medica 2015 [online] (Dec. 2015).

[108] V. K. Pecharsky, K. A. Gschneidner Jr, Advanced magnetocaloric materials: What does the future hold?, International Journal of Refrigeration **29** (8) (2006) 1239–1249. doi:10.1016/j.ijrefrig.2006.03.020.

[109] S. Nishikawa, Structure of Some Crystals of Spinel Group, Proceedings of the Tokyo Mathematico-Physical Society. nd Series **8** (7) (1915) 1–12.

[110] W. H. Bragg, XXX. The structure of the spinel group of crystals, Philosophical Magazine Series 6 **30** (176) (1915) 305–315. doi:10.1080/14786440808635400.

[111] K. E. Sickafus, J. M. Wills, N. W. Grimes, Structure of Spinel, Journal of the American Ceramic Society **82** (12) (2004) 3279–3292. doi:10.1111/j.1151-2916.1999.tb02241.x.

[112] J. B. Goodenough, W. Gräper, F. Holtzberg, D. L. Huber, R. A. Lefever, J. M. Longo, T. R. McGuire, S. Methfessel, Magnetic and Other Properties of Oxides and Related Compounds, Volume 4,Parte 1 of Landolt-Börnstein: Numerical Data and Functional Relationships in Science and Technology - New Series Condensed Matter, Springer, 1970. doi:10.1007/b19968.

[113] G. D. Price, S. L. Price, J. K. Burdett, The factors influencing cation site-preferences in spinels a new mendelyevian approach, Physics and Chemistry of Minerals **8** (2) (1982) 69–76. doi:10.1007/BF00309016.

[114] T. F. W. Barth, E. Posnjak, Spinel structures: with and without variate atom equipoints, Zeitschrift für Kristallographie - Crystalline Materials **82** (1-6). doi:10.1524/zkri.1932.82.1.325.

[115] C. B. Azzoni, M. C. Mozzati, P. Ghigna, L. Malavasi, G. Flor, Magnetic Investigation of Mn Ions in $(Cd_{1-x}Mn_x)Mn_2O_4$ Spinels, Solid State Communications **117** (9) (2001) 511–515. doi:10.1016/S0038-1098(00)00514-7.

[116] R. A. W. Haul, F. R. L. Sch ning, Zur thermischen Zersetzung von Dolomit. V. Kristallitgrößen der Zersetzungsprodukte, Zeitschrift Fur Anorganische Und Allgemeine Chemie **269** (3) (1952) 120–134. doi:10.1002/zaac.19522690306.

[117] J. B. Goodenough, A. L. Loeb, Theory of Ionic Ordering, Crystal Distortion, and Magnetic Exchange Due to Covalent Forces in Spinels, Physical Review **98** (2) (1955) 391–408. doi:10.1103/PhysRev.98.391.

[118] J. D. Dunitz, L. E. Orgel, Electronic properties of transition-metal oxides - I, Journal of Physics and Chemistry of Solids **3** (1-2) (1957) 20–29. doi:10.1016/0022-3697(57)90043-4.

[119] C. J. Fennie, K. M. Rabe, Polar phonons and intrinsic dielectric response of the ferromagnetic insulating spinel $CdCr_2S_4$ from first principles **72** (21) (2005) 214123. doi:

10.1103/PhysRevB.72.214123.

[120] F. Laves, G. Bayer, A. Panagos, Strukturelle Beziehungen zwischen den Typen a-PbO_2, $FeWO_4$(Wolframit) und $FeNb_20_6$(Columbit), and fiber die Polymorphie des $FeNbO_4$, Schweiz. , Mineral. Petrogr. Mitt **43** (1963) 217–234.

[121] P. K. Baltzer, P. J. Wojtowicz, M. Robbins, E. Lopatin, Exchange Interactions in Ferromagnetic Chromium Chalcogenide Spinels, Physical Review **151** (2) (1966) 367–377. doi:10.1103/PhysRev.151.367.

[122] V. Samokhvalov, S. Unterricker, I. Burlakov, Investigation of ferromagnetic spinel semiconductors by hyperfine interactions of implanted nuclear probes, Journal of Physics and Chemistry of Solids **64** (2003) 2069–2073. doi:10.1016/S0022-3697(03)00152-5.

[123] P. K. Baltzer, H. W. Lehmann, M. Robbins, Insulating Ferromagnetic Spinels, Physical Review Letters **15** (1) (1965) 493–495. doi:10.1103/PhysRevLett.15.493.

[124] T. Rudolf, C. Kant, F. Mayr, J. Hemberger, V. Tsurkan, A. Loidl, Polar phonons and spin-phonon coupling in $HgCr_2S_4$ and $CdCr_2S_4$ studied with far-infrared spectroscopy **76** (17) (2007) 174307. doi:10.1103/PhysRevB.76.174307.

[125] J. Hemberger, H. A. K. von Nidda, V. Tsurkan, A. Loidl, Large Magnetostriction and Negative Thermal Expansion in the Frustrated Antiferromagnet $ZnCr_2Se_4$, Physical Review Letters **98** (14) (2007) 147203–4. doi:10.1103/PhysRevLett.98.147203.

[126] T. Rudolf, C. Kant, F. Mayr, J. Hemberger, V. Tsurkan, A. Loidl, Spin-phonon coupling in antiferromagnetic chromium spinels, New Journal of Physics **9** (3) (2007) 76–76. doi:10.1088/1367-2630/9/3/076.

[127] V. Fritsch, J. Hemberger, N. Büttgen, E. W. Scheidt, H. A. Krug von Nidda, A. Loidl, V. Tsurkan, Spin and Orbital Frustration in $MnSc_2S_4$and $FeSc_2S_4$, Physical Review Letters **92** (11) (2004) 116401–4. doi:10.1103/PhysRevLett.92.116401.

[128] J. Hemberger, P. Lunkenheimer, R. Fichtl, H. A. Krug von Nidda, V. Tsurkan, A. Loidl, Relaxor ferroelectricity and colossal magnetocapacitive coupling in ferromagnetic $CdCr_2S_4$, Nature **434** (7031) (2005) 364–367. doi:10.1038/nature03348.

[129] J. Hemberger, P. Lunkenheimer, R. Fichtl, S. Weber, V. Tsurkan, A. Loidl, Multiferroic Behavior in $CdCr_2X_4$(X=S,Se), Physica B: Condensed Matter **378-380** (2006) 363–366. doi:10.1016/j.physb.2006.01.407.

[130] N. W. Grimes, 'Off-Centre' Ions in Compounds with Spinel Structure, Philosophical Magazine **26** (5) (1972) 1217–1226.

[131] J. Hemberger, T. Rudolf, H. A. Krug von Nidda, F. Mayr, A. Pimenov, V. Tsurkan, A. Loidl, Spin-Driven Phonon Splitting in Bond-Frustrated $ZnCr_2S_4$, Physical Review Letters **97** (8) (2006) 087204. doi:10.1103/PhysRevLett.97.087204.

[132] S. H. Lee, C. L. Broholm, W. Ratcliff, G. Gasparovic, Q. Huang, T. H. Kim, S.-W. Cheong, Emergent Excitations in a Geometrically Frustrated Magnet, Nature **418** (6900) (2002) 856–858. doi:10.1038/Nature00964.

[133] V. Tsurkan, J. Hemberger, A. Krimmel, H. A. Krug von Nidda, P. Lunkenheimer, S. Weber, V. Zestrea, A. Loidl, Experimental evidence for competition between antiferromagnetic and ferromagnetic correlations in $HgCr_2S_4$ **73** (22) (2006) 224442. doi:

10.1103/PhysRevB.73.224442.

[134] S. Weber, P. Lunkenheimer, R. Fichtl, J. Hemberger, V. Tsurkan, A. Loidl, Colossal Magnetocapacitance and Colossal Magnetoresistance in $HgCr_2S_4$, Physical Review Letters **96** (15) (2006) 157202. doi:10.1103/PhysRevLett.96.157202.

[135] Y. Yamashita, K. Ueda, Spin-Driven Jahn-Teller Distortion in a Pyrochlore System, Physical Review Letters **85** (2) (2000) 4960–4963. doi:10.1103/PhysRevLett.85.4960.

[136] O. Tchernyshyov, R. Moessner, S. L. Sondhi, Spin-Peierls phases in pyrochlore antiferromagnets, Physical Review B **66** (6) (2002) 064403–12. doi:10.1103/PhysRevB.66.064403.

[137] H. Martinho, N. O. Moreno, J. A. Sanjurjo, C. Rettori, A. J. García-Adeva, D. L. Huber, S. B. Oseroff, W. Ratcliff, S.-W. Cheong, P. G. Pagliuso, J. L. Sarrao, G. B. Martins, Magnetic properties of the frustrated antiferromagnetic spinel $ZnCr_2O_4$ and the spin-glass $Zn_{1-x}Cd_xCr_2O_4$(x=0.05,0.10), Physical Review B **64** (2) (2001) 024408–6. doi:10.1103/PhysRevB.64.024408.

[138] J. Ostoréro, A. Mauger, M. Guillot, A. Derory, M. Escorne, A. Marchand, Influence of topological frustration on the magnetic properties of the normal oxyspinel $CdFe_2O_4$, Physical Review B **40** (1) (1989) 391–395. doi:10.1103/PhysRevB.40.391.

[139] G. C. Lau, R. S. Freitas, B. G. Ueland, P. Schiffer, R. J. Cava, Geometrical magnetic frustration in rare-earth chalcogenide spinels **72** (5) (2005) 054411–5. doi:10.1103/PhysRevB.72.054411.

[140] P. G. Radaelli, Orbital ordering in transition-metal spinels, New Journal of Physics **7** (2005) 53–53. doi:10.1088/1367-2630/7/1/053.

[141] O. Tchernyshyov, R. Moessner, S. Sondhi, Order by Distortion and String Modes in Pyrochlore Antiferromagnets, Physical Review Letters **88** (6) (2002) 067203. doi:10.1103/PhysRevLett.88.067203.

[142] V. Tsurkan, M. Mücksch, V. Fritsch, J. Hemberger, M. Klemm, S. Klimm, S. Körner, H. A. Krug von Nidda, D. Samusi, E. W. Scheidt, A. Loidl, S. Horn, R. Tidecks, Magnetic, heat capacity, and conductivity studies of ferrimagnetic $MnCr_2S_4$single crystals, Physical Review B **68** (13) (2003) 134434–9. doi:10.1103/PhysRevB.68.134434.

[143] N. Büttgen, J. Hemberger, V. Fritsch, A. Krimmel, M. Mücksch, H. A. K. v. Nidda, P. Lunkenheimer, R. Fichtl, V. Tsurkan, A. Loidl, Orbital physics in sulfur spinels: ordered, liquid and glassy ground states, New Journal of Physics **6** (2004) 191–191. doi:10.1088/1367-2630/6/1/191.

[144] K. Belakroum, Magnetism Et Structure Dans Le Systeme Spinelle $Cu_yCr_yZr_{2-y}Se_4$ (1.00<y<1.30) : Frustation Et Comportement Verre De Spin, Ph.D. thesis, ProQuest (May 2009).
URL http://bu.umc.edu.dz/theses/physique/BEL5343.pdf

[145] A. L. Wessels, R. Czekalla, W. Jeitschko, Structure of the Mercury(II) Chromate(III) $HgCr_2O_4$ and Lattice Constants of the Isotypic Mercury(I) Compounds Hg_2MoO_4 and Hg_2WO_4, Materials Research Bulletin **33** (1) (1998) 95–101. doi:10.1016/S0025-5408(97)00194-3.

[146] H. Ueda, Y. Ueda, Pressure-enhanced direct exchange coupling observed in chromium

spinels **77** (2) (2008) 224411. doi:10.1103/PhysRevB.77.224411.

[147] G.-W. Chern, C. J. Fennie, O. Tchernyshyov, Broken Parity and a Chiral Ground State in the Frustrated Magnet $CdCr_2O_4$ **74** (6) (2006) 060405. doi:10.1103/PhysRevB.74.060405.

[148] J. H. Chung, M. Matsuda, S. B. Lee, K. Kakurai, H. Ueda, T. Sato, H. Takagi, K. P. Hong, S. Park, Statics and Dynamics of Incommensurate Spin Order in a Geometrically Frustrated Antiferromagnet $CdCr_2O_4$, Physical Review Letters **95** (24) (2005) 247204. doi:10.1103/PhysRevLett.95.247204.

[149] M. Hamedoun, A. Wiedenmann, J. L. Dormann, M. Nogues, J. Rossat-Mignod, Magnetic structure and magnetic properties of the spinel solid solutions $ZnCr_{2x}Al_{2-2x}S_4(0.85\leq x\leq 1)$. I. Neutron diffraction study, Journal of Physics C: Solid State Physics **19** (11) (2000) 1783–1800. doi:10.1088/0022-3719/19/11/016.

[150] R. Plumier, Étude par diffraction de neutrons de l'antiferromagnétisme hélicoïdal du spinelle $ZnCr_2Se_4$ en présence d'un champ magnétique, Journal de Physique **27** (3-4) (1966) 213–219. doi:10.1051/jphys:01966002703-4021300.

[151] J. Akimitsu, K. Siratori, G. Shirane, M. Iizumi, T. Watanabe, Neutron Scattering Study of $ZnCr_2Se_4$ with Screw Spin Structure, Journal of the Physical Society of Japan **44** (1) (1978) 172–180. doi:10.1143/JPSJ.44.172.

[152] L. C. Chapon, P. G. Radaelli, Y. S. Hor, M. T. F. Telling, J. F. Mitchell, Non-collinear long-range magnetic ordering in $HgCr_2S_4$, arXiv (2006) 1–10. arXiv:cond-mat/0608031.

[153] G. W. Martin, Exchangestriction in $CdCr_2S_4$ and $CdCr_2Se_4$, Journal of Applied Physics **40** (3) (2003) 1–2. doi:10.1063/1.1657509.

[154] H. Göbel, Local lattice distortions in chromium chalcogenide spinels at low temperatures, Journal of Magnetism and Magnetic Materials **3** (1976) 143–146. doi:10.1016/0304-8853(76)90025-1.

[155] G. Harbeke, H. Pinch, Magnetoabsorption in Single-Crystal Semiconducting Ferromagnetic Spinels, Physical Review Letters **17** (21) (1966) 1090–1092. doi:10.1103/PhysRevLett.17.1090.

[156] K. Wakamura, T. Arai, Effect of magnetic ordering on phonon parameters for infrared active modes in ferromagnetic spinel $CdCr_2S_4$, Journal of Applied Physics **63** (12) (1988) 5824–7. doi:10.1063/1.340321.

[157] A. P. Ramirez, R. J. Cava, J. Krajewski, Colossal magnetoresistance in Cr-based chalcogenide spinels, Nature **386** (6621) (1997) 156–159. doi:10.1038/386156a0.

[158] A. P. Ramirez, Colossal magnetoresistance, Journal of Physics: Condensed Matter **9** (39) (1999) 8171–8199. doi:10.1088/0953-8984/9/39/005.

[159] C. P. Sun, C. L. Huang, C. C. Lin, J. L. Her, C. J. Ho, J. Y. Lin, H. Berger, H. D. Yang, Colossal Electroresistance and Colossal Magnetoresistance in Spinel Multiferroic $CdCr_2S_4$, Applied Physics Letters **96** (1) (2010) 122109. doi:10.1063/1.3368123.

[160] G. Catalan, J. F. Scott, Magnetoelectrics: Is $CdCr_2S_4$ a multiferroic relaxor?, Nature **448** (7156) (2007) E4–E5. doi:10.1038/nature06156.

[161] C. P. Sun, C. C. Lin, J. L. Her, C. J. Ho, S. Taran, H. Berger, B. K. Chaudhuri, H. D. Yang,

Field-dependent dielectric and magnetic properties in multiferroic $CdCr_2S_4$ **79** (2) (2009) 214116. doi:10.1103/PhysRevB.79.214116.

[162] A. P. Ramirez, Geometric frustration: Magic moments, Nature **421** (6) (2003) 483–483. doi:10.1038/421483a.

[163] V. Gnezdilov, P. Lemmens, Y. G. Pashkevich, C. Payen, K. Y. Choi, J. Hemberger, A. Loidl, V. Tsurkan, Phonon Anomalies and Possible Local Lattice Distortions in Giant Magnetocapacitive $CdCr_2S_4$ **84** (4) (2011) 045106. doi:10.1103/Physrevb.84.045106.

[164] P. Lunkenheimer, R. Fichtl, J. Hemberger, V. Tsurkan, A. Loidl, Relaxation Dynamics and Colossal Magnetocapacitive Effect in $CdCr_2S_4$ **72** (6) (2005) 060103. doi:10.1103/PhysRevB.72.060103.

[165] H.-J. Noh, S. Yeo, J. S. Kang, C. L. Zhang, S.-W. Cheong, S.-J. Oh, P. D. Johnson, Jahn-Teller Effect in Spinel Manganites Probed by Soft X-Ray Absorption Spectroscopy, Applied Physics Letters **88** (8) (2006) 081911. doi:10.1063/1.2178474.

[166] S. Behar, P. Gonzalez, P. Agulhon, F. Quignard, D. Świerczyński, New Synthesis of Nanosized Cu-Mn Spinels as Efficient Oxidation Catalysts, Catalysis Today **189** (1) (2012) 35–41. doi:10.1016/j.cattod.2012.04.004.

[167] P. Schiffer, Condensed-Matter Physics: Magnetic Frustration Squeezed Out, Nature **420** (6911) (2002) 35–38. doi:10.1038/420035a.

[168] L. Saviot, E. Duval, N. Surovtsev, J. F. Jal, A. J. Dianoux, Propagating to nonpropagating vibrational modes in amorphous polycarbonate **60** (1) (1999) 18–21. doi:10.1103/PhysRevB.60.18.

[169] G. N. P. Oliveira, A. M. Pereira, A. M. L. Lopes, J. S. Amaral, A. M. dos Santos, Y. Ren, T. M. Mendonça, C. T. Sousa, V. S. Amaral, J. G. Correia, J. P. Araújo, Dynamic Off-Centering of Cr^{3+} Ions and Short-Range Magneto-Electric Clusters in $CdCr_2S_4$ **86** (22) (2012) 224418. doi:10.1103/PhysRevB.86.224418.

[170] S. N. N. Mishra, M. Rots, S. Cottenier, Dynamic lattice distortions in Sr_2RuO_4: microscopic studies by perturbed angular correlation spectroscopy and ab initio calculations., Journal of Physics: Condensed Matter **22** (38) (2010) 385602–385602. doi:10.1088/0953-8984/22/38/385602.

[171] F. Cheng, J. Shen, B. Peng, Y. Pan, Z. Tao, J. Chen, Rapid Room-Temperature Synthesis of Nanocrystalline Spinels as Oxygen Reduction and Evolution Electrocatalysts, Nature Chemistry **3** (1) (2011) 79–84. doi:10.1038/nchem.931.

[172] H. Takagi, S. Niitaka, Highly Frustrated Magnetism in Spinels, in: Introduction to Frustrated Magnetism, Springer, 2011, pp. 155–175.
URL http://link.springer.com/chapter/10.1007/978-3-642-10589-0_7

[173] I. O. Troyanchuk, H. Szymczak, N. V. Kasper, Phase Transitions in the $Mn_x(Zn,Cd)_{1-x}Mn_2O_4$ Spinels, Physica Status Solidi (a) **157** (1) (1996) 159–166. doi:10.1002/pssa.2211570120.

[174] N. Miura, G. Lu, N. Yamazoe, H. Kurosawa, M. Hasei, Mixed Potential Type NO_x Sensor Based on Stabilized Zirconia and Oxide Electrode, Journal of The Electrochemical Society **143** (2) (1996) L33–L35. doi:10.1149/1.1836448.

[175] N. Miura, H. Kurosawa, M. Hasei, G. Lu, N. Yamazoe, Stabilized Zirconia-Based Sensor Using Oxide Electrode for Detection of NO_x In High-Temperature Combustion-Exhausts, Solid State Ionics **86-88** (1996) 1069–1073. doi:10.1016/0167-2738(96)00252-4.

[176] N. Yamazoe, N. Miura, Prospect and Problems of Solid Electrolyte-Based Oxygenic Gas Sensors, Solid State Ionics **86-88** (1996) 987–993. doi:10.1016/0167-2738(96)00239-1.

[177] N. Miura, G. Lu, N. Yamazoe, High-Temperature Potentiometric/Amperometric NO_x Sensors Combining Stabilized Zirconia with Mixed-Metal Oxide Electrode, Sensors and Actuators B: Chemical **52** (1) (1998) 169–178. doi:10.1016/S0925-4005(98)00270-6.

[178] L. Kótai, I. E. Sajó, E. Jakab, G. Keresztury, C. Németh, I. Gács, A. Menyhárd, J. Kristóf, L. Hajba, V. M. Petrusevski, V. Ivanovski, D. Timpu, P. K. Sharma, Studies on the Chemistry of $[Cd(NH_3)_4](MnO_4)_2$. A Low Temperature Synthesis Route of the $CdMn_2O_{4+x}$ Type NO_x and CH_3SH Sensor Precursors, Zeitschrift Fur Anorganische Und Allgemeine Chemie **638** (1) (2011) 177–186. doi:10.1002/zaac.201100467.

[179] X. Li, Y. Xu, C. Wang, Suppression of Jahn-Teller Distortion of Spinel $LiMn_2O_4$ Cathode, Journal of Alloys and Compounds **479** (1–2) (2009) 310–313. doi:10.1016/j.jallcom.2008.12.081.

[180] S. Asbrink, A. Waśkowska, J. S. Olsen, L. Gerward, High-Pressure Phase of the Cubic Spinel $NiMn_2O_4$ **57** (9) (1998) 4972–4974. doi:10.1103/PhysRevB.57.4972.

[181] A. M. L. Lopes, V. S. Amaral, J. G. Correia, J. P. Araújo, Jahn-Teller distortion relaxation across the $LaMnO_{3+\triangle}$ phase diagram, Journal of Physics: Condensed Matter **25** (38) (2013) 385602–385602. doi:10.1088/0953-8984/25/38/385602.

[182] A. M. L. Lopes, J. G. Correia, V. S. Amaral, J. P. Araújo, Local probe studies in the weakly Jahn-Teller distorted $LaMnO_{3.08}$ manganite, Physica Status Solidi (b) **251** (3) (2014) 565–568. doi:10.1002/pssb.201350075.

[183] S. K. Dey, J. C. Anderson, The Magnetic Properties of Cadmium Manganite, Philosophical Magazine **12** (119) (1965) 975–984. doi:10.1080/14786436508228128.

[184] S. K. Dey, Antiferromagnetism of $CdMn_2O_4$, Physics Letters **22** (4) (1966) 375–377. doi:10.1016/0031-9163(66)91185-1.

[185] A. P. B. Sinha, N. R. Sanjana, A. B. Biswas, The Crystal Structure of Cadmium Manganite, $Cd[Mn_2]O_4$, Zeitschrift für Kristallographie **109** (1-6) (1957) 410–421. doi:10.1524/zkri.1957.109.1-6.410.

[186] K. Irani, Effect of Temperature on the Structure of Manganites, Journal of Physics and Chemistry of Solids **23** (6) (1962) 711–727. doi:10.1016/0022-3697(62)90530-9.

[187] K. Oikawa, Structural Phase Transition of the Spinel-Type Oxide $LiMn_2O_4$, Solid State Ionics **109** (1-2) (1998) 35–41. doi:10.1016/s0167-2738(98)00073-3.

[188] X. Liu, C. Prewitt, High-temperature X-ray diffraction study of Co_3O_4: Transition from normal to disordered spinel, Physics and Chemistry of Minerals **17** (2). doi:10.1007/bf00199669.

[189] Y. Gao, J. R. Dahn, The High Temperature Phase Diagram of $Li_{1+x}Mn_{2-x}O_4$ and Its Implications, Journal of The Electrochemical Society **143** (6) (1996) 1783. doi:10.1149/1.1836904.

[190] T. Yamanaka, Y. Takéuchi, Order-Disorder Transition in $MgAl_2O_4$ Spinel at High Temperatures Up to 1700 ºC, Zeitschrift für Kristallographie - Crystalline Materials **165** (1-4) (1983) 65–78. doi:10.1524/zkri.1983.165.1-4.65.

[191] T. Katsura, E. Ito, The System Mg_2SiO_4-Fe_2SiO_4 At High Pressures and Temperatures: Precise Determination of Stabilities of Olivine, Modified Spinel, and Spinel, Journal of Geophysical Research: Solid Earth **94** (B11) (1989) 15663–15670. doi:10.1029/JB094iB11p15663.

[192] D. J. Weidner, H. Sawamoto, S. Sasaki, M. Kumazawa, Single-Crystal Elastic Properties of the Spinel Phase of Mg_2SiO_4, Journal of Geophysical Research: Solid Earth **89** (B9) (1984) 7852–7860. doi:10.1029/JB089iB09p07852.

[193] C. L. Zhang, S. Yeo, Y. Horibe, Y. J. Choi, S. Guha, M. Croft, S.-W. Cheong, S. Mori, Coercivity and Nanostructure in Magnetic Spinel $Mg(Mn,Fe)_2O_4$, Applied Physics Letters **90** (13) (2007) 133123. doi:10.1063/1.2717568.

[194] S. Yeo, Y. Horibe, S. Mori, C. M. Tseng, C. H. Chen, A. G. Khachaturyan, C. L. Zhang, S.-W. Cheong, Solid state self-assembly of nanocheckerboards, Applied Physics Letters **89** (2) (2006) 3120. doi:10.1063/1.2402115.

[195] P. Ghigna, G. Flor, G. Spinolo, An Mn–K Edge XAS Investigation on the Crystal Chemistry of $Cd_{1-\delta}Mn_2O_y$, Journal of Solid State Chemistry **149** (2) (2000) 252–255. doi:10.1006/jssc.1999.8524.

[196] R. H. Buttner, E. N. Maslen, Electron difference density and structural parameters in $CaTiO_3$, Acta Crystallographica Section B **48** (5) (1992) 644–649. doi:10.1107/S0108768192004592.

[197] M. L. Keith, R. Roy, Structural relations among double oxides of trivalent elements, American Mineralogist **39** (1-2) (1954) 1–23.

[198] R. S. Roth, Classification of perovskite and other ABO_3-type compounds, Journal of Research of the National Bureau of Standards **58** (2) (1957) 75. doi:10.6028/jres.058.010.

[199] A. H. Slavney, T. Hu, A. M. Lindenberg, A bismuth-halide double perovskite with long carrier recombination lifetime for photovoltaic applications, Journal of the American Ceramic Society **138** (7) (2016) 2138–2141. doi:10.1021/jacs.5b13294.

[200] L. Pan, G. Zhu, Perovskite Materials - Synthesis, Characterisation, Properties, and Applications, InTech, 2016. doi:10.5772/60469.

[201] M. Guennou, P. Bouvier, G. S. Chen, B. Dkhil, R. Haumont, G. Garbarino, J. Kreisel, Multiple high-pressure phase transitions in $BiFeO_3$ **84** (17) (2011) 174107–10. doi:10.1103/PhysRevB.84.174107.

[202] L. M. W. Daniels, Structures and Properties of Perovskites and Pyrochlores from Hydrothermal Synthesis, Ph.D. thesis, University of Warwick (May 2015).
URL http://webcat.warwick.ac.uk/record=b2861276~S1

[203] M. C. Weber, J. Kreisel, P. A. Thomas, M. Newton, K. Sardar, R. I. Walton, Phonon Raman scattering of $RCrO_3$ perovskites (R=La, Pr, Sm, Gd, Dy, Ho, Yb, Lu) **85** (5) (2012) 054303–054309. doi:10.1103/PhysRevB.85.054303.

[204] A. Durán, E. Verdin, R. Escamilla, F. Morales, R. Escudero, Mechanism of small-polaron

formation in the biferroic $YCrO_3$ doped with calcium, Materials Chemistry and Physics **133** (2-3) (2012) 1011–1017. doi:10.1016/j.matchemphys.2012.02.008.

[205] V. S. Bhadram, D. Swain, R. Dhanya, M. Polentarutti, A. Sundaresan, C. Narayana, Effect of pressure on octahedral distortions in $RCrO_3$ (R = Lu, Tb, Gd, Eu, Sm): the role of R-ion size and its implications, Materials Research Express **1** (2) (2014) 026111. doi:10.1088/2053-1591/1/2/026111.

[206] S. Niitaka, Crystal structure and dielectric and magnetic properties of $BiCrO_3$ as a ferroelectromagnet, Solid State Ionics **172** (1-4) (2004) 557–559. doi:10.1016/j.ssi.2004.01.060.

[207] H. J. Zhao, W. Ren, X. M. Chen, L. Bellaiche, Effect of Chemical Pressure, Misfit Strain and Hydrostatic Pressure on Structural and Magnetic Behaviors of Rare-Earth Orthochromates., Journal of Physics: Condensed Matter **25** (38) (2013) 385604–385604. doi:10.1088/0953-8984/25/38/385604.

[208] B. Rajeswaran, D. I. Khomskii, A. K. Zvezdin, C. N. R. Rao, A. Sundaresan, Field-induced polar order at the Nel temperature of chromium in rare-earth orthochromites: Interplay of rare-earth and Cr magnetism **86** (21) (2012) 1–5. doi:10.1103/PhysRevB.86.214409.

[209] A. K. Raychaudhuri, Metal-insulator transition in perovskite oxides: A low-temperature perspective, Advances in Physics **44** (1) (1995) 21–46. doi:10.1080/00018739500101486.

[210] J. G. Bednorz, K. A. M ller, Possible high T_C superconductivity in the Ba-La-Cu-O system, Zeitschrift für Physik B **64** (2) (1986) 189–193. doi:10.1007/BF01303701.

[211] A. McDannald, M. Jain, Magnetocaloric properties of rare-earth substituted $DyCrO_3$, Journal of Applied Physics **118** (4) (2015) 043904–6. doi:10.1063/1.4927440.

[212] B. Tiwari, A. Dixit, R. Naik, G. Lawes, M. S. R. Rao, Magnetostructural and magnetocaloric properties of bulk $LaCrO_3$ system, Materials Research Express **2** (2) (2015) 1–5. doi:10.1088/2053-1591/2/2/026103.

[213] S. Jin, M. McCormack, T. H. Tiefel, R. Ramesh, Colossal magnetoresistance in La-Ca-Mn-O ferromagnetic thin films (invited), Journal of Applied Physics **76** (10) (1994) 6929–6. doi:10.1063/1.358119.

[214] X. L. Wang, P. Gehringer, W. Lang, H. K. Liu, S. X. Dou, Colossal and constant magnetoresistance over a large temperature range between 230 and 4.2 K in $La_{0.8}Li_{0.2}MnO_3$ prepared by a partial melting technique, Journal of Alloys and Compounds **270** (1) (1998) L10–L12. doi:10.1016/S0925-8388(98)00151-0.

[215] A. Loidl, S. Krohns, J. Hemberger, P. Lunkenheimer, Bananas go paraelectric, Journal of Physics: Condensed Matter **20** (1) (2008) 191001. doi:10.1088/0953-8984/20/19/191001.

[216] V. M. Goldschmidt, Die Gesetze der Krystallochemie, Naturwissenschaften **14** (21) (1926) 477–485. doi:10.1007/BF01507527.

[217] H. Kronmüller, S. Parkin, Handbook of magnetism and advanced magnetic materials: Spintronics and magnetoelectronics, John Wiley & Sons, 2007.

[218] J. R. Sahu, C. R. Serrao, N. Ray, U. V. Waghmare, C. N. R. Rao, Rare earth chromites: a new family of multiferroics, Journal of Materials Chemistry **17** (1) (2006) 42–44. doi:

10.1039/B612093H.

[219] K. Ramesha, A. Llobet, T. Proffen, C. R. Serrao, C. N. R. Rao, Observation of local non-centrosymmetry in weakly biferroic $YCrO_3$, Journal of Physics: Condensed Matter **19** (10) (2007) 102202–9. doi:10.1088/0953-8984/19/10/102202.

[220] E. Bousquet, A. Cano, Non-collinear magnetism in multiferroic perovskites, Journal of Physics: Condensed Matter **28** (12) (2016) 1–28. doi:10.1088/0953-8984/28/12/123001.

[221] C. N. R. Rao, B. Raveau, Transition Metal Oxides: Structure, Properties, and Synthesis of Ceramic Oxides, 2nd Edition, Wiley-VCH.

[222] C. N. R. Rao, B. Raveau, Colossal Magnetoresistance, Charge Ordering and Related Properties of Manganese Oxides, World Scientific, 1998.

[223] Y. Tokura, Colossal Magnetoresistive Oxides, CRC Press, 2000.

[224] E. Dagotto, Nanoscale Phase Separation and Colossal Magnetoresistance, Vol. 136 of Springer Series in Solid-State Sciences, Springer Berlin, Berlin, Heidelberg, 2003. doi:10.1007/978-3-662-05244-0.

[225] C. N. R. Rao, A. K. Kundu, M. M. Seikh, L. Sudheendra, Electronic phase separation in transition metal oxide systems, Dalton Transactions (19) (2004) 3003–3011. doi:10.1039/b406785a.

[226] V. B. Shenoy, C. N. R. Rao, Electronic phase separation and other novel phenomena and properties exhibited by mixed-valent rare-earth manganites and related materials, Philosophical transactions. Series A, Mathematical, physical, and engineering sciences **366** (1862) (2008) 63–82. doi:10.1098/rsta.2007.2140.

[227] G. Catalan, J. F. Scott, Physics and Applications of Bismuth Ferrite, Advanced Materials **21** (24) (2009) 2463–2485. doi:10.1002/adma.200802849.

[228] T. Kimura, S. Kawamoto, I. Yamada, M. Azuma, M. Takano, Y. Tokura, Magnetocapacitance effect in multiferroic $BiMnO_3$ **67** (18) (2003) 180401. doi:10.1103/PhysRevB.67.180401.

[229] N. Ikeda, H. Ohsumi, K. Ohwada, K. Ishii, T. Inami, K. Kakurai, Y. Murakami, K. Yoshii, S. Mori, Y. Horibe, H. Kitô, Ferroelectricity from iron valence ordering in the charge-frustrated system $LuFe_2O_4$, Nature **436** (7054) (2005) 1136–1138. doi:10.1038/nature04039.

[230] C. Serrao, A. Kundu, S. Krupanidhi, U. Waghmare, C. Rao, Biferroic $YCrO_3$ **72** (22) (2005) 220101. doi:10.1103/PhysRevB.72.220101.

[231] B. Kundys, A. Maignan, C. Simon, Multiferroicity with high-T_C in ceramics of the $YBaCuFeO_5$ ordered perovskite, Applied Physics Letters **94** (7) (2009) 072506. doi:10.1063/1.3086309.

[232] N. Hur, S. Park, P. A. Sharma, J. S. Ahn, S. Guha, S.-W. Cheong, Electric polarization reversal and memory in a multiferroic material induced by magnetic fields., Nature **429** (6990) (2004) 392–395. doi:10.1038/nature02572.

[233] I. A. Sergienko, E. Dagotto, Role of the Dzyaloshinskii-Moriya interaction in multiferroic perovskites **73** (9) (2006) 094434. doi:10.1103/PhysRevB.73.094434.

[234] I. A. Sergienko, C. Sen, E. Dagotto, Ferroelectricity in the Magnetic *E*-Phase of

Orthorhombic Perovskites, Physical Review Letters **97** (22) (2006) 227204. doi: 10.1103/PhysRevLett.97.227204.

[235] W. Lee, O. Kahya, C. T. Toh, B. Özyilmaz, J.-H. Ahn, Flexible graphene–PZT ferroelectric nonvolatile memory, Nanotechnology **24** (47) (2013) 475202. doi: 10.1088/0957-4484/24/47/475202.

[236] A. V. Kimel, B. A. Ivanov, R. V. Pisarev, P. A. Usachev, A. Kirilyuk, T. Rasing, Inertia-driven spin switching in antiferromagnets, Nature Physics **5** (10) (2009) 727–731. doi: 10.1038/nphys1369.

[237] E. F. Bertaut, Some Neutron-Diffraction Investigations at the Nuclear Center of Grenoble, Journal of Applied Physics **37** (3) (1966) 1038. doi:10.1063/1.1708325.

[238] S. Geller, E. A. Wood, Crystallographic studies of perovskite-like compounds. I. Rare earth orthoferrites and $YFeO_3$, $YCrO_3$, $YAlO_3$, Acta Crystallographica Section A **9** (7) (1956) 563–568. doi:10.1107/S0365110X56001571.

[239] H. Satoh, S.-i. Koseki, M. Takagi, W. Y. Chung, N. Kamegashira, Heat capacities of $LnCrO_3$ (Ln=rare earth), Journal of Alloys and Compounds **259** (1-2) (1997) 176–182. doi:10.1016/S0925-8388(97)00053-4.

[240] N. Shamir, H. Shaked, S. Shtrikman, Magnetic structure of some rare-earth orthochromites, Physical Review B **24** (11) (1981) 6642–6651. doi: 10.1103/PhysRevB.24.6642.

[241] A. K. Tripathi, H. B. Lal, Electrical transport in rare-earth orthochromites, Materials Research Bulletin **15** (2) (1980) 233–242. doi:10.1016/0025-5408(80)90125-7.

[242] M. Siemons, U. Simon, High throughput screening of the propylene and ethanol sensing properties of rare-earth orthoferrites and orthochromites, Sensors and Actuators B: Chemical **126** (1) (2007) 181–186. doi:10.1016/j.snb.2006.11.022.

[243] K. Tsushima, Magnetic and Magneto-Optical Properties of Some Rare-Earth and Yttrium Orthochromites, Journal of Applied Physics **41** (3) (1970) 1238. doi:10.1063/1.1658890.

[244] B. Rajeswaran, D. I. Khomskii, A. Sundaresan, C. Rao, Ferroelectricity at the Neel Temperature of Chromium in Rare-Earth Orthochromites: Magnetic Jahn-Teller Effect, arXiv.

[245] P. Gupta, R. Bhargava, P. Poddar, Colossal increase in negative magnetization, exchange bias and coercivity in samarium chromite due to a strong coupling between Sm^{3+}-Cr^{3+} spins sublattices, Journal of Physics D: Applied Physics **48** (2) (2015) 025004. doi:10.1088/0022-3727/48/2/025004.

[246] K. R. S. Preethi Meher, A. Wahl, A. Maignan, C. Martin, O. I. Lebedev, Observation of electric polarization reversal and magnetodielectric effect in orthochromites: A comparison between $LuCrO_3$ and $ErCrO_3$ **89** (14) (2014) 144401–7. doi:10.1103/PhysRevB.89.144401.

[247] X. L. Qian, D. M. Deng, Y. Jin, B. Lu, S. X. Cao, J. C. Zhang, Complex ferromagnetic-antiferromagnetic phase transition and glass-like arrest of kinetics in $Sm_{1-x}Ba_xCrO_3$ (x = 0 and 0.1), Journal of Applied Physics **115** (19) (2014) 193902–7. doi:10.1063/1.4876488.

[248] Y. Su, J. Zhang, Z. Feng, L. Li, B. Li, Y. Zhou, Z. Chen, S. Cao, Magnetization reversal and Yb^{3+}/Cr^{3+} spin ordering at low temperature for perovskite $YbCrO_3$ chromites, Journal of Applied Physics **108** (1) (2010) 013905. doi:10.1063/1.3457905.

[249] P. Mandal, A. Sundaresan, C. N. R. Rao, A. Iyo, P. M. Shirage, Y. Tanaka, C. Simon, V. Pralong, O. I. Lebedev, V. Caignaert, B. Raveau, Temperature-induced magnetization reversal in $BiFe_{0.5}Mn_{0.5}O_3$synthesized at high pressure **82** (10) (2010) 100416–4. doi:10.1103/PhysRevB.82.100416.

[250] J. Mao, Y. Sui, X. Zhang, Y. Su, X. Wang, Z. Liu, Y. Wang, R. Zhu, Y. Wang, W. Liu, J. Tang, Temperature- and magnetic-field-induced magnetization reversal in perovskite $YFe_{0.5}Cr_{0.5}O_3$, Applied Physics Letters **98** (19) (2011) 192510–6. doi:10.1063/1.3590714.

[251] H. Adachi, H. Ino, A ferromagnet having no net magnetic moment, Nature **401** (6749) (1999) 148–150. doi:10.1038/43634.

[252] H. Shen, Z. Cheng, F. Hong, J. Xu, S. Yuan, S. Cao, X. Wang, Magnetic field induced discontinuous spin reorientation in $ErFeO_3$ single crystal, Applied Physics Letters **103** (19) (2013) 192404–6. doi:10.1063/1.4829468.

[253] G. V. Subba Rao, G. V. Chandrashekhar, C. N. R. Rao, Are rare earth orthochromites ferroelectric?, Solid State Communications **6** (3) (1968) 177–179. doi:10.1016/0038-1098(68)90027-6.

[254] R. Saha, A. Sundaresan, C. N. R. Rao, Novel features of multiferroic and magnetoelectric ferrites and chromites exhibiting magnetically driven ferroelectricity, Materials Horizons **1** (1) (2014) 20. doi:10.1039/c3mh00073g.

[255] J.-H. Lee, Y. K. Jeong, J. H. Park, M.-A. Oak, H. M. Jang, J. Y. Son, J. F. Scott, Spin-Canting-Induced Improper Ferroelectricity and Spontaneous Magnetization Reversal in SmFeO3, Physical Review Letters **107** (11) (2011) 117201–5. doi:10.1103/PhysRevLett.107.117201.

[256] R. D. Johnson, N. Terada, P. G. Radaelli, Comment on “Spin-Canting-Induced Improper Ferroelectricity and Spontaneous Magnetization Reversal in $SmFeO_3$”, Physical Review Letters **108** (21) (2012) 219701–1. doi:10.1103/PhysRevLett.108.219701.

[257] J.-H. Lee, Y. K. Jeong, J. H. Park, M.-A. Oak, H. M. Jang, J. Y. Son, J. F. Scott, Lee et al.Reply:, Physical Review Letters **108** (21) (2012) 219702–1. doi:10.1103/PhysRevLett.108.219702.

[258] A. K. Zvezdin, A. A. Mukhin, Magnetoelectric interactions and phase transitions in a new class of multiferroics with improper electric polarization, JETP Letters **88** (8) (2009) 505–510. doi:10.1134/S0021364008200083.

[259] A. Ghosh, K. Dey, M. Chakraborty, S. Majumdar, S. Giri, Polar Octahedral Rotations, Cation Displacement and Ferroelectricity in Multiferroic $SmCrO_3$, Europhysics Letters **107** (4) (2014) 47012. doi:10.1209/0295-5075/107/47012.

[260] C. Darie, C. Goujon, M. Bacia, H. Klein, P. Toulemonde, P. Bordet, E. Suard, Magnetic and crystal structures of $BiCrO_3$, Solid State Sciences **12** (5) (2010) 660–664. doi:10.1016/j.solidstatesciences.2008.12.004.

[261] E. Bertaut, J. Mareschal, G. De Vries, R. Aleonard, R. Pauthenet, J. Rebouillat, V. Zarubicka, Etude des propriétés magnétostatiques et des structures magnétiques des chromites des terres rares et d’yttrium, IEEE Transactions on Magnetics **2** (3) (1966) 453–458. doi:10.1109/TMAG.1966.1065951.

[262] E. F. Bertaut, Magnetic structure analysis and group theory, Le Journal de Physique Col-

loques **32** (2-3) (1971) C1–462. doi:10.1051/jphyscol:19711156>.

[263] I. S. Jacobs, Field-Induced Spin Reorientation in $YFeO_3$ and $YCrO_3$, Journal of Applied Physics **42** (4) (1971) 1631–3. doi:10.1063/1.1660372.

[264] W. Yi, Y. Matsushita, Y. Katsuya, K. Yamaura, Y. Tsujimoto, I. A. Presniakov, A. V. Sobolev, Y. S. Glazkova, Y. O. Lekina, N. Tsujii, S. Nimori, K. Takehana, Y. Imanaka, A. A. Belik, High-pressure synthesis, crystal structure and magnetic properties of $TlCrO_3$ perovskite, Dalton Transactions **44** (23) (2015) 10785–10794. doi:10.1039/c4dt03823a.

[265] J. Prado-Gonjal, R. Schmidt, J.-J. Romero, D. Ávila, U. Amador, E. Morán, Microwave-Assisted Synthesis, Microstructure, and Physical Properties of Rare-Earth Chromites, Inorganic Chemistry **52** (1) (2012) 313–320. doi:10.1021/ic302000j.

[266] P. Gupta, P. Poddar, Using Raman and dielectric spectroscopy to elucidate the spin phonon and magnetoelectric coupling in $DyCrO_3$ nanoplatelets, RSC Advances **5** (2015) 10094–10101. doi:10.1039/C4RA11022F.

[267] M. T. Weller, Inorganic Materials Chemistry, 23rd Edition, Oxford University Press, USA, 1994.

[268] W. C. Sheets, E. Mugnier, A. Barnabé, T. J. Marks, K. R. Poeppelmeier, Hydrothermal Synthesis of Delafossite-Type Oxides, Chemistry of Materials **18** (1) (2006) 7–20. doi:10.1021/cm051791c.

[269] A. M. L. Lopes, G. N. P. Oliveira, S. Ferdov, Mild Hydrothermal Synthesis, Isomorphous Substitution, Crystal Structure Characterization and Magnetic Properties of $BaMP_2O_7$ (M = Mn, Cu), Solid State Sciences **26** (2013) 59–64. doi:10.1016/j.solidstatesciences.2013.09.013.

[270] C. Vázquez-Vázquez, M. C. Blanco, M. A. López-Quintela, R. D. Sánchez, J. Rivas, s. B. Oseroff, Characterization of $La_{0.67}Ca_{0.33}MnO_{3\pm\delta}$ particles prepared by the sol–gel route, Journal of Materials Chemistry **8** (4) (1998) 991–1000. doi:10.1039/a707226k.

[271] A. I. Rudenko, A. N. Gershuni, L. V. Kalabina, Some Characteristics of Ethylene Glycol as a Heat-transfer Agent for Closed Two-phase Systems, Journal of Engineering Physics and Thermophysics **70** (5) (1997) 799–804.

[272] C. H. Bamford, Comprehensive Chemical Kinetics, Vol. 22 of Reactions in the Solid State, Elsevier Scientific, 1980.

[273] K. C. Patil, S. T. Aruna, S. Ekambaram, Combustion synthesis, Current Opinion in Solid State & Materials Science **2** (2) (1997) 158–165. doi:Combustionsynthesis.

[274] K. C. Patil, S. T. Aruna, T. Mimani, Combustion synthesis: an update, Current Opinion in Solid State & Materials Science **6** (6) (2002) 507–512. doi:10.1016/S1359-0286(02)00123-7.

[275] G. F. Bassani, G. L. Liedl, P. Wyder, Encyclopedia of Condensed Matter Physics, Elsevier Academic Press, Amsterdam ; Oxford, 2005.

[276] R. E. Dinnebier, S. J. L. Billinge, Powder Diffraction: Theory and Practice, Royal Society of Chemistry, Cambridge, 2008. doi:10.1039/9781847558237.

[277] V. K. Pecharsky, P. Y. Zavalij, Fundamentals of Powder Diffraction and Structural Characterization of Materials, Springer, Boston; London, 2006. doi:10.1007/b106242.

[278] P. P. Ewald, Fifty Years of X-ray Diffraction. , Dedicated to the International Union of Crystallography on the Occasion of the Commemoration Meeting in Munich, July 1962, International Union of Cristallography, Utrecht, 1962.

[279] J. Rodríguez-Carvajal, Magnetic structure determination from powder diffraction using the program FullProf, Applied Crystallography - Proceedings of the XVIII Conference (2001) 30–36. doi:10.1142/9789812811325_0005.

[280] M. A. Rodriguez-Carvajal, P. Tejero-Mateo, J. L. Espartero, J. E. Ruiz-Sainz, A. M. Buendia-Claveria, F. J. Ollero, S. S. Yang, A. M. Gil-Serrano, Determination of the Chemical Structure of the Capsular Polysaccharide of Strain B33, a Fast-growing Soya Bean-nodulating Bacterium Isolated from an Arid Region of China, Biochemical Journal **357** (2001) 505–511.

[281] J. Rodríguez-Carvajal, Magnetic Structure Determination from Powder Diffraction Symmetry Analysis and Simulated Annealing, Materials Science Forum **378-381** (2001) 268–273. doi:10.4028/www.scientific.net/msf.378-381.268.

[282] McCusker, L. B. McCusker, von Dreele, D. E. Cox, D. Louër, Scardi, R. B. von Dreele, P. Scardi, Rietveld refinement guidelines, Journal of Applied Crystallography **32** (1) (2008) 36–50. doi:10.1107/S0021889898009856.

[283] D. S. Donoso, Spin Dependent Transport in Double Perovskites and Magnetic Nanostructures, Ph.D. thesis, ProQuest (Sep. 2005).

[284] S. Amelinckx, Handbook of Microscopy : Applications In Materials Science, Solid-state Physics and Chemistry, VCH, Weinheim ; New York, 1997.

[285] J. Goldstein, Scanning Electron Microscopy and X-ray Microanalysis, Kluwer Academic/Plenum Publishers, New York, 2003. doi:10.1007/978-1-4615-0215-9.

[286] E. Muso, Principle of EDX (Dec. 2007).
URL https://upload.wikimedia.org/wikipedia/commons/9/9f/EDX-scheme.svg

[287] R. E. Sager, Quantum Design – a Brief History, Tech. rep. (Jan. 2010).
URL http://snf.ieeecsc.org/sites/ieeecsc.org/files/EUCAS2009-RN13.pdf

[288] J. Clarke, SQUIDs, Scientific American **271** (2) (1994) 46–53. doi:10.1038/scientificamerican0894-46.

[289] L. Caron, Z. Q. Ou, T. T. Nguyen, D. C. Thanh, O. Tegus, E. Brück, On the determination of the magnetic entropy change in materials with first-order transitions, Journal of Magnetism and Magnetic Materials **321** (21) (2009) 3559–3566. doi:10.1016/j.jmmm.2009.06.086.

[290] J. M. D. Coey, Magnetism and Magnetic Materials, Cambridge University Press, 2010. doi:10.1017/CBO9780511845000.

[291] J. Clarke, A. I. Braginski, The SQUID Handbook, Fundamentals and Technology of SQUIDs and SQUID Systems, Wiley-VCH, Weinheim, 2004. doi:10.1002/3527603646.

[292] G. Schatz, A. Weidinger, Nuclear condensed matter physics: nuclear methods and applications, Wiley, New York, NY, 1996.

[293] A. Lopes, Local probe studies on lattice distortions and electronic correlations in manganites, Ph.D. thesis, University of Aveiro (2006).

[294] T. Butz, S. Saibene, T. Fraenzke, M. Weber, A "TDPAC-Camera", Nuclear Instruments

and Methods in Physics **284** (2) (1989) 417–421. doi:10.1016/0168-9002(89)90311-2.

[295] V. Samokhvalov, PAC investigations of ferromagnetic spinel semiconductors, Ph.D. thesis, ProQuest (Feb. 2003).
URL http://www.qucosa.de/recherche/frontdoor/?tx_slubopus4frontend%5Bid%5D=urn:nbn:de:swb:105-4827279

[296] M. O. Zacate, H. Jaeger, Perturbed Angular Correlation Spectroscopy – A Tool for the Study of Defects and Diffusion at the Atomic Scale, Defect and Diffusion Forum **311** (2011) 3–38. doi:10.4028/www.scientific.net/DDF.311.3.

[297] K. Siegbahn, Alpha-, Beta- and Gamma-Ray Spectroscopy, Vol. 1, Elsevier, 2012.

[298] A. R. Arends, C. Hohenemser, F. Pleiter, H. de Waard, L. Chow, R. M. Suter, Data reduction methodology for perturbed angular correlation experiments, Hyperfine Interactions **8** (1-3) (1980) 191–213. doi:10.1007/BF01026869.

[299] E. N. Kaufmann, R. J. Vianden, The electric field gradient in noncubic metals, Reviews of Modern Physics **51** (1) (1979) 161–214. doi:10.1103/RevModPhys.51.161.

[300] A. C. Beri, T. Lee, T. P. Das, R. M. Sternheimer, Theory of nuclear quadrupole interactions in ionic iron-group compounds-Role of antishielding effects, Hyperfine Interactions **4** (1-2) (1978) 509–514. doi:10.1007/BF01021880.

[301] N. C. Mohapatra, Quadrupole antishielding factors of atoms and ions, Physical Review A **17** (3) (1978) 829–833. doi:10.1103/PhysRevA.17.829.

[302] R. P. Gupta, S. K. Sen, Sternheimer Shielding-Antishielding. II, Physical Review A **8** (3) (1973) 1169–1172. doi:10.1103/PhysRevA.8.1169.

[303] R. P. Gupta, S. K. Sen, Sternheimer Shielding-Antishielding; Rare-Earth Ions, Physical Review A **7** (3) (1973) 850–858. doi:10.1103/PhysRevA.7.850.

[304] H. Chihara, N. Nakamura, Tables of Nuclear Quadrupole Interaction Parameters, Springer Berlin Heidelberg, Berlin, Heidelberg, 2010, pp. 7–15. doi:10.1007/978-3-642-02943-1_2.
URL http://materials.springer.com/lb/docs/sm_lbs_978-3-642-02943-1_2

[305] P. C. Schmidt, K. D. Sen, T. P. Das, A. Weiss, Effect of self-consistency and crystalline potential in the solid state on nuclear quadrupole Sternheimer antishielding factors in closed-shell ions **22** (9) (1980) 4167–4179. doi:10.1103/physrevb.22.4167.

[306] F. D. Feiock, W. R. Johnson, Atomic susceptibilities and shielding factors, Physical Review **187** (1) (1969) 39–50. doi:10.1103/PhysRev.187.39.

[307] P. Raghavan, E. N. Kaufmann, R. S. Raghavan, E. J. Ansaldo, R. A. Naumann, Sign and magnitude of the quadrupole interaction of ^{111}Cd in noncubic metals: Universal correlation of ionic and electronic field gradients, Physical Review B **13** (7) (1976) 2835–2847. doi:10.1103/PhysRevB.13.2835.

[308] I. Solovyev, N. Hamada, K. Terakura, t_{2g} versus all 3*d* localization in LaMO3 perovskites (M=Ti-Cu): first-principles study **53** (11) (1996) 7158–7170. doi:10.1103/physrevb.53.7158.

[309] R. Lizárraga, M. Ramzan, C. M. Araujo, A. Blomqvist, R. Ahuja, E. Holmström, Structural characterization of amorphous $YCrO_3$ from first principles, Europhysics Letters **99** (5)

(2012) 57010–. doi:10.1209/0295-5075/99/57010.

[310] K. P. Ong, P. Blaha, P. Wu, Origin of the light green color and electronic ground state of $LaCrO_3$ **77** (7) (2008) 073102. doi:10.1103/PhysRevB.77.073102.

[311] Z. Yang, Z. Huang, L. Ye, X. Xie, Influence of parameters U and J in the LSDA+U method on electronic structure of the perovskites $LaMO_3$ (M=Cr,Mn,Fe,Co,Ni) **60** (2) (1999) 15674–15682. doi:10.1103/PhysRevB.60.15674.

[312] N. Soltani, S. M. Hosseini, A. Kompany, Nanoscale ab-initio calculations of optical and electronic properties of $LaCrO_3$ in cubic and rhombohedral phases, Physica B: Physics of Condensed Matter **404** (21) (2009) 4007–4014. doi:10.1016/j.physb.2009.07.151.

[313] P. Ravindran, R. Vidya, H. Fjellvåg, A. Kjekshus, Electronic Structure and Excited-state Properties of Perovskite-like Oxides, Journal of Crystal Growth **268** (3-4) (2004) 554–559. doi:10.1016/j.jcrysgro.2004.04.090.

[314] V. G. Nair, C. Ganeshraj, P. N. Santhosh, V. Subramanian, Ab initio calculations of yttrium chromite, AIP Conference Proceedings **1512** (1) (2013) 846–847. doi:10.1063/1.4791303.

[315] P. Hohenberg, W. Kohn, Inhomogeneous Electron Gas, Physical Review **136** (3B) (1964) B864–B871. doi:10.1103/PhysRev.136.B864.

[316] W. Kohn, L. J. Sham, Self-Consistent Equations Including Exchange and Correlation Effects, Physical Review **140** (4A) (1965) A1133–A1138. doi:10.1103/PhysRev.140.A1133.

[317] K. Schwarz, P. Blaha, Solid state calculations using WIEN2k, Computational Materials Science **28** (2) (2003) 259–273. doi:10.1016/S0927-0256(03)00112-5.

[318] P. Blaha, K. Schwarz, G. K. H. Madsen, D. Kvasnicka, J. Luitz, *WIEN2k*, An Augmented Plane Wave plus Local Orbitals Program for Calculating Crystal Properties, Vienna University of Technology (2014).
URL https://indico.cells.es/indico/event/53/material/0/0.pdf

[319] P. Blaha, K. Schwarz, P. Sorantin, S. B. Trickey, Full-potential, linearized augmented plane wave programs for crystalline systems, Computer Physics Communications **59** (2) (1990) 399–415. doi:10.1016/0010-4655(90)90187-6.

[320] J. P. Perdew, K. Burke, M. Ernzerhof, Generalized Gradient Approximation Made Simple, Physical Review Letters **77** (18) (1996) 3865–3868. doi:10.1103/PhysRevLett.77.3865.

[321] J. N. Gonçalves, V. S. Amaral, J. G. Correia, A. Stroppa, A. S. Fenta, A. Baghizadeh, S. Picozzi, Local probing of multiferroics: First-principles study of hyperfine parameters in $YMnO_3$ and YMn_2O_5, EPJ Web of Conferences **75** (2014) 9002. doi:10.1051/epjconf/20147509002.

[322] J. N. Gonçalves, V. S. Amaral, J. G. Correia, A. M. L. Lopes, J. P. Araújo, P. B. Tavares, Hyperfine local probe study of alkaline-earth manganites $SrMnO_3$ and $BaMnO_3$, Journal of Physics: Condensed Matter **26** (21) (2014) 215401–215413. doi:10.1088/0953-8984/26/21/215401.

[323] H. Bayer, Zur Theorie der Spin-Gitterrelaxation in Molekülkristallen, Zeitschrift für Physik **130** (2) (1951) 227–238. doi:10.1007/BF01337696.

[324] T. Kushida, The influence of lattice vibration on the pure quadrupole line, J. Sci. Hiroshima Univ., 1955.

[325] T. Kushida, G. B. Benedek, N. Bloembergen, Dependence of the Pure Quadrupole Resonance Frequency on Pressure and Temperature, Physical Review **104** (1956) 1364–1377. doi:10.1103/PhysRev.104.1364.

[326] T.-C. Wang, Pure nuclear quadrupole spectra of chlorine and antimony isotopes in solids, Physical Review **99** (2) (1955) 566–577. doi:10.1103/PhysRev.99.566.

[327] J. Christiansen, P. Heubes, R. Keitel, W. Klinger, W. Loeffler, W. Sandner, W. Witthuhn, Temperature Dependence of the Electric Field Gradient in Noncubic Metals, Zeitschrift für Physik B **24** (2) (1976) 177–187. doi:10.1007/BF01312998.

[328] P. Jena, Temperature dependence of electric field gradients in noncubic metals, Physical Review Letters **36** (8) (1976) 418–421. doi:10.1103/PhysRevLett.36.418.

[329] M. D. Thompson, P. C. Pattnaik, T. P. Das, Theory of antishielding effects and temperature dependence of field-gradients in metals, Hyperfine Interactions **4** (1-2) (1978) 515–522. doi:10.1007/BF01021881.

[330] P. Jena, J. Rath, Ab initio calculation of the temperature dependence of the electric field gradient in Be **23** (8) (1981) 3823–3827. doi:10.1103/PhysRevB.23.3823.

[331] A. C. Junqueira, A. W. Carbonari, J. M. Filho, R. N. Saxena, Electric Field Gradient at Nb Site in the Intermetallic Compounds Nb_3X (X= Al, In, Si, Ge, Sn) Measured by PAC, Zeitschrift für Naturforschung A **55** (2000) 41–44. doi:10.1515/zna-2000-1-208.

[332] M. A. Nagl, M. Barbosa, U. Vetter, J. G. Correia, H. C. Hofsäss, A new tool for the search of nuclides with properties suitable for nuclear solid state physics based on the Evaluated Nuclear Structure Data Files, Nuclear Instruments and Methods in Physics Research Section A: Accelerators, Spectrometers, Detectors and Associated Equipment **726** (2013) 17–30. doi:10.1016/j.nima.2013.05.045.

[333] P. Raghavan, Table of Nuclear Moments, Atomic Data and Nuclear Data Tables **42** (2) (1989) 189–291. doi:10.1016/0092-640X(89)90008-9.

[334] T. Proffen, K. L. Page, S. E. McLain, B. Clausen, T. W. Darling, J. A. TenCate, S.-Y. Lee, E. Ustundag, Atomic pair distribution function analysis of materials containing crystalline and amorphous phases, Zeitschrift für Kristallographie **220** (12/2005) (2005) 1002–1008. doi:10.1524/zkri.2005.220.12_2005.1002.

[335] S. J. L. Billinge, M. F. Thorpe, Local Structure from Diffraction, Fundamental Materials Research, Springer Science & Business Media, Boston, 1998. doi:10.1007/b119172.

[336] H. P. Klug, L. E. Alexander, x-ray diffraction procedures **77** (1975) 349. doi: 10.1016/S0003-2670(01)95199-2.

[337] S. J. L. Billinge, The atomic pair distribution function: past and present, Zeitschrift für Kristallographie - Crystalline Materials **219** (3) (2004) 117–121. doi:10.1524/zkri.219.3.117.29094.

[338] G. S. Cargill III, Structure of Metallic Alloy Glasses, in: Solid State Physics: Advances in Research and Applications, Elsevier, 1975, pp. 227–320. doi:10.1016/S0081-1947(08)60337-9.
URL http://linkinghub.elsevier.com/retrieve/pii/S0081194708603379

[339] D. Louca, T. Egami, E. L. Brosha, H. Röder, A. R. Bishop, Local Jahn-Teller distortion in

La1-xSrxMnO3 observed by pulsed neutron diffraction **56** (14) (1997) R8475—-R8478. doi:10.1103/PhysRevB.56.R8475.

[340] E. S. Božin, M. Schmidt, A. J. DeConinck, G. Paglia, J. F. Mitchell, T. Chatterji, P. G. Radaelli, T. Proffen, S. J. L. Billinge, Understanding the Insulating Phase in Colossal Magnetoresistance Manganites: Shortening of the Jahn-Teller Long-Bond across the Phase Diagram of $La_{1-x}Ca_xMnO_3$, Physical Review Letters **98** (13) (2007) 137203. doi:10.1103/PhysRevLett.98.137203.

[341] E. S. Božin, C. D. Malliakas, P. Souvatzis, T. Proffen, N. A. Spaldin, M. G. Kanatzidis, S. J. L. Billinge, Entropically stabilized local dipole formation in lead chalcogenides., Science **330** (6011) (2010) 1660–1663. doi:10.1126/science.1192759.

[342] G. H. Kwei, A. C. Lawson, S. J. L. Billinge, S.-W. Cheong, Structures of the Ferroelectric Phases of Barium Titanate, The Journal of Physical Chemistry **97** (10) (1993) 2368–2377. doi:10.1021/j100112a043.

[343] S. Teslic, T. Egami, IUCr, Atomic Structure of $PbZrO_3$ Determined by Pulsed Neutron Diffraction, Acta Crystallographica Section B **54** (6) (1998) 750–765. doi:10.1107/S0108768198003802.

[344] D. P. Olds, P. M. Duxbury, Efficient algorithms for calculating small-angle scattering from large model structures, Journal of Applied Crystallography **47** (3) (2014) 1077–1086. doi:10.1107/S1600576714005925.

[345] X. Qiu, J. W. Thompson, S. J. L. Billinge, PDFgetX2: a GUI-driven program to obtain the pair distribution function from X-ray powder diffraction data, Journal of Applied Crystallography **37** (4) (2004) 678–678. doi:10.1107/S0021889804011744.

[346] C. L. Farrow, P. Juhas, J. W. Liu, D. Bryndin, E. S. Božin, J. Bloch, T. Proffen, S. J. L. Billinge, PDFfit2 and PDFgui: computer programs for studying nanostructure in crystals, Journal of Physics: Condensed Matter **19** (33) (2007) 335219. doi:10.1088/0953-8984/19/33/335219.

[347] J. Rodríguez-Carvajal, Recent advances in magnetic structure determination by neutron powder diffraction, Physica B: Condensed Matter **192** (1-2) (1993) 55–69. doi:10.1016/0921-4526(93)90108-I.

[348] I. S. Chaus, I. A. Sheka, Reactivity of Sulphides, Russian Chemical Reviews **38** (5) (1969) 375–388. doi:10.1070/RC1969v038n05ABEH001748.

[349] T. N. Borovskaya, L. A. Butman, V. G. Tsirelson, M. A. Poraikoshits, T. G. Aminov, R. P. Ozerov, Electron-Density Distribution in $CdCr_2S_4$ and $CdCr_2Se_4$ Crystals - Accurate X-Ray-Diffraction Study, Kristallografiya **36** (3) (1991) 612–616.

[350] V. Tsurkan, Private Communication, Tech. rep. (2010).

[351] T. Goto, T. Kimura, G. Lawes, A. P. Ramirez, Y. Tokura, Ferroelectricity and Giant Magnetocapacitance in Perovskite Rare-Earth Manganites, Physical Review Letters **92** (25) (2004) 257201. doi:10.1103/PhysRevLett.92.257201.

[352] A. M. L. Lopes, J. P. Araújo, V. S. Amaral, J. G. Correia, Y. Tomioka, Y. Tokura, New Phase Transition in the $Pr_{1-x}Ca_xO_3$ System: Evidence for Electrical Polarization in Charge Ordered Manganites, Physical Review Letters **100** (15) (2008) 155702. doi:10.1103/PhysRevLett.100.155702.

[353] G. Xu, J. Wen, C. Stock, P. M. Gehring, Phase Instability Induced by Polar Nanoregions in a Relaxor Ferroelectric System, Nature Materials **7** (7) (2008) 562–566. doi:10.1038/nmat2196.

[354] A. M. L. Lopes, J. P. Araújo, J. J. Ramasco, V. S. Amaral, R. Suryanarayanan, J. G. Correia, Percolative transition on ferromagnetic insulator manganites: Uncorrelated to correlated polaron clusters **73** (2006) 100408–100412. doi:10.1103/PhysRevB.73.100408.

[355] D. Bohm, D. Pines, A Collective Description of Electron Interactions: III. Coulomb Interactions in a Degenerate Electron Gas, Physical Review **92** (3) (1953) 609–625. doi:10.1103/PhysRev.92.609.

[356] H. Winkler, E. Gerdau, ɣ -Angular Correlations Perturbed by Stochastic Fluctuating Fields, Zeitschrift für Physik **262** (5) (1973) 363–376. doi:10.1007/BF01394538.

[357] C. Magen, P. A. Algarabel, L. Morellon, J. P. Araújo, C. Ritter, M. R. R. Ibarra, A. M. Pereira, J. B. Sousa, Observation of a Griffiths-Like Phase in the Magnetocaloric Compound $Tb_5Si_2Ge_2$, Physical Review Letters **96** (1) (2006) 167201. doi:10.1103/PhysRevLett.96.167201.

[358] L. E. Cross, Relaxor ferroelectrics, Ferroelectrics **76** (1) (1987) 241–267. doi:10.1080/00150198708016945.

[359] R. Pirc, R. Blinc, Vogel-Fulcher freezing in relaxor ferroelectrics. doi:10.1103/PhysRevB.76.020101.

[360] F. Bridges, L. Downward, Y. Jiang, T. O'Brien, What Can We Learn from a Detailed Study of the Temperature Dependence of σ, the Width of the Pair Distribution Function?, AIP Conference Proceedings **882** (1) (2007) 59–63. doi:10.1063/1.2644430.

[361] A. Baudry, P. Boyer, Approximation of the Blume's stochastic model by asymptotic models for PAC relaxation analysis, Hyperfine Interactions **35** (1) (1987) 803–806. doi:10.1007/BF02394496.

[362] A. Lahmar, S. Habouti, C.-H. Solterbeck, M. Es-Souni, B. Elouadi, Correlation between structure, dielectric, and ferroelectric properties in $BiFeO_3$-$LaMnO_3$ solid solution thin films, Journal of Applied Physics **105** (1) (2009) 4111. doi:10.1063/1.3063813.

[363] E. L. Nagaev, Colossal Magnetoresistance and Phase Separation in Magnetic Semiconductors, World Scientific (2002). doi:10.1142/9781860949661.
URL http://www.worldscientific.com/worldscibooks/10.1142/p246

[364] V. N. Berzhansky, V. I. Ivanov, A. V. Lazuta, Magnetic Field Effect on the Critical EPR-Dynamics of the Cubic Ferromagnets $CdCr_2Se_4$ and $CdCr_2S_4$, Solid State Communications **44** (6) (1982) 771–775. doi:10.1016/0038-1098(82)90271-x.

[365] E. Haines, R. Clauberg, R. Feder, Short-range magnetic order near the Curie temperature iron from spin-resolved photoemission, Physical Review Letters **54** (9) (1985) 932–934. doi:10.1103/PhysRevLett.54.932.

[366] J. E. Greedan, N. P. Raju, I. J. Davidson, Long Range and Short Range Magnetic Order in Orthorhombic $LiMnO_2$, Journal of Solid State Chemistry **128** (2) (1997) 209–214. doi:10.1006/jssc.1996.7189.

[367] A. K. Bera, S. M. Yusuf, S. K. Banerjee, Short-range magnetic ordering in the geometrically

frustrated layered compound $YBaCo_4O_7$ with an extended Kagomé structure, Solid State Sciences **16** (2013) 57–64. doi:10.1016/j.solidstatesciences.2012.10.028.

[368] M. V. Medvedev, S. M. Goryainova, Short-Range Magnetic Order in a Disordered Ising Ferromagnet, Physica Status Solidi (b) **97** (2) (1980) 415–419. doi:10.1002/pssb.2220970204.

[369] A. N. Ignatenko, A. A. Katanin, V. Y. Irkhin, Strong short-range magnetic order in a frustrated FCC lattice and its possible role in the iron structural transformation, JETP Letters **87** (10) (2008) 555–559. doi:10.1134/S0021364008100093.

[370] A. M. Pereira, L. Morellon, C. Magen, J. Ventura, P. A. Algarabel, M. R. R. Ibarra, J. B. Sousa, J. P. Araújo, Griffiths-Like Phase of Magnetocaloric $R_5(Si_xGe_{1-x})_4$ (R=Gd, Tb, Dy, and Ho) **82** (1) (2010) 172406. doi:10.1103/PhysRevB.82.172406.

[371] X. Qiu, T. Proffen, J. F. Mitchell, S. J. L. Billinge, Orbital Correlations in the Pseudocubic O and Rhombohedral R Phases of $LaMnO_3$, Physical Review Letters **94** (17) (2005) 177203. doi:10.1103/PhysRevLett.94.177203.

[372] Z. Yang, X. Bao, S. Tan, Y. Zhang, Magnetic polaron conduction in the colossal magnetoresistance material $Fe_{1-x}Cd_xCr_2S_4$ **69** (1) (2004) 144407. doi:10.1103/PhysRevB.69.144407.

[373] V. S. Amaral, J. P. Araújo, Y. G. Pogorelov, J. B. Sousa, P. B. Tavares, J. M. Vieira, J. M. B. Lopes dos Santos, A. A. C. S. Lourenco, P. A. Algarabel, Anomalous Low-Field Magnetization in $La_{2/3}Ca_{1/3}MnO_3$ Near the Critical Point: Stable Clusters?, Journal of Applied Physics **83** (11) (1998) 7154–7156. doi:10.1063/1.367859.

[374] W. Jiang, X. Zhou, G. Williams, Y. Mukovskii, R. Privezentsev, The evolution of Griffiths-phase-like features and colossal magnetoresistance in $La_{1-x}Ca_xMnO_3$ ($0.18 \leq x \leq 0.27$) across the compositional metal–insulator boundary, Journal of Physics: Condensed Matter **21** (41) (2009) 415603. doi:10.1088/0953-8984/21/41/415603.

[375] M. Matsuda, K. Ohoyama, S. Yoshii, H. Nojiri, P. Frings, F. Duc, B. Vignolle, G. L. J. A. Rikken, L. P. Regnault, S. H. Lee, H. Ueda, Y. Ueda, Universal Magnetic Structure of the Half-Magnetization Phase in Cr-Based Spinels, Physical Review Letters **104** (4) (2010) 47201. doi:10.1103/PhysRevLett.104.047201.

[376] A. N. Yaresko, Electronic Band Structure and Exchange Coupling Constants in ACr_2X_4 Spinels (A=Zn, Cd, Hg; X=O, S, Se) **77** (11) (2008) 115106. doi:10.1103/PhysRevB.77.115106.

[377] S. Kitani, M. Tachibana, H. Kawaji, Spin-glass-like behavior in ferromagnetic phase of $CdCr_2S_4$, Solid State Communications **179** (0) (2014) 16–19. doi:10.1016/j.ssc.2013.06.004.

[378] D. Ehlers, V. Tsurkan, H. A. K. von Nidda, A. Loidl, Intrinsic Anomalous Magnetic Anisotropy of $CdCr_2S_4$ **86** (17) (2012) 174423. doi:10.1103/PhysRevB.86.174423.

[379] I. Efthimiopoulos, A. Yaresko, V. Tsurkan, J. Deisenhofer, A. Loidl, C. Park, Y. Wang, Multiple Pressure-Induced Transitions in $HgCr_2S_4$, Applied Physics Letters **103** (2) (2013) 1908. doi:10.1063/1.4830225.

[380] Y. M. Xie, Z. R. Yang, Z. T. Zhang, L. H. Yin, X. L. Chen, W. H. Song, Y. P. Sun, S. Q. Zhou, W. Tong, Y. H. Zhang, Magnetic-Polaron–Induced Colossal Magnetocapacitance in

$CdCr_2S_4$, Europhysics Letters **104** (1) (2013) 17005. doi:10.1209/0295-5075/104/17005.

[381] D. Matsunami, A. Fujita, K. Takenaka, M. Kano, Giant barocaloric effect enhanced by the frustration of the antiferromagnetic phase in Mn_3GaN, Nature Materials **14** (1) (2014) 73–78. doi:10.1038/nmat4117.

[382] D. Di Castro, P. Dore, R. Khasanov, H. Keller, P. Mahadevan, S. Ray, D. D. Sarma, P. Postorino, Pressure Effects on the Magnetic Transition Temperature in Ordered Double Perovskites **78** (1) (2008) 184416. doi:10.1103/PhysRevB.78.184416.

[383] Y. Jo, J. G. Park, H. C. Kim, W. Ratcliff, S.-W. Cheong, Pressure-Dependent Magnetic Properties of Geometrically Frustrated $ZnCr_2O_4$ **72** (1) (2005) 184421. doi:10.1103/PhysRevB.72.184421.

[384] V. C. Srivastava, Pressure Dependence of Ferromagnetic Phase Transitions of Chromium Chalcogenide Spinels, Journal of Applied Physics **40** (3) (1969) 1017–1019. doi:10.1063/1.1657510.

[385] A. Mirmelstein, A. Podlesnyak, A. M. dos Santos, G. Ehlers, O. Kerbel, V. Matvienko, A. S. Sefat, B. Saparov, G. J. Halder, J. G. Tobin, Pressure-induced structural phase transition in CeNi: X-ray and neutron scattering studies and first-principles calculations **92** (5) (2015) 054102–8. doi:10.1103/PhysRevB.92.054102.

[386] Y. Fei, A. Ricolleau, M. Frank, K. Mibe, G. Shen, V. Prakapenka, Toward an internally consistent pressure scale., Proceedings of the National Academy of Sciences **104** (22) (2007) 9182–9186. doi:10.1073/pnas.0609013104.

[387] S. N. Kaul, Low-Temperature Magnetization and Spin-Wave Excitations in Amorphous Ni-Rich Transition-Metalmetalloid Alloys **27** (9) (1983) 5761–5774. doi:10.1103/PhysRevB.27.5761.

[388] G. S. Rushbrooke, P. J. Wood, On the Curie points and high temperature susceptibilities of Heisenberg model ferromagnetics, Molecular Physics **1** (3) (1958) 257–283. doi:10.1080/00268975800100321.

[389] M. Tachibana, N. Taira, H. Kawaji, Heat capacity and thermal expansion of $CdCr_2Se_4$and $CdCr_2S_4$, Solid State Communications **151** (23) (2011) 1776–1779. doi:10.1016/j.ssc.2011.08.029.

[390] G. N. P. Oliveira, R. Teixeira, T. M. Mendonça, M. R. Silva, J. G. Correia, A. M. L. Lopes, J. P. Araújo, Local symmetry lowering in $CdMn_2O_4$ spinel, Journal of Applied Physics **116** (22) (2014) 223907. doi:10.1063/1.4903949.

[391] D. Lupascu, S. Habenicht, K. Lieb, M. Neubauer, M. Uhrmacher, T. Wenzel, Relaxation of Electronic Defects in Pure and Doped La_2O_3 Observed by Perturbed Angular Correlations **54** (2) (1996) 871–883. doi:10.1103/PhysRevB.54.871.

[392] A. M. L. Lopes, G. N. P. Oliveira, T. M. Mendonça, J. A. Moreira, A. Almeida, J. P. Araújo, V. S. Amaral, J. G. Correia, Local Distortions in Multiferroic $AgCrO_2$ Triangular Spin Lattice **84** (1) (2011) 14434. doi:10.1103/PhysRevB.84.014434.

[393] M. Neubauer, A. Bartos, K. P. Lieb, D. Lupascu, M. Uhrmacher, T. H. Wenzel, Dynamic hyperfine interaction in Cr_2O_3 observed via pac., Europhysics Letters **29** (2) (1995) 175–180. doi:10.1209/0295-5075/29/2/012.

[394] E. L. Muñoz, M. E. Mercurio, M. R. Cordeiro, L. F. Pereira, A. W. Carbonari, M. Rentería, Dynamic Hyperfine Interactions in ^{111}In(^{111}Cd)-Doped ZnO Semiconductor: PAC Results Supported by Ab Initio Calculations, Physica B: Condensed Matter **407** (16) (2012) 3121–3124. doi:10.1016/j.physb.2011.12.041.

[395] S. Habenicht, D. Lupascu, M. Uhrmacher, L. Ziegeler, K.-P. Lieb, PAC-Studies of Sn-Doped In_2O_3: Electronic Defect Relaxation Following the ^{111}In(EC) ^{111}Cd-Decay, Zeitschrift für Physik B **101** (2) (1996) 187–196. doi:10.1007/s002570050199.

[396] N. P. Barradas, M. Rots, A. A. Melo, J. C. Soares, Magnetic anisotropy and temperature dependence of the hyperfine fields of ^{111}Cd in single-crystalline cobalt **47** (14) (1993) 8763–8768. doi:10.1103/PhysRevB.47.8763.

[397] A. P. B. Sinha, N. R. Sanjana, A. B. Biswas, On the Structure of Some Manganites, Acta Crystallographica Section A **10** (1957) 439–440. doi:10.1107/S0365110X57001450.

[398] S. G. Porji, V. A. Thakur, B. A. Mulla, X-Ray and Transport Properties of the System $Cu_{1-x}Cd_xMn_2O_4$, Procedings of the Indian Natural Science Academy **61** (3 & 4) (1995) 229–235.

[399] A. F. Pasquevich, Electric field gradients at indium sites in spinels measured by perturbed angular correlations, Physica Status Solidi (b) **242** (9) (2005) 1771–1774. doi:10.1002/pssb.200461700.

[400] A. F. Pasquevich, A. M. RodrÍguez, H. Saitovitch, P. R. J. Silva, Electric Fields Gradients at ^{111}In Sites in $CdIn_2O_4$ Spinel, Hyperfine Interactions **158** (1) (2004) 383–387. doi:10.1007/s10751-005-9063-x.

[401] B. J. Evans, Electric Field Gradients at ^{57}Fe in $ZnFe_2O_4$ And $CdFe_2O_4$, The Journal of Chemical Physics **55** (11) (1971) 5282. doi:10.1063/1.1675668.

[402] S. Unterricker, Hyperfine Interactions in Chromium Chalcogenide Spinels, Isotopes in Environmental and Health Studies **27** (2) (1991) 69–72. doi:10.1080/10256019108622471.

[403] G. Catchen, S. Wukitch, D. Spaar, M. Blaszkiewicz, Temperature dependence of the nuclear quadrupole interactions at Ti sites in ferroelectric $PbTiO_3$ and in ilmenite and perovskite $CdTiO_3$: Evidence for order-disorder phenomena. **42** (4) (1990) 1885–1894. doi:10.1103/PhysRevB.42.1885.

[404] G. L. Catchen, S. J. Wukitch, E. M. Saylor, W. Huebner, M. Blaszkiewicz, Investigating phase transitions in ABO_3 perovskites using perturbed angular correlation spectroscopy, Ferroelectrics **117** (1) (1991) 175–195. doi:10.1080/00150199108222416.

[405] S. T. Kshirsagar, Electrical and Crystallographic Studies of the System $Cu_xNi_{1-x}Mn_2O_4$, Journal of the Physical Society of Japan **27** (5) (1969) 1164–1170. doi:10.1143/JPSJ.27.1164.

[406] Y. Zhao, C. W. Dunnill, Y. Zhu, D. H. Gregory, W. Kockenberger, Y. Li, W. Hu, I. Ahmad, D. G. McCartney, Low-Temperature Magnetic Properties of Hematite Nanorods, Chemistry of Materials **19** (4) (2007) 916–921. doi:10.1021/cm062375a.

[407] C. L. Farrow, M. Shaw, H. Kim, P. Juhás, S. J. L. Billinge, Nyquist-Shannon Sampling Theorem Applied to Refinements of the Atomic Pair Distribution Function **84** (13) (2011) 134105. doi:10.1103/PhysRevB.84.134105.

[408] P. Radaelli, M. Marezio, H. Hwang, S. Cheong, B. Batlogg, Charge Localization by Static and Dynamic Distortions of the MnO_6 Octahedra in Perovskite Manganites **54** (13) (1996) 8992–8995. doi:10.1103/PhysRevB.54.8992.

[409] G. N. P. Oliveira, P. Machado, A. L. Pires, A. M. Pereira, J. P. Araújo, A. M. L. Lopes, Magnetocaloric effect and refrigerant capacity in polycrystalline $YCrO_3$, Journal of Physics and Chemistry of Solids **91** (2016) 182–188. doi:10.1016/j.jpcs.2015.12.012.

[410] M. Kumaresavanji, C. T. Sousa, A. Pires, A. M. Pereira, A. M. L. Lopes, J. P. Araújo, Room Temperature Magnetocaloric Effect and Refrigerant Capacitance in $La_{0.7}Sr_{0.3}MnO_3$ Nanotube Arrays, Applied Physics Letters **105** (8) (2014) 083110. doi:10.1063/1.4894175.

[411] S. Thota, Q. Zhang, F. Guillou, U. Lüders, N. Barrier, W. Prellier, A. Wahl, P. Padhan, Anisotropic Magnetocaloric Effect in All-Ferromagnetic ($La_{0.7}Sr_{0.3}MnO_3/SrRuO_3$) Superlattices, Applied Physics Letters **97** (11) (2010) 112506–4. doi:10.1063/1.3488828.

[412] M. Manekar, S. B. Roy, Reproducible room temperature giant magnetocaloric effect in Fe-Rh, Journal of Physics D: Applied Physics **41** (1) (2008) 192004. doi:10.1088/0022-3727/41/19/192004.

[413] V. K. Sharma, M. K. Chattopadhyay, L. S. S. Chandra, S. B. Roy, Elevating the temperature regime of the large magnetocaloric effect in a Ni–Mn–In alloy towards room temperature, Journal of Physics D: Applied Physics **44** (14) (2011) 145002. doi:10.1088/0022-3727/44/14/145002.

[414] V. S. Bhadram, B. Rajeswaran, A. Sundaresan, C. Narayana, Spin-phonon coupling in multiferroic $RCrO_3$ (R-Y, Lu, Gd, Eu, Sm): A Raman study, Europhysics Letters **101** (1) (2013) 17008. doi:10.1209/0295-5075/101/17008.

[415] B. Tiwari, M. K. Surendra, M. S. R. Rao, $HoCrO_3$ and $YCrO_3$: a comparative study, Journal of Physics: Condensed Matter **25** (21) (2013) 216004–216004. doi:10.1088/0953-8984/25/21/216004.

[416] A. H. Cooke, D. M. Martin, M. R. Wells, Magnetic Interactions in Gadolinium Orthochromite, $GdCrO_3$, Journal of Physics C: Solid State Physics **7** (1) (1974) 3133–3144. doi:10.1088/0022-3719/7/17/021.

[417] I. Singh, A. K. Nigam, K. Landfester, R. Muñoz-Espí, A. Chandra, Anomalous Magnetic Behavior Below 10 K in $YCrO_3$ Nanoparticles Obtained Under Droplet Confinement, Applied Physics Letters **103** (18) (2013) 182902. doi:10.1063/1.4826503.

[418] X. Moya, S. Kar-Narayan, N. D. Mathur, Caloric materials near ferroic phase transitions., Nature Materials **13** (5) (2014) 439–450. doi:10.1038/nmat3951.

[419] O. Gutfleisch, M. A. Willard, E. Brück, C. H. Chen, S. G. Sankar, J. P. Liu, Magnetic materials and devices for the 21st century: stronger, lighter, and more energy efficient, Advanced Materials **23** (7) (2011) 821–842. doi:10.1002/adma.201002180.

[420] J. R. Sahu, C. R. Serrao, C. N. R. Rao, Modification of the Multiferroic Properties of $YCrO_3$ and $LuCrO_3$ by Mn Substitution, Solid State Communications **145** (1-2) (2008) 52–55. doi:10.1016/j.ssc.2007.09.027.

[421] G. K. Williamson, W. H. Hall, X-ray line broadening from filed aluminium and wolfram, Acta Metallurgica et Materialia **1** (1) (1953) 22–31. doi:10.1016/0001-6160(53)90006-6.

[422] M. P. Proença, C. T. Sousa, A. M. Pereira, P. B. Tavares, J. O. Ventura, M. Vazquez, J. P. Araújo, Size and surface effects on the magnetic properties of NiO nanoparticles., Physical Chemistry Chemical Physics **13** (20) (2011) 9561–9567. doi:10.1039/c1cp00036e.

[423] I. T. Gomes, B. G. Almeida, J. P. Araújo, $Pr_{0.5}Ca_{0.5}MnO_3$ thin films deposited on $LiNbO_3$ substrates, JEMS 2012 - Joint European Magnetic Symposia **40** (2013) 15010. doi:10.1051/epjconf/20134015010.

[424] M. Udagawa, K. Kohn, N. Koshizuka, T. Tsushima, K. Tsushima, Influence of magnetic ordering on the phonon Raman spectra in $YCrO_3$ and $GdCrO_3$, Solid State Communications **16** (6) (1975) 779–783. doi:10.1016/0038-1098(75)90074-5.

[425] T. Morishita, K. Tsushima, Susceptibility of the Weak Ferromagnets $ErCrO_3$ And $YCrO_3$ Near the Critical Anomaly **24** (1) (1981) 341–346. doi:10.1103/PhysRevB.24.341.

[426] G. L. Alvarez, M. P. Cruz, A. C. Durán, H. Montiel, R. Zamorano, Weak ferromagnetism in the magnetoelectric $YCrO_3$ detected by microwave power absorption measurements, Solid State Communications **150** (35-36) (2010) 1597–1600. doi:10.1016/j.ssc.2010.06.047.

[427] A. Durán, A. M. Arévalo-López, E. Castillo-Martínez, M. García-Guaderrama, E. Moran, M. P. Cruz, F. Fernández, M. A. Alario-Franco, Magneto-Thermal and Dielectric Properties of Biferroic $YCrO_3$ Prepared by Combustion Synthesis, Journal of Solid State Chemistry **183** (8) (2010) 1863–1871. doi:10.1016/j.jssc.2010.06.001.

[428] Y. Su, L. Li, Z. Xing, Z. Feng, D. Deng, B. Kang, S. Cao, J. Zhang, Study of Magnetism and specific-heat properties for multiferroic $YCrO_3$ chromites, in: Nanoscale Phenomena in Polar Materials, IEEE, 2011, pp. 1–4. doi:10.1109/ISAF.2011.6014122.
URL http://doi.org/10.1109/ISAF.2011.6014122

[429] I. Obaidat, B. Issa, Y. Haik, Magnetic Properties of Magnetic Nanoparticles for Efficient Hyperthermia, Nanomaterials **5** (1) (2015) 63–89. doi:10.3390/nano5010063.

[430] J. W. Kim, Y. S. Oh, K. S. Suh, Y. D. Park, K. H. Kim, Specific heat of a $YCrO_3$ single crystal as investigated by a Si–N membrane based microcalorimeter, Thermochimica Acta **455** (1-2) (2007) 2–6. doi:10.1016/j.tca.2006.12.007.

[431] T. Gao, N. Qi, Y. Zhang, T. Zhou, Magnetic properties and large magnetocaloric effect in Laves phase metallic compound, Journal of Physics: Conference Series **568** (4) (2014) 042006–6. doi:10.1088/1742-6596/568/4/042006.

[432] J. Lyubina, R. Schäfer, N. Martin, L. Schultz, O. Gutfleisch, Novel design of $La(Fe,Si)_{13}$ alloys towards high magnetic refrigeration performance, Advanced Materials **22** (33) (2010) 3735–3739. doi:10.1002/adma.201000177.

[433] A. McDannald, L. Kuna, M. Jain, Magnetic and magnetocaloric properties of bulk dysprosium chromite, Journal of Applied Physics **114** (11) (2013) 113904. doi:10.1063/1.4821016.

[434] J. Lyubina, M. D. Kuz'min, K. Nenkov, O. Gutfleisch, M. Richter, D. L. Schlagel, T. A. Lograsso, K. A. J. Gschneidner, Magnetic field dependence of the maximum magnetic entropy change **83** (1) (2011) 012403. doi:10.1103/PhysRevB.83.012403.

[435] S. K. Banerjee, On a Generalised Approach to First and Second Order Magnetic Transitions, Physics Letters **12** (1) (1964) 16–17. doi:10.1016/0031-9163(64)91158-8.

[436] A. Cho, Helium-3 shortage could put freeze on low-temperature research., Science **326** (5954) (2009) 778–779. doi:10.1126/science.326_778.

[437] T. Cai, S. Ju, J. Lee, N. Sai, A. Demkov, Q. Niu, Z. Li, J. Shi, E. Wang, Magnetoelectric Coupling and Electric Control of Magnetization in Ferromagnet/Ferroelectric/Normal-Metal Superlattices **80** (14) (2009) 140415. doi:10.1103/PhysRevB.80.140415.

[438] L. H. Yin, J. Yang, X. C. Kan, W. H. Song, J. M. Dai, Y. P. Sun, Giant magnetocaloric effect and temperature induced magnetization jump in $GdCrO_3$ single crystal, Journal of Applied Physics **117** (1) (2015) 133901. doi:10.1063/1.4916701.

[439] C. M. Araujo, S. Nagar, M. Ramzan, R. Shukla, O. D. Jayakumar, A. K. Tyagi, Y.-S. Liu, J.-L. Chen, P.-A. Glans, C. Chang, A. Blomqvist, R. Lizárraga, E. Holmström, L. Belova, J. Guo, R. Ahuja, K. V. Rao, Disorder-induced Room Temperature Ferromagnetism in Glassy Chromites, Scientific Reports **4** (2014) 1–6. doi:10.1038/srep04686.

[440] P. Gupta, P. Poddar, Study of magnetic and thermal properties of $SmCrO_3$ polycrystallites, RSC Advances **6** (85) (2016) 82014–82023. doi:10.1039/C6RA17203B.

[441] K. Miura, M. Azuma, H. Funakubo, Electronic and Structural Properties of ABO_3: Role of the B-O Coulomb Repulsions for Ferroelectricity, Materials **4** (12) (2011) 260–273. doi:10.3390/ma4010260.

[442] H.-Y. Guo, J. I. L. Chen, Z. G. Ye, A. S. Arrott, Enhanced ferroelectricity and ferromagnetism in $La_{1-x}Bi_xCrO_3$ by Bi^{3+} substitution, Journal of Materials Research **22** (08) (2011) 2081–2086. doi:10.1557/jmr.2007.0263.

[443] T. M. Rearick, G. L. Catchen, J. M. Adams, Combined magnetic-dipole and electric-quadrupole hyperfine interactions in rare-earth orthoferrite ceramics **48** (1) (1993) 224–238. doi:10.1103/PhysRevB.48.224.

[444] R. Dogra, A. C. Junqueira, R. N. Saxena, A. W. Carbonari, J. Mestnik-Filho, M. Moralles, Hyperfine interaction measurements in $LaCrO_3$ and $LaFeO_3$ perovskites using perturbed angular correlation spectroscopy **63** (2) (2001) 224104. doi:10.1103/PhysRevB.63.224104.

[445] A. C. Junqueira, A. W. Carbonari, R. N. Saxena, J. Mestnik-Filho, R. Dogra, Temperature dependence of electric field gradient in $LaCoO_3$ perovskite investigated by perturbed angular correlation spectroscopy, Journal of Physics: Condensed Matter **17** (43) (2005) 6989–6997. doi:10.1088/0953-8984/17/43/016.

[446] A. C. Junqueira, A. W. Carbonari, R. N. Saxena, J. Mestnik-Filho, Study of the local magnetic environment in $LaMnO_3$ perovskite by measuring hyperfine interactions, Journal of Magnetism and Magnetic Materials **272** (2004) E1639–E1641. doi:10.1016/j.jmmm.2003.12.589.

[447] H. Rinneberg, W. Semmler, G. Antesberger, Trapping of defects at ^{111}In impurities In e^--irradiated Al, Physics Letters A **66** (1) (1978) 57–59. doi:10.1016/0375-9601(78)90103-2.

[448] G. S. Collins, Q. M. Wang, J. P. Bevington, Impurity Diffusion in Highly-Ordered Intermetallic Compounds Studied by Nuclear Quadrupole Interactions, Diffusion Foundations **2** (2014) 95–105. doi:10.4028/www.scientific.net/df.2.95.

[449] Y. Li, W. Yan, Y. Li, S. Wang, W. Wang, Z. Bian, L. Xiao, Q. Gong, Direct Observation of Long Electron-Hole Diffusion Distance in $CH_3NH_3PbI_3$Perovskite Thin Film, Scientific

Reports **5** (2015) 14485–14485. doi:10.1038/srep14485.

[450] P. de la Presa, R. E. Alonso, A. Ayala, S. Habenicht, V. V. Krishnamurthy, K. P. Lieb, A. López García, M. Neubauer, M. Uhrmacher, Hyperfine interactions in the perovskites $SrHfO_3$ and $BaHfO_3$ observed with $^{111}In/^{111}Cd$ perturbed angular correlations, Journal of Physics and Chemistry of Solids **60** (6) (1999) 749–757. doi:10.1016/S0022-3697(98)00344-8.

[451] R. A. d. Silva, R. N. Saxena, A. W. Carbonari, G. A. Cabrera-Pasca, Investigation of hyperfine interactions in $GdCrO_3$ perovskite oxide using PAC spectroscopy, Hyperfine Interactions **197** (1) (2010) 53–58. doi:10.1007/s10751-010-0182-7.

[452] A. W. Carbonari, F. H. M. Cavalcante, A. C. Junqueira, D. M. T. Leite, R. N. Saxena, J. Mestnik-Filho, Investigation of hyperfine interactions in RMO_3 (R = La, Nd; M = Cr, Fe) antiferromagnetic perovskite oxides using PAC spectroscopy, Hyperfine Interactions **178** (1-3) (2008) 45–49. doi:10.1007/s10751-008-9654-4.

[453] S. C. Singhal, K. Kendall, High Temperature Solid Oxide Fuel Cells: Fundamentals, Design and Applications, MPG Books Ltd, 2004.

[454] N. Choudhury, L. Walizer, S. Lisenkov, L. Bellaiche, Geometric frustration in compositionally modulated ferroelectrics, Nature **470** (7335) (2011) 513–517. doi:10.1038/nature09752.

[455] G. Lawes, A. Harris, T. Kimura, N. Rogado, R. J. Cava, A. Aharony, O. Entin-Wohlman, T. Yildirim, M. Kenzelmann, C. L. Broholm, A. Ramirez, Magnetically Driven Ferroelectric Order in $Ni_3V_2O_8$, Physical Review Letters **95** (8) (2005) 087205. doi:10.1103/PhysRevLett.95.087205.

APPENDIX A

PDF Results in $CdCr_2S_4$

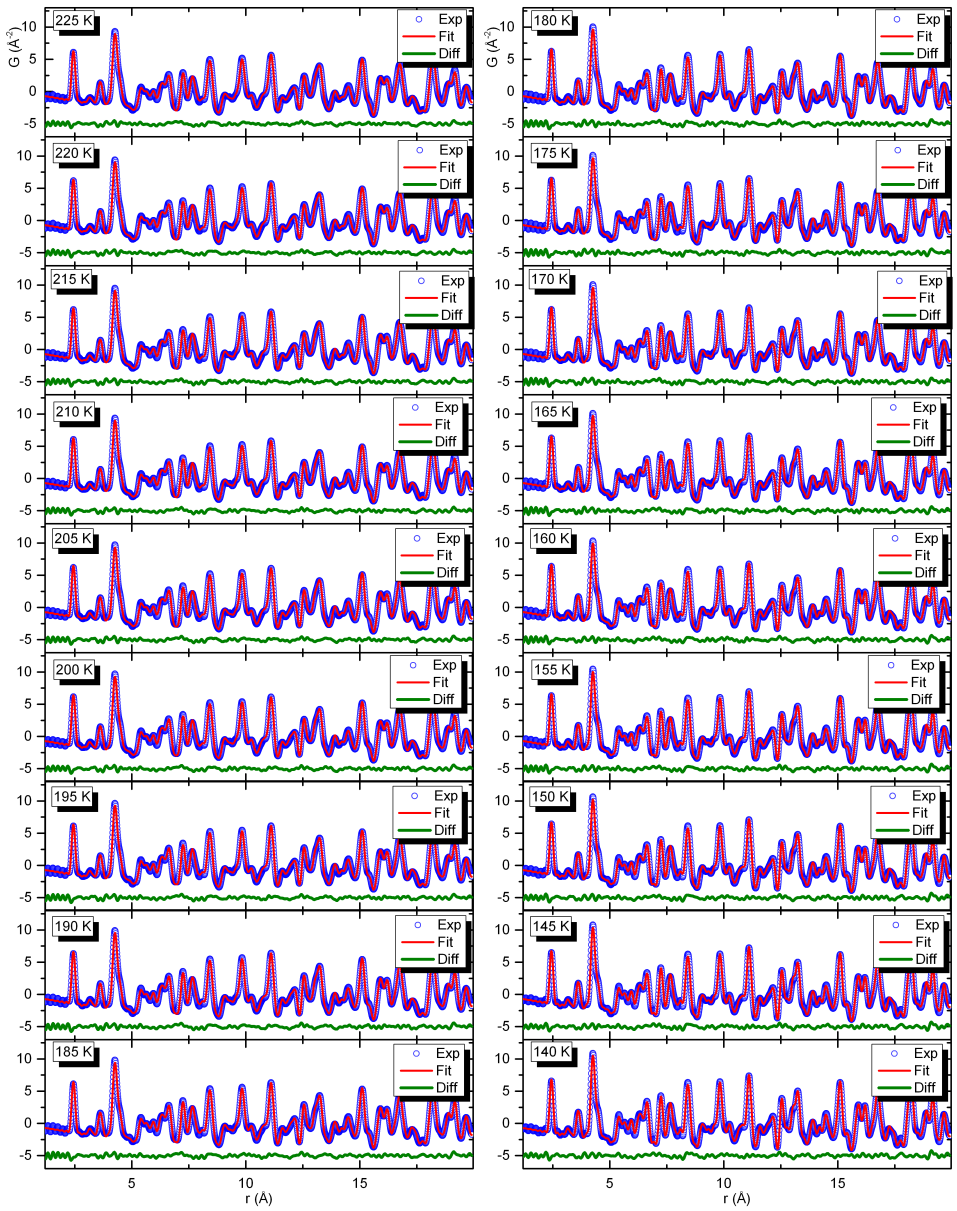

Figure A.1 – PDFs of the spinel $CdCr_2S_4$ structure in the temperature range of 225 K to 140 K.

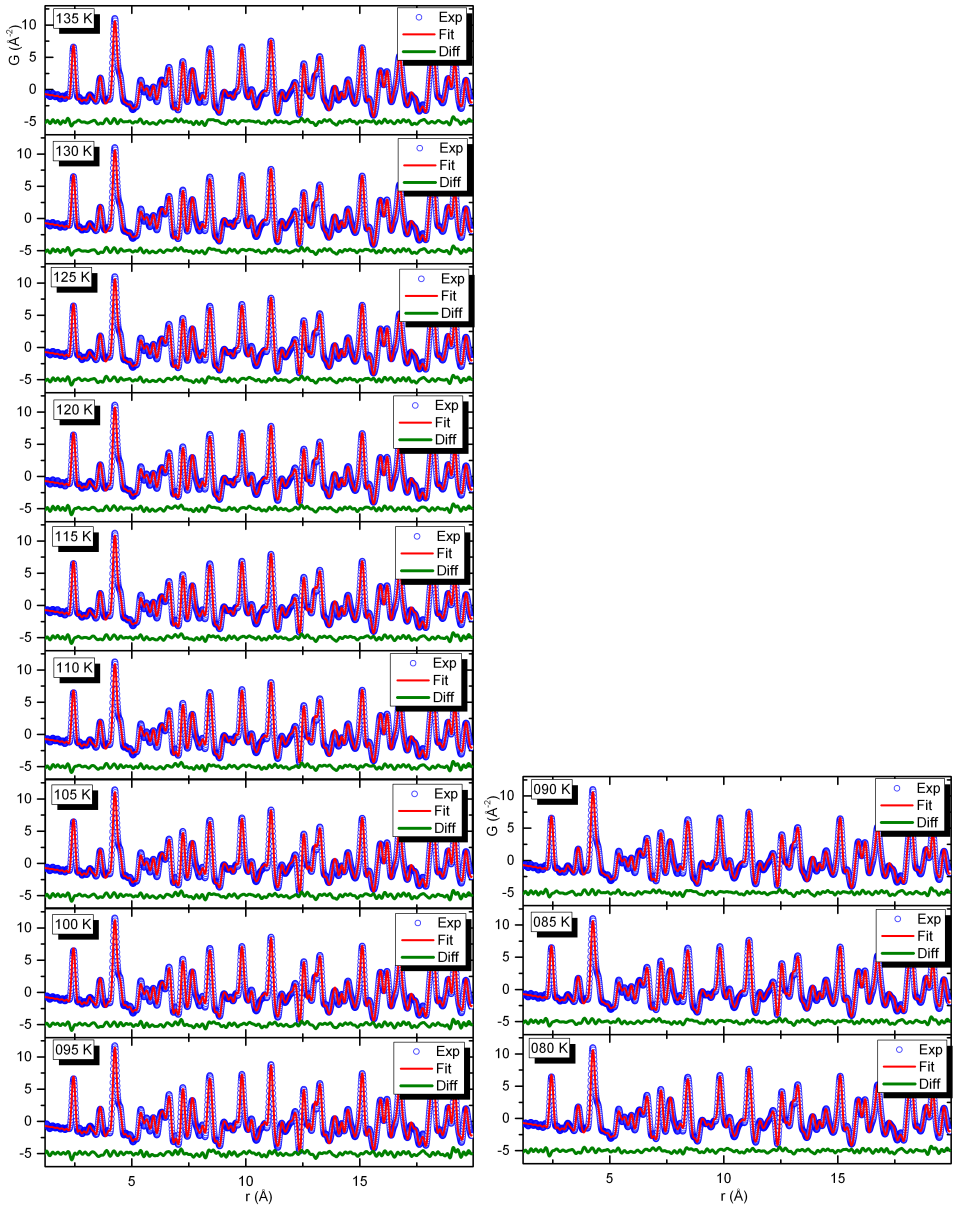

Figure A.2 – PDFs of the spinel $CdCr_2S_4$ structure in the temperature range of 135 K to 80 K.

APPENDIX B

PAC Results in $ErCrO_3$

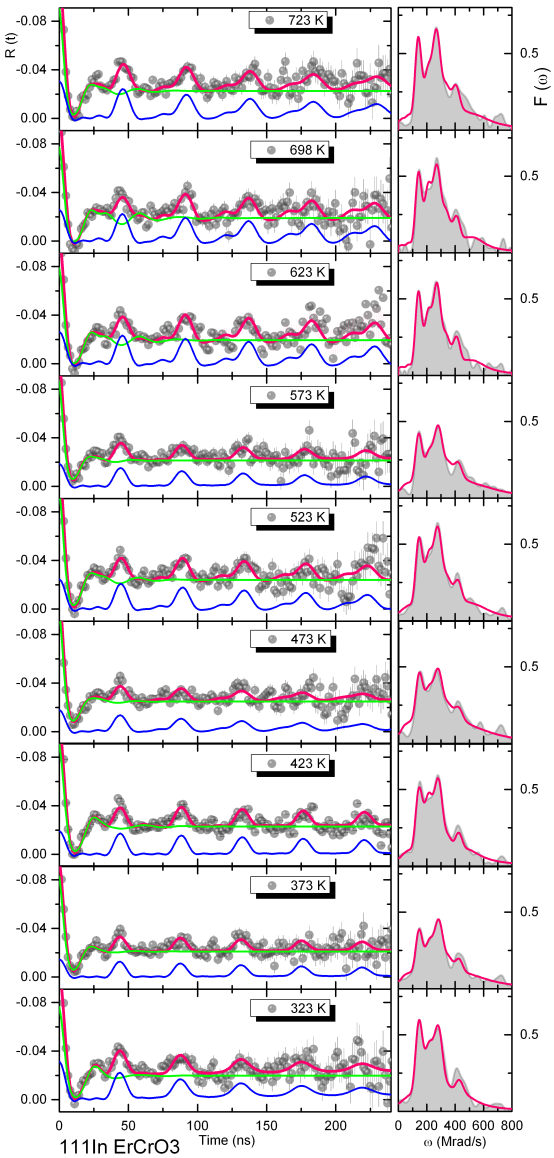

Figure B.1 – Representative R(t) functions, corresponding fits (partial fits, corresponding to each individual EFG, are represented in blue and green) and respective Fourier transform taken in the temperature range of 723 to 323 K for the ^{111}In probe on $ErCrO_3$.

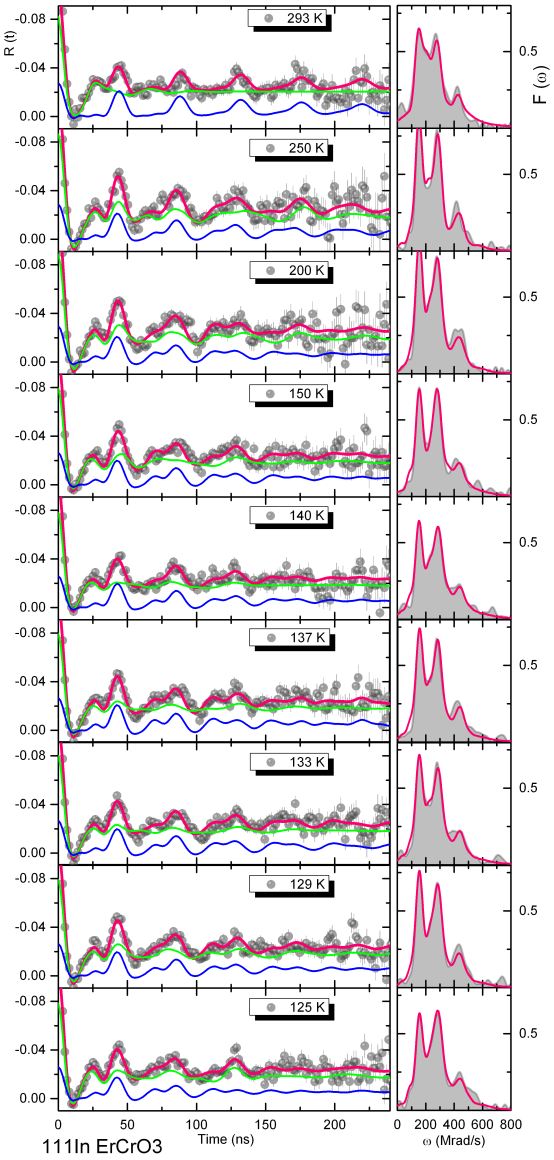

Figure B.2 – Representative R(t) functions, corresponding fits (partial fits, corresponding to each individual EFG, are represented in blue and green) and respective Fourier transform taken in the temperature range of 293 to 125 K for the ^{111}In probe on $ErCrO_3$.

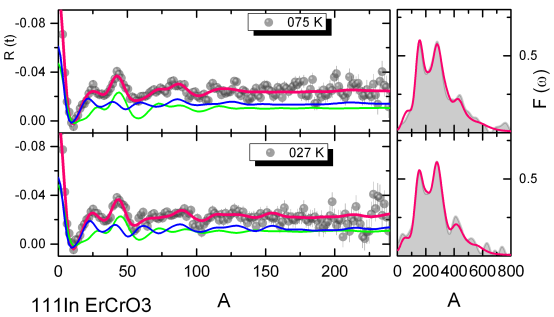

Figure B.3 – Representative R(t) functions, corresponding fits (partial fits, corresponding to each individual EFG, are represented in blue and green) and respective Fourier transform taken in the temperature range of 723 to 323 K for the ^{111}In probe on $ErCrO_3$.

APPENDIX C

PAC Results in $YCrO_3$

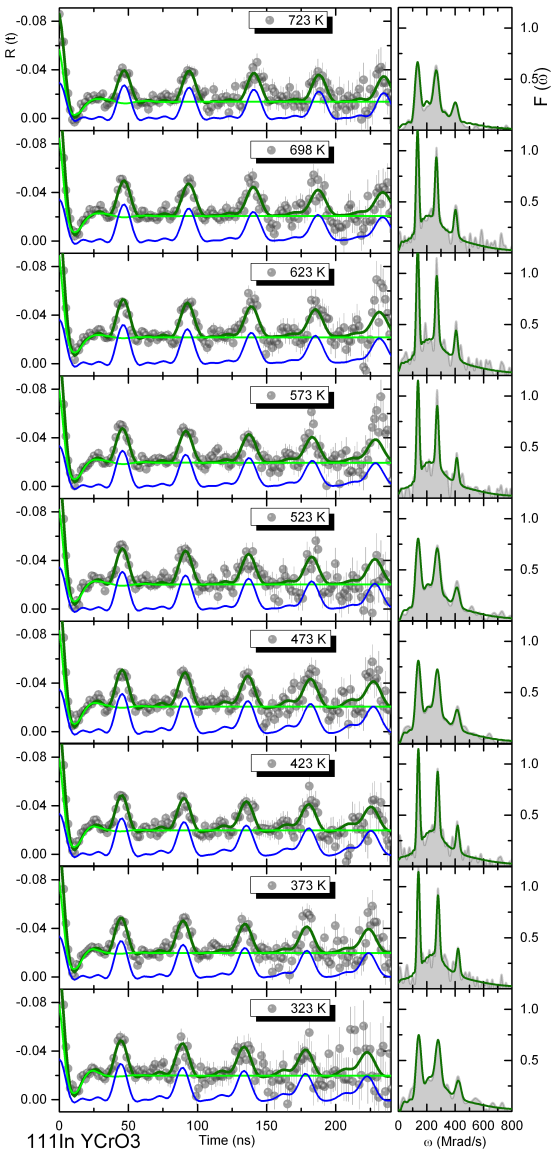

Figure C.1 – Representative R(t) functions, corresponding fits (partial fits, corresponding to each individual EFG, are represented in blue and green) and respective Fourier transform taken in the temperature range of 723 to 323 K for the ^{111}In probe on $YCrO_3$.

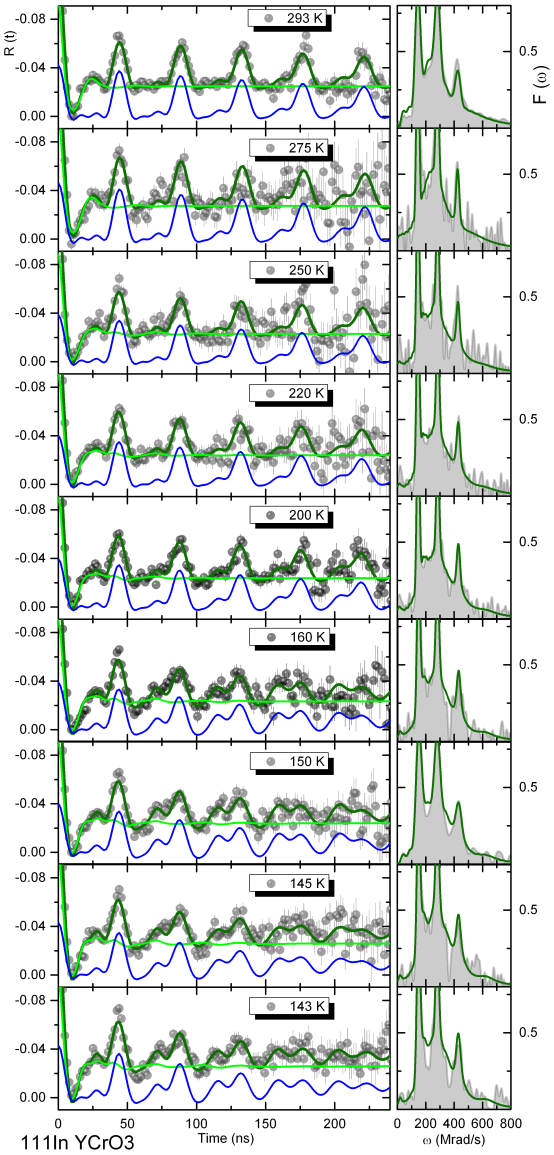

Figure C.2 – Representative R(t) functions, corresponding fits (partial fits, corresponding to each individual EFG, are represented in blue and green) and respective Fourier transform taken in the temperature range of 293 to 143 K for the ^{111}In probe on $YCrO_3$.

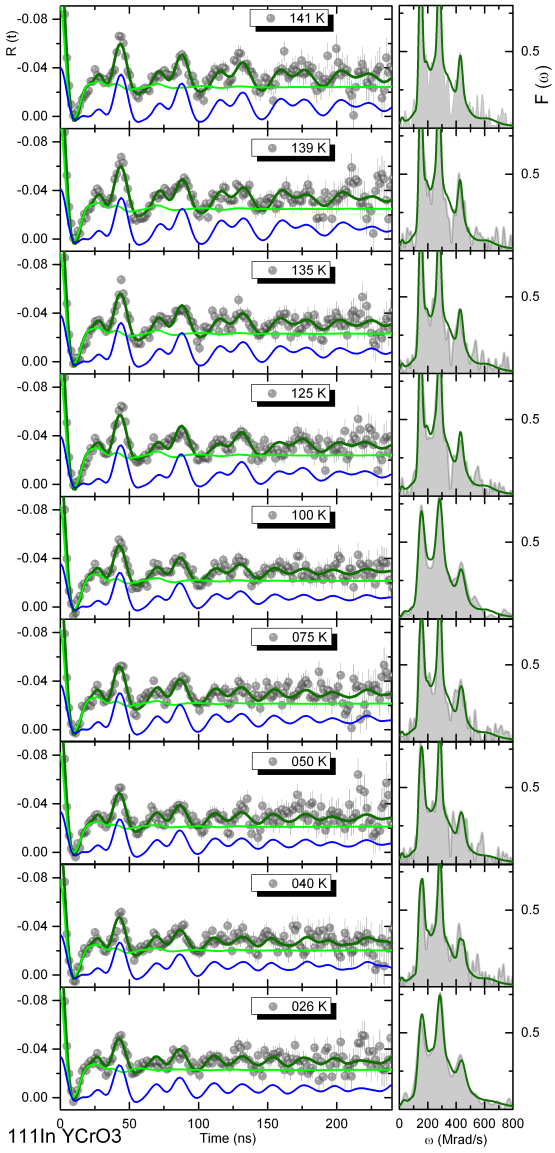

Figure C.3 – Representative R(t) functions, corresponding fits (partial fits, corresponding to each individual EFG, are represented in blue and green) and respective Fourier transform taken in the temperature range of 141 to 26 K for the ^{111}In probe on $YCrO_3$.

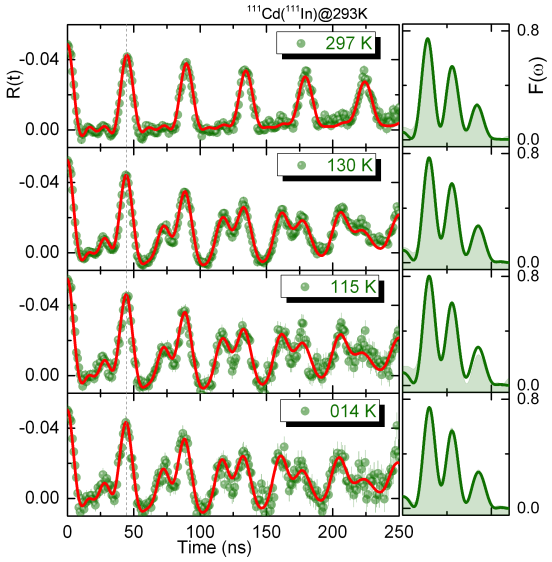

Figure C.4 – Representative R(t) functions, corresponding fits (partial fits, corresponding to each individual EFG, are represented in blue and green) and respective Fourier transform taken at different temperatures for the ^{111}In probe on $YCrO_3$. Results where a slow cooling was performed after the annealing.

APPENDIX D

PAC Results in $SmCrO_3$

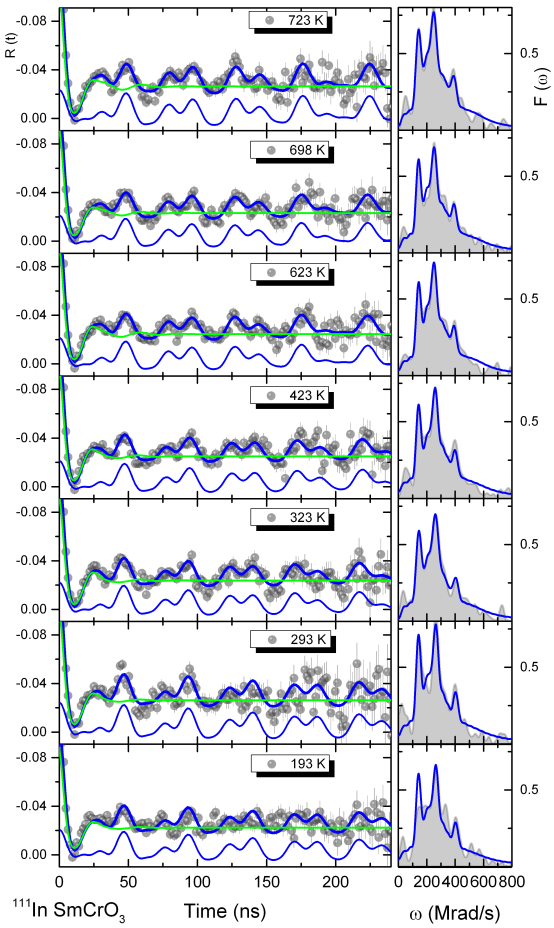

Figure D.1 – Representative R(t) functions, corresponding fits (partial fits, corresponding to each individual EFG, are represented in blue and green) and respective Fourier transform taken in the temperature range of 723 to 193 K for the ^{111}In probe on $SmCrO_3$.

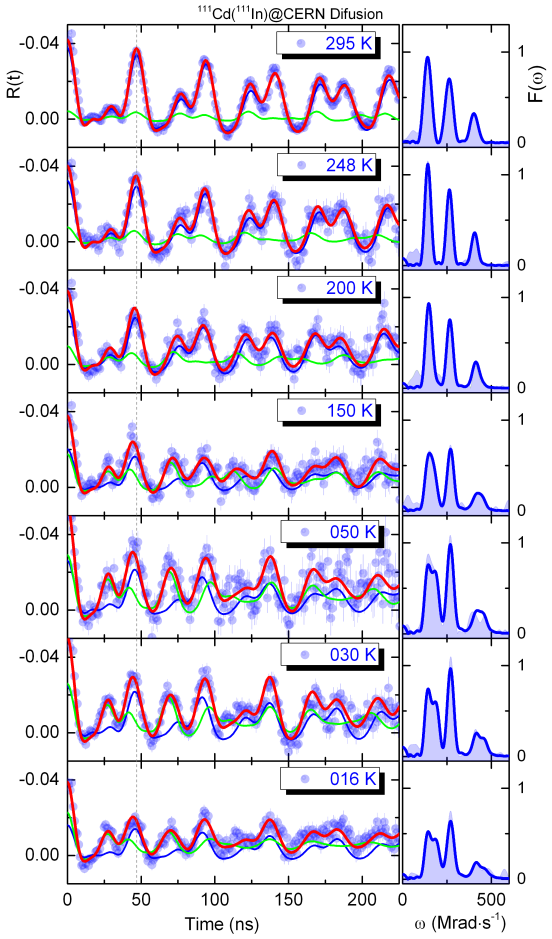

Figure D.2 – Representative R(t) functions, corresponding fits (partial fits, corresponding to each individual EFG, are represented in blue and green) and respective Fourier transform taken at different temperatures and dwell times for the ^{111}In probe on $SmCrO_3$. Results where a slow cooling was performed after the annealing.

APPENDIX E

M(*H*) Curves in $RCrO_3$

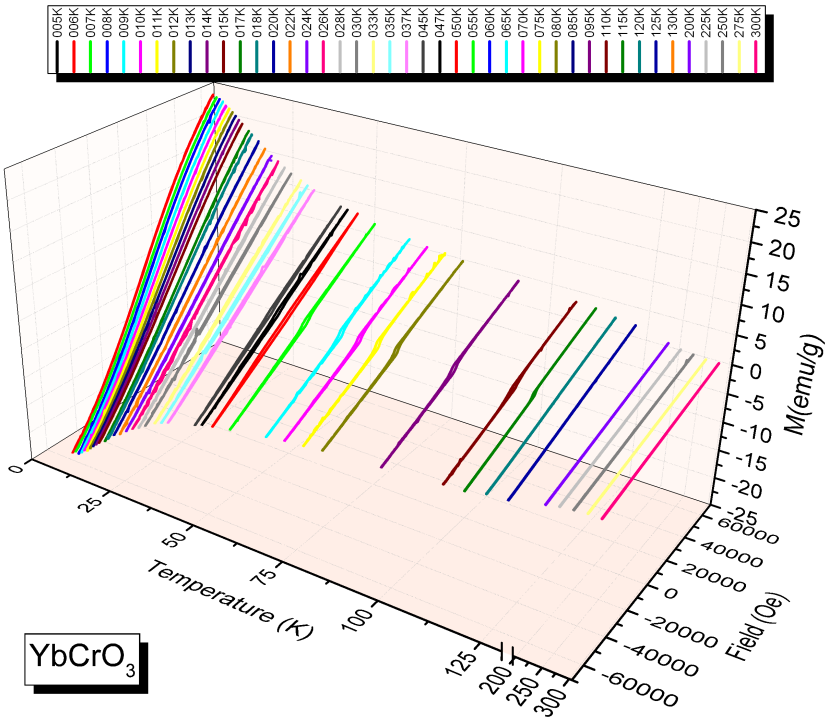

Figure E.1 – Isothermal *M*(*H*) curves as a function of temperature for $YbCrO_3$.

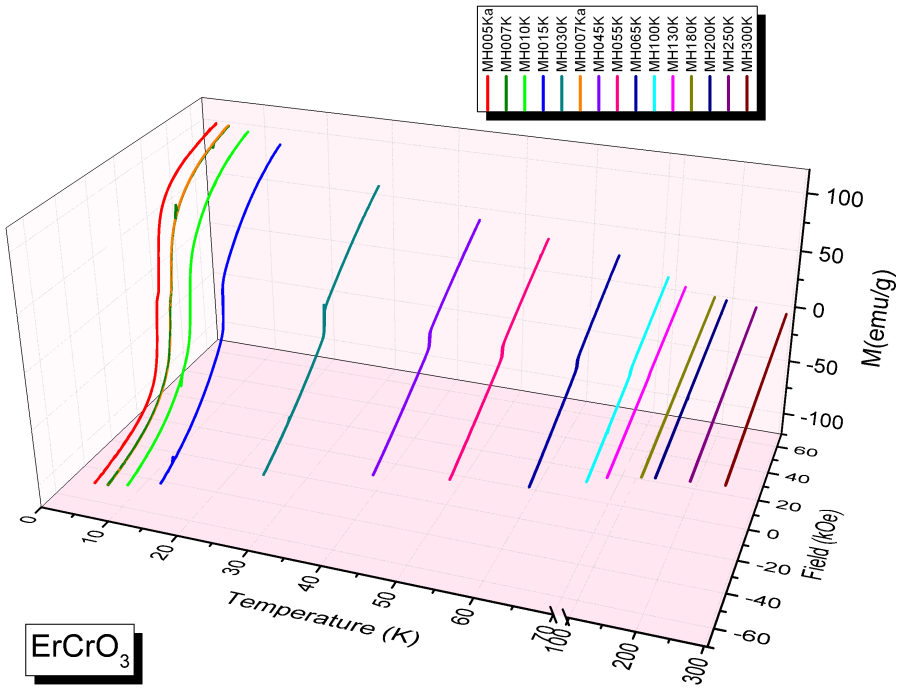

Figure E.2 – Isothermal *M*(*H*) curves as a function of temperature for $ErCrO_3$.

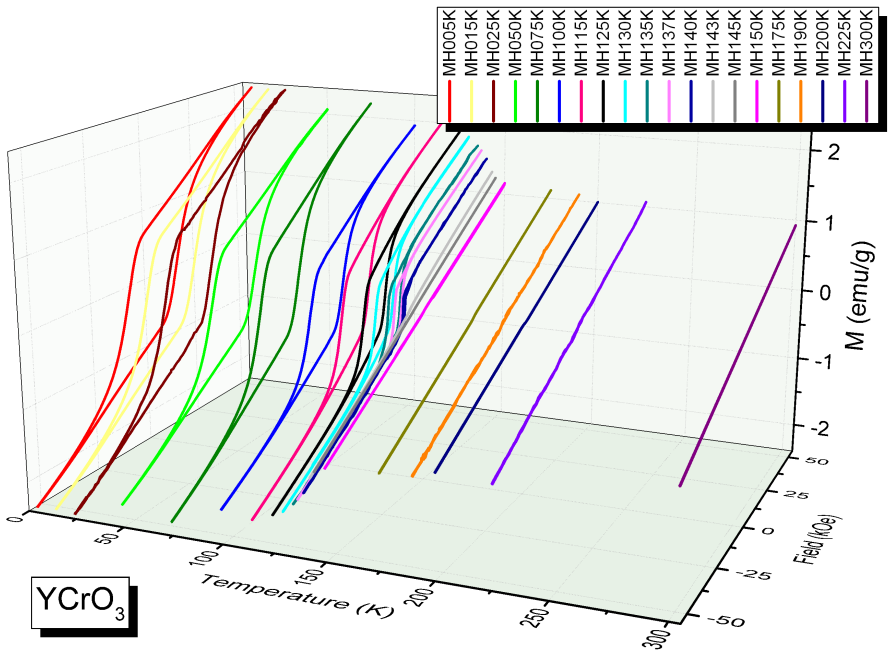

Figure E.3 – Isothermal *M*(*H*) curves as a function of temperature for $YCrO_3$.

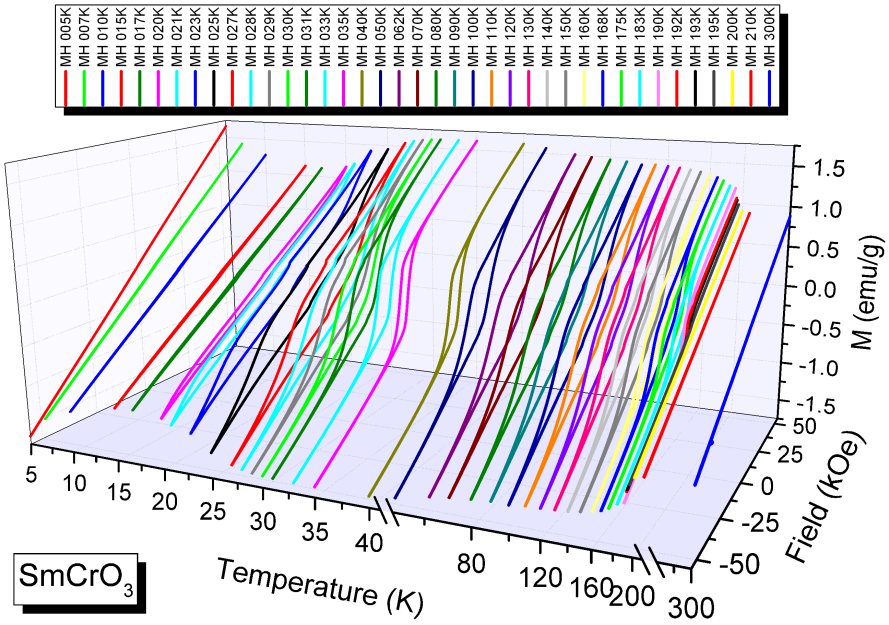

Figure E.4 – Isothermal *M*(*H*) curves as a function of temperature for $SmCrO_3$.